Many-body phases of open Rydberg systems and signatures of topology in quantum gases

Dissertation

Michael Höning

Vom Fachbereich Physik der Technischen Universität Kaiserslautern zur Verleihung des akademischen Grades "Doktor der Naturwissenschaften" genehmigte Dissertation

Betreuer: Prof. Dr. Michael Fleischhauer
Zweitgutachter: Dr. Thomas Pohl
Drittgutachter: Prof. Dr. Sebastian Eggert

Datum des wissenschaftlichen Aussprache: 19. Dezember 2014
D 386

Contents

Abstract

For a long time quantum optics and condensed matter physics appeared to exist at different ends of the spectrum of physics. Whereas the first deals with single quanta of light and matter and attempts to control every microscopic degree of freedom with meticulous precision, the second is all about complex many body systems and abstract concepts for their description and classification. At the intersection of control and complexity, experiments with ensembles of ultra cold atoms have emerged in the last 20 years, beginning with the realization of the first Bose-Einstein condensate of atoms in 1995 [1]. The Mott insulator to superfluid transition observed in 2002 [2] was the proof of principle that strongly correlated phases of matter can be realized and studied with the tools of quantum optics [3].

Major additions were made to the toolbox of cold atom experiments in recent years and enable experiments beyond the study of conventional order. This work rests on improvements like novel detection techniques at sub micron resolution [4, 5], the implementation of artificial gauge fields [6] and the introduction of long range interactions [7], in combination with a high degree of control and flexibility. In this thesis I study phases of matter beyond conventional order; I propose experiments that probe and characterize topological order and explore the emergence of order in non equilibrium ensembles of strongly interacting atoms excited to Rydberg states.

Topological order is at the heart of materials relevant for modern technology and schemes based on topological excitations are among the most promising candidates for the realization of a robust quantum computer [8]. The discovery of the quantum Hall effect revealed that the classification of phases by symmetry breaking and local order parameters is not sufficient and has to be complemented by the notion of topological order. The natural domain of topology is within condensed matter and new material classes such as Chern insulators have been developed based on the deeper understanding of topological order. Progress in experiments with cold atoms makes them promising candidates to study topological systems in a more controllable way. I here address two questions: First of all, how to prepare and detect symmetry protected topological order in cold atom experiments and second, how to classify topology in strongly interacting systems. One of the simplest models with a topological band structure is the Su Schrieffer Heeger (SSH) model for non interacting fermions. In Chapter 2 I show for the bosonic analogue that edge states emerge as a signature of topology, but that the bulk boundary correspondence for free fermion systems must be revised. The addition of long range interaction to the SSH model gives rise to fractional Chern numbers and fractional quasiparticle excitations. The classification scheme introduced in Chapter 3 requires a combination of symmetry breaking and topological order. Motivated by recent experimental progress towards the observation of the Hofstadter butterfly for non interaction particles [9], I propose a closely related experiment in Chapter 4 towards the realization of a fractional Chern insulator in the thin-torus limit.

Experiments with ultra cold atoms can go beyond equilibrium due to a very controlled environment. It has been proposed to engineer the interaction with reservoirs and thereby introduce dissipation, which drives the system towards strongly correlated states in non equilibrium [10]. The classification of these non equilibrium stationary states is the subject of ongoing research. For one dimensional systems of non interacting fermions I demonstrate the classification of critical transitions towards long range ordered states for a specific type of reservoir coupling in Chapter 5.

Since the advent of atomic physics, highly excited states of atoms, so called Rydberg states, have been of interest for their extraordinary properties. They feature near macroscopic sizes,

are very susceptible to external fields and have long spontaneous emission times. Rydberg states are one of the most promising candidates towards the addition of long range interaction to the toolbox of ultra cold atom experiments. Two approaches can be distinguished regarding the application of this tool. The conventional ansatz is to prepare exotic phases such as supersolids or models with emergent gauge fields at low temperature in equilibrium [11, 12]. I follow a second avenue and show that order can emerge in non equilibrium as a consequence of the competition between interaction and dissipation.

The strong interaction of two Rydberg atoms suppresses the excitation of atoms in close distance, an effect known as Rydberg blockade. I address the question, whether this short range blockade can give rise to a long range crystalline order of excited atoms in the stationary state of a driven system. In Chapter 6, I develop an analytic model, which shows the absence of such order in one dimensional lattice system, but make positive predictions for higher dimensions. I demonstrate in Chapter 7 that by using sophisticated driving schemes, a long range ordered state of Rydberg excited atoms can indeed be prepared in two dimensional systems. The associated non-equilibrium phase transition, displays a critical slow down of relaxation and shows the signatures of a classical Ising phase transition. In Chapter 8, I generalize the model towards continuum systems and show that the spatial correlations in a gas of van der Waals interacting atoms can be understood in terms of a much simpler hard rod potential.

The progress in the field of cold atoms is a collaborative endeavor of experiment and theory. The experimental group of Herwig Ott demonstrated the preparation and excitation of a mesoscopic superatom based on Rydberg blockade [13] and I supported them with theoretical analysis and contributed to the deeper understanding of the experiment. Good agreement between theoretical simulations and experimental measurements was reached and a variety of effects from blockade to antiblockade were observed and are discussed in Chapter 9.

Antiblockade naturally arises for off resonant excitation of Rydberg states. An excited atom can facilitate the excitation of other atoms by shifting them into resonance with its interaction and thus potentially gives rise to an avalanche effect. Experimental results [14] seem to suggest the emergence of bistable behavior in driven Rydberg gases, which has not been seen in numerical studies so far. In Chapter 10, I present results on a mean field approach for off resonantly driven systems and show that very good agreement can be achieved regarding the density of excitations and their fluctuations in comparison with exact numeric calculations. In accordance with other theoretical results [15], I find no evidence for bistability in the stationary state of a continuum gas.

The dissipative transverse Ising model is an extreme example for antiblockade in a one dimensional lattice system. I here show that numerical methods based on matrix product states enable to simulate the dynamics towards the stationary state under the influence of dissipation, whereas they fail in the purely unitary case. Using this tool I go beyond previous studies and discuss the emergence of long range correlations and bistability in Chapter 11.

The long range interaction of Rydberg excited atoms bears great potential beyond the study of non equilibrium many body physics. One example I touch in Chapter 12 is the combination with coherent control of light propagation. This promises the realization of strongly interacting photons on a few particle level with important applications for quantum information technology. In [16] the creation of a Wigner crystal of photons with interaction mediated by Rydberg excited atoms was proposed. I here show the feasibility of this approach, by exact numerical solution for the case of two excitations. My analysis goes beyond perturbative effects of the interaction and I explain how the strong forces between excited atoms, give rise to resonances at short distances.

Kurzfassung

Quantenoptik und Festkörperphysik wurden für lange Zeit als Disziplinen betrachtet die an verschiedenen Enden des Spektrums der Physik liegen. Während die erste Disziplin sich mit der präzisen Kontrolle der mikroskopischen Freiheitsgrade einzelner Photonen und Atome beschäftigte, entwickelte die zweite abstrakte Konzepte für die Beschreibung und Klassifizierung von komplexen Vielteilchensystemen. Erst in den letzten 20 Jahren haben sich an der Schnittstelle von Kontrolle und Komplexität, durch Experimente mit ultra kalten Quantengasen interessante Synergien eröffnet, begonnen mit der Realisierung des ersten Bose-Einstein-Kondensats von Atomen im Jahr 1995 [1]. Die Beobachtung des Phasenübergangs vom Mott-Isolator zum Superfluid [2] demonstrierte, dass stark korrelierte Phasen der Materie mit den Werkzeugen der Quantenoptik untersucht werden können [3].

In den vergangenen Jahren wurden die Möglichkeiten von Experimenten mit kalten Atomen maßgeblich erweitert, was die Untersuchung von stark wechselwirkenden Systemen über gewöhnliche Gleichgewichtsordnung hinaus ermöglicht. Diese Arbeit beruht auf neuen Detektionsmethoden mit Auflösungen unter einem Mikrometer [4, 5], der Realisierung von künstlichen Eichfeldern [6] und der Verfügbarkeit von langreichweitiger Wechselwirkung [7], kombiniert mit dem hohen Maß an Kontrolle und Flexibilität, das die Quantenoptik auszeichnet. In dieser Arbeit untersuche ich Phasen der Materie, die über gewöhnliche Ordnung hinausgehen; ich schlage Experimente vor, die topologische Ordnung detektieren und charakterisieren, und untersuche das Auftreten von Ordnung in atomaren Gasen stark wechselwirkender Rydberg Atome außerhalb des Gleichgewichts.

Topologische Ordnung ist die Grundlage für neue Materialien und moderne Technologien. Auf topologischen Anregungen basierende Algorithmen, zählen zu den vielversprechendsten Kandidaten für die Realisierung eines fehlertoleranten Quantencomputers [8]. Die Entdeckung des Quanten-Hall-Effekts zeigte, dass die Klassifizierung von Phasen durch Symmetriebrechungen und lokale Ordnungsparameter, um den Begriff der topologischen Ordnung erweitert werden muss. Die Motivation für die Untersuchung von topologischer Ordnung geht von Festkörpersystemen aus und ein tieferes Verständnis hat bereits zur Entwicklung neuer Material Klassen wie dem Chern-Isolator geführt. Der Fortschritt von Experimenten mit kalten Atomen macht diese zu vielversprechenden Kandidaten für die kohärente Kontrolle von Systemen mit topologischer Ordnung. Ich fokussiere mich in dieser Arbeit auf zwei Fragestellungen: Wie kann Symmetrie-geschützte topologische Ordnung in kalten Gasen erzeugt und beobachtet werden und im Weiteren, wie können stark wechselwirkende Systeme klassifiziert werden? Eines der einfachsten Modelle mit einer topologischen Bandstruktur ist das Su-Schriefer-Heeger (SSH) Modell für nicht wechselwirkende Fermionen. In Kapitel 2 zeige ich für das analoge bosonische Modell, dass Randzustände als Signatur für topologische Ordnung dienen können, aber dass die *bulk-boundary* Korrespondenz, bekannt von Systemen freier Fermionen, neu formuliert werden muss. Unter Hinzunahme von langreichweitiger Wechselwirkung im SSH-Modell, ergeben sich neue inkompressible Phasen mit fraktionaler Chern-Zahl und fraktionalen Quasiteilchen Anregungen. Die Klassifizierung der verschiedenen Phasen dieses Systems in Kapitel 3 erfordert sowohl das Konzept der Symmetriebrechung als auch das der topologischen Ordnung. Angeregt durch experimentelle Fortschritte im Hinblick auf die Messung des Hofstadter-*butterfly* für nicht wechselwirkende Teilchen [9], schlage ich in Kapitel 4 ein Experiment zur Realisierung eines fraktionalen Chern-Isolators im *thin-torus* Limit vor.

Experimente mit kalten Atomen ermöglichen eine nahezu perfekte Kontrolle der Wechselwirkung mit der Umgebung und somit die Untersuchung von Systemen außerhalb des Gleichgewichts. In [17] wurde vorgeschlagen die Wechselwirkung mit Reservoiren so zu gestal-

ten, dass die kontrollierte Dissipation einen stark korrelierten Zustand außerhalb des Gleichgewichts präpariert. Eine vollständige Klassifizierung solcher Nicht-Gleichgewichts Zustände steht noch aus. Für eindimensionale Systeme nicht wechselwirkender Fermionen mit spezieller Form der Reservoir-Kopplung, zeige ich in Kapitel 5 eine Klassifizierung von kritischen Übergängen zu langreichweitiger Ordnung auf.

Seit den Anfangstagen der Atomphysik sind hoch angeregte Zustände, so genannte Rydberg Zustände, auf Grund ihrer außergewöhnlichen Eigenschaften von besonderem Interesse. Rydberg angeregte Atome haben eine nahezu makroskopische Ausdehnung, lange spontane Zerfallszeiten und sind zudem sehr empfindlich für externe Felder. Diese Eigenschaften machen sie zu den erfolgsversprechendsten Kandidaten um Experimente mit kalten Atomen um langreichweitige Wechselwirkung zu erweitern. Zwei Ansätze können bezüglich der Verwendung dieses Werkzeuges unterschieden werden. Der konventionelle Ansatz ist dabei die Präparation von exotischen Zuständen, wie *supersolids* oder Quanten-Spin-Eis, als Gleichg̃ewichtszustand niedriger Temperatur [11, 12]. Ich verfolge in dieser Arbeit einen zweiten Ansatz und zeige, dass Ordnung im Nichtgleichgewicht aus dem Zusammenspiel von starker Wechselwirkung und Dissipation entstehen kann.

Die starke Wechselwirkung zwischen zwei Rydberg angeregten Atomen unterdrückt die Anregung von Atomen in nahem Abstand, ein Effekt bekannt als Rydberg-Blockade. Ich untersuche die Frage, ob diese kurzreichweitige Blockade der Ausgangspunkt von langreichweitiger kristalliner Ordnung von angeregten Atomen sein kann. In Kapitel 6 entwickele ich hierzu ein analytisch lösbares Modell, dass das Nichtvorhandensein einer solchen Ordnung in eindimensionalen System aufzeigt, aber auch das Auftreten geordneter Phasen in höheren Dimensionen vorhersagt. Ich zeige in Kapitel 7, dass durchdachte Anregungsprozesse nötig sind, um den geordneten Zustand in zwei dimensionalen Gittersystemen zu erzeugen. Der Übergang zur geordneten Phase weist neben einem kritischen *slow down* der Relaxation, die typischen Signaturen der Ising-Universitalitäts Klasse auf. In Kapitel 8 verallgemeinere ich das Modell auf Systeme ohne Gitterstruktur und zeige das räumliche Korrelationen in einem Gas von van der Waals wechselwirkenden Atomen durch ein einfaches harte Kugel Modell beschrieben werden können.

Der Fortschritt auf dem Feld der kalten Atome ist Resultat einer gemeinschaftlichen Anstrengung von Theorie und Experiment. Die Gruppe von Herwig Ott demonstriere die Präparation und Anregung eines mesoskopischen Superatoms basierend auf Rydberg Blockade [13] und ich habe diese Arbeiten mit theoretischen Analysen unterstützt und zum tieferen Verständnis des Experiments beigetragen. Zwischen theoretischen Simulationen und experimentellen Ergebnissen wurde eine gute Übereinstimmung gefunden und eine Vielzahl an Effekten, von Blockade bis Antiblockade wurde beobachtet, und wird in Kapitel 9 diskutiert.

Antiblockade tritt für nicht resonante Anregung von Rydberg-Zuständen auf. Ein angeregtes Atom beschleunigt die Anregung anderer Atome, indem es durch seiner Wechselwirkung die Verstimmung des Anregungslasers kompensiert und ist damit ein potentieller Ausgangspunkt einer Lawine von Anregungen. Experimentelle Resultate [18] legen das Auftreten von bistabilem Verhalten in nicht resonant getriebenen Rydberg-Gasen nahe, ein Effekt der aber bisher nicht in numerischen Simulationen bestätigt werden konnte. In Kapitel 10 präsentiere ich Ergebnisse eines *mean field* Ansatzes für die Dynamik der Anregungsdichte in nicht resonant getriebenen Gasen, der im Vergleich mit exakten numerischen Resultaten sehr gute Übereinstimmungen zeigt. Im Einklang mit anderen theoretischen Resultaten [15], finde ich keine Evidenz für Bistabilität im stationären Zustand des Kontinuumgases.

Das dissipative Ising-Modell mit transversalem Feld ist ein extremes Beispiel für Antiblockade in eindimensionalen Gittermodellen. Ich zeige, dass numerische Methoden auf der

Basis von Matrix-Produkt-Zuständen geeignet sind, um die Dynamik hin zum stationären Zustand unter dem Einfluss von Dissipation zu beschreiben, wohingegen die rein unitäre Dynamik nicht beschrieben werden kann. Dieses Werkzeug ermöglicht mir über frühere Diskussionen hinaus zu gehen und das Auftreten von langreichweitigen Korrelationen und Bistabilität im stationären Zustand dieses Gittermodells in Kapitel 11 zu untersuchen.

Über die Nichtgleichgewichts-Vielteilchenphysik hinaus haben die langreichweitigen Wechselwirkungen von Rydberg angeregten Atomen ein großes Anwendungspotential. In Kapitel 12 gebe ich einen kurzen Einblick in die Propagation von Photonen in kohärenten EIT Medien unter Hinzunahme von atomarer Wechselwirkung. Diese Kombination verspricht die Realisierung von stark wechselwirkenden Photonen auf dem Niveau weniger Photonen, eine Eigenschaft, die wichtige Anwendungen auf dem Gebiet der Quanten-Informations-Technologie ermöglicht. In [16] wurde die Präparation eines Wigner-Kristalls von Photonen vorgeschlagen und ich diskutiere anhand von numerisch exakten Rechnungen für den Fall von zwei Anregungen, die Machbarkeit dieses Ansatzes. Meine Diskussion geht über das perturbative Modell in [16] hinaus und ich erkläre das Auftreten von Resonanzen für kurze Abstände, die ihren Ursprung in den starken Kräften zwischen angeregten Atomen haben.

Part I

Introduction

1.1 The Cold Atom Toolbox

In 1952 one of the pioneers of quantum mechanics, Erwin Schroedinger wrote, that "We never experiment with just one electron or atom or (small) molecule. In thought-experiments we sometimes assume that we do; this invariably entails ridiculous consequences" [19]. The rapid development of technology since then has proven him wrong. In this section we want to introduce the relevant models and techniques for experiments with ultra cold atoms and we will continue in Section 1.3 with an introduction to controlled long range interaction between single atoms using Rydberg states.

In 1995 the first Bose-Einstein condensates of weakly interacting neutral atoms were observed for different atomic isotopes and in different groups [20, 21, 1], based on techniques and theoretical foundations laid by research in the field of quantum optics. Results from fluorescence imaging of the first BEC in the group of Cornell are displayed in Fig. 1.1(a). Advances in trapping and cooling of atoms, by the development of new techniques such as optical Doppler cooling and evaporative cooling, paved the way towards temperatures in the nK regime for dilute atomic vapors. Since then, not only has preparation of condensates become a standard procedure, a manifold of tools has been established to control and observe ultra cold atoms [3].

At sufficiently low temperatures the collisional properties of a spin polarized, neutral gas of bosonic atoms are dominated by s-wave scattering, whereas higher angular momentum scattering channels are energetically suppressed. Under the influence of an external potential $V_{\text{ext}}(\mathbf{r})$ and with contact interaction $g_{3\text{D}}$ between atoms, the system is described by the Hamiltonian

$$\begin{aligned}\hat{\mathcal{H}} = \int d\mathbf{r} \Big\{ \hat{\Psi}^\dagger(\mathbf{r}) \Big[-\frac{1}{2m}(\partial_x^2 + \partial_y^2 + \partial_z^2) + V_{\text{ext}}(\mathbf{r}) \Big] \hat{\Psi}(\mathbf{r}) \\ + \frac{g_{3\text{D}}}{2} \hat{\Psi}^\dagger(\mathbf{r}) \hat{\Psi}^\dagger(\mathbf{r}) \hat{\Psi}(\mathbf{r}) \hat{\Psi}(\mathbf{r}) \Big\},\end{aligned} \tag{1.1}$$

where m is the atomic mass and $\hat{\Psi}^\dagger(\mathbf{r})$ creates a boson at position $\mathbf{r}$. The operators $\hat{\Psi}^\dagger(\mathbf{r})$ and $\hat{\Psi}(\mathbf{r})$ fulfill the usual commutation relations

$$\big[\hat{\Psi}^\dagger(\mathbf{r}), \hat{\Psi}(\mathbf{r}')\big] = \delta(\mathbf{r} - \mathbf{r}'), \quad \big[\hat{\Psi}^\dagger(\mathbf{r}), \hat{\Psi}^\dagger(\mathbf{r}')\big] = \big[\hat{\Psi}(\mathbf{r}), \hat{\Psi}(\mathbf{r}')\big] = 0. \tag{1.2}$$

To simplify notation we use ($\hbar = 1$) throughout this thesis unless noted differently.

1.1.1 Optical lattices and Mott insulators

The physics described by the Hamiltonian (1.1) goes much beyond BECs and we will here discuss the implementation of optical lattices and control over short range interaction, towards the realization of the superfluid to Mott insulator transition [2].

Optical standing waves enable the creation of periodic lattice potentials for atoms via the AC Stark shift in near resonant electric fields. The interference pattern of two counter propagating laser beams of wavelength λ, yields an intensity pattern of period $\lambda/2$, where intensity maxima either attract or repel atoms depending on the detuning.

The natural basis for the description of non interacting particles in these periodic potentials is the Bloch basis, with the Bloch wave functions $u_{\mathbf{k}}^{\nu}(\mathbf{r})$ in the ν-th band. An important energy scale is given by the recoil energy

$$E_{\text{r}} = \frac{(2\pi)^2}{2m\lambda^2}. \tag{1.3}$$

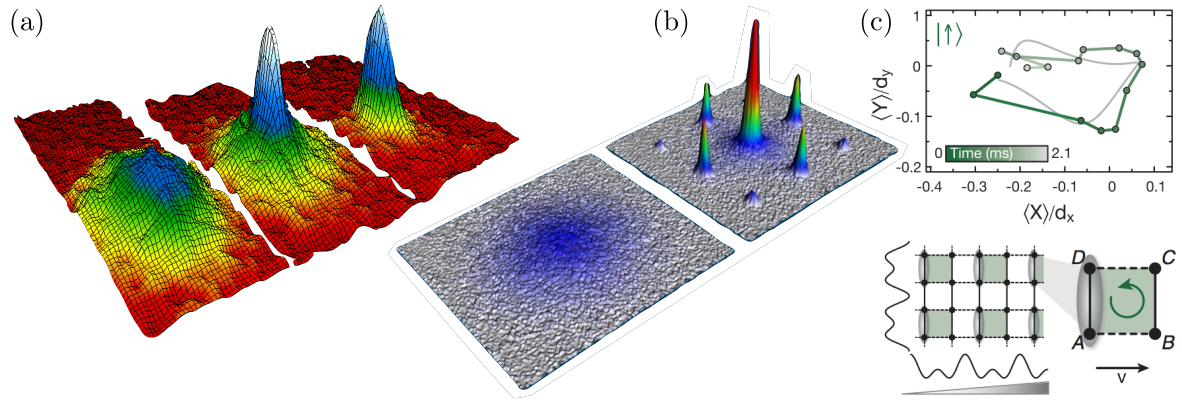

Figure 1.1: (a) Experimental signature of Bose Einstein condensation (taken from [20]) (b) Time of flight interference pattern of a Mott insulator (left) and a superfluid (left). (taken from [22]) (c) Cyclotron orbit of single neutral atoms in an artificial magnetic field on a lattice (taken from [23]).

At temperatures below the recoil energy, $k_{\mathrm{B}}T < E_{\mathrm{r}}$ and for sufficiently small interactions, all but the lowest Bloch band can be neglected. For deep optical lattices we introduce the Wannier basis of states localized in the wells of the external potential. The Wannier functions are constructed from the Bloch functions by

$$w(\mathbf{r}-\mathbf{n}) = \frac{1}{2\pi}\int d\mathbf{k}\ \exp(i\mathbf{k}\mathbf{n})\ u_{\mathbf{k}}(\mathbf{r}), \tag{1.4}$$

with lattice vectors $\mathbf{n}$. The last step towards the Bose-Hubbard (BH) model is the introduction of bosonic operators that create localized particles at the individual lattice sites

$$\hat{b}^{\dagger}_{\mathbf{n}} = \int d\mathbf{r}\ w(\mathbf{r}-\mathbf{n})\hat{\Psi}^{\dagger}(\mathbf{r}), \tag{1.5}$$

which fulfill bosonic commutation relations $[\hat{b}_{\mathbf{n}}, \hat{b}^{\dagger}_{\mathbf{m}}] = \delta_{\mathbf{n},\mathbf{m}}$ and $[\hat{b}^{\dagger}_{\mathbf{n}}, \hat{b}^{\dagger}_{\mathbf{m}}] = [\hat{b}_{\mathbf{n}}, \hat{b}_{\mathbf{m}}] = 0$.

Rewriting the Hamiltonian (1.1) in terms of the newly defined bosonic operators, yields the by now famous Bose Hubbard (BH) Hamiltonian [24]

$$\hat{\mathcal{H}}_{\mathrm{BH}} = \sum_{\mathbf{n},\mathbf{m}} \left[-J_{\mathbf{n},\mathbf{m}}\ \hat{b}^{\dagger}_{\mathbf{n}}\hat{b}_{\mathbf{m}} + U_{\mathbf{n},\mathbf{m}}\ \hat{b}^{\dagger}_{\mathbf{n}}\hat{b}^{\dagger}_{\mathbf{m}}\hat{b}_{\mathbf{m}}\hat{b}_{\mathbf{n}}\right], \tag{1.6}$$

which predates its modern realization in ultra cold atom experiments by four decades [24]. Note, that we neglected interaction terms that couple more than two lattice sites already in the last step. The tunneling matrix elements $J_{\mathbf{n},\mathbf{m}}$ and the interaction $U_{\mathbf{n},\mathbf{m}}$ are calculated via the Wannier functions

$$J_{\mathbf{n},\mathbf{m}} = \int d\mathbf{r}\ w^{*}(\mathbf{r}-\mathbf{n})\left[-\frac{1}{2m}(\partial_x^2+\partial_y^2+\partial_z^2) + V_{\mathrm{ex}}(\mathbf{r})\right] w(\mathbf{r}-\mathbf{m}), \tag{1.7}$$

$$U_{\mathbf{n},\mathbf{m}} = g_{3\mathrm{D}}\int d\mathbf{r}\ w^{*}(\mathbf{r}-\mathbf{n})w^{*}(\mathbf{r}-\mathbf{m})w(\mathbf{r}-\mathbf{m})w(\mathbf{r}-\mathbf{n}). \tag{1.8}$$

For sufficiently deep, sinusoidal optical lattices, an approximate expression for the tunneling

between adjacent lattice sites can be derived using Mathieu functions [25]

$$J/E_{\mathrm{R}} \approx 1.4\tilde{V}_0 e^{-2.1\tilde{V}_0}, \tag{1.9}$$

where V_0 is the height of the lattice barrier between two potential wells and $\tilde{V}_0 = V_0/E_{\mathrm{R}}$. The strength of the interaction U can be modified, for example by the use of Feshbach resonances, that modify the s-wave scattering length $a_{3\mathrm{D}}$ and thereby $g_{3\mathrm{D}} = 4\pi a_{3\mathrm{D}}$ [26].

For deep optical lattices, only local interaction terms and hopping to adjacent sites need to be taken into account

$$\hat{\mathcal{H}}_{\mathrm{BH}} = -J \sum_{\langle \mathbf{n},\mathbf{m} \rangle} \left[\hat{b}^\dagger_{\mathbf{n}} \hat{b}_{\mathbf{m}} + h.c. \right] + U \sum_{\mathbf{n}} \hat{n}_{\mathbf{n}} (\hat{n}_{\mathbf{n}} - 1). \tag{1.10}$$

At large interaction $U/J \gg 1$ the ground state of the BH model is given by Mott insulator states with integer filling, where the number of particles per site is determined by the chemical potential μ [27]. When increasing the tunneling J the system undergoes a phase transition towards a superfluid phase, where the U(1) symmetry of the Hamiltonian

$$\hat{b}^\dagger_{\mathbf{n}} \rightarrow \hat{b}^\dagger_{\mathbf{n}} e^{i\phi} \tag{1.11}$$

is spontaneously broken. In 1998 Jaksch et al. proposed the realization of the BHM with cold atoms in optical lattices [27] and in 2002, Greiner et al. used time of flight imaging, to experimentally demonstrate the superfluid to Mott insulator transition [2]. In Fig. 1.1(b) the emergence of interference peaks in time of flight measurements for the superfluid phase is displayed.

1.1.2 Single site resolution, exotic lattices and artificial gauge fields

The field of ultra cold atom experiments has rapidly developed over the last decade and we here only give reference to the three most important developments regarding the remainder of this thesis.

First of all, detection techniques have been improved far beyond the capabilities of time of flight spectroscopy, that was well suited for the detection of the $U(1)$ symmetry breaking of the Mott insulator to superfluid transition. Length scales in optical lattices are fixed by the wavelength of the lasers used for trapping and typical lattice constants are on the order of $a = 0.5$ μm. This renders single site resolution by optical techniques challenging, but both Sherson et al. and Bakr et al. developed single site detection and manipulation techniques [4, 5, 28, 29], employing high aperture lenses. An alternative approach using high resolution electron microscopy was successfully demonstrated by Gericke et al. [30, 31].

A strength of experiments with cold atoms is the flexibility that can be achieved by only controlling the external potential $V_{\mathrm{ext}}(\mathbf{r}, t)$ in both space and time. Foremost the dimensionality of experiments can be reduced to one or two dimensions and the basic lattice structure can be changed from simple cubic lattices to more complicated triangular, hexagonal, Kagome or other lattices [32]. Advances in spatial light modulation promise an almost restriction free control over future optical lattices [33].

The third important development is the introduction of artificial gauge fields into the toolbox for neutral cold atoms. Initial experiments exploited the similarity of Coriolis force and Lorentz force in a magnetic field, to study the appearance of vortices in rotating systems [34]. However, limitations towards the rotation frequency restrict such approaches to weak magnetic fields. A wide variety of techniques has been proposed to implement artificial Abelian

and non-Abelian gauge fields using the laser dressing of atoms [35, 36, 6].

In the absence of a scalar potential $\Phi(\mathbf{r}, t)$, electric and magnetic fields are derived from the vector potential $\mathbf{A}(\mathbf{r}, t)$

$$\mathbf{E}(\mathbf{r}, t) = -\partial_t \mathbf{A}(\mathbf{r}, t), \tag{1.12}$$

$$\mathbf{B}(\mathbf{r}, t) = \nabla \times \mathbf{A}(\mathbf{r}, t). \tag{1.13}$$

The motion of a particle with charge q is then described by a modification of the kinetic energy in Eq. (1.1)

$$\frac{\mathbf{p}^2}{2m} \to \frac{[\mathbf{p} - q\mathbf{A}(\mathbf{r}, t)]^2}{2m}. \tag{1.14}$$

This change in the original Hamiltonian can be translated into changes of the hopping matrix elements of the derived Bose Hubbard Hamiltonian and one finds that the introduction of Peierls phases for the tunneling matrix elements is required [37]

$$J_{\mathbf{n},\mathbf{m}} = |J_{\mathbf{n},\mathbf{m}}| e^{i\theta_{\mathbf{m},\mathbf{n}}}. \tag{1.15}$$

Whereas the individual phases $\theta_{\mathbf{m},\mathbf{n}}$ depend on the choice of gauge, the sum of phases along a closed path $\mathcal{P}$ of the lattice is gauge invariant and given by

$$\sum_{\mathcal{P}} \theta_{\mathbf{m},\mathbf{n}} = q \oint d\mathbf{r}\ \mathbf{A}(\mathbf{r}) = q \int_{\mathcal{A}} d\mathbf{n}\ \mathbf{B}(\mathbf{r}), \tag{1.16}$$

where $\mathcal{A}$ is the area enclosed by the path $\mathcal{P}$. Therefore the sum of Peierls phases is identical to the flux of the magnetic field through the area enclosed by the path and must be gauge invariant.

Whereas the introduction of charge into cold atom experiments is infeasible, the artificial generation of Peierls phases by engineering of tunneling processes is possible. This idea was put forward by Jaksch and Zoller employing laser assisted tunneling [38]. Kolovsky proposed an alternative approach using shaking assisted tunneling, where time dependent lattice modulations restore tunneling, which at first was suppressed by static, staggered optical lattices [39]. The approach has been further developed to generate non Abelian gauge fields by Hauke et al. [40].

Observation of the superfluid to Mott insulator was a first milestone for experiments with cold atoms in optical lattices. The combination of ideas we here reviewed are employed in recent experiments that realize the Hofstadter and Haldane Hamiltonians with cold atoms [23, 41, 42]. The experimental observation of cyclotron orbits for cold neutral atoms in artificial magnetic fields was recently reported in [23] (cf. Fig. 1.1(c)) and paves the way towards the next landmark of cold atom physics. The observation of topological phases of matter such as the quantum Hall effect, using strongly interacting particles in artificial magnetic fields.

1.2 Topological Phases of Matter

Before the discovery of the integer quantum Hall effect [43, 44], it was believed that phases of matter can be classified entirely by the concept of spontaneous symmetry breaking, which was mathematically formulated in the Ginzburg-Landau theory. The Mott insulator to superfluid transition of the BH model is an example of such a phase transition, where the $U(1)$ symmetry of the Hamiltonian is spontaneously broken in the superfluid. The belief that this classification is complete was disenchanted after the discovery of topological insulators [45, 46, 47, 48, 49] and subsequent theoretical analysis [50, 51, 52], which revealed the class of topologically ordered states. Topological phases have become an intensively studied subject in many fields of physics. Key features of condensed-matter systems such as topological insulators [47, 46, 45] or superconductors [53] as well as quantum Hall systems [54, 55, 43, 44] have been related to robust edge states at interfaces between phases with different topological character [56].

In this section we want to discuss the Hofstadter model that describes charged particles on a two dimensional lattice with a transverse homogeneous magnetic field. The notion of topology will be introduced for the band structure of this model and relations between polarization, Chern number and edge states will be discussed and related to the quantum Hall effect. We conclude with a short outlook on topology in systems with interaction.

1.2.1 The Hofstadter model

The Hofstadter model, similar to the Bose Hubbard model in the last section for bosons, describes the dynamics of fermions in a two dimensional periodic potential in tight binding approximation. Under the influence of an external magnetic field, described by vector potential

$$\mathbf{A}(\mathbf{r}) = (0, Bx, 0)^t, \tag{1.17}$$

for particles with charge $q = 1$, Peierls phases have to be introduced for the tunneling matrix elements along the lattice

$$\hat{\mathcal{H}}_{\mathrm{H}} = -J \sum_{n_x,n_y} (\hat{c}^\dagger_{n_x,n_y} \hat{c}_{n_x+1,n_y} + \hat{c}^\dagger_{n_x,n_y} \hat{c}_{n_x,n_y+1} e^{i2\pi\alpha n_x} + h.c.). \tag{1.18}$$

Here n_x, n_y are the integer indices of the lattice with lattice constant a and $\alpha = (a^2 B)/(2\pi)$ is the magnetic flux per plaquette. When following a closed path $\mathcal{P}$ around a single plaquette of the lattice, we find for the sum of Peierls phases

$$\sum_{\mathcal{P}} \theta_{\mathbf{m},\mathbf{n}} = \theta_{(n_x+1,n_y),(n_x+1,n_y+1)} + \theta_{(n_x,n_y+1),(n_x,n_y)} \tag{1.19}$$

$$= 2\pi \times \alpha. \tag{1.20}$$

For fractional values of the flux, $\alpha = p/q$ with $p, q \in \mathbb{Z}$, with p, q coprime, we can choose a unit cell of size $(q \times 1)$ sites and determine the energies and Bloch wavefunctions of the q bands. As a consequence of particle hole symmetry the band structure is symmetric regarding zero energy

$$E^{(\nu)}_{kx,ky} = -E^{(q-\nu)}_{kx,ky}. \tag{1.21}$$

In general the bands of the Hofstadter model are flat for $\alpha = 1/q$, compared to the interband gap. Only in the case of q being even are the two central bands connected through Dirac points [57].

In Fig. 1.2(b) we display the band structure for $\alpha = 1/4$ and find two very flat bands at low

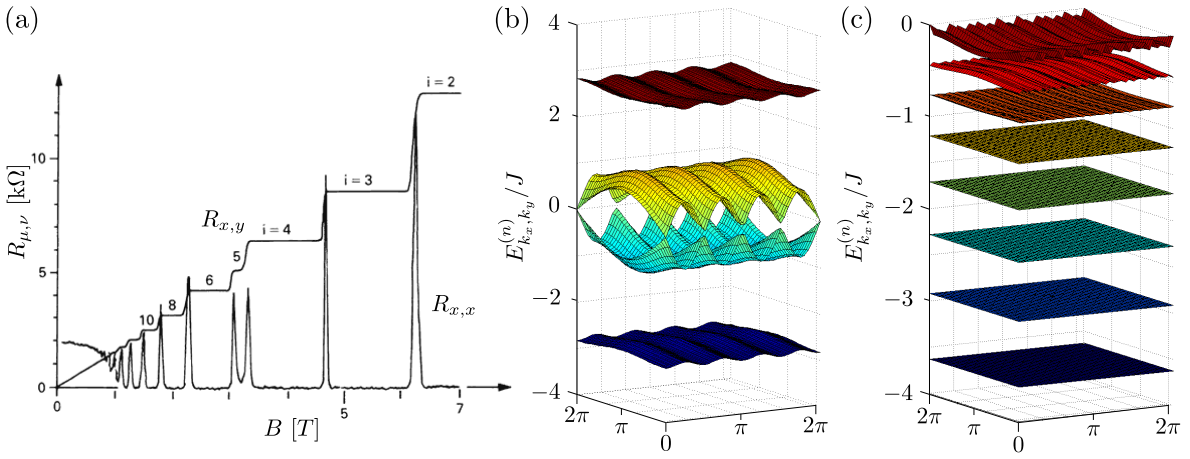

Figure 1.2: (a) In the regime of the integer quantum Hall effect the Hall resistivity σ_{xy} changes stepwise, as a function of the applied magnetic field B. (taken from [58]) (b) Band structure of the Hofstadter with at flux $\alpha = 1/4$. (c) Emergence of Landau levels from the bands of the Hofstadter model for $\alpha = 1/16$.

and high energies. For temperatures small compared to the band gap and chemical potentials in the gap between two bands, we expect this model to behave as an insulator. Before we discuss, why this derivation is incomplete for real systems, we want to shortly comment on the limit $\alpha \to 0$.

For small $\alpha \to 0$, cf. Fig. 1.2(c) for $\alpha = 16$, the lowest bands of the Hofstadter model correspond to the so called Landau levels of a charged particle in a magnetic field in the continuum. All Landau levels have zero dispersion, related to the cyclic motion of electrons in magnetic fields, and are separated by the cyclotron frequency

$$\omega_c = \frac{eB}{m}. \tag{1.22}$$

1.2.2 Topology and edge states

In 1980 von Klitzing measured the Hall resistivity of thin two dimensional semiconductors at large magnetic fields and found results similar to those shown in Fig. 1.2(a) [44]. The Hall resistivity is defined as the ratio of transverse current to an applied electric field in the presence of an external magnetic field,

$$R_{x,y} = \frac{E_y}{J_x} = n^{-1}\frac{h}{e^2}, \quad n \in \mathbb{Z}, \tag{1.23}$$

where the second equation is the surprising result of his measurement. For strong magnetic fields, the Hall conductivity $\sigma_{x,y} = R^{-1}_{x,y}$, is precisely quantized to integer multiples of e^2/h, where e is the charge of an electron and h Plancks constant. By changing the magnetic field n could be changed, with n getting smaller for stronger fields. In between the plateaus of quantized resistivity, very sharp steps were measured.

A second surprising result was found regarding the longitudinal resistivity $R_{x,x} = E_x/J_x$. Where the transversal resistivity was quantized, the longitudinal resistivity was zero within the measurement error. Both effects where shown to originate from the non trivial topology of the band structure by Thouless and others [43, 59].

Zak phases in one dimension

Before reviewing the explanation of the integer quantum Hall effect in two dimension, we introduce the relevant notations for the topological classification of one dimensional band structures.

Consider a one dimensional system with lattice constant set to unity, $a = 1$, and L unit cells. The Zak phase is defined by [60]

$$\varphi_{\text{Zak}} = i \int_{-\pi}^{\pi} dk \int dx \; u_k^*(x) \partial_k u_k(x). \tag{1.24}$$

and closely related to the geometric phase introduced by Berry [61]. Note, that the Zak phase is only defined up to multiples of 2π, due to gauge freedom regarding the Bloch functions. For example

$$u_k(x) \to e^{ik} u_k(x) \tag{1.25}$$

changes the Zak phase by 2π.

Vanderbilt and Kingsmith pointed out the relation between Zak phase and the polarization of a material [62]. The Bloch wavefunctions in the definition of the Zak phase can be expanded in terms of Wannier functions, which yields

$$\varphi_{\text{Zak}} = \frac{i}{L} \int_{-\pi}^{\pi} dk \int dx \sum_{m,n} w^*(x-m) e^{ik(m-x)} \partial_k e^{-ik(n-x)} w(x-n) \tag{1.26}$$

$$= \frac{i}{L} \int_{-\pi}^{\pi} dk \int dx \sum_{m,n} e^{ik(m-n)} \partial_k w^*(x-ma) i(m-x) w(x-n) \tag{1.27}$$

$$= \frac{2\pi}{L} \int dx \sum_{m} w^*(x-m)(x-m) w(x-m) \tag{1.28}$$

$$= 2\pi \int dx \; x |w(x)|^2 := 2\pi P, \tag{1.29}$$

wherein the last step we used the definition of the polarization P. We will later make use of this correspondence, when we connect changes in the polarization with the current of the quantum Hall effect in two dimensional systems.

Chern numbers and edge states

Whereas the Zak phase of a one dimensional band is not necessarily quantized, the Chern number associated with a two dimensional band is always quantized. Consider a bulk system with a two dimensional band structure, $|u^{(\nu)}(k_x, k_y)\rangle$, where the lowest ν' bands are occupied with electrons. Applying an external electric field E_y, acts as force eE_y and for sufficiently small forces drives only Bloch oscillations for the particles in the occupied bands. Associated with the changes in k_y are changes in the polarization in x direction as a consequence of Eq. (1.29). After exactly one Bloch period we find for the change in polarization

$$\Delta P^{(\nu)} = \frac{1}{2\pi} \int_0^{2\pi} dk_y \; \partial_{k_y} \varphi_{\text{Zak}}^{(\nu)}(k_y), \tag{1.30}$$

where $\varphi_{\text{Zak}}^{(\nu)}$ is the Zak phase of one of the occupied bands with parameter k_y. Whereas the Zak phase itself is not quantized, it holds $\varphi_{\text{Zak}}(k_y) = \varphi_{\text{Zak}}(k_y + 2\pi) \bmod 2\pi$ and therefore the change in polarization is quantized.

It was shown by Thouless, that the quantization of the conductivity in the integer quantum Hall effect is due to the strict relation between the properties of the bandstructure and the transverse Hall conductance [43]

$$\sigma_{x,y} = \frac{e}{h^2}\mathrm{Ch}, \tag{1.31}$$

$$\mathrm{Ch} = \sum_{\nu} \mathrm{Ch}^{(\nu)} = \frac{1}{2\pi}\sum_{\nu}\int dk_y \partial_{k_y}\varphi^{(\nu)}_{\mathrm{Zak}}(k_y), \tag{1.32}$$

where the sum is over all occupied bands. The Chern number has a physical interpretation as the winding of the Zak phase along a closed path in parameter space, which is related to the physical flow of a current through Eq. (1.30).

The quantization of the Chern number also has a mathematical foundation in the theory of fiber bundles [63]. The mapping between Bloch Hamiltonian $\hat{\mathcal{H}}(\mathbf{k})$ and momentum $\mathbf{k}$ can be classified by considering equivalence classes of Hamiltonians, which can be continuously deformed into each other without closing the energy gap [64]. For the Hofstadter model with magnetic flux $\alpha = 1/q$ and q even, the Chern numbers are given by +1 for all bands, except the two bands in the center, which have a combined Chern number of -q+2 [43].

Not only the quantization of the transverse conductivity was a surprising result of the experiment in Fig. 1.2(a), but furthermore the drop in longitudinal resistivity $R_{x,x}$ to zero. Again this is a consequence of topological order. By definition of the Chern number, two bands with different topological invariant can not be continuously deformed into each other without closing the energy gap. As pointed out by Halperine [65], the vacuum has a trivial topology and therefore at the boundary between a bulk system with a non trivial topology and the vacuum, gap closing edge states must exist. For the integer quantum Hall effect, these states can be imagined as the cyclotron orbits that are repeatedly reflected at the boundary to the vacuum and therefore circle around the edges of the sample. An important consequence is the chirality of these edge states, at every edge only states propagating in one direction are found such that backscattering is strongly suppressed.

At the boundary between two bulk systems, which are characterized by Chern numbers $\mathrm{Ch}^{(1)}$ and $\mathrm{Ch}^{(2)}$ respectively, the bulk boundary correspondence states for the number of edge states

$$N_{\mathrm{es}} = |\mathrm{Ch}^{(1)} - \mathrm{Ch}^{(2)}|. \tag{1.33}$$

This correspondence has been proven for systems of non interacting fermions and can be applied to a wide variety of band structures [66]. Whether it carries over to non interacting phases with topological order is subject of ongoing research.

1.2.3 Topology and interaction

While all possible topological phases of non-interacting fermions in arbitrary dimensions have been classified [50], it is established that interactions can enrich the number of possible topological phases enormously, see e.g. [52]. Of particular interest are fractional Chern insulators, where the band of a non interacting model with integer Chern number, is only partially filled in the presence of strong interaction [67]. The resulting phases support exotic excitations with fractional charge and statistics [68, 69, 55, 70, 71], which have possible applications for topological quantum computation [8, 72].

1.3 Long Range Interaction and Rydberg States

Systems of ultra cold atoms offer unprecedented control of single particle parameters and enable direct observation of microscopic degrees of freedom as discussed in the previous Section 1.1. Local interaction of atoms can be controlled using Feshbach resonances [73, 74], however the introduction of long range interaction to the experimental toolbox is a challenge. Different avenues towards this goal have been pursued in past years as the motivation is manifold, ranging from the study of dipolar Bose gases [7], to quantum simulation [75] and computation [76]. We here shortly review two possibilities before discussing in detail the realization of long range interactions facilitated by Rydberg states.

First of all atomic isotopes with a large magnetic dipole moment such as ^{52}Cr, ($\mu \approx 6\mu_{\mathrm{B}}$), have been cooled successfully and allowed observation of anisotropy effects in spinor BECs [77]. However for observation of the effects of long range interaction in optical lattices, the magnetic dipole dipole interaction is in general to small. An alternative approach is the synthesis and cooling of diatomic molecules such as KRb that have a large permanent dipole moment, for the ground states $X^1\Sigma^+$ one finds $\mu_{\mathrm{e}} \approx 0.3\ ea_0$ [78]. The interaction resulting from such large dipole moments is in the kHz range for distances of few micrometers, but the complex structure of molecules poses many experimental challenges regarding cooling and control, that hinder implementation in cold atom experiments. Nonetheless, current experiments offer sufficient control to be used as benchmarks for the theory of many body systems [79].

Within this thesis we want to focus on a third approach towards long range interaction, which is the excitation to Rydberg states [80]. These are highly excited atomic states, where at least one of the valence electrons is in a large principal quantum number state. The binding energies of these states follow the original Rydberg formula for the hydrogen atom

$$E_{n,l} = -\frac{\mathrm{Ry}}{(n-\delta_l)^2} \tag{1.34}$$

with the Rydberg constant Ry and the quantum defect δ_l. For large principal quantum number n, all but one positive charge of the atomic core are shielded by the inner electron shells. Only for small angular momentum states, ($l < 3$), the valence electron penetrates this core region, which leads to the quantum defect δ_l. Note that the degeneracy of energies for states with equal principal quantum number n is lifted by this defect for non hydrogen atoms. The heuristic Ritz formula can be used to calculate the quantum defect and thereby the individual binding energies [81]. For ^{87}Rb one finds for example quantum defects of $\delta_{s_{1/2}} = 3.13, \delta_{p_{1/2}} = 2.65, \delta_{d_{3/2}} = 1.35$ [82].

The large principal quantum number and high energy, results in a number of remarkable scalings for the properties of Rydberg atoms. First of all the wavefunction can be of macroscopic size with radii scaling as $r \sim n^2$ and therefore approaching the μm regime for $n \gtrapprox 50$. As a consequence of this large spatial extension, the dipole matrix element

$$\langle n_0, l_0, j_0, m_0 | e\mathbf{r} | n, l, j, m \rangle, \tag{1.35}$$

between the ground state wavefunctions $\langle \Psi_0 |$ and Rydberg wavefunction becomes smaller with increasing n. As a consequence of Fermis golden rule, the radiative lifetime therefore increases with the principal quantum number as $\tau \sim n^3$ and typical numbers for $n \gtrapprox 50$ Rydberg states are on the order of 100 μs. The large extend of the wavefunction has further effects on the dipole matrix element between adjacent Rydberg states, $\langle nP|er|nS\rangle \sim n^2$ and the polarizability, $\alpha \sim n^7$, which strongly scales with the principal quantum number. This makes large Rydberg atoms very susceptible for external electric fields. A prominent example

for the application of Rydberg atoms as probes for weak fields, is the detection and control of few photons in a cavity by Haroche et al. [83].

1.3.1 Detection of Rydberg excited atoms

Rydberg excited atoms can be detected in a multitude of ways and we here want to review the most relevant approaches developed within the last years. First of all Bloch et al. have shown the detection of Rydberg excited atoms with almost single site resolution in a two dimensional optical lattice. To detect the Rydberg excited atoms, ground state atoms are removed first by applying strong near resonant pulse driving the transition to a nearby hyperfine state. The remaining Rydberg excited atoms are transfered to the ground state by resonant driving and imaged as ground state atoms with the techniques developed in [5].

The conventional way of detecting Rydberg atoms is via ionization and subsequent detection of the ions. Multiple experiments have utilized field ionization in static electric fields to rapidly convert all excited atoms into ions [84, 85, 14]. Experiments in the group of Raithel have demonstrated that the spatial position of atoms before ionization can be reconstructed by accurate ion microscopy. The required fields are small due to the close ionization threshold and for large principal quantum number n, a very good field control is required to not ionize excited atoms accidentally.

Precise control of the spatial degrees of freedom is required for quantum computation and simulation applications of Rydberg atoms, which could be realized via trapping in optical lattices [86]. Potvliege et al. showed that the trapping fields can result in a second, fast photo ionization channel for Rydberg atoms [87]. Here atoms are continuously ionized and could be detected, while the remaining atomic ensemble continues to be trapped and excited.

A fourth approach towards the detection of Rydberg excited atoms has been proposed by Günter et al. They employ electromagnetically induced transparency (EIT) to map the distribution of excited atoms onto a classical light field [88]. Further details on EIT will be given in the next section of the introduction. Whereas the initial experimental realization of the EIT imaging scheme did not provide the spatial resolution for the detection of single excited atoms, it showed an interesting dipole-mediated transport mechanism between Rydberg excited atoms, which however goes beyond the scope of this thesis [89].

1.3.2 Interaction between Rydberg atoms

The large polarizability of the Rydberg atoms is the origin of the strong and long range interaction between two excited atoms. The interaction energy of two dipoles μ_1 and μ_2 with relative distance vector $\mathbf{R}$ is given by

$$U_{\mathrm{dd}} = \frac{\mu_1 \cdot \mu_2}{|\mathbf{R}|^3} - \frac{(\mu_1 \cdot \mathbf{R})(\mu_2 \cdot \mathbf{R})}{|\mathbf{R}|^5}. \tag{1.36}$$

We are interested in the coupling of an atomic pair state $|\varphi, \varphi\rangle$, with two atoms in identical single atom state $|\varphi\rangle = |n, k, j, m\rangle$, to other pair states $|\varphi_1, \varphi_2\rangle$. This coupling results from the dipole dipole interaction

$$\langle \varphi_1, \varphi_2 | \hat{U}_{\mathrm{dd}} | \varphi, \varphi \rangle, \tag{1.37}$$

where we have replaced the classical dipoles with the dipole operators $\hat{\mu}_\nu = e\mathbf{r}_\nu$ in $\hat{U}$. Besides the coupling element, one must consider the energy mismatch

$$\Delta_{\varphi,\varphi,\varphi_1,\varphi_2} = 2E_\varphi - E_{\varphi_1} - E_{\varphi_2}. \tag{1.38}$$

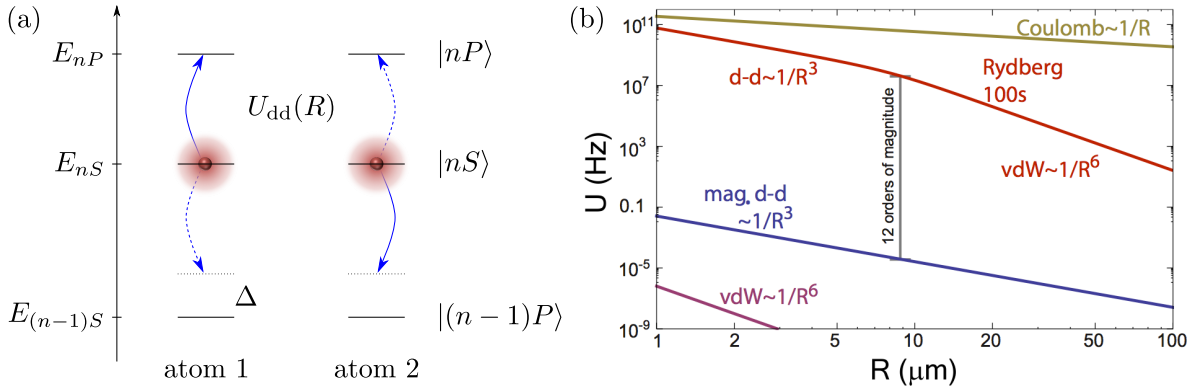

Figure 1.3: (a) Schematic illustration for the single channel model that explains the vdW and DD interaction between pairs of atoms excited to Rydberg states. (b) Typical strength of the binary Rydberg interaction in comparison to magnetic and vdW interaction of ground state atoms as a function of the interatomic distance (taken from [76]).

Reinhard et al. did exact numeric calculations for the binary level shifts of Rydberg excited atoms for a wide variety of principal quantum numbers n and the different angular momentum states S, P and D relevant for current experiments [90]. They found that of the many possible couplings to other pair states, in general only one pair state has to be considered for large separations $|\mathbf{R}|$.

This single channel model for the perturbation of two atoms in an nS state is illustrated in Fig. 1.3(a). Dipole moments from a S state $|n, S\rangle$ are largest to the adjacent nP and $(n-1)P$ pair states, and the energy mismatch Δ, which can be calculated from Eq. (1.34), scales as $\Delta \sim n^{-3}$. The Hamiltonian and eigenvalues are given by

$$\hat{\mathcal{H}} = \begin{pmatrix} 0 & U_{\mathrm{dd}}(R) \\ U_{\mathrm{dd}}(R) & \Delta \end{pmatrix}, \tag{1.39}$$

$$\Rightarrow \; E_{\pm} = \frac{\Delta}{2} \pm \sqrt{\frac{\Delta^2}{4} + U_{\mathrm{dd}}(R)^2}, \tag{1.40}$$

with our choice of basis $\left\{|nS, nS\rangle, [|nP, (n-1)P\rangle + |(n-1)P, nP\rangle]/\sqrt{2}\right\}$.

One distinguishes two regimes according to the ratio of dipole interaction $U_{\mathrm{dd}}(R)$ and energy mismatch Δ. In the van der Waals (vdW) regime $U_{\mathrm{dd}}(R) \ll \Delta$ and the relevant pair state energy is approximately

$$E_{\mathrm{vdW}} = -\frac{U_{\mathrm{dd}}^2}{\Delta} = -\frac{C_6}{R^6}, \tag{1.41}$$

where we have introduced the interaction coefficient C_6. Due to the different scalings of the energy mismatch Δ and dipole matrix elements this coefficient in general scales dramatically with the principal quantum number as $C_6 \sim n^{11}$. When the energy mismatch Δ is the small parameter, i.e. in the regime of resonant dipole-dipole interaction, one instead finds $E_{\pm} \approx \pm C_3/|R|^3$. Here, the interaction coefficient only scales as $C_3 \sim n^4$ but the interaction decays much slower with interatomic distance than in the vdW regime.

A detailed derivation of the binary interaction between Rydberg atoms is given by Reinhardt et al. in [90], where they furthermore discuss the anisotropic interaction of P and D states. Within this thesis we mostly consider the dynamics of excited atoms with an isotropic interaction potential, but others have proposed interesting uses of anisotropic interaction for the creation of exotic phases of matter such as spin ice in equilibrium systems [12].

The magnitude of interaction between Rydberg atoms is illustrated in Fig. 1.3(b) and compared with other typical interaction scales. Whereas it is smaller than the pure Coulomb interaction between ions, it can be many orders of magnitude larger than the interaction between magnetic dipoles or the conventional vdW interaction between ground state atoms. Precise experiments with few atoms have been used to probe the binary interaction between Rydberg excited atoms and found very good agreement with theoretical predictions [91, 92, 93].

1.4 Electromagnetically Induced Transparency

The coherent manipulation of photons and the realization of strong interactions between single photons is a long standing goal of quantum optics. We here want to introduce the relevant concepts for the propagation of light in atomic three level systems as illustrated in Fig. 1.4(a) and is closely follow the derivations in [94] regarding the propagation of classical pulses and [95] regarding the propagation of single photons.

The coupling of an electric probe field $\hat{E}$ at frequency ω_p to a single three-level atom in dipole and rotating wave approximation is described by

$$\hat{\mathcal{H}}_{\mathrm{atom-light}} = -[\Delta_p \hat{\sigma}_{\mathrm{ee}} + \delta\hat{\sigma}_{\mathrm{ss}}] - [p_{\mathrm{ge}}\hat{E}\hat{\sigma}_{\mathrm{eg}} + \Omega e^{ik_d z}\hat{\sigma}_{\mathrm{es}} + h.c.]. \tag{1.42}$$

Here p_{ge} is the dipole moment of the transition from ground to short lived excited state and z is the position of the atom and it is assumed that both fields propagate in the $+z$ direction. We define $\Delta_\mathrm{p} = \omega_\mathrm{p} - \omega_{\mathrm{ge}}$ as the one photon detuning of the probe field, with $\omega_{\mu\nu}$ denoting the transition frequency between states μ, ν. In addition to the probe field a second classical control field at frequency ω_c couples the transition from the excited state to a long lived spin state with Rabi frequency Ω. The detuning of the control field is denoted as $\Delta_\mathrm{c} = \omega_{\mathrm{eg}} - \omega_{\mathrm{sg}} - \omega_\mathrm{c}$ and the two photon detuning is defined as $\delta = \Delta_\mathrm{p} - \Delta_\mathrm{c}$.

The propagation of a quantized light field is described by the wave equation derived from Maxwells equation

$$\left[\frac{\partial^2}{\partial_t^2} - c^2\Delta\right]\hat{E}(\mathbf{r},t) = -\frac{1}{\varepsilon_0}\frac{\partial^2}{\partial_t^2}\hat{P}(\mathbf{r},t), \tag{1.43}$$

where $\hat{P}$ is the polarization of the medium. For a near monochromatic electric field, which propagates in z direction, one introduces new slowly varying fields, where the carrier frequency and wave vector are split off

$$\hat{E}(\mathbf{r},t) = \sqrt{\frac{\hbar\omega_\mathrm{p}}{2\varepsilon_0}}\left(\hat{\mathcal{E}}(\mathbf{r},t)e^{i(k_p z - \omega_\mathrm{p} t)} + h.c.\right). \tag{1.44}$$

With an analogously defined ansatz for the polarization $\hat{P} = \hat{\mathcal{P}}\exp(i[k_p z - \omega_p t]) + h.c.$, one finds

$$\left[\partial_t + c\partial_z - i\frac{1}{2k_p}\Delta_\perp\right]\hat{\mathcal{E}}(\mathbf{r},t) = \frac{i}{\hbar}\sqrt{\frac{\hbar\omega_p}{2\varepsilon_0}}\hat{\mathcal{P}}(\mathbf{r},t), \tag{1.45}$$

where we have dropped higher temporal and spatial derivatives of the slowly varying variable. This is justified as long as $|\partial_t^2\hat{\mathcal{E}}| \ll |\omega_\mathrm{p}\partial_t\hat{\mathcal{E}}|$ and $|\partial_z^2\hat{\mathcal{E}}| \ll |k_\mathrm{p}\partial_z\hat{\mathcal{E}}|$. We furthermore neglect the transversal degrees of freedom here and thereby restrict to the one dimensional propagation equation.

1.4.1 Classical light propagation

In the weak probe regime, a linear relationship between the classical electric field and the polarization of the medium is found in Fourier space

$$\mathcal{P}(\omega) = \varepsilon_0\chi(\omega)\mathcal{E}(\omega), \tag{1.46}$$

where $\chi(\omega)$ is the susceptibility. The propagation of an electric field is governed by [94]

$$\partial_z\mathcal{E} + \frac{1}{v_g}\partial_t\mathcal{E} = i\frac{k}{2}\chi(\omega)\mathcal{E}, \tag{1.47}$$

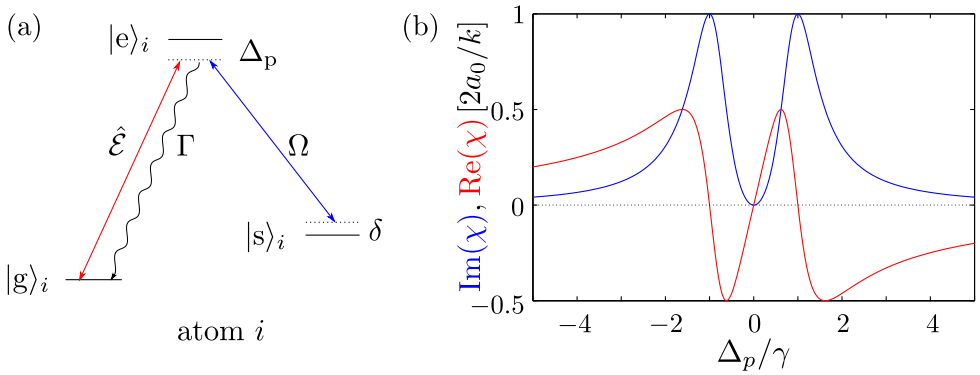

Figure 1.4: (a) Lambda type level scheme used for coherent control of of photons in atomic media. (b) Real (red) and imaginary (blue) part of EIT susceptibility as a function of the probe-frequency for resonant control field with $\Omega = \gamma$.

with the susceptibility for a three level system

$$\chi(\omega) = \frac{2a_0}{k} \frac{i\gamma}{\gamma - i\Delta_\mathrm{p} + i\Omega^2/\delta}. \tag{1.48}$$

The group velocity is defined as $v_g = c/(1+\frac{\omega}{2}\frac{\partial \mathrm{Re}(\chi)}{\partial \omega})$ and the resonant absorption cross section is given by

$$a_0 = \frac{\omega_{\mathrm{eg}}|p_{\mathrm{eg}}|^2}{2\varepsilon_0 c\hbar\gamma} n_\mathrm{a}, \tag{1.49}$$

where n_a is the atomic density.

Let us first consider the limit of vanishing control field Ω or large two photon detuning, specifically $\Omega^2/\delta \ll \Delta_\mathrm{p}$. In this limit, the system is effectively reduced to a conventional two level medium with susceptibility

$$\chi_2(\omega) = \frac{2a_0}{k}\left[i\frac{\gamma^2}{\gamma^2+\Delta_p^2} - \frac{\gamma\Delta_p}{\gamma^2+\Delta_p^2}\right]. \tag{1.50}$$

For a spectrally narrow pulse the propagated pulse is given by

$$\mathcal{E}(z,t) = \mathcal{E}(z - v_\mathrm{g}t, 0)e^{-i\chi(k/2)v_\mathrm{g}t}, \tag{1.51}$$

$$\Rightarrow |\mathcal{E}(z,t)| = |\mathcal{E}(z - v_\mathrm{g}t, 0)|e^{-\mathrm{Im}(\chi)(k/2)v_\mathrm{g}t}, \tag{1.52}$$

which shows the attenuation of the field in the lossy medium. For a resonant pulse one finds an exponential attenuation with the absorption length given by $l_\mathrm{abs} = 1/a_0$.

We now return to the full expression for the susceptibility. In Fig. 1.4(b) we show the real (red) and imaginary (blue) part of χ for $\Omega = \gamma$ and resonant control field $\Delta_\mathrm{c} = 0$ (solid). On exact two photon resonance, $\delta = 0$, the imaginary part of the susceptibility vanishes. A narrow bandwidth pulse can therefore propagate without losses, which is the phenomenon known as electromagnetically induced transparency (EIT) [96].

As a consequence of the large second derivative of $\mathrm{Im}(\chi)$ near two photon resonance and the Kramers-Kronig relations between real and imaginary part of χ, one finds a large first derivative of $\mathrm{Re}(\chi)$ near resonance. A narrow, resonant pulse experiences a dramatic reduction of the group velocity besides transparency, which is the basis of slow light [97].

1.4.2 Continuum Maxwell Bloch equations

An elegant formulation of slow light can be given by introducing new polariton fields, which are quasiparticles of photonic and matter component. To this end, we first introduce new coarse grained fields for the atoms and discuss their coupling to the light field. We then introduce the polariton basis and show that on two photon resonance, both EIT and slow light can be explained by so called dark state polaritons (DSP).

When the density of atoms is sufficiently high compared to the length scales set by changes in the slowly varying amplitudes and phases, it is justified to introduce coarse grained field for the description of the atoms. Following reference [95], we consider small volumes $\Delta V(\mathbf{r})$ with $\Delta N \gg 1$ atoms inside and define

$$\hat{\sigma}_{\mu\nu}(\mathbf{r}) = \frac{\sqrt{n_\mathrm{a}}}{\Delta N} \sum_{j \in \Delta V(\mathbf{r})} \hat{\sigma}_{\mu\nu}^{(j)}. \tag{1.53}$$

These operators inherit the commutation relations of the single atom operators in the continuum limit

$$[\hat{\sigma}_{\alpha,\beta}(\mathbf{r}), \hat{\sigma}_{\mu\nu}(\mathbf{r}')] = \frac{1}{\sqrt{n}} \delta(\mathbf{r} - \mathbf{r}')[\delta_{\beta\mu}\hat{\sigma}_{\alpha\nu}(\mathbf{r}) - \delta_{\nu\alpha}\hat{\sigma}_{\mu\beta}(\mathbf{r})]. \tag{1.54}$$

We are only interested in the weak probe regime, meaning that to lowest order atoms remain in their ground state, therefore $\hat{\sigma}_{gg}^{(0)} = \sqrt{n_\mathrm{a}}$. The relevant operators for our discussion are the coherence of excited and ground state $\hat{\sigma}_{eg} := \hat{\mathcal{P}}^\dagger$ and between spin and ground state $\hat{\sigma}_{sg} := S^\dagger$. In the weak probe regime, these fulfill the commutation relations

$$[\hat{\mathcal{P}}(\mathbf{r}), \hat{\mathcal{P}}(\mathbf{r}')^\dagger] = [\hat{\mathcal{S}}(\mathbf{r}), \hat{\mathcal{S}}(\mathbf{r}')^\dagger] = \delta(\mathbf{r} - \mathbf{r}'). \tag{1.55}$$

From the Hamiltonian of the atom field interaction and the Heisenberg equations of motion, one can derive equations of motion, known as the Maxwell Bloch equations

$$(\partial_t + c\partial_c)\hat{\mathcal{E}}(z,t) = ig(z)\hat{\mathcal{P}}(z,t) \tag{1.56}$$

$$\partial_t \hat{\mathcal{P}}(z,t) = ig(z)\hat{\mathcal{E}}(z,t) - (\gamma - i\Delta_\mathrm{p})\hat{\mathcal{P}}(z,t) + i\Omega\hat{\mathcal{S}}(z,t) \tag{1.57}$$

$$\partial_t \hat{\mathcal{S}}(z,t) = i\Omega\hat{\mathcal{P}}(z,t) + i\delta\hat{\mathcal{S}}(z,t) \tag{1.58}$$

where $g(z)$ is the collective atom-field coupling [98]

$$g(z) = p_\mathrm{ge}\sqrt{n_\mathrm{a}(z)}\sqrt{\frac{\omega_\mathrm{p}}{2\hbar\varepsilon_0}}, \tag{1.59}$$

which includes the atomic density. In the presence of decay γ, solutions to above dynamic equations violate the commutation relations in Eq. 1.55 because we did not include the Langevin noise operators [99]. This approximation is justified in the weak probe regime we consider, because population in the excited state $\hat{\sigma}_\mathrm{ee}$ is small.

1.4.3 Dark state polaritons

The DSP has been introduced in [100] as an intuitive picture for the propagation of light near two photon resonance in an EIT medium. Two polariton branches are introduced, which are

coherent superpositions of the electric field and the spin excitation

$$\hat{\Psi} = \cos(\theta)\hat{\mathcal{E}} - \sin(\theta)\hat{\mathcal{S}}, \tag{1.60}$$

$$\hat{\Phi} = \sin(\theta)\hat{\mathcal{E}} + \cos(\theta)\hat{\mathcal{S}}. \tag{1.61}$$

The mixing angle is defined as $\cos(\theta) = \Omega/\sqrt{\Omega^2 + g^2} := \Omega/\Omega_\mathrm{e}$. For an inhomogeneous density of the atomic medium, the collective coupling $g(\mathbf{r})$ is position dependent and therefore the mixing angle and the polariton fields are position dependent. We here however consider only homogeneous media and thus $g(\mathbf{r}) = g$.

For the dynamics of the polariton fields we find from the Maxwell Bloch equations of the original fields

$$[\partial_t + \cos^2(\theta)c\ \partial_z]\hat{\Psi} = -i\delta\sin^2(\theta)\hat{\Psi} - \dot{\theta}\hat{\Phi} + \cos(\theta)\sin(\theta)(i\delta - c\partial_z)\hat{\Phi}, \tag{1.62}$$

$$[\partial_t + \sin^2(\theta)c\ \partial_z]\hat{\Phi} = i\Omega_\mathrm{e}\ \hat{\mathcal{P}} + \dot{\theta}\hat{\Psi} - i\delta\cos^2(\theta)\hat{\Phi} + \cos(\theta)\sin(\theta)(i\delta - c\partial_z)\hat{\Psi}. \tag{1.63}$$

In the case of vanishing two photon detuning $\delta = 0$ and small momentum, the dark state polariton (DSP) $\hat{\Psi}$ is decoupled from the bright state polariton (BSP) $\hat{\Psi}$ and the polarization $\hat{\mathcal{P}}$. As a result, it does not decay and instead propagates at a reduced group velocity of $v_\mathrm{g} = \cos^2(\theta)c$. Changes of the mixing angle θ also contribute to the coupling of DSP and BSP.

To consider the effect of a finite two photon detuning, we first adiabatically eliminate the polarization $\hat{\mathcal{P}}$, which yields $\hat{\mathcal{P}} = -\Omega_\mathrm{e}/(\Delta_\mathrm{p} + i\gamma)\hat{\Phi}$. Substituting this result in Eq. (1.63) yields for the BSP dynamics

$$[\partial_t + \sin(\theta)^2 c\ \partial_z]\hat{\Phi} = -i[\Omega_\mathrm{e}^2/\Delta + \delta\cos^2(\theta)]\hat{\Phi} + \dot{\theta}\hat{\Psi} + \cos(\theta)\sin(\theta)(i\delta - c\partial_z)\hat{\Psi} \tag{1.64}$$

where we introduced $\Delta = \Delta_\mathrm{p} + i\gamma$. A second adiabatic approximation of the BSP yields $\hat{\Phi} = i\Delta/\Omega_\mathrm{e}^2[\cos(\theta)\sin(\theta)c\partial_z - \dot{\theta}]\hat{\Psi}$, such that the effective DSP dynamics in the limit $\sin(\theta) \approx 1$ is given by

$$\left[\partial_t + v_g(1 - 2\frac{\delta\Delta}{\Omega_e^2})\ \partial_z\right]\hat{\Psi} = i\frac{\Delta\dot{\theta}^2}{\Omega_\mathrm{e}^2}\hat{\Psi} - i\delta\hat{\Psi} - i\frac{cv_g\Delta}{\Omega_\mathrm{e}^2}\partial_z^2\hat{\Psi}. \tag{1.65}$$

Non adiabatic losses related to fast changes of the control field are given by the first term on the right hand side and the second term is simply an energy shift due to the two photon detuning δ. The third term describes the dispersion of the DSP and can be interpreted as an effective, real mass in the limit of large one photon detuning $\Delta_\mathrm{p} \gg \gamma$.

Part II

Topological Order in Cold Atom Experiments

Chapter 2

Edge States in a Superlattice Potential

One of the simplest models possessing non-trivial symmetry protected topological properties is the inversion symmetric Su-Schrieffer-Heeger (SSH) model [101], which can be realized by ultra-cold fermions in a 1D tight-binding super-lattice (SL) potential with alternating hopping amplitudes. Its topological properties are classified by a $\mathbb{Z}_2$ invariant given by the Zak phase [61, 60] and have been explored both theoretically [102, 66, 103] and recently experimentally [104]. Here we show that in the case of interacting bosons, MI phases with filling $n = 1/2$ can be non-trivial topological insulators as well, where the topological invariant is the $\mathbb{Z}_2$ many-body Berry phase, first introduced in this context by Hatsugai [105]. It has been pointed out in [105, 106] that the phases of the Haldane model [107] can be characterized by a similar $\mathbb{Z}_2$ Berry phase. This system is well known to support topological many-body edge states [108], which we take as motivation to study the relation between the quantized Berry phase and topological edge states of the SL-Bose-Hubbard model (SL-BHM). The following discussion is based on the publication [H-2013c].

For the case of an ultra-cold bosonic lattice gas it will be shown that introducing a localized potential step allows to create an interface between gapped MI phases with different topological invariants. Due to the interface, many-body ground states emerge that display density minima or maxima at the interface in analogy to an unoccupied or occupied single-particle edge state for free fermions. This can easily be observed with techniques developed in recent years [31, 5, 4]. While for the SSH model a strict relation between the existence of a single-particle mid-gap edge state at open boundaries and the bulk topological invariant has been identified [102, 66], a similar relation does in general not hold for the bosonic SL model with finite interactions due to the absence of particle-hole symmetry. Instead, as we will show using numerical DMRG simulations [109, 110, 111] and analytic approximations, a generalized bulk-edge correspondence holds: While either the empty (hole) or the occupied (particle) edge state remain localized and thus stable until the MI melts due to tunneling, one of the two many-body states hybridizes with the bulk already for much smaller values of the tunneling rate.

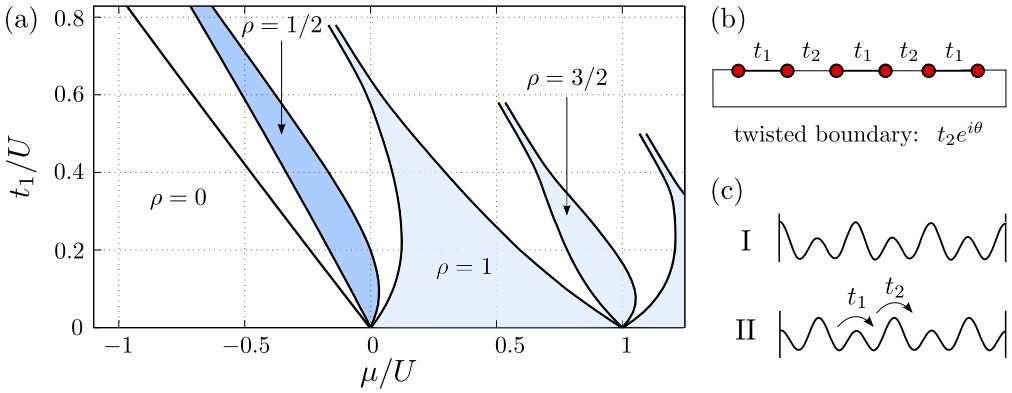

Figure 2.1: (a) Phase-diagram for the SL-BHM with $t_2 = t_1/5$ obtained by DMRG and taken from Ref. [112]. One recognizes the presence of MI phases with integer and half-integer filling. (b) The topological invariant ν is defined via twisted boundary conditions introduced through the phase $e^{i\theta}$ of the ring closing connection. (c) Different dimerizations I and II of SL potential corresponding to Zak phases $\nu^{\mathrm{I}} = 0$ and $\nu^{\mathrm{II}} = \pi$.

2.1 Superlattice Bose-Hubbard Model

The starting point of the discussion is the 1D SL-BHM described by the Hamiltonian

$$\begin{aligned}\hat{\mathcal{H}} &= -\sum_{j \text{ odd}} \left(t_1\, \hat{a}_j^\dagger \hat{a}_{j+1} + \text{h.c.}\right) - \sum_{j \text{ even}} \left(t_2\, \hat{a}_j^\dagger \hat{a}_{j+1} + \text{h.c.}\right) \\ &\quad + \frac{U}{2} \sum_j \hat{n}_j \left(\hat{n}_j - 1\right) + \sum_j (\varepsilon_j - \mu)\hat{n}_j, \end{aligned} \tag{2.1}$$

where $\hat{a}_j$ and $\hat{a}_j^\dagger$ are the bosonic annihilation and creation operators at lattice site j, and $\hat{n}_j = \hat{a}_j^\dagger \hat{a}_j$ the on-site particle number. Particles tunnel with alternating hopping amplitudes t_1 and t_2 and there is an on-site interaction U. ε_j describes a potential and we will be interested in the ground state of the grand-canonical ensemble $\hat{K} = \hat{\mathcal{H}} - \mu \hat{N}$, where μ is the chemical potential. A generic ground-state phase diagram of the SL-BHM, taken from Ref. [112], is shown in Fig. 2.1 for $\varepsilon_j \equiv 0$. Besides MI phases with integer filling it shows loophole insulating regions with half integer filling for $t_2 = t_1/5 < t_1$ [113, 114]. These regions shrink when t_2 increases for fixed t_1, and vanish for equal hopping amplitudes $t_2 = t_1$. At this point the SL-BHM simplifies to the conventional Bose-Hubbard model and only integer filling MI phases are found. The loophole phases reappear when $t_2 > t_1$ and the point $t_2 = t_1$ marks the topological phase transition.

2.1.1 Relation to SSH model

We now discuss the limiting case of onsite interaction $U \to \infty$, which connects our bosonic model to the fermionic SSH model. In the strong interaction limit the double or higher occupation of single lattice sites is energetically suppressed and we can replace the bosonic operators $\hat{a}, \hat{a}^\dagger$ by hard core bosons $\hat{b}, \hat{b}^\dagger$ that fulfill the commutator relations

$$\{\hat{b}_j, \hat{b}_j^\dagger\} = 1,\ \{\hat{b}_j, \hat{b}_j\} = 0,\ [\hat{b}_j, \hat{b}_{k\neq j}^\dagger] = 0, \tag{2.2}$$

which are identical to the operators of a spin 1/2-system. By use of the Jordan-Wigner transformation

$$\hat{c}_j^\dagger = \exp(\prod_{k<j} \pi \hat{b}_k^\dagger \hat{b}_k)\ \hat{b}_j^\dagger, \tag{2.3}$$

the non local commutator is replaced with an anticommutator and we can map the SL-BHM onto non interacting fermions [115]. It is then identical to the SSH model

$$\hat{\mathcal{H}}_{\mathrm{SSH}} = -t_1 \sum_{j,\mathrm{odd}} (\hat{c}_j^\dagger \hat{c}_{j+1} + \mathrm{h.c.}) - \mathrm{t}_2 \sum_{\mathrm{j,even}} (\hat{\mathrm{c}}_\mathrm{j}^\dagger \hat{\mathrm{c}}_{\mathrm{j}+1} + \mathrm{h.c.}), \tag{2.4}$$

which in an infinite system with periodic boundary conditions is diagonalized in momentum space,

$$\hat{\mathcal{H}}_{\mathrm{SSH}} = -\int_k \begin{pmatrix} \hat{d}_k^\dagger & \hat{e}_k^\dagger \end{pmatrix} \begin{pmatrix} 0 & t_1 + t_2 e^{ik} \\ t_1 + t_2 e^{-ik} & 0 \end{pmatrix} \begin{pmatrix} \hat{d}_k \\ \hat{e}_k \end{pmatrix}. \tag{2.5}$$

Here we took into account the two site unit cell by introducing $\hat{d}_k = \frac{1}{\sqrt{L}} \sum_{j,\mathrm{odd}} \hat{c}_j^\dagger e^{ikj/L}$, $\hat{e}_k = \frac{1}{\sqrt{L}} \sum_{j,\mathrm{even}} \hat{c}_j^\dagger e^{ikj/L}$ and going to the thermodynamic limit $L \to \infty$. For $t_1 \neq t_2$ the band-structure has two bands $\varepsilon_\pm = \pm\sqrt{t_1^2 + t_2^2 + 2t_1 t_2 \cos(k)}$ of width $\max(t_1, t_2)$ and separated by energy $2|t_1 - t_2|$. The Bloch functions are given by

$$|u(k)\rangle = \begin{pmatrix} \pm(t_1 + t_2 e^{-ik})/\sqrt{t_1^2 + t_2^2 + 2t_1 t_2 \cos(k)} \\ 1 \end{pmatrix} / \sqrt{2}, \tag{2.6}$$

where we have chosen the gauge such, that only the first component is k dependent. Due to inversion symmetry the amplitude of both components is identical $1/\sqrt{2}$ and only the phase relation is of relevance. In the case of non-interacting fermions, the topology of the band structure is determined by its Zak phase [60] or winding number,

$$\nu = i \int_0^{2\pi} dk \langle u(k) | \partial_k | u(k) \rangle. \tag{2.7}$$

While for a general 1D band structure the Zak phase may take arbitrary values, it is integer (i.e. $\mathbb{Z}$) quantized (in units of π) [50] when inversion symmetry is present, and $\mathbb{Z}_2$ quantized for the SSH case. The winding numbers of the upper and lower band are equal but opposite $\nu = 0$ ($\pm\pi$) for dimerization I (II), see Fig. 2.1.

The Bloch functions $|u(k; t_1, t_2)\rangle$ can be represented on the Bloch sphere as shown in Fig. 2.2(a). As a consequence of inversion symmetry the amplitudes of first and second component are identical $1/\sqrt{2}$ and the Bloch vectors are restricted to the equator of the sphere. Due to the presence of an energy gap the Bloch vectors change continuously with k and trace a well defined path over the range $k \in (0, 2\pi)$. Given the symmetry, the Zak phase is equivalent to the number of windings of the Bloch vector around the sphere and it is therefore strictly quantized and distinguishes the two phases. Inversion symmetry can be broken by introducing an offset potential

$$\hat{\mathcal{H}}_\Delta = \Delta \sum_{j\ \mathrm{even}} \hat{n}_j. \tag{2.8}$$

Without symmetry protection the Bloch vector moves away from the equator plane (see Fig. 2.2(a)) and the Zak phase can no longer be identified with the winding, thus we find no

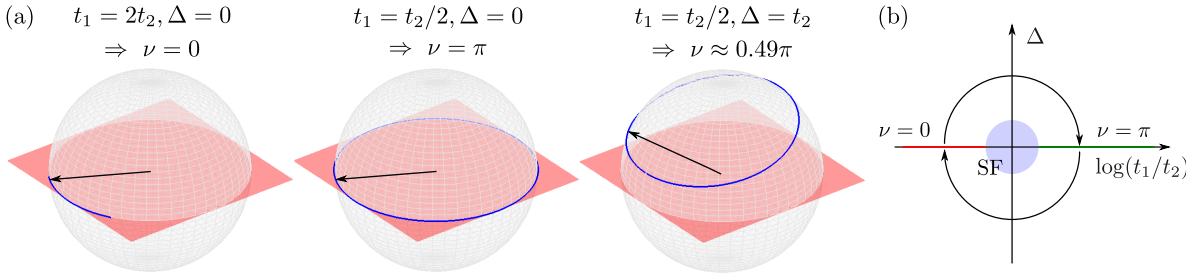

Figure 2.2: (a) Representation of the Bloch functions $|u(k)\rangle$ on the Bloch sphere. The black arrow marks the state for generic k and the blue line traces the state for all k in the range $(0, 2\pi)$. Only for non broken symmetry the Bloch vector is restricted to the equator and the Zak phase is well defined and quantized in the sense of a winding number. (b) Parameter space for the Thouless pump in system of interacting bosons. To stabilize the incompressible loophole phase either a large imbalance of t_1, t_2 or an offset potential Δ is required. The two topological phases can not be connected by a symmetry preserving ($\Delta = 0$) path without crossing the super fluid region. The depicted Thouless cycle adiabatically connects the two phases by breaking the symmetry.

quantization of ν for $\Delta \neq 0$.

Topological properties often reveal themselves at the interface between two topologically different phases. In the case of the SSH model such an interface is simply realized between a system at half filling with non trivial topology $\nu = \pi$ and the vacuum. The emergence of edge states becomes apparent when calculating the single particle wave function in an odd length SSH model $L = 2l + 1$ with open boundary conditions. Whereas the l states of highest and lowest energy are bulk states, which are delocalized over the entire system, in the center gap a single edge state appears. Dependent on the exact choice of where the boundaries cut the system and the ratio of t_1/t_2, this state is exponentially localized at the left or right edge on a length scale of

$$\xi = \frac{\sqrt{t_1 t_2}}{|t_1 - t_2|}. \tag{2.9}$$

At the point of the topological phase transition, $t_1 = t_2$, this length scale diverges and the localized edge state vanishes.

2.1.2 Finite interaction

We now turn to bosons with finite interaction U and discuss how and whether concepts developed for the SSH model can be carried over. Two immediate consequences have to be addressed first. The mapping to non interacting fermions and therefore the solution via this approach is no longer possible for general U and we must instead rely on approximate methods such as the cell strong coupling perturbative expansion (CSCPE) [116] or sophisticated numeric methods such as DMRG [109]. Furthermore the momentum k is not a conserved quantity for the interacting system and we must employ a many-body generalization of the winding number. Like the Chern number [117] it can be defined via generalized boundary conditions [118], $\psi(x_j + L) = e^{i\theta}\psi(x_j)$ for all coordinates $j = 1, ..., N$ and system size L. These boundary conditions correspond to a magnetic flux θ threading the system. When this flux is adiabatically varied, the many-body wavefunction $|\Psi(\theta)\rangle$ picks up a Berry phase [61]

$$\nu = i \int_0^{2\pi} d\theta \ \langle \psi(\theta) | \partial_\theta | \psi(\theta) \rangle. \tag{2.10}$$

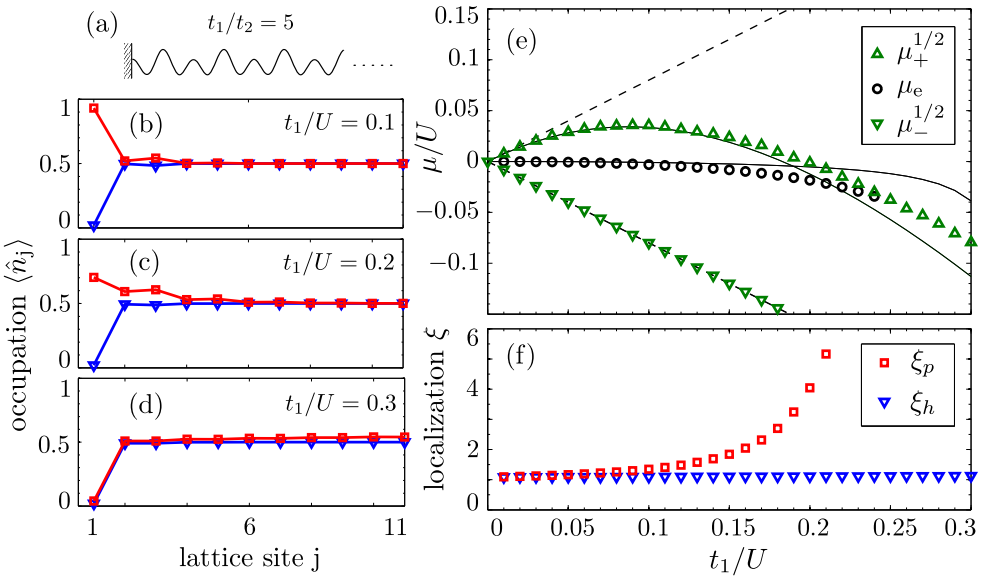

Figure 2.3: (a) $n = 1/2$ MI with open boundary corresponding to topologically non-trivial dimerization (II). Plots in (b)-(d), calculated by DMRG, show density distributions below (blue triangles) and above (red squares) the critical chemical potential of edge-state occupation μ_e for $t_1/U = 0.1, 0.2, 0.3$ respectively. While a well localized hole state (empty edge) can be observed in all cases, the particle state (occupied edge) becomes unstable already before the MI melts (e). Due to the absence of particle hole symmetry $\mu_+^{1/2}$ (green up-pointing triangles) approaches μ_e (black circles) already at small values of t_1/U. Solid curves show analytic results from CSCPE, dashed straight lines correspond to hard-core results. (f) When μ_e approaches $\mu_+^{1/2}$ the particle state becomes delocalized as can be see from the localization length $\xi_{p,h}$ of particle and hole edge states. Systems of length $L = 65$ are considered in the DMRG simulation and numeric error bars are within the symbol size.

This topological order parameter is identical to the Zak phase defined in the hard-core limit $U \to \infty$. Most importantly the topological invariant is well defined and stays strictly quantized even for finite U as long as the particle-hole gap is finite. This however is a consequence of inversion symmetry alone and was realized already by Zak [60] . An exact proof including the interacting case can be given following the proof of Hatsugai [105]. Our system is invariant under both spatial inversion (P) and time-reversal (T), even when twisted boundary conditions are used. Then the combined symmetry PT is of the type considered in [105]. Fabian Grusdt verified the quantization for small systems by exact diagonalization, but the $\mathbb{Z}_2$ invariant could as well be calculated using DMRG or using quantum Monte Carlo [119]. Thus we expect the non-trivial topology of the SSH bands to carry over to bosons with finite interactions. This is our motivation to study edge states of topologically non-trivial MI phases in the SL-BHM as indicators for a quantized topological invariant.

2.2 Interfaces of Topological Phases

Let us consider a system within the first loophole phase, the half filled MI. For a chemical potential within the range

$$\mu_-^{1/2} < \mu < \mu_+^{1/2} \tag{2.11}$$

the bulk is in a gapped phase with $n = 1/2$. For large interactions $U \gg t_1 > t_2$ the values of $\mu_\pm^{1/2}$ can be determined perturbatively within CSCPE [116, 120] up to order $\mathcal{O}(t_2^2/U,\, t_2 t_1^2/U^2)$:

$$\mu_-^{1/2} = -(t_1 - t_2), \tag{2.12}$$

$$\mu_+^{1/2} = (t_1 - t_2) + \frac{U}{2} - \frac{1}{2}\sqrt{16t_1^2 + U^2} - \frac{4t_1 t_2}{U}. \tag{2.13}$$

Choosing e.g. a ratio $t_1/t_2 = 5$, the bulk gap $\Delta = \mu_+^{1/2} - \mu_-^{1/2}$ remains finite until about $t_1/U \approx 1.2$ In the limit $U \to \infty$ we expect from analogy with the SSH model a mid-gap edge state if we add an open boundary with the topologically non-trivial dimerization (II), see Fig. 2.3(a). And indeed for small values of $t_1/U = 0.1$ and 0.2 DMRG simulations show both a well localized hole (ψ_h) and particle (ψ_p) state below and above a critical chemical potential μ_e, see Fig. 2.3(b) and (c). These grand canonical ground states differ in their total particle number by one. However, as shown in Fig. 2.3(d), already for $t_1/U = 0.3$, i.e. well within the MI phase the situation changes: when increasing the chemical potential the density of the bulk increases non-locally instead of filling up the hole at the edge.

Interestingly our results show that the localized hole at the left edge survives even when the chemical potential exceeds $\mu_+^{1/2}$ and the bulk becomes gapless. We will not discuss this here and restrict the discussion to the gapped phase. Within CSCPE we find for the critical chemical potential μ_e, where the grand canonical ground state turns from ψ_h to ψ_p

$$\mu_e = -2t_2^2 \frac{U - 2t_1}{(U + t_1)(U - 3t_1)}. \tag{2.14}$$

We have plotted this result for μ_e along with the values from DMRG simulations in Fig. 2.3(e). As particle hole symmetry is broken for finite values of the interaction, μ_e is no longer exactly in between $\mu_-^{1/2}$ and $\mu_+^{1/2}$. Furthermore at a tunneling rate of $t_1/U \approx 0.25$, the curve touches $\mu_+^{1/2}$, indicating that it becomes energetically favorable to add a particle to the bulk, rather than to the empty edge state (hole state). Within CSCPE we find for the critical value

$$\left(\frac{t_1}{U}\right)_c \approx \frac{1 - \eta}{4(1 + \eta - \eta^2/2)}, \quad \eta = \frac{t_2}{t_1}, \tag{2.15}$$

which is slightly below the numerical value.

One recognizes that the curve of μ_e remains almost a straight line and starts to bend only when it approaches $\mu_+^{1/2}$. This is due to an increasing delocalization of the particle edge state ψ_p. In Fig. 2.3(f) we have plotted the numerically determined localization length $\xi_{p,h}$ for the particle and hole states in units of the lattice constant, defined through the participation ratio

$$\xi = \big(\sum_j \Delta n_j\big)^2 / \sum_j \big(\Delta n_j\big)^2, \tag{2.16}$$

where $\Delta n_j = |n_j - \frac{1}{2}| \Theta\left(\pm(n_j - \frac{1}{2})\right)$ with "+" for ξ_p and "−" for ξ_h and where Θ is the Heaviside step function [121]. While the hole state remains well localized, the localization length of the particle state diverges as the tunneling rate approaches the critical value $(t_1/U)_c$.

Although the bulk-edge correspondence does not hold in the sense of a protected and localized many-body *mid-gap state*, we found that the edge features of topologically trivial and non-trivial phases at an open boundary are markedly different. Whereas in the topologically non-trivial case, the localized particle feature disappears at $(t_1/U)_c$, we generally find that *at least one* of the particle and hole states remains stable. This holds true for all parame-

ters corresponding to a gapped MI in the bulk. This is a direct consequence of topology: A non-trivial bulk of Zak phase $\nu = \pi$ can be reached from the trivial bulk with $\nu = 0$ only through a topological phase transition. However when the underlying symmetries (inversion in our case) are broken one phase can be adiabatically transformed into another, which corresponds to a *quantized, half* Thouless pump (TP) cycle [59]. Since the Zak phase changes by $\Delta\nu = \pi$, the polarization, i.e. the center of mass must change by one lattice site. This follows from the one-to-one relation between Zak phase Eq. (2.10) and polarization [62, 122] discussed in the introduction 1.2. This argument is strict in an infinite system and it carries over to semi-infinite systems with a single open boundary, say on the left side, provided the systems many-body gap still remains finite during the entire TP cycle. In this case the pump effectively creates an excess particle of charge 1/2 localized on the open boundary, (I.e. the density relative to the topologically trivial case increases by an amount corresponding to half a particle). The same holds true for a hole of charge $-1/2$ when the TP is reversed and $\Delta\nu = -\pi$. Since the relevant gaps in the particle (hole) case are $\mu_+^{1/2} - \mu_e$ ($\mu_e - \mu_-^{1/2}$), both are stable for $t_1/U < (t_1/U)_c$. Furthermore, at least one must be stable as long as the bulk particle-hole gap $\mu_+^{1/2} - \mu_-^{1/2}$ is positive.

2.3 Experimental Realization

In the following we discuss a possible experimental realization of edge states using ultra-cold atoms. Although a sharp open boundary is difficult to realize, an interface between two MI phases with integer (e.g. $n = 1$) and half-integer filling (e.g. $n = 1/2$) can be created by increasing the potential energy ε_j by $\Delta\varepsilon$ for a number of consecutive lattice sites such that

$$\mu_-^1 < \mu < \mu_+^1, \tag{2.17}$$

$$\mu_-^{1/2} + \Delta\varepsilon < \mu < \mu_+^{1/2} + \Delta\varepsilon. \tag{2.18}$$

Here $\mu_\pm^{1/2}$ and $\mu_\pm^1$ denote the upper (+) and lower (−) boundaries of the insulating regions in the phase diagram of Fig. 2.1. As shown e.g. in Ref. [123] for the case of Bose-Fermi mixtures, an effective potential step can be created by an admixture of a second atomic species, e.g. fermions, with very small hopping rates. Under appropriate conditions (see [123]) the fermions form a connected cluster at the center of the trap with unity filling and sharp boundaries. This results in an increase of the potential energy of the bosons $\Delta\varepsilon$ which extends over all sites of the fermion cluster. Depending on the location of the interfaces relative to the sub-lattices the winding number either stays, $\Delta\nu = \nu_{1/2}^{\mathrm{I}} - \nu_1 = 0$, or jumps, $\Delta\nu = \nu_{1/2}^{\mathrm{II}} - \nu_1 = \pi$.

Fig. 2.4 shows the density distribution in a weak harmonic trap with an additional potential step $\Delta\varepsilon$ calculated by DMRG. One clearly recognizes interfaces between a central $n = 1/2$ MI and surrounding $n = 1$ MI regions. Since the number of heavy particles was taken to be even, both interfaces are characterized by the same change $|\Delta\nu|$. The upper plot shows the case $\Delta\nu = 0$, the lower one $\Delta\nu = \pi$. In the first case there is a simple step in the density and no additional structure at the edge. The same holds at an interface between any two MI phases with integer fillings irrespective of the dimerization. In the second case, however, one sees pronounced dips or peaks in the average density.

Generalizing the CSCPE to the case of an interface with a finite potential step one can easily determine the potential heights $\Delta\varepsilon$ for which non of the states $\psi_{h,p}$ hybridizes with the bulk, as well as the critical chemical potential at which the many-body ground state turns from the hole edge state ψ_h to the particle edge state ψ_p. The first case (ψ_h) can be detected by measurement of a local particle number less than 1/2 on the $n = 1/2$ MI side of the

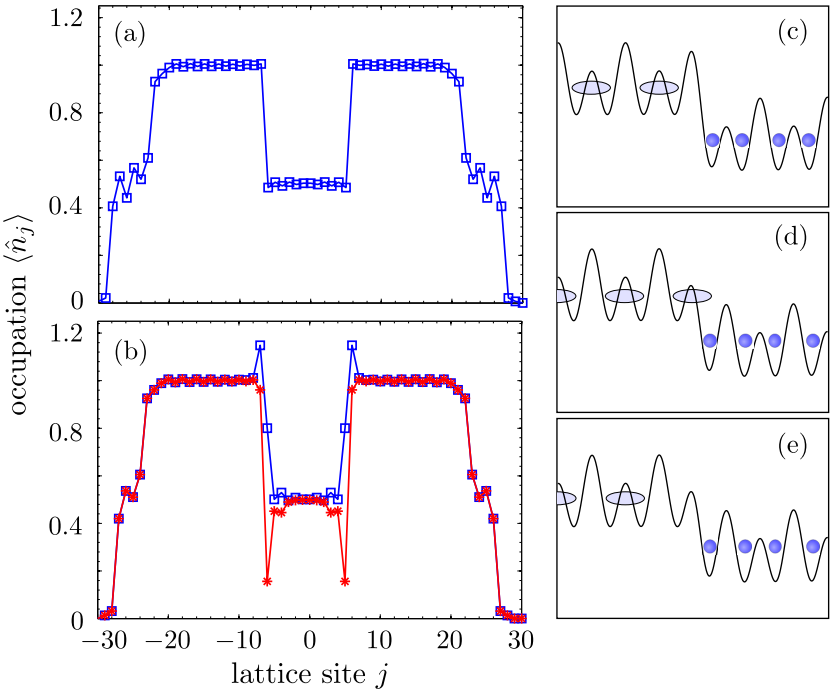

Figure 2.4: Ground state density distribution of the SL-BHM with harmonic trap and potential step between sites $j = -6$ and $j = 5$ leading to interfaces between $n = 1/2$ (in the center) and $n = 1$ MI regions. $\varepsilon_j^{\text{trap}} = \omega(j+0.5)^2$, with $\omega/U = 0.001$. Results are obtained by DMRG simulations for $\mu/U = 0.55$. (a) topological trivial $n = 1/2$ MI phase with $t_1/U = 0.04$, $t_2/U = 0.2$ and $\Delta\varepsilon/U = 0.6$. (b) topological non trivial $n = 1/2$ phase with $t_1/U = 0.2$, $t_2/U = 0.04$ and $\Delta\varepsilon/U = 0.6$(blue squares), 0.7(red stars). Right panel illustrates interface in topologically trivial case (c) and in nontrivial case with occupied (d) and unoccupied interface (e).

interface, the second (ψ_p) by measurement of a particle number larger than 1 on the $n = 1$ MI side.

To verify these results we performed DMRG simulations for a step potential $\varepsilon_j/U = \Delta\varepsilon\Theta(j - j_{\text{step}} + 0.5)$. In Fig. 2.5a we show the local particle number for different values of μ. For $\mu/U = 0.45$ the system is inside the stability region of both edge states. One clearly recognizes a well localized dip in the local particle number. $\mu/U = 0.50$ corresponds to an occupied edge inside the stability region. Here a clearly pronounced density peak appears. When μ is chosen such that the system is outside the region of the $n = 1/2$ Mott insulator ($\mu/U = 0.37$ and $\mu/U = 0.65$) the density dip on the $n = 1/2$ side starts to vanish while interestingly the peak on the $n = 1$ MI side remains. Fig. 2.5(b) shows the local occupation number $\langle \hat{n}_1^{\text{edge}} \rangle$ at the edge of the $n = 1$ MI side as function of μ/U. As soon as μ exceeds μ_e as calculated in CSCPE (red dashed line), there is a clear jump indicating the transition from hole to particle edge state.

A particular feature of the edge state in the SL-BHM, not present in the hard-core limit, is the peak of the local density on the border of the $n = 1$ MI region above unity. Within CSCPE we calculate this density, which yields in zeroth order of t_2

$$\langle \hat{n}_1^{\text{edge}} \rangle = 1 + \frac{4\Delta\varepsilon t_1^2}{U^3} + \frac{6\Delta\varepsilon^2 t_1^2}{U^4} + \mathcal{O}(1/U^5). \tag{2.19}$$

We checked the validity of this result by comparing to DMRG data and found good agreement

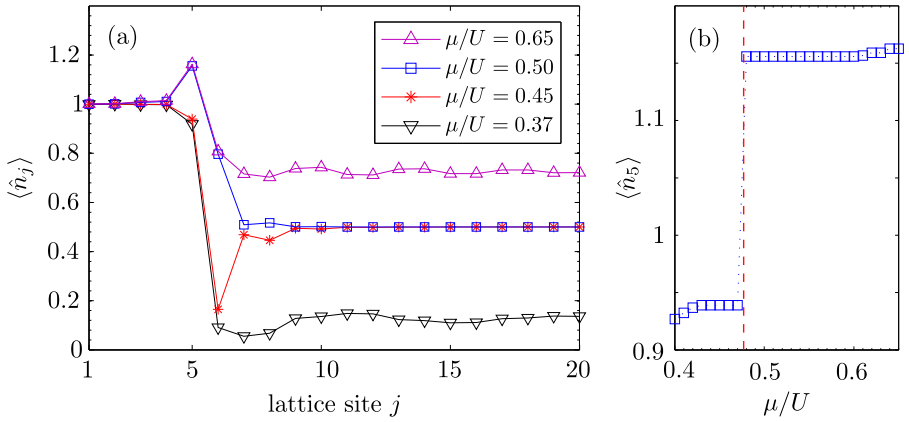

Figure 2.5: (a) Density distribution at potential step $\Delta\varepsilon/U = 0.6$ at $j_{\text{step}} = 6$ for $t_1/U = 0.2$, $t_1/t_2 = 5$ and increasing chemical potential μ/U. (b) Local particle number $\langle \hat{n}_1^{\text{edge}} \rangle$ at the edge of the $n = 1$ MI region as function of μ/U showing the occupation at the edge if $\mu > \mu_e = 0.47$ (dashed red line).

until the $n = 1$ MI starts to melt.

Conclusion

In summary we have discussed topological properties of the one dimensional SL-BHM with alternating hopping rates t_1 and t_2. In the limit of infinite interaction U this model corresponds to the SSH model for free fermions, which is known to possess topologically non-trivial insulating phases for $t_1 \neq t_2$ with a strict bulk-edge correspondence. We introduced a many-body generalization of the Zak phase as topological order parameter, which is quantized as a consequence of inversion symmetry. We analyzed edge states of a MI with filling $n = 1/2$ for open boundary conditions using DMRG and analytic perturbative calculations and found that the bulk-edge correspondence does not hold strictly in the sense of a protected and localized many-body mid-gap state. Instead we showed that, as a direct consequence of non-trivial topology, at least a particle- or a hole-like edge state remains localized and stable until the MI melts. While sharp open boundaries may be difficult to realize in cold-atom experiments, we showed that an interface between a $n = 1$ and $n = 1/2$ MI can be created where two topologically distinct phases are in contact. The required potential step can be realized by an admixture of a second heavy atom species. We found that similar edge states emerge as in the case of open boundary conditions. These edge states are characterized by a density dip at the edge below 1/2 and a density peak at the edge with local particle number exceeding 1. These features allow a simple detection of the edge states and thus a verification of the different topological nature of the MI phases in cold-atom experiments.

Chapter 3

Extended Bose-Hubbard Model on a Superlattice

The topology of the superlattice Bose-Hubbard model discussed in the previous chapter originates from the close relation to the SSH model for free fermions. A conclusive classification of topological phases for such models is found [50]. As we illustrated for the SL-BHM the classification concepts such as the Chern number and the Thouless pump can be generalized towards interacting systems and give useful insight regarding for example the emergence of edge states.

We want to use the established methods to now study truly interacting models, that do not possess a continuous transformation towards a non interacting model. The motivation therefore is twofold, first of all the classification of topological phases of interacting systems already revealed a large number of classes, but it is not yet complete [52]. Furthermore, interacting topological phases promise to feature exotic excitations with fractional charge and statistics [68, 69, 55, 70, 71], which could serve as the basis for quantum computation [8, 72].

Promising candidate systems often combine two properties. The underlying band structure of the non interacting model is flat, in the sense that the interaction is much larger than the bandwidth. On the other hand, the separation to other bands of the model is large compared to the interaction, such that little band mixing occurs. Such systems have attracted much attention for both fermions [124, 125, 126, 127] and bosons [128, 129, 130] with interaction and the emergence of new fractional filling phases has been discussed.

We here consider the generalization of the SL-BHM with the addition of a strong short range interaction. To begin with we discuss the phase diagram obtained using numeric DMRG methods and introduce an effective model, that arises from the projection onto the flat lower band of the SSH model. The relation to the SSH model leads us to a classification scheme using the concept of a Thouless pump and we show that a combination of symmetry breaking and topological winding numbers is required for the complete classification of this system. A signature of topology in the previous chapter were edge states that emerge at the boundary of the system and we find similar edge features here. Due to the interplay with the fractional excitations in the bulk of the system, the melting of these is however significantly altered. The results of this chapter will be published in [H-2014d].

3.1 The Extended Bose-Hubbard Model

The addition of non local interaction between bosons to the model defined in Eq. (2.1) and discussed in the previous chapter is known as the extended Bose-Hubbard model

$$\hat{\mathcal{H}}_{\mathrm{EBHSL}} = \hat{\mathcal{H}}_{\mathrm{BHSL}} + \hat{\mathcal{H}}_{\mathrm{int}}, \tag{3.1}$$

$$\text{with } \hat{\mathcal{H}}_{\mathrm{int}} = V_1 \sum_j \hat{n}_j \hat{n}_{j+1} + V_2 \sum_j \hat{n}_j \hat{n}_{j+2}. \tag{3.2}$$

We here restrict to interactions of finite range two between bosons on adjacent sites and next to adjacent sites. In the trivial limit of vanishing hopping $t_i \ll U, V$, the lowest energy configuration of particles is a classic distribution on the lattice as described in [131]. Depending on the shape and range of the interaction potential a staircase of incompressible phases is found. Whereas for truly long range interaction, a devils staircase of all fractional fillings is realized, for the interaction potential of range two chosen here, incompressible phases are found at fillings

$$\varrho_{t_1=t_2=0} \in \left\{0, \frac{1}{3}, \frac{1}{2}, \frac{2}{3}, 1\right\}. \tag{3.3}$$

At the topological trivial point $t_1 = t_2$ of the superlattice, the melting of these incompressible phases has been discussed in the context of Rydberg excitation crystals [132].

3.1.1 Effective model in the lower SSH band

The SSH model discussed in the previous chapter displays loophole phases at half filling that are only present for $t_1 \neq t_2$. Based on our discussion of the SSH model, we will now motivate the presence of a quarter filling phase for the EBH model for $t_1 \neq t_2$. Consider therefore the limiting case of $U \gg t_1 \gg V_1, V_2 \gg t_2$. The two bands of the non interacting model are flat compared to the separation of the two bands, with a large ratio of $2t_1/t_2 \gg 1$. This makes the SL-EBH model a promising candidate to support non trivial topological phases.

We make use of the lower flat band by projecting onto the lower energy eigenstates of the strong tunneling t_1 within each unit cell. The two eigenstates are given by symmetric and antisymmetric superpositions within the unit cells and we introduce new bosonic operators

$$\hat{b}_j = (\hat{a}_{2j-1} + \hat{a}_{2j})/\sqrt{2}, \qquad \hat{c}_j = (\hat{a}_{2j-1} - \hat{a}_{2j})/\sqrt{2}, \tag{3.4}$$

where $\hat{b}_j^\dagger$ creates a boson in the lower energy state of a single unit cell and $\hat{c}_j^\dagger$ in the higher energy state. We rewrite $\hat{\mathcal{H}}_{\mathrm{EBHSL}}$ in terms of the new operators and project to the low energy sector

$$\begin{aligned}\hat{\mathcal{H}}_{\mathrm{eff}} = &-(t_1+\mu)\sum_{j=1}^{L/2} \hat{b}_j^\dagger \hat{b}_j - t \sum_{j=1}^{L/2-1} (\hat{b}_j^\dagger \hat{b}_{j+1} + \mathrm{h.c.}) \\ &+ w \sum_{j=1}^{L/2-1} \hat{b}_j^\dagger \hat{b}_j \hat{b}_{j+1}^\dagger \hat{b}_{j+1} + \mathcal{O}(\hat{c}).\end{aligned} \tag{3.5}$$

This Hamiltonian again belongs in the class of EBH models, however it is simplified in various ways. First of all the superlattice of alternating hoppings is encoded in the additional local potential $-t_1$ and the reduced hopping $t = t_2/2$. Note that the index j for the effective model iterates the two site unit cells of the original model. The interaction of range two is inherited in an interaction of adjacent bosons with strength $w = (V_1 + 2V_2)/4$.

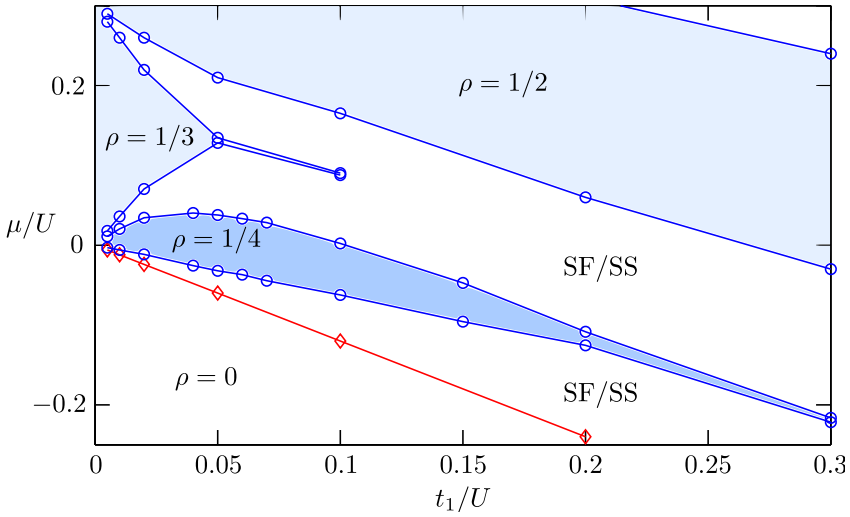

Figure 3.1: Phase Diagram of the extended Bose-Hubbard model in a superlattice with $t_1 = 5t_2$ from DMRG calculations carried out by Richard Jen. Parameters of the interaction are $V_1 = 0.2U$ and $V_2 = 0.1U$.

We discussed the properties of EBH models without superlattice and in the absence of tunneling in the previous section. The interaction of one unit cell range in the effective model, stabilizes incompressible phases of filling $\tilde{\varrho} = 0, 1/2, 1$ per unit cell, which correspond to fillings

$$\varrho_{t_1 \gg t_2} \in \left\{0, \frac{1}{4}, \frac{1}{2}\right\} \tag{3.6}$$

of the original model. To lowest order in t the boundaries of the quarter filling phase are given by

$$\mu_+^{(1/4)} = -t_1 + 2w - 4t, \;\; \mu_-^{(1/4)} = -t_1 + 4t, \tag{3.7}$$

and we therefore expect this phase to vanish for $t \gtrapprox w/4$.

3.1.2 DMRG results

To quantitatively validate the presence of the various incompressible phases predicted from the zero hopping limit of the original model and the effective model we have used numeric DMRG simulations. For strong local interaction U compared to the non local interaction $V_1 = U/5, V_2 = U/10$ and a fixed ratio $t_1 = 5t_2$ we map out the phase diagram at intermediate hopping amplitude shown in Fig. 3.1. In absence of tunneling we observe the expected incompressible phases at zero and $\varrho = 1/3$ filling, where the transition occurs at $\mu = 0$. For non zero hopping t_1 the filling one-third phase melts and a loophole phase of filling one-fourth emerges at $\mu = 0$. Quantitatively the emergence of this phase can not be captured by the effective model, its melting however can. The effective interaction energy $w = 0.1U$ and the effective hopping is given by $t = t_1/10$ and therefore lowest order perturbation theory predicts the melting of the $\varrho = 1/4$ phase for $t_1/U \approx 0.3$ in good agreement with our numeric findings.

Besides the one-fourth filling phase we find the half filling phase that originates from the conventional SSH model. In between the incompressible phases we find evidence for supersolid phases, but we postpone the quantitative discussion of these to a future publication [H-2014d]and focus here on the classification of the incompressible one-fourth filling phase.

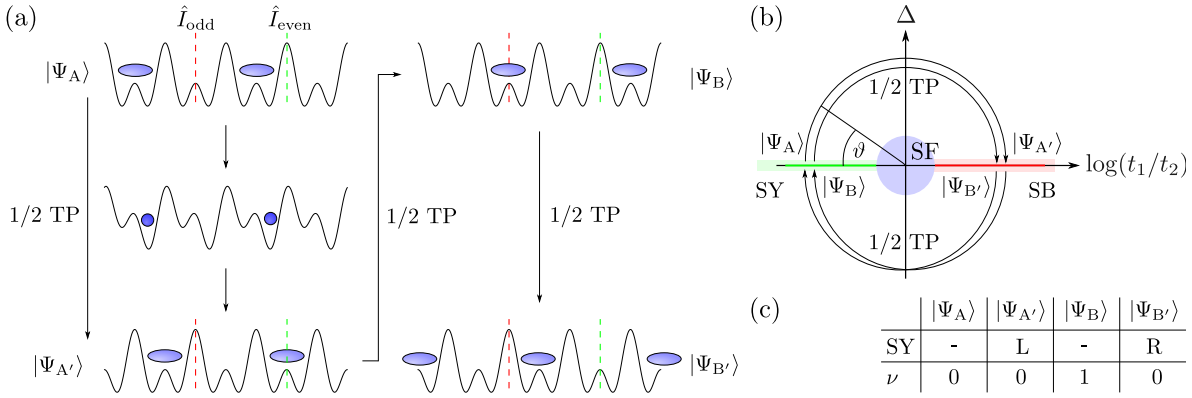

	$\|\Psi_{\text{A}}\rangle$	$\|\Psi_{\text{A}'}\rangle$	$\|\Psi_{\text{B}}\rangle$	$\|\Psi_{\text{B}'}\rangle$
SY	-	L	-	R
ν	0	0	1	0

Figure 3.2: (a) Phases of the quarter filling EBH model in a superlattice with two fold degenerate ground states. Symmetry breaking Thouless pumps connect the individual states. (b) Whereas in the SSH model a single Thouless pump in parameter space is sufficient to return to the origin state, here in general two cycles are necessary. (c) Summary of the classification in terms of symmetry breaking and winding number for the four different states during the cycle in (b).

3.2 Degeneracy and Topology

In the previous chapter we identified two distinct topological phases of the SSH model that could be classified by their Zak phase ν. Here again, we must distinguish between the two dimerizations of the superlattice but the situation is more involved due to the interaction. The quarter filling ground state in an infinite system is not unique but the two states $|\Psi_{\text{A}}\rangle$, $|\Psi_{\text{B}}\rangle$, illustrated in Fig. 3.2(a) are degenerate. The infinite size model is inversion symmetric regarding odd and even bonds as defined in the figure, the odd bond symmetry however does not distinguish between $|\Psi_{\text{A}}\rangle$ and $|\Psi_{\text{B}}\rangle$.

3.2.1 Classification

To reveal the topological nature of this symmetry protected phase, we add diagonal disorder that breaks all but one inversion symmetry around the bond between site $j = 1$ and $j = 2$

$$\hat{\mathcal{H}}_{\text{disorder}} = \sum_{j=1}^{\infty} \varepsilon_j (\hat{n}_{1+j} + \hat{n}_{-j}), \tag{3.8}$$

where ε_j is bounded disorder that is uniformly distributed in a fixed interval $(-\varepsilon, \varepsilon)$. Note that the disorder strength ε should be small compared to the energy gap between the two low energy states and the continuum of states above. Without loss of generality we can choose the origin of the disorder potential such, that the remaining inversion symmetry is an odd bond inversion $\hat{I}_{\text{odd}}$. The only symmetry remaining does not distinguish the two ground states

$$\hat{I}_{\text{odd}}|\text{A}\rangle = |\text{A}\rangle \text{ and } \hat{I}_{\text{odd}}|\text{B}\rangle = |\text{B}\rangle. \tag{3.9}$$

We now reconsider the Thouless pump introduced in the previous chapter. Again the addition of a symmetry breaking potential as defined in Eq. (2.8) is used to define a path through two dimensional parameter space spanned by Δ and t_1/t_2 such that the two low energy states always remain separated from the continuum. After every half cycle of this

pump the symmetry $\hat{I}_{\text{odd}}$ is restored, however it requires more than a full cycle to return to the systems initial state as shown in Fig. 3.2(a) and (b).

After half a Thouless cycle the Hamiltonian is again inversion symmetric regarding the bond between $j = 1, 2$. The state $|\Psi_{\text{A}'}\rangle$ of the system, however breaks this inversion symmetry. After three more half Thouless cycles the state returns to the initial $|\Psi_{\text{A}}\rangle$ and we find for the bond inversion symmetry of all states involved

$$\hat{I}_{\text{odd}}|\Psi_{\text{A}}\rangle \approx \pm|\Psi_{\text{A}}\rangle \text{ and } \hat{I}_{\text{odd}}|\Psi_{\text{B}}\rangle \approx \pm|\Psi_{\text{B}}\rangle, \tag{3.10}$$

$$\hat{I}_{\text{odd}}|\Psi_{\text{B}'}\rangle \approx |\Psi_{\text{A}'}\rangle. \tag{3.11}$$

Whereas for $|\Psi_{\text{A}'}\rangle$ the site to the left of the symmetry bond is occupied (L), for $|\Psi_{\text{B}'}\rangle$ the site to the right is occupied (R) and we can therefore classify them by this symmetry breaking. In order to classify the bulk non symmetry breaking states $|\Psi_{\text{A}}\rangle$ and $|\Psi_{\text{B}}\rangle$, we instead must use the winding number ν, regarding the symmetric bond, as defined in Eq. (2.10). Whereas for state $|\Psi_{\text{A}}\rangle$ the winding is $\nu_{\text{A}} = 0$, for $|\Psi_{\text{B}}\rangle$ a particle is delocalized across the relevant bond and we find a winding of $\nu_{\text{B}} = 1$. Therefore all four configurations of the quarter filled EBH model can be classified only with the combination of a topological quantum number and a symmetry related quantum number as summarized in Fig. 3.2(c).

3.2.2 Chern number

The non trivial topology of the EBH model can furthermore be revealed in the two dimensional parameter space spanned by the Thouless pump cycle ϑ defined in Fig. 3.2 (b) and the twisting angle θ used for the definition of the winding number ν. For gapped systems with a single, unique ground state the Chern number is defined as

$$\text{Ch} = \frac{1}{2\pi}\int_0^{2\pi} d\theta\ \partial_\theta \nu(\theta) \in \mathbb{Z}, \tag{3.12}$$

which is the winding of the winding number. For the BH model discussed in the previous chapter we found Ch = 1 inherited from the bandstructure of the free fermion SSH model. Here the situation is more intricate as the ground state manifold contains two states. Before we turn to the stringent calculation via a generalized Berry connection, we motivate the fractional nature of the quarter filling phase.

Consider a system of $L = 4l, l \in \mathbb{Z}$ sites with periodic boundary conditions. The two low energy states are hybrids of the symmetry breaking states $|\Psi_{\text{A}}\rangle, |\Psi_{\text{B}}\rangle$ are near degenerate with a gap exponentially small in system size. If we follow only state $|\Psi_{\text{A}}\rangle$ through a TP cycle it will be mapped to state $|\Psi_{\text{B}}\rangle$ and only after a second TP cycle it returns to itself. Along this path we can calculate the winding number. The winding number becomes non zero, when a particle is delocalized across the boundary of the system and it changes from 0 to 2π during the crossing. Note that here only after two cycles a single particles has once crossed the boundary and therefore the average winding of the winding number per TP is

$$\text{Ch} = 1/2. \tag{3.13}$$

A more formal derivation of this result can be given by fully taking into account the

degeneracy of the ground state manifold [133].

$$\mathrm{Ch} = \frac{1}{2}\int_0^{2\pi} d\theta\ \partial_\theta[\mathrm{Im}\log\det\hat{W}(\theta)], \tag{3.14}$$

$$\text{with } \hat{W}(\theta) = \mathcal{P}\big[-i\int_0^{2\pi} d\theta' \hat{A}(\theta',\theta)\big], \tag{3.15}$$

where $\hat{A}(\theta',\theta)$ is the non-Abelian generalization of the Berry connection. For the EBH model here, above expression has been evaluated numerically by Fabian Grusdt for small systems via exact diagonalization and the result is identical to the intuitive $\mathrm{Ch} = 1/2$.

3.3 Edges and Fractional Excitations

So far we have only considered the bulk properties of the EBH model with a superlattice. In the following section we will introduce boundaries and begin the discussion of edge physics within the simpler projected model. We then apply our classification scheme for bulk systems and introduce the notion of quasiholes and quasiparticles. Finally we show how introducing twisted bonds in open boundary systems is related to the polarization and how this can be used to illustrate the emergent fractional excitations.

3.3.1 Projected model

The basis of the projected model was the introduction of new bosonic operators for the low energy state within the individual unit cells. Importantly we choose as unit cell the two sites that are connected by the larger hopping amplitude. The introduction of boundaries is trivial when they only cut weak bonds. If however the boundary cuts a strong bond, we must redefine the effective operators at the edge. For example at the left edge we then identify $\hat{b}_1 = \hat{a}_1$, which has consequences for the hopping and interactions near the boundary, but most importantly for the local potential. This is illustrated in Fig. 3.3(a), where we show the projected model for a system of size $L = 2+4l, l \in \mathbb{Z}$, where both boundaries cut weak bonds.

At smaller than half filling in the projected model, particles can avoid both, interaction with particles in adjacent unit cells and to be placed on higher energy sites at the edges. Due to repulsion, the unit cells adjacent to the single edge site will be occupied. Exactly at half filling two options have to be considered and they are both illustrated in Fig. 3.3(a). Either one particle is placed at the edge at the energy cost of approximately t_1 or the edges are unoccupied and a single pair of bosons on adjacent sites has to be placed in the bulk with energy cost w.

3.3.2 Fractional excitations and edge delocalization

Here the fractional nature of the quarter filling MI becomes apparent. Consider a separation of the one dimensional system into three connected regions. A center bulk region and the two regions that can be attributed to the boundaries. We want to classify the state within each region in terms of the scheme introduced in Sec. 3.2.1. As the underlying lattice is fixed we must only distinguish between states $|\mathrm{A}\rangle$ and $|\mathrm{B}\rangle$, where we choose the left edge as a reference point without loss of generality. Microscopic details determine whether both edges enforce identical or different bulk states A,B in the adjacent region. From topology we deduce that regions with different configurations can not be connected without closing the energy gap. For the EBH model this closing of the gap is realized via the introduction of fractional excitations.

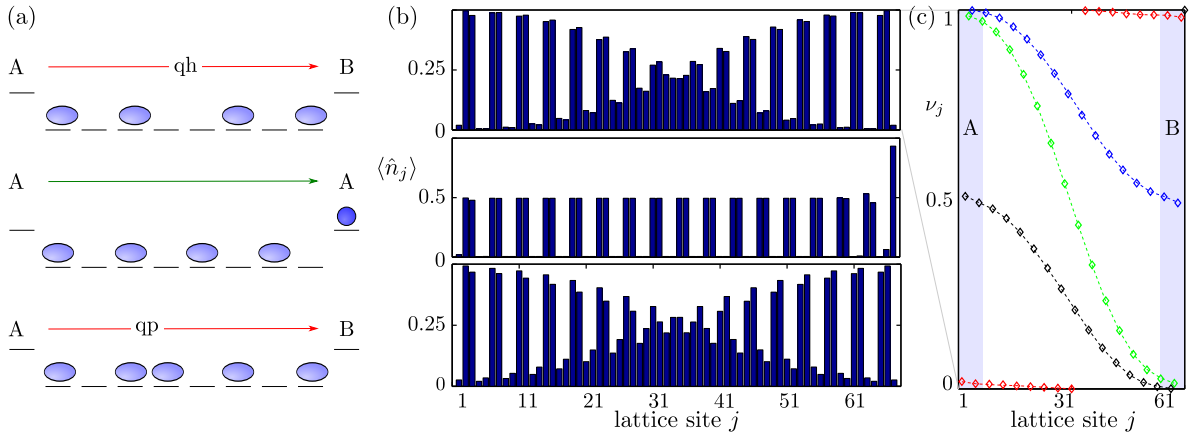

Figure 3.3: Finite size systems of length $L = 2 + 4l, l \in \mathbb{Z}$ of the EBH model with next and next-next neighbor interaction and a superlattice with $t_1 = 5t_2$. The boundaries are chosen such that they cut weak bonds t_2 (a) Schematic representation of the projected model and the possible configurations of particles around half filling. (b) Density distribution in a large system of $L = 66$ obtained by Richard Jen using DMRG methods. (c) Local winding ν_j for the quasihole example in (b). Colors represent lattice sites $\mathrm{mod}(j, 4) = 1$ (red), $\mathrm{mod}(j, 4) = 1$ (black), $\mathrm{mod}(j, 4) = 1$ (green) and $\mathrm{mod}(j, 4) = 1$ (blue) and lines are guides to the eye.

In the first and third example we give in Fig. 3.3(a) the edges are incompatible and the difference is resolved by a quasihole (quasiparticle) that is delocalized in the center bulk region. These fractional excitations are different from the excitations of for example a conventional unit filling MI. Whereas single holes and doublons can be created by strictly local operations, one can not introduce quasiexcitation into the system without applying a global transformation, shifting the entire bulk to the left or right of the excitation by one unit cell.

In Fig. 3.3(b) we show the density distribution obtained from DMRG simulations of the full SL-EBH model for a system of size $L = 66 = 2+2\times 32$. Parameters are in correspondence to the three scenarios discussed above and displayed in Fig. 3.3(a). As for the SL-BHM we must modify the bulk phase diagram when considering systems with boundaries and add critical lines for the addition of a single particle. We here must further take into account the transition from an excitation bound to the edge and a delocalized quasiexcitation in the bulk. In Fig. 3.4(a) we show the subdivided phase diagram for the quarter filling phase with non trivial edges.

Results can be interpreted within the effective model introduced in Section 3.1.1 and the quasiexcitation picture. Within the effective model, we have to consider an even number of unit cells with local potential $-t_1$ and two edge sites, which have zero local potential. Below the critical red line, the edge sites remain empty and the bulk is exactly quarter filled with particles and a single quasihole. When increasing the chemical potential beyond a critical chemical potential μ_c, at small hopping a single particle is added at one of the two edges, cf. the inset of Fig. 3.3(a). Notice the spontaneous symmetry breaking, the state is degenerate with the configuration where the particle is localized on the opposite end. The presence of this edge particle compresses the bulk phase and the quasihole is removed. Therefore the critical chemical potential is to lowest order given by $\mu_c = t_2$.

For hopping t_1 larger than a critical value, displayed in Fig. 3.3(a) as the separating solid line between red and blue shaded area, it becomes favorable to place the additional particle within the bulk. This reduces the overall energy by t_1, but costs a single interaction energy

w. The critical chemical potential in this regime is then given by $\mu_c = w - t_1$. We have added these approximate results as dashed lines in Fig. 3.4(a) and find qualitative agreement. Quantitatively the two results disagree because of the neglected effects of finite t_2. This for example becomes apparent for the density distribution of the quasiparticle in Fig. 3.3(b), where densities within a unit cell are not symmetric.

Using the participation ratio defined in Eq. (2.16), we have characterized the transition from a localized edge excitation to a delocalized quasiparticle in the bulk. Results for various system size are displayed in Fig. 3.4(b).

3.3.3 Polarization and winding number

We generalized the Zak phase for non interacting fermionic systems in the previous chapter by introducing the winding number for systems with periodic boundary conditions. We here briefly discuss similar winding numbers in open boundary condition systems that are easily accessible with DMRG simulations. Given a Hubbard model as defined in Eq. (3.1) the local winding number ν_j is defined as the Berry phase we obtain by introducing a local flux at hopping j, $t_j \to t_j e^{i\varphi}$ and calculating

$$\nu_j = \frac{1}{2\pi i}\int_0^{2\pi} d\varphi \langle \Psi(\varphi)|\partial_\varphi|\Psi(\varphi)\rangle, \tag{3.16}$$

where $|\Psi(\varphi)$ is the ground state with introduced flux. The initial problem has purely real hopping $t_j \in \mathcal{R}$ and we introduce the local flux φ at hopping s into the system. In absence of periodic boundary conditions, we can always introduce a gauge transformation of the bosonic operators and return to the original problem. The ground state is identical in the transformed basis

$$|\Psi(\varphi)\rangle = \sum_{m_1,\cdots,m_L} \Psi_{m_1,\cdots,m_L} \hat{d}_1^{\dagger,m_1}\cdots\hat{d}_L^{\dagger,m_L}|0\rangle, \tag{3.17}$$

$$= \sum_{m_1,\cdots,m_L} \Psi_{m_1,\cdots,m_L} \hat{a}_1^{\dagger,m_1}\cdots\hat{a}_L^{\dagger,m_L} e^{-i\varphi(m_{s+1}+\cdots+m_L)}|0\rangle. \tag{3.18}$$

If we calculate the winding number

$$\nu_s = \frac{1}{2\pi i}\int_0^{2\pi} d\varphi \langle \Psi(\varphi)|\partial_\varphi|\Psi(\varphi)\rangle \tag{3.19}$$

$$= \frac{1}{2\pi i}\int_0^{2\pi} d\varphi \langle \Psi(0)| - i\sum_{j=s+1}^{L}\hat{n}_j|\Psi(0)\rangle \tag{3.20}$$

$$= -\sum_{j=s+1}^{L}\langle\hat{n}_j\rangle. \tag{3.21}$$

and consider the remaining gauge freedom, the winding number is only well defined modulo one

$$\nu_s = -\sum_{j=s+1}^{L}\langle\hat{n}_j\rangle \bmod 1. \tag{3.22}$$

It is therefore nothing but counting the number of particles to the right, respectively to the left with a negative sign, of the bond the flux was introduced.

Only in the presence of additional symmetries ν_s is guaranteed to be quantized. Nonethe-

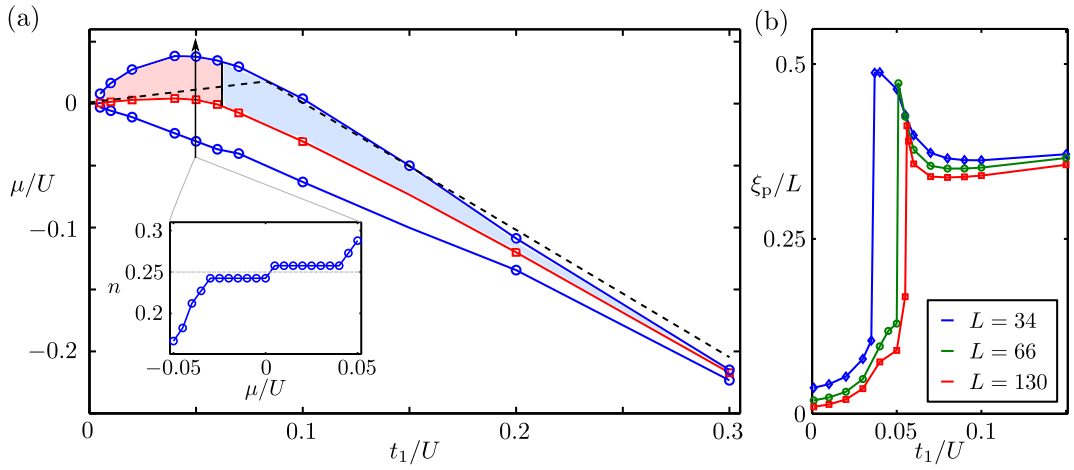

Figure 3.4: (a) Phase diagram of the quarter filling MI with nontrivial topology as discussed in the text. Besides the upper and lower boundary of the incompressible phase at quarter filling, we find an intermediate critical chemical potential, where a single particle is added as shown in the lower left inset. (b) Melting of the edge excitation into the bulk as characterized by the participation ratio ξ_p for varying system sizes as a function of hopping t_1. Other parameters are $t_1 = 5t_2$, $V_1 = U/5$ and $V_2 = U/10$. Numerical simulations were carried out by Richard Jen.

less it allows a very insightful representation of the density distributions. Consider the first example in Fig. 3.3(a), as discussed earlier within a small region close to the left edge the state is approximately in configuration A, whereas at the opposite end of the chain, the system is in the second configuration B and this difference has to be interpolated by a quasihole within the bulk. For the winding number ν_s we then find

$$\begin{array}{cccc} \nu_1 = 0, & \nu_2 = 0.5, & \nu_3 = 0, & \nu_4 = 0, \\ \vdots & \vdots & \vdots & \vdots \\ \nu_{61} = 0, & \nu_{62} = 0, & \nu_{63} = 0, & \nu_{64} = 0.5. \end{array} \tag{3.23}$$

The density distribution in extended systems is approximately periodic with period 4. The mismatch from left to right state is illustrated by the mismatch in the winding numbers. In Fig. 3.3(c) we display ν_s for all lattice sites and find that due to the delocalized quasihole the mismatch is smoothly interpolated in the center bulk region.

Conclusion

In this chapter we studied the incompressible quarter filling phase in the SL-EBH model that emerges from the flat topological bands of the SL-BH model studied in the previous chapter and additional long range interaction. Similar to related work in the past, we found a degeneracy of the ground state and a fractional Chern number of $\mathrm{Ch} = 1/2$ per ground state [125]. Based on our experience with the Thouless pump we introduced a second classification scheme based on symmetry protected topological order in one dimension. We showed that a combination of a topological winding number and inversion symmetry breaking is required to completely classify the different phases of the SL-EBH model. Classification in terms of both a conventional symmetry breaking order and topological order, has been proposed as a general approach towards interacting topological phases of matter by Chen et al. [52].

As for the SL-BH model, edge states emerge for non trivial boundary conditions. Again, we find that for increasing hopping, the bulk boundary correspondence does only guarantee the existence of the hole state, as long as one stays in the incompressible phase. States with a localized particle at the edge, hybridize with quasiparticle states in the bulk and are not occupied for large hoppings. We introduced the local winding number as an intuitive representation for the local density, which reveals how fractional excitations in the bulk interpolate between different configurations at the boundaries of the system.

Chapter 4

Thin-Torus Limit of a FCI in Bosonic Systems

It is a long standing goal in the cold atom community to realize interacting models with strong *magnetic* fields and prepare interesting ground states, such as the Laughlin states [71]. We here propose a setup for the realization of topological states with strongly interacting bosons and experimental techniques that are already realized in present experiments. To this end, we consider the thin-torus-limit [134, 135, 136] of a 2D fractional Chern insulator on a square lattice [137, 138] (cf. Fig. 4.1(a)), and show how it can be implemented in experiments with ultracold quantum gases. The resulting ground state is a CDW at average filling $\varrho = 1/8$ per lattice site and is related to the $\nu = 1/2$ Laughlin state [71] in the 2D limit. It can as well be interpreted as a symmetry protected topological phase [136] (protected by inversion symmetry), similar to the discussion of the extended BHM in the previous chapter. In addition our model includes the possibility of twisted boundary conditions around the short perimeter of the torus, with a fully tunable twist angle θ_x (cf. Fig. 4.1 (b)). Adiabatically changing this twist angle by 2π realizes a many-body version of a Thouless pump [59, 129], which is *fractionally* quantized, see Fig. 4.1 (c). The following discussion is based on the publication [H-2014b].

In Sec. 4.1 we introduce the model and show that it is identical to the thin-torus limit of the 2D Hofstadter-Hubbard model. Possible experimental realizations are discussed, that use time dependent lattice modulations to generate the artificial gauge fields required. In Sec. 4.2 we elucidate on the topological properties in the non-interacting case, and show that they enable a realization of a Thouless pump. In Sec. 4.3 we return to the discussion of interacting bosons, where DMRG results for the melting of the CDW at weak interactions and the system in a harmonic trap are presented. We finally discuss the topological classification of the ground state in Sec. 4.4.

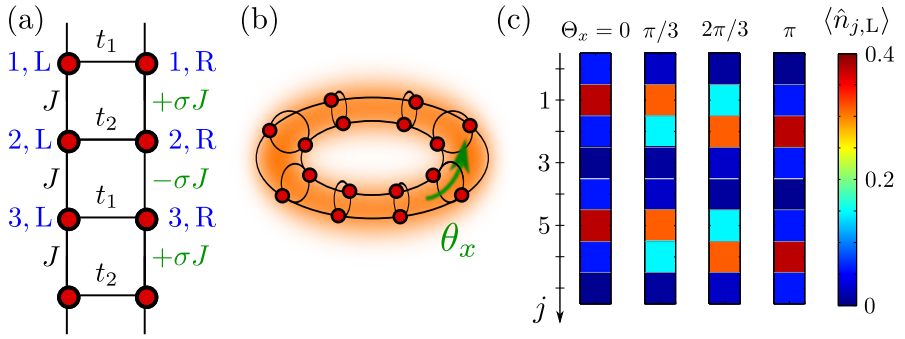

Figure 4.1: Using commensurate optical lattice potentials, interacting bosons in 1D ladder systems (a) can be realized. When the hopping elements across the ladder alternate between values t_1 and t_2, see Eq. (4.4), and every second hopping on one leg along the ladder has a phase π, the thin-torus limit of the 2D Hofstadter Hubbard model (at flux per plaquette $\alpha = 1/4$) can be realized (b). Which of the hoppings on the right leg have a non-trivial phase π depends on the value of $\sigma = \pm 1$. The boundary conditions are periodic across the ladder, with a tunable twist angle θ_x, corresponding to magnetic flux $\theta_x/2\pi$ threading the smaller perimeter of the torus. The ground state is an incompressible CDW with average occupation $\varrho = 1/8$ per lattice site, related to the 1/2 Laughlin state of the 2D model. The density distribution $\langle \hat{n}_{j,\mathrm{L}} \rangle = \langle \hat{n}_{j,\mathrm{R}} \rangle$ is shown in two unit-cells, taken from a larger system with open boundary conditions, for different values of θ_x in (c). The change of θ_x from 0 to π corresponds to a quarter-cycle of the fractionally quantized Thouless pump.

4.1 Model

We consider the following Bose-Hubbard type model of bosons hopping between the links of a 1D ladder, see Fig. 4.1(a),

$$\begin{aligned}\hat{\mathcal{H}} = &-J\sum_{j=1}^{L}(\hat{a}^\dagger_{j+1,\mathrm{L}}\hat{a}_{j,\mathrm{L}} + \sigma(-1)^j\hat{a}^\dagger_{j+1,\mathrm{R}}\hat{a}_{j,\mathrm{R}} + \mathrm{h.c.}) \\ &-\sum_{n=1}^{L/2}(t_1\hat{a}^\dagger_{2n-1,\mathrm{L}}\hat{a}_{2n-1,\mathrm{R}} + t_2\hat{a}^\dagger_{2n,\mathrm{L}}\hat{a}_{2n,\mathrm{R}} + \mathrm{h.c.}) \\ &+\sum_{j=1}^{L}\Big[\frac{U}{2}\sum_{\mu=\mathrm{L,R}}\hat{n}_{j,\mu}(\hat{n}_{j,\mu}-1) + V(j-(L+1)/2)^2\hat{n}_{j,\mu}\Big]. \end{aligned} \tag{4.1}$$

Here $\hat{a}_{j,\mu}$ and $\hat{a}^\dagger_{j,\mu}$ are bosonic annihilation and creation operators on the left ($\mu = \mathrm{L}$) or the right ($\mu = \mathrm{R}$) leg of the ladder, at the horizontal link j. The first line describes hopping along the ladder (vertical links in Fig. 4.1(a)) with amplitude J. On the right leg an additional phase π is picked up on every second bond, for $\sigma = +1$ from even j to odd $j+1$ and for $\sigma = -1$ from odd j to even $j+1$. Along the horizontal bonds in Fig. 4.1(a) the tunneling rates are alternating between t_1 and t_2, both assumed to be real-valued and positive. In the third line we added on-site Hubbard-type interactions of strength U and an external harmonic trapping potential.

4.1.1 Relation to the thin-torus-limit of the Hofstadter-Hubbard model

Now we show how the model (4.1) can be related to the thin-torus-limit of the 2D Hofstadter-Hubbard model with flux per plaquette $\alpha = 1/4$ (in units of the flux quantum). For a general

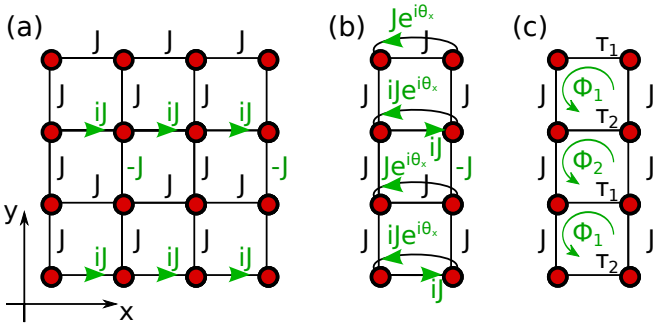

Figure 4.2: (a) For the 2D Hofstadter Hubbard model at flux per plaquette $\alpha = 1/4$ we make a gauge choice leading to a two-by-two magnetic unit-cell. Supplemented by twisted boundary conditions in x-direction (twist-angle θ_x), an effective 1D ladder model is obtained when the thin-torus-limit is considered (b). When an additional gauge transformation is applied, leaving invariant the magnetic flux $\Phi_{1,2}$ in every plaquette, the ladder model described by Eq.(4.1) is obtained (c).

flux per plaquette α the latter is described by a Hamiltonian [137, 138]

$$\hat{\mathcal{H}}_{\mathrm{HH}} = -J \sum_{x,y} (\hat{a}^\dagger_{x,y} \hat{a}_{x+1,y} e^{-i\pi\alpha y} + \hat{a}^\dagger_{x,y} \hat{a}_{x,y+1} e^{i\pi\alpha x} + \mathrm{h.c.}) \tag{4.2}$$

$$+ \frac{U}{2} \sum_{x,y} \hat{n}_{x,y}(\hat{n}_{x,y} - 1), \tag{4.3}$$

where the gauge field is encoded in the Peierls phases. When a particle is hopping around a plaquette these phases sum up to $\alpha \times 2\pi$. For the special case of $\alpha = 1/4$ we here make a different gauge choice shown in Fig. 4.2 (a). Next we consider this model on a torus of size $L_x \times L_y$ with twisted boundary conditions along x, i.e. $\psi(x_m + L_x) = e^{i\theta_x}\psi(x_m)$ where x_m is the coordinate of the m-th particle, $m = 1, ..., N$. Such boundary conditions can be implemented by adding additional phases θ_x to the hoppings from (L_x, j_y) to $(1, j_y)$ for all $j_y = 1, ..., L_y$.

We perform the thin-torus-limit by setting the length $L_x = 2$ equal to two lattice sites, yielding an effective ladder system as shown in Fig. 4.2(b). Because of the periodic boundary conditions along x there are two possibilities how a boson can tunnel from the left to the right leg of the ladder, originating from paths across the top and bottom of the torus. When summing up these contributions, we obtain complex hoppings across the ladder $\tau_1 = J(1 + e^{-i\theta_x})$ from $(2n-1, \mathrm{L})$ to $(2n-1, \mathrm{R})$ and $\tau_2 = iJ(1-e^{-i\theta_x})$ from $(2n, \mathrm{L})$ to $(2n, \mathrm{R})$ (site-labels as in Eq.(4.1)), see Fig. 4.2(c). The hopping elements along the legs of the ladder are real and given by $-J$ at links $(2n-1, \mathrm{R})$ to $(2n, \mathrm{R})$ and J at all other links.

To show the equivalence of the thin-torus Hofstadter-Hubbard model to the Hamiltonian (4.1) we now define $t_{1,2} := |\tau_{1,2}|$, yielding

$$t_1 = J\sqrt{2(1 + \cos\theta_x)}, \quad t_2 = J\sqrt{2(1 - \cos\theta_x)}, \tag{4.4}$$

such that the absolute values of all hopping amplitudes in both models coincide. Thus, we only have to calculate the magnetic fluxes through each of the plaquettes of the ladder and show that they coincide in both models. In the thin-torus-limit of the 2D model we obtain fluxes $\Phi_1 = [1 + \mathrm{sign}(\sin\theta_x)]/4$ and $\Phi_2 = [1 - \mathrm{sign}(\sin\theta_x)]/4$ in units of the magnetic flux

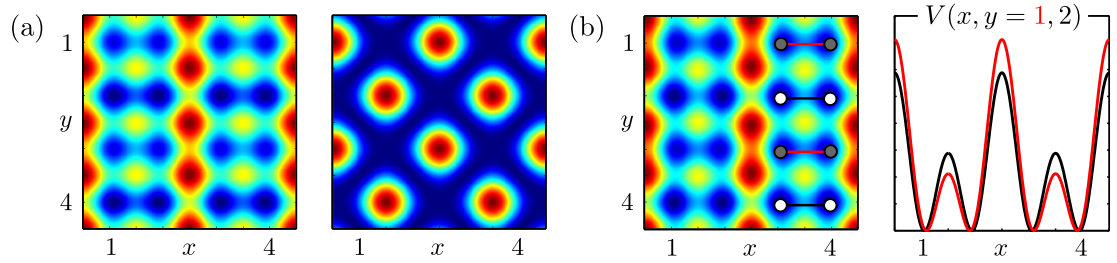

Figure 4.3: (a) Static optical lattices for the ladder system. (left) The initial lattice realizes the ladder separation with $t_1 = t_2$, which can be modified by adding the interference pattern of two short wavelength beams (right). (b) The modulated optical lattice (left) still has a ladder type structure but in general the hoppings $t_1 \neq t_2$ are non equal as illustrated by the cuts of the potential (right).

quantum, see Fig. 4.2(b), (c). Choosing

$$\sigma = -\text{sign}(\sin\theta_x) \tag{4.5}$$

in Eq. (4.1) we obtain the same fluxes in the 1D ladder model. Therefore the thin-torus-limit of the $\alpha = 1/4$ Hofstadter-Hubbard model is equivalent to the model in Eq. (4.1), up to a unitary gauge transformation $\hat{U}(\theta_x)$, which depends explicitly on the twist-angle θ_x.

Let us mention that a different version of the thin-torus-limit of the Hofstadter model at arbitrary flux per plaquette α was studied in [139]. In contrast to our model, this work did not take into account periodic boundary conditions across the ladder, resulting in a *homogeneous* flux $\Phi_1 = \Phi_2 = \alpha$ per plaquette and equal hopping amplitudes corresponding to $|t_1| = |t_2| = |J|$ using our notations. As a consequence the authors could study interesting edge states, carrying chiral currents along opposite edges of the ladder. Within our model on the other hand, we can study the effect of tunable twisted boundary conditions across the ladder. In addition, we study interactions between bosons.

4.1.2 Possible experimental implementation

Next we discuss a possible experimental realization of our scheme. The first required ingredient is a superlattice for creating ladders (with a four-site unit-cell), which has been implemented experimentally, see e.g. [140, 141]. The second ingredient is a (staggered) artificial gauge field, which has been experimentally demonstrated as well [142, 23, 41, 42, 9]. The implementation of the Hamiltonian (4.1) is motivated and closely related to the recent experiment [9], and we here propose a simple modification to realize the thin-torus limit.

The realization of the necessary Peierls phases is based on a proposal by Kolovsky [39]. Bare hopping along the along the legs of the ladders is strongly suppressed by a static staggered potential. By introducing additional time dependent lattice modulations, the hopping can be restored with a controlled phase. Details of the derivation are given in Appendix 14. We will first discuss the necessary static optical lattices to realize the ladder system with tunable t_1 and t_2 and staggered potential. Hereafter we present our proposal for the implementation of the required lattice shaking.

To begin with, our scheme requires a cubic lattice created by standing waves with short wavelength λ_S both in x and y direction. We choose the origin such, that lattice sites are centered at $x_{j,\text{L}} = 0, x_{j,\text{R}} = \lambda_S/2, y_{j,\mu} = (j-1)\lambda_S/2$. Additional standing waves with long wavelength $\lambda_L = 2\lambda_S$ are required in both directions. The strong long-lattice along x separates

the individual ladders, whereas the weaker long-lattice along y induces a staggered potential of strength Δ along the legs that is indicated by alternating white and grey filled sites in Fig. 4.3(b). This staggered potential is required for realizing the artificial magnetic field. We will denote the bare hopping elements in the so-obtained ladder by J_y (along the ladder) and J_x (across the ladder). We now turn to the implementation of the hoppings $t_{1,2}$ connecting the legs of the ladder. Without further modifications of the described setup, they are given by $t_1 = t_2 = J_x$. Applying a time-periodic modulation with strength V_0 such that $J = J_x/\sqrt{2}$ readily realizes the cases $\theta_x = \pm\pi/2$. They are of special relevance, because the resulting model is inversion symmetric around the center of links on the legs. As will be shown below, the model supports inversion-symmetry protected topological phases at these parameter values.

In order to realize arbitrary values of θ_x, the hoppings $t_{1,2}$ can be manipulated with a second independent square lattice rotated by 45°, such that the potential barrier along every second horizontal bond of the ladder is increased, when the lattice is properly adjusted. This increase in the potential barrier results in an exponential suppression of tunneling according to Eq. 1.9. To create the rotated square lattice, an additional sideband of the short wavelength laser is added in x and y direction and both beams are retro reflected. The resulting interference pattern realizes the required rotated square lattice with lattice constant $\lambda_S/\sqrt{2}$. Lastly we note that the periodic modulation used to restore hoppings along the ladder reduces the tunneling amplitudes $t_{1,2}$ between the legs. This gives rise to effective hoppings $t^{\text{eff}}_{1,2}/t_{1,2} = 1 - (2-\sqrt{2})V_0^2/(4\Delta^2)$, but the effect can be neglected for large Δ.

The alternating flux $\Phi_{1,2} = 0, 1/2$ (in units of the magnetic flux quantum) can be realized with a similar configuration as in the experiment [9], where a homogeneous flux of $\alpha = 1/4$ was realized via laser assisted tunneling [143]. Bare hopping along the legs is strongly suppressed by the staggered potential $\Delta \gg J_y$, but can be restored by resonant modulation of the potential landscape. This can be achieved by a time-dependent potential of the form $V(x, y, t) = V_0 \cos(\Delta t + g_{x,y})$, and as pointed out by Kolovsky [39] the freedom in choosing the phase-shifts $g_{x,y}$ allows to implement Peierls phases – and thus to create artificial gauge fields. To implement a suitable time-dependent potential experimentally, two side-bands of the long-wavelength laser can be employed. They make up four additional beams, two red-detuned ones with frequencies ω_{r1} and ω_{r2}, and two blue-detuned ones at frequencies ω_{b1} and ω_{b2}. When the red sidebands are sufficiently far detuned from the blue sidebands, i.e. $\omega_{rj} - \omega_{bj} \gg \Delta$ for both $j = 1, 2$, interference terms between them can be neglected and they can be treated separately form each other. For the (complex) electric fields we have

$$\begin{aligned}
\mathcal{E}_i &= E_0[e^{i(k_{i,1}x - \omega_{i,1}t + \varphi_{i,1})} + e^{i(-k_{i,1}x - \omega_{i,1}t - \varphi_{i,1})} + e^{i(k_{i,2}y - \omega_{i,2} + \varphi_{i,2})}] \\
&= E_0\big[2\cos(k_{i,1}x + \varphi_{i,1})e^{-i\omega_{i,1}t}) + e^{i(k_{i,2}y - \omega_{i,2} + \varphi_{i,2})}\big], \qquad (4.6) \\
|\mathcal{E}_i|^2 &= E_0^2\big[1 + 4\cos^2(k_{i,1x} + \varphi_{i,1}) \\
&\quad + 4\cos(k_{i,1}x + \varphi_{i,1})\cos(k_{i,2}y + (\omega_{i,1} - \omega_{i,2})t + \varphi_{i,2})\big]. \qquad (4.7)
\end{aligned}$$

We now move on by constructing suitable interference patterns between the red-detuned and blue-detuned pairs of beams respectively, with relative frequencies $\omega_i = \omega_{i,2} - \omega_{i,1}$ where $i = r, b$. These beat frequencies give rise to the required modulation of the potential in time with frequency Δ, and we chose them to be $\omega_r = -\Delta$, $\omega_b = \Delta$. As in [9] both beams $(r, 1)$ and $(b, 1)$ are retro reflected in x direction to form standing waves, see Fig. 4.4(a), and they interfere with running waves $(r, 2)$ and $(b, 2)$ in y direction. This configuration gives rise to

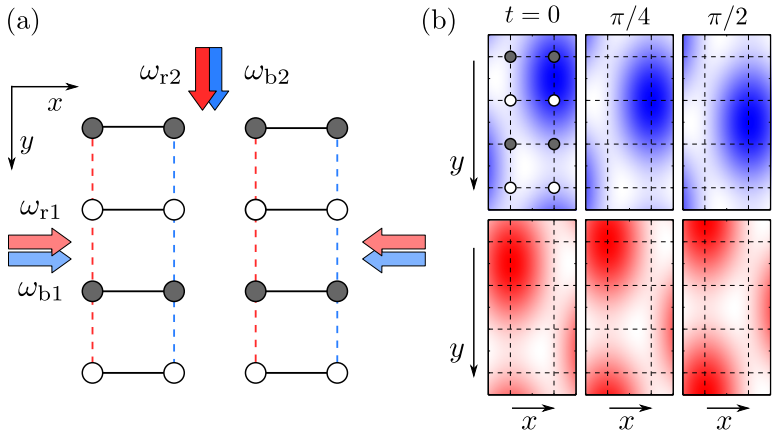

Figure 4.4: (a) Possible realization of the ladder system with half a magnetic flux-quantum piercing every second plaquette, cf. Ref. [9]. By interference of standing waves from a red (r) and a blue (b) detuned sideband of the long-lattice laser in x direction with corresponding, slightly detuned running waves along y direction, two independent lattice modulations (upper blue and lower red plot in (b)) are created. Each acts on a single leg of the ladder and they move in opposite directions along y, as shown by the amplitude of the modulations for different times in (b).

the time-dependent interference patterns shown in Fig. 4.4(b)

$$\begin{aligned} V_r(x,y,t) &= V_0/4\big[1 + 4\cos^2(k_L x) \\ &\quad + 4\cos(k_L x)\cos(k_L y + \Delta t - \pi/4\big], \end{aligned} \tag{4.8}$$

$$\begin{aligned} V_b(x,y,t) &= V_0/4\big[1 + 4\sin^2(k_L x) \\ &\quad + 4\sin(k_L x)\cos(k_L y - \Delta t - \pi/4\big]. \end{aligned} \tag{4.9}$$

From Fig. 4.4(b) we recognize that the phase of the retro reflected red sideband is chosen such that the modulation created is restricted to the left leg of the ladder and moves in negative y direction in time. The blue sideband, vice-versa, leads to a modulation restricted to the right leg of the ladder which is moving in positive y-direction in time. This counter-directed movement of the potential modulation introduces angular momentum into the system, which mimics the effect of a magnetic field.

Now, as desired, every lattice site is subject to a time-dependent modulation of the local potential $V_{j,\mu} = V_0\cos(\Delta t + g_{j,\mu})$ (with $\mu = \mathrm{L}, \mathrm{R}$). From Eq. (4.9) we read off the phase shifts, which are given by

$$g_{j,L} = -3\pi/4 + j\pi/2, \quad \text{and} \quad g_{j,R} = 3\pi/4 - j\pi/2. \tag{4.10}$$

To proceed and calculate the resulting Peierls phases, let us consider the simplified case when two lattice sites 1 and 2 are coupled by a hopping element J_y, where the second site is detuned by an energy $\Delta \gg J_y$ from the first one. Resonant periodic modulations of adjacent local potentials $V_{y,\mu}, V_{y+1,\mu}$ with frequency Δ and phases $g_{y,\mu}$ and $g_{y,\mu}$ restore strong hopping. Indeed, the effective tunneling matrix element from (y,μ) to $(y+1,\mu)$ is given by $J_{\text{eff}} = J(e^{-ig_{y,\mu}} - e^{-ig_{y+1,\mu}})/\sqrt{2}$ [9, 39], where we defined the amplitude J as

$$J = J_y V_0/(\sqrt{2}\Delta). \tag{4.11}$$

Further details on shaking assisted tunneling and the regime of validity for the effective de-

scription are given in Appendix 14.

Returning to the ladder model, we finally find for the induced hoppings

$$\begin{aligned} J_{(j,L),(j+1,L)} &= -e^{ij\pi} J_y V_0/(2\Delta)(e^{ig_{j,L}} - e^{ig_{j+1,L}}) \\ &= Je^{ij\pi/2}, \end{aligned} \tag{4.12}$$

$$\begin{aligned} J_{(j,R),(j+1,R)} &= -e^{ij\pi} J_y V_0/(2\Delta)(e^{ig_{j,L}} - e^{ig_{j+1,L}}) \\ &= Je^{-ij\pi/2}. \end{aligned} \tag{4.13}$$

The above configuration can be mapped to Eq. (4.1) via a gauge transformation.

4.2 Topology in the non-Interacting System – Thouless Pump

We start the analysis of our model by investigating non-interacting bosons. In this case all properties of the bandstructure for the ladder model immediately follow from the 2D Hofstadter model [144]. The lowest band of the 2D Hofstadter Hamiltonian at $\alpha = 1/4$ is characterized by a Chern number $\mathrm{Ch}_\mathrm{H} = 1$, which gives rise to a quantized Hall current perpendicular to an applied external force. We show below that such quantized particle transport along the 1D ladder survives in the thin-torus-limit, when the external force is induced by inserting magnetic flux through the smaller perimeter of the torus. Experimentally this corresponds to an adiabatic change of the twisted boundary conditions, $\partial_t \theta_x \neq 0$. A change of θ_x by 2π can also be interpreted as one cycle of a Thouless pump [59].

By construction of the ladder model the Bloch wavefunctions $|v(\theta_x; k_y)\rangle$ are related to the Bloch solutions of the two dimensional Hofstadter model via a gauge transformation

$$|v(\theta_x; k_y)\rangle = \hat{U}(\theta_x)|u(\theta_x, k_y)\rangle. \tag{4.14}$$

The Zak phase is invariant under gauge transformation and therefore the 1D ladder model reproduces the 2D model $\varphi_\mathrm{Zak}(\theta_x) = \varphi_\mathrm{Zak}(\theta_x)|_\mathrm{H}$.

A characteristic feature of the Hofstadter model at $\alpha = 1/4$ is that its lowest band is topologically non-trivial, with a Chern number $C_\mathrm{H} = 1$. The Chern number can be directly related to the winding of the Zak phase [145],

$$\mathrm{Ch}_\mathrm{H} = \frac{1}{2\pi} \int_\mathrm{BZ} dk_x \; \partial_{k_x} \phi_\mathrm{Zak}(k_x)|_\mathrm{H} \tag{4.15}$$

$$= \frac{1}{2\pi} \int_0^{2\pi} d\theta_x \; \partial_{\theta_x} \phi_\mathrm{Zak}(\theta_x) = \mathrm{Ch}. \tag{4.16}$$

Now we discuss the physical consequences of the non-trivial Chern numbers $\mathrm{Ch} = \mathrm{Ch}_\mathrm{H} = 1$. In the case of the 2D Hofstadter model, it is related to the Hall current induced by a constant external force [43, 44]. This current was recently measured with essentially non-interacting atoms, in ultra cold Fermi gases [42] and also with ultra cold bosons homogeneously populating the lowest Bloch band [9]. In the thin-torus limit of the Hofstadter model, a constant force around the short perimeter of the torus can be applied by adiabatically changing the twist angle in the boundary conditions, $F \propto \partial_t \theta_x$. Like in the 2D model, this leads to a Hall current perpendicular to the induced force – i.e. along the ladder – which is quantized and proportional to the Chern number Ch.

An alternative interpretation of the quantized current in the 1D model (4.1) is given by the concept of a Thouless pump [59]. To understand this, we note that the Zak phase is

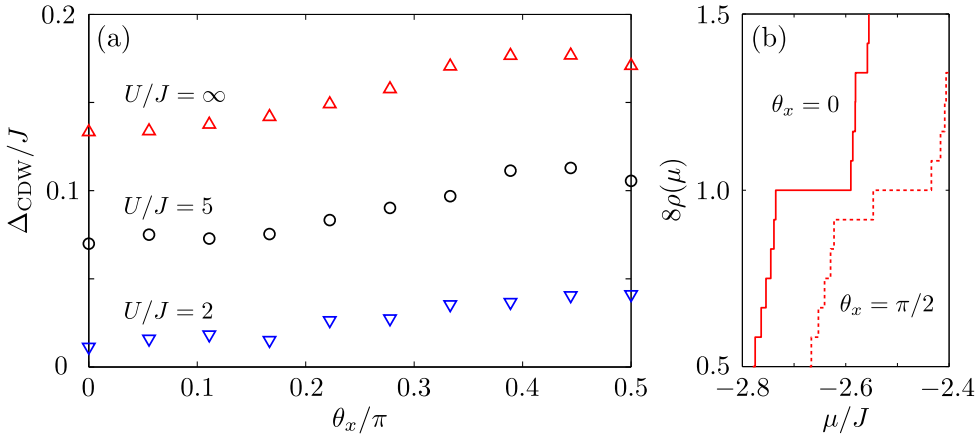

Figure 4.5: (a) The particle-hole gap Δ_{CDW} of the incompressible phase at filling $\varrho = 1/8$ for varying interaction strength $U/J = \infty, 5, 2$ extrapolated from finite system size calculations at $L_y = 18, 24, 32$. This gap corresponds to the plateaus in the $\varrho(\mu)$ diagrams shown in (b) for $U/J = \infty$ at system size $L_y = 48$. Note that for $\theta_x = \pi/2$ the plateau has a kink in its middle where $\varrho(\mu)$ changes, corresponding to the addition of a single particle. This is not a bulk effect, however, because the additional particle is localized at the edge of the system.

related to the macroscopic polarization $P = a\phi_{\mathrm{Zak}}/2\pi$, where a is the extent of the magnetic unit-cell in y-direction [146]. Now, by definition (4.16), it follows that the Zak-phase changes continuously from 0 to Ch $\times\, 2\pi$ when the parameter θ_x is adiabatically changed by 2π in a time T. This corresponds to a quantized change of the polarization by $\Delta P = \mathrm{Ch} \times a$, or a quantized current $\mathrm{Ch} \times a/T$. In Sec. 4.4 we will give an intuitive explanation of the microscopic mechanism of this effect in the 1D ladder system.

Experimentally the Thouless pump could be detected by loading non-interacting ultra cold atoms (bosons or fermions) into the lowest Bloch band. Then, comparing in-situ images of the atomic cloud before and after adiabatically changing θ_x by 2π reveals the quantized current. This is similar to the measurements performed recently on the 2D Hofstadter model [42, 9]. Now we turn to the discussion of interacting atoms, where we will give an example for a *fractionally quantized* Thouless pump corresponding to a Chern number $\mathrm{Ch} = 1/2$.

4.3 Interacting Topological States

We now turn to the discussion of the ladder model with local Hubbard-type interaction U of the bosons. In the 2D limit of the Hofstadter-Hubbard model the existence of an incompressible Laughlin-type ground state has been established numerically for fluxes within a range $\alpha = 0...0.4$ [137, 138]. For $\alpha = 1/4$ studied in this paper we thus expect a fractional Chern insulator at a magnetic filling $\nu = N/N_\varphi = 1/2$, where N is the number of particles and N_φ the number of flux quanta in the system. The average occupation number of each lattice site is thus $\varrho = 1/8$ in this phase. Now we will show using DMRG calculations that in the thin-torus limit an incompressible CDW survives at the same filling. We study the robustness of this phase when the interaction strength U is lowered. In an additional harmonic trap the incompressible phase is shown to be robust enough to form plateaus of constant density.

4.3.1 Grand-canonical phase diagram

We use a Matrix Product State (MPS) based algorithm to find the ground state of finite size ladder systems with open boundary conditions (obc) [109]. MPS are very well suited to approximate the CDW like states, which we expect in the incompressible phase and can – with increased resources – also describe the melting of the CDW at fillings near $\varrho = 1/8$. By varying the chemical potential we have determined the ground state energy for particle numbers around $N \approx L_y/4$ (corresponding to $\varrho = 1/8$) and three different interaction energies $U/J = 2, 5, \infty$. Due to symmetries it is sufficient to consider twist angles in the parameter range $\theta_x \in [0, \pi/2]$.

We now define the critical chemical potentials $\mu_{1/8\pm}$ as the upper and lower boundaries of the incompressible CDW phase. In Fig. 4.5(a) we show the corresponding particle hole gap $\Delta_{\mathrm{CDW}} = \mu_{1/8+} - \mu_{1/8-}$ extrapolated to thermodynamic limit from finite system results at $L_y = 16, 24, 32$. Strong interactions stabilize the non trivial CDW that is protected by a gap on the order of $\Delta_{\mathrm{CDW}}^{U=\infty} \approx J/6$. At moderate interaction $U = 5$ the incompressible phase is still protected by $\Delta_{\mathrm{CDW}}^{U=5} \approx J/12$, whereas for $U = 2$ the gap almost closes and the CDW phase vanishes.

The topological nature of our system and the presence of obc edges have to be taken into account when analyzing dependence of the particle number $N(\mu)$ on the chemical potential, as shown in Fig. 4.5(b). At $\theta_x = 0$ we find a single plateau at filling $\varrho = 1/8$, however at $\theta_x = \pi/2$ this plateau is split by the addition of a single particle at intermediate chemical potential. This is an edge effect and strongly dependent on the choice of boundary conditions [H-2014d], allowing us to interpret the full plateau as an incompressible bulk phase.

4.3.2 Harmonic trapping potential

The incompressible, integer filling phases of the conventional Bose-Hubbard model can be nicely demonstrated in harmonically trapped systems where Mott-insulating plateaus of constant density emerge, surrounded by superfluid regions ("wedding-cake" structure). We here show that in a similar fashion the non trivial CDW phase on the ladder could be visualized in harmonically trapped gases.

Using the MPS code (with increased bond dimension to correctly describe the compressible regions in the trap) we have calculated the density distribution in traps up to size $L_y = 128$ for fixed global chemical potential μ. The trap depth V is chosen such that from local density approximation we expect a wedding cake structure of quarter filling in the center, a compressible transition region and a large incompressible region of filling $\varrho = 1/8$ before vacuum. As we show in Fig. 4.6 this picture is well reproduced by the numeric simulation, where the local density $\langle \hat{n}_{j,L} \rangle$ reveals the CDW nature. To check the incompressibility of the phases, we calculated the averaged density $\overline{n}_j = 1/8 \sum_{i=j-1}^{j+2} \langle \hat{n}_{i,\mathrm{L}} + \hat{n}_{i,\mathrm{R}} \rangle$. It illustrates the two density plateaus in the regions predicted by the local chemical potential $\mu(x) = \mu + V_{\mathrm{trap}}(x)$ and the critical chemical potentials $\mu_{1/8,\pm}$ calculated in the previous section.

The outer incompressible phase is the CDW state at filling $\varrho = 1/8$ we are mostly interested in, corresponding to a half-filled lowest Bloch band. The inner incompressible phase at quarter-filling corresponds to a completely filled lowest Bloch band, and is similar to the Mott phase of bosons in the lowest band of the 1D Su-Schrieffer-Heeger model [H-2014d].

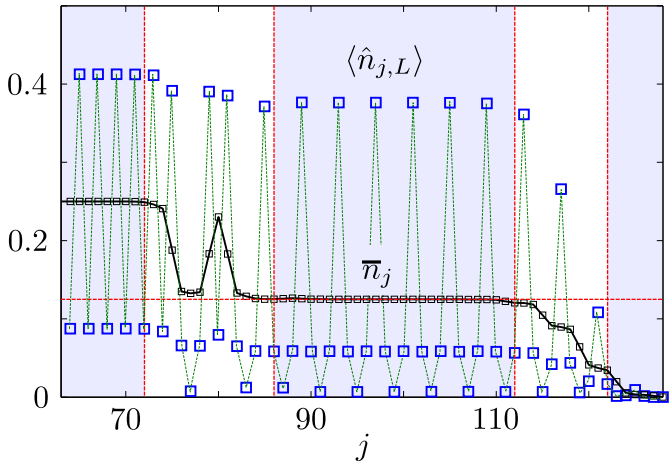

Figure 4.6: Local density of hard-core bosons with $U/J = \infty$ at $\theta_x = 0$ in a harmonic trap centered around $j = 64.5$ with $V = 8.4 \times 10^{-5} J$ and $\mu = -2.4J$ and $L_y = 128$. While the density along the left leg (blue squares) demonstrates the density wave character, the averaged density (black solid line) reveals incompressible phases at fillings $\varrho = 1/4$ and $\varrho = 1/8$. The vertical red lines indicate the phase boundaries between compressible and incompressible (blue shading) phases in local density approximation

4.4 Topological Classification and Fractional Thouless Pump

Now we discuss the topological properties of the $\varrho = 1/8$ CDW phase. We distinguish two cases for the classification of the phase, the 1+1D model where the second dimension is defined by the twist-angle $\theta_x = 0...2\pi$, and the 1D model at points of highest symmetry $\theta_x = \pm\pi/2$. In the first case, robust topological properties carry over from the $\nu = 1/2$ LN state from the 2D Hofstadter-Hubbard model. In the second case, the CDW constitutes a (inversion-) symmetry-protected topological (SPT) phase which is not robust against symmetry breaking disorder.

4.4.1 $1+1$D model and fractional Thouless pump

The $\nu = 1/2$ LN state in the 2D Hofstadter-Hubbard model is characterized by a fractionally quantized Chern number $\mathrm{Ch} = 1/2$ [117, 138], and as will be shown shortly this carries over to the $1+1$D gapped CDW state. Before going through the details of the calculation, however, let us give an intuitive physical picture.

As mentioned above, the Chern number is directly related to the quantized Hall current in the 2D model (on a torus). If one unit of magnetic flux is introduced through the short perimeter of the torus, i.e. $\Delta\theta_x = 2\pi$, a quantized Hall current around the torus is induced. While in the case of an integer-quantized Chern number $\mathrm{Ch} = p$ the state returns to itself immediately, when $\mathrm{Ch} = p/q$ takes a fractional value the state returns to itself only after introduction of q flux quanta, $\Delta\theta_x = q \times 2\pi$.

As discussed in the non-interacting case, an integer-quantized Thouless pump still exists in the thin-torus limit when the twist-angle θ_x is adiabatically increased. This mechanism carries over to the $\varrho = 1/8$ CDW, as can be understood from a simple Gutzwiller-ansatz. To this end we approximate the CDW by a product state

$$|\mathrm{CDW}\rangle = \prod_n \hat{b}^\dagger_{2n}(\theta_x)|0\rangle, \tag{4.17}$$

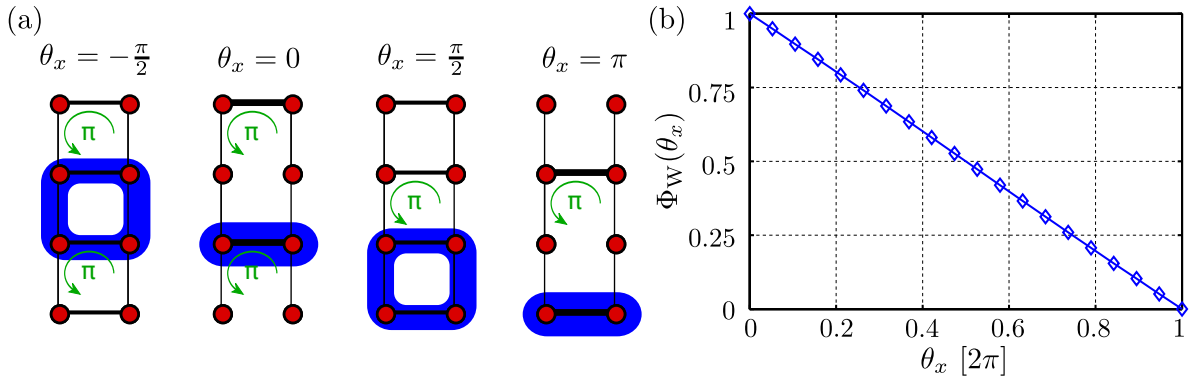

Figure 4.7: (a) Approximate Wannier orbitals (blue shaded) at the points θ_x of highest symmetry. (b) The $U(2)$ Wilson-loop phase $\phi_W(\theta_x) = \mathrm{Im}\log\det\hat{W}(\theta_x)$ is shown for the $\varrho = 1/8$ CDW, the winding of which gives the total Chern number. Exact diagonalization results obtained by Fabian Grusdt for a system of size $L_x = 2$, $L_y = 12$ with periodic boundary conditions and $N = 3$ particles for $N_\varphi = 6$ flux quanta.

where $\hat{b}_j^\dagger(\theta_x)$ creates a boson in the Wannier orbital corresponding to unit-cell j. To understand how the Wannier orbitals depend on θ_x, we approximate them at the points of highest symmetry, $\theta_x = 0, \pi/2, \pi, ...$ To this end we search for the state of lowest energy within each unit-cell, and note that in principle the residual coupling between unit-cells could be treated perturbatively. The result is illustrated in Fig. 4.7(b). At $\theta_x = 0$ the hoppings are J, $t_1 = 2J$ and $t_2 = 0$, such that Wannier orbitals are localized on every other rung, with an energy of $-t_2 = -2J$ to zeroth order in the described perturbation theory. At $\theta_x = \pm\pi/2$ on the other hand, the hoppings read J and $t_1 = t_2 = \sqrt{2}J$ such that considering only rungs is not sufficient. Instead we compare the energy of a particle hopping around a single four-site plaquette with zero and π flux respectively. While in the latter case there are two degenerate states with energy $-\sqrt{3}J$, for vanishing flux we find a non-degenerate state with lower energy $-(1+\sqrt{2})J$.

Although we consider only local Hubbard-type interactions, the CDW state (4.17) is stabilized by a finite gap Δ_{CDW} to any excitations (it can also be interpreted as a Mott insulator). This is due to a hopping-induced finite range interaction. If we calculate the Wannier orbitals beyond the zeroth order approximation introduced above, nearest and next-nearest neighbor orbitals acquire a finite overlap. Thus, if the twist-angle θ_x is adiabatically changed, the state (4.17) follows the modified Wannier orbitals. Because they re-connect to their neighbors after a full pumping cycle, see Fig. 4.7(a), a quantized atomic current flows along the ladder. Because – assuming periodic boundary conditions along y – the state only returns to itself after *two* full pumping cycles, the Thouless pump is fractionally quantized, with a coefficient (the Chern number) $\mathrm{Ch} = 1/2$. This quantization is robust against any perturbations which are small compared to the gap Δ_{CDW}. The Thouless pump is also illustrated in Fig. 4.1(c).

A formal topological classification of the 1 + 1D model, following [129] has been carried out by Fabian Grusdt. The degeneracy of the ground state on a torus requires a generalized definition of the Chern number in terms of the winding Φ_W of the $U(2)$ Wilson loop $\hat{W}$, which is a non-Abelian generalization of the Zak phase [133]. Exact numeric evaluations for small systems shown in Fig. 4.7(b) confirm the expected result for the many-body Chern number of $\mathrm{Ch} = 1/2$ per ground state.

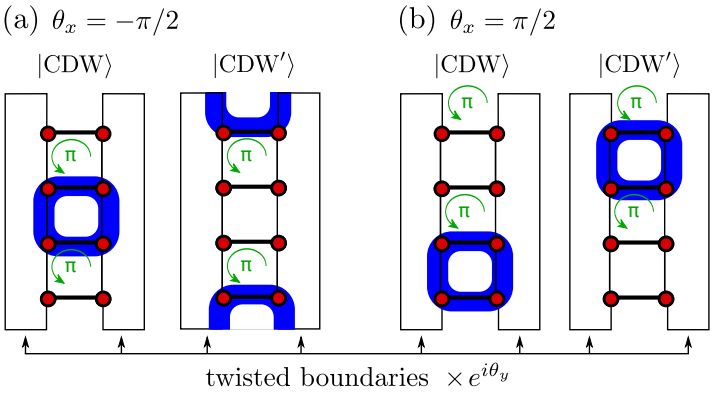

Figure 4.8: SPT classification of the many-body states at the points of highest symmetry $\theta_x = \pm\pi/2$. The topological invariant ν is strictly quantized in presence of inversion symmetry and defined via twisted boundary conditions as illustrated here.

4.4.2 1D model and SPT charge density wave

At special values of the twist angle $\theta_x = \pm\pi/2$ the model (4.1) is inversion-symmetric around the center of links on the legs of the ladder. In this case, the CDW phase can be understood as a SPT phase [136]. To come up with an elegant formal classification, the spontaneous breaking of inversion symmetry by the CDW has to be carefully accounted for. Here we restrict ourselves to the definition and calculation of a topological invariant ν, which is quantized to $\nu = 0, \pi$ and protected by inversion symmetry.

The topological invariant we employ is the many-body Zak or Berry phase defined by twisted boundary conditions along the ladder [118][H-2014d]. Like in the case of the Chern number in the 1+1D case, we introduce the twist angle θ_y, however now the second parameter $\theta_x = \pm\pi/2$ is fixed. In practice the most convenient way to implement twisted boundary conditions is to multiply the hopping elements from the last to the first sites of the ladder (which realize periodic boundary conditions) by the complex phase $e^{i\theta_y}$. Then the eigenstate $|\Psi(\theta_y)\rangle$ depends on θ_y and the Berry phase can be calculated as usual,

$$\nu = \int_0^{2\pi} d\theta_y \, \langle \Psi(\theta_y) | i\partial_{\theta_y} | \Psi(\theta_y) \rangle. \tag{4.18}$$

From inversion symmetry it follows that $\nu = 0, \pi$ is strictly quantized [60, 105].

To calculate the topological invariant ν, we restrict ourselves to the simple representation (4.17) of the CDW state $|\Psi\rangle$. Then we distinguish four different cases, illustrated in Fig. 4.8, characterized by $\theta_x = \pm\pi/2$ and by which of the two states $|\text{CDW}\rangle$ and $|\text{CDW}'\rangle$ we use. To begin with we note that only for $\theta_x = \pi/2$ the link with the complex phase $e^{i\theta_y}$ is part of an atomic orbital, as defined in Fig. 4.8. Then in the trivial case (Fig. 4.8(b)) $\theta_x = \pi/2$, $|\Psi\rangle$ is independent of θ_y and thus $\nu = 0$ vanishes for both CDW states. For $\theta_x = -\pi/2$ on the other hand, we have to distinguish between CDW and CDW'. Only for one of the two states, here $|\text{CDW}'\rangle$, the link with the complex phase $e^{i\theta_y}$ is part of an *occupied* atomic orbital. Thus for the state described by CDW the wavefunction $|\Psi\rangle$ is independent of θ_y and $\nu = 0$ again. Finally we will show that the state CDW' is topologically non-trivial with $\nu = \pi$. To this end, note that there is an occupied atomic orbital on the link connecting the last and the first rung of the ladder. The energy of this orbital can not be changed by the complex phase $e^{i\theta_y}$, which is merely a gauge transformation, but the eigenfunction of the orbital $\psi_m(\theta_y)$ (with $m = 1, ..., 4$ labeling the four sites), depends on θ_y. In fact, a simple calculation shows that

the corresponding Berry phase is $\int_0^{2\pi} d\theta_y \sum_m \psi_m^* i\partial_{\theta_y}\psi_m = \pi$. Because $|\text{CDW'}\rangle$ is a simple product state it follows that $\nu = \pi$ in this case.

Conclusion

In summary, we have proposed and analyzed a realistic setup for the realization of a topologically non-trivial CDW state (at filling $\varrho = 1/8$) of strongly interacting bosons in a 1D ladder geometry. Our model was derived by taking the thin-torus limit of the 2D Hofstadter-Hubbard model at flux $\alpha = 1/4$ per plaquette. The $\nu = 1/2$ Laughlin-type fractional Chern insulator in this 2D model is directly related to the 1D CDW at filling $\varrho = 1/8$. As a consequence, the CDW has interesting topological properties: When adiabatically introducing magnetic flux $\theta_x/2\pi$ through the small perimeter of the thin-torus, which can be realized by changing the hoppings in our model, a fractionally quantized Hall current is induced along the ladder. Alternatively, the CDW phase can be interpreted as inversion symmetry-protected topological phase, characterized by a quantized topological invariant taking values $\nu = 0, \pi$.

We proposed a scheme for the realization of our model using time-periodic lattice modulations, which already are realized in experiments. Using numeric DMRG calculations, we determined the particle-hole gap of the CDW and found values of $\Delta_{\text{CDW}} \sim 0.1J$, a sizable fraction of the bare hopping J. When placed in a harmonic trap, the wedding cake structure of the density provides a clear signature of the appearance of the topological CDW state.

Part III

Flux-Equilibrium in Open and Free Systems

Chapter 5

Critical Exponents in Driven Fermionic Lattice Models

In the following chapters we will study models that are intrinsically out of equilibrium. Unlike the closed systems we considered before, where interaction with external degrees of freedom is merely an unwanted disturbance, here the strong interaction with external reservoirs is a defining aspect. Fig. 5.1(a) illustrates the structure of the systems we consider. A complex many-body systems with internal unitary dynamics that is subject to the *strong* influence of an external reservoir coupling. We restrict to unidirectional couplings, where no back action from system to reservoir is considered. The starting point of our discussion will always be the dynamic equation for the density matrix of the internal system, much like Schrödingers equation for the state of conventional closed quantum systems. Whereas ground states, or thermal states, are an important part of the discussion of closed quantum systems, one important aspect of a non equilibrium system is its stationary state, the long time attractor of the competition of internal dynamics and external influence.

We will characterize these states using our knowledge of closed quantum systems.

The kind of non equilibrium system we discuss, can be parted in two flavors. The first of which is reservoir engineering, where intricate coupling schemes of well controlled systems to external reservoirs realize specific driving forces [147, 10, 148, 17]. The second approach is engineering specific internal dynamics, that together with trivial external decoherence drive the system towards a desired stationary state [149, 150]. Most systems of course are a mixture of these two, in this chapter we however focus on a system that is driven solely by the reservoir couplings with minor importance of the internal dynamics. Starting point of our discussion is work by Eisert and Prosen, that identified a class of non equilibrium problems that admit exact solution [151]. To begin with we introduce our model system and its solution in terms of Gaussian states. We then analyze the emergent stationary states with respect to their critical properties that manifest in divergent length and time scales and give a complete classification. Finally we discuss a realization of the model system in a quantum optics setting.

The following chapter is summarized in reference [H-2012] and is an extension of my diploma thesis [152].

5.1 Free Lattice Fermions with Linear Reservoir Couplings

The system we study is a one dimensional lattice model of non interacting, spinless fermions. Dynamics are generated by a Hermitian Hamiltonian $\mathcal{H}$ and couplings to reservoirs that render the evolution nonunitary. Within this thesis we will restrict to Markovian reservoirs, that can

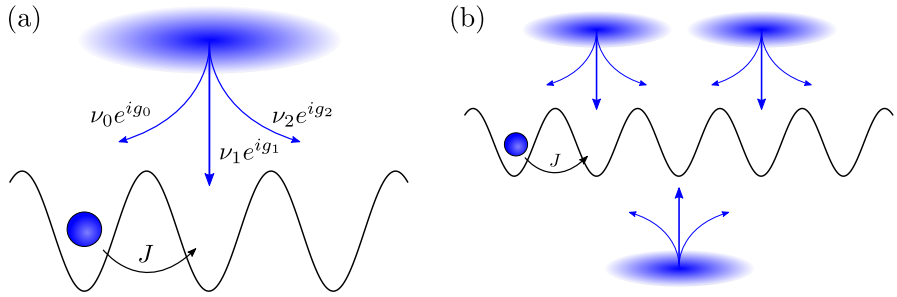

Figure 5.1: Scheme of our one dimensional model of non interacting fermions. We consider reservoirs that have a finite range $N > 1$, as shown in (a) for $N = 3$. Long range correlations of fermions in the chain are established via the overlap of many identical, but spatially shifted reservoirs, see (b).

be described via Lindblad operators L_μ and the dynamic equation for the system density matrix is given by the Lindblad equation

$$\begin{aligned} \frac{d}{dt}\varrho &= \mathcal{L}(\varrho) \\ &= -i[\mathcal{H}, \varrho] + \frac{1}{2}\sum_\mu \left(2L_\mu \varrho L_\mu^\dagger - \{L_\mu^\dagger L_\mu, \varrho\}\right). \end{aligned} \tag{5.1}$$

In absence of reservoir couplings this of course simplifies to the conventional von Neumann equation. Due to our assumption of Markovian reservoirs, the dynamic equation for ϱ is not dependent on $\varrho(t' < t)$ at earlier times.

Instead of fermionic creation and annihilation operators we here use the notation of Majorana fermions, $\hat{w}_{2j-1} = \hat{c}_j^\dagger + \hat{c}_j, \hat{w}_{2j} = -i(\hat{c}_j^\dagger - \hat{c}_j)$. These operators are the analogue to bosonic position and momentum operators, are Hermitian, and fulfill the anticommutation relation $\{\hat{w}_j, \hat{w}_k\} = 2\delta_{j,k}$. The use of Majorana fermions will allow for a simpler representation of the following results.

We will begin by defining the system on a chain of finite length L and later move on to translation invariant systems with periodic boundary conditions. Both the Hamiltonian and the set of Lindblad generators shall be restricted, such that they can be fully represented by a matrix of size $2L \times 2L$ and vectors of size $2L$ respectively

$$\mathcal{H} = \sum_{j,k=1}^{2L} (H)_{j,k} \hat{w}_j \hat{w}_k, \tag{5.2}$$

$$L_\mu = \sum_{j=1}^{L} (l)_{\mu,j,1} \hat{w}_{2j-1} + (l)_{\mu,j,2} \hat{w}_{2j}. \tag{5.3}$$

Due to the absence of higher order terms in Eqs. (5.2) and (5.3), the dynamic equations of one $\langle \hat{w}_j \rangle$ and two point correlation functions $\langle \hat{w}_j w_k \rangle$ form a closed set. The density matrix of a Gaussian state can be written as

$$\varrho = \frac{1}{2^L} \exp\left(\frac{i}{2}\xi^T \Gamma \xi\right), \tag{5.4}$$

where $\xi = (\xi_1, \cdots, \xi_{2L})$ are Grassmann variables that replace the Majorana fermions. Γ is

the covariance matrix

$$(\Gamma)_{j,k} = \frac{i}{2}\,\mathrm{Tr}\big\{\varrho_0(\hat{w}_j\hat{w}_k - \hat{w}_k\hat{w}_j)\big\}, \tag{5.5}$$

which is an antisymmetric $2L \times 2L$ matrix. For the equations of motion as discussed here, an initial Gaussian state remains Gaussian in time. Higher order correlations can be factorized for Gaussian states [153, 154]. Consider the operator

$$\hat{O} = \prod_{k=1}^{2L} \hat{w}_k^{x_k}, \tag{5.6}$$

with $x = (x_1, \cdots, x_{2L})$ being a string of bits, with weight $l = \sum_k x_k$. Expectation values are given by

$$\langle\hat{O}\rangle = 0, \quad l \text{ odd}, \tag{5.7}$$

$$\langle\hat{O}\rangle = i^l \ \mathrm{Pf}(\Gamma[x]), \tag{5.8}$$

where $\Gamma[x]$ is a submatrix of the covariance matrix and $\mathrm{Pf}(X)$ is the Pfaffian of square matrix X. In the case of antisymmetric matrices the Pfaffian is related to the determinant by $\mathrm{Pf}(X)^2 = \det(X)$.

Under the restrictions imposed on our model, we can consider the dynamic equation of the covariance matrix instead of the full density matrix

$$\frac{d}{dt}\Gamma = X^T\Gamma + \Gamma X - Y. \tag{5.9}$$

The damping matrix X and driving matrix Y represent the Hamiltonian and the Lindblad generators

$$X = -4iH - (R + R^*), \tag{5.10}$$

$$Y = 2i(R - R^*), \tag{5.11}$$

with the reservoir matrix $R = \sum_\mu l_\mu \otimes l_\mu^*$. Instead of the exponential scaling of the density matrix with increasing system size, the linear scaling of the covariance matrix renders the numeric solution of large systems feasible. We will however pursue analytic derivations which are possible for translation invariant systems.

5.1.1 Translation invariant systems

We can further restrict the definition of Hamiltonian and jump operators to ensure translation invariance and enforce periodic boundary conditions

$$\mathcal{H} = \sum_j \tau_j\Big(\sum_{m,n}(h)_{m,n}\hat{w}_m\hat{w}_n\Big), \tag{5.12}$$

$$L_d = \tau_d\Big(\sum_{m=0}^{N-1}\nu_{m,1}e^{ig_m}\hat{w}_{2m-1} + \nu m, 2e^{i\tilde{g}_m}\hat{w}_{2m}\Big), \quad d \in \mathbb{Z} \tag{5.13}$$

where τ_d shifts all local operators by d lattice sites. The damping matrix X now has block diagonal form

$$X = \begin{pmatrix} x_0 & x_1 & \cdots & x_{L-1} \\ x_{-1} & x_0 & \cdots & x_{L-2} \\ \vdots & \vdots & \ddots & \vdots \\ x_{-L+1} & x_{-L+2} & \cdots & x_0 \end{pmatrix}, \tag{5.14}$$

with 2×2 blocks x_d that fulfill $x_d = x_{L-d}$. We represent Y and Γ in similar form. The dynamic equation for the blocks of the covariance matrix is given by

$$\frac{d}{dt}\gamma_d = \sum_m \left[x_{-m}\gamma_{d-m} + \gamma_m x_{d-m}\right] + y_d. \tag{5.15}$$

We now define $u_m = -x_{-m}^T$, make use of the convolution theorem and find for the covariance matrix in momentum space Eq. (5.14)

$$\begin{aligned} \frac{d}{dt}\gamma(\varphi) &= u(\varphi)\gamma(\varphi) + \gamma(\varphi)x(\varphi) + y(\varphi) \\ &= x(-\varphi)^t\gamma(\varphi) + \gamma(\varphi)x(\varphi) + y(\varphi), \end{aligned} \tag{5.16}$$

where $\gamma(\varphi) = \sum_{d=1}^{L} e^{2\pi i\varphi d/L}\gamma_d$ and similar for $x(\varphi)$ and $y(\varphi)$. The momentum space representations of X, Y and Γ are 2×2 matrices and are called symbol functions.

5.2 Criticality of Stationary States

The stationary state of the introduced fermionic models is given by solution of the Lyapunov equation

$$x(-\varphi)^t\gamma(\varphi) + \gamma(\varphi)x(\varphi) = y(\varphi). \tag{5.17}$$

To simplify the discussion we restrict the coupling with reservoirs to a single species of Majorana fermions, such that $\nu m, 2 = 0$ and $\nu_m = \nu_{m,1}$. For the symbol function of X this yields

$$x(\varphi) = -4ih(\varphi) - \begin{pmatrix} r(\varphi) + r(-\varphi) & 0 \\ 0 & 0 \end{pmatrix} \tag{5.18}$$

$$\Rightarrow x(-\varphi)^t = 4ih(\varphi) - \begin{pmatrix} r(\varphi) + r(-\varphi) & 0 \\ 0 & 0 \end{pmatrix}, \tag{5.19}$$

$$\text{with} \qquad r(\varphi) = \sum_{m=0,n=0}^{N-1} \nu_m\nu_n e^{-i\varphi(m-n)}e^{i(g_m - g_n)}. \tag{5.20}$$

Inserted into the Lyapunov equation we find

$$[\gamma(\varphi), h(\varphi)] + \left\{\gamma(\varphi), \begin{pmatrix} r(\varphi) + r(-\varphi) & 0 \\ 0 & 0 \end{pmatrix}\right\} = 2i \begin{pmatrix} r(\varphi) - r(-\varphi) & 0 \\ 0 & 0 \end{pmatrix}, \tag{5.21}$$

which can be analytically solved using the symmetries of the problem. The steady state is however not unique if $h_{1,2}(\varphi) = 0$, because in this case the second species of Majorana fermions is decoupled from the reservoir damping. If this coupling is however realized by an appropriate Hamiltonian the stationary state is determined by the reservoir alone.

$$\gamma(\varphi) = \frac{r(\varphi) - r(-\varphi)}{r(\varphi) + r(-\varphi)} \mathbb{1}_{2\times 2}. \tag{5.22}$$

5.2.1 Remarks on time reversal symmetry and purity gap

In [147] Bardyn et al. discuss the topological classification of non interacting dissipative systems that belong to the BDI class defined in [155]. The BDI class has two symmetry requirements, particle hole symmetry (PHS) and time reversal symmetry (TRS) and different phases within the BDI class can be classified with a topological winding number.

The models we here consider do in general not preserve TRS due to the non trivial phases of the couplings. Bardyn et al. show that the symmetries of the reservoir couplings are inherited by the covariance matrix. For a TRS system one finds $\gamma(-\varphi)^* = \gamma(\varphi)$ and the examples we discuss in Section 5.4 break this symmetry.

Bardyn et al. identify three distinctive ways of a topological phase transition. One possibility is the closure of the purity gap, that is defined via the minimum value of the real symmetric matrix $(i\Gamma)^2$. For the models we discuss the eigenvalues of the covariance matrix are given by the symbol function $\gamma(\varphi)$ and therefore the purity gap always closes at $\varphi = 0$.

Besides a closure of the purity gap, a topological phase transition in the notation of Bardyn can occur at the closure of the dissipative gap, which is determined by the eigenvalues of the X matrix and will be a signature of criticality for our systems.

5.2.2 Correlation length

One signature of critical behavior is a divergence of length scales when approaching critical points. From the symbol function solution we here derive spatial correlations via an inverse Fourier transform, for example

$$\langle \hat{w}_1 \hat{w}_{1+2d} \rangle = \frac{1}{2\pi} \int_0^{2\pi} d\varphi \; e^{i\varphi d} \; \gamma_{11}(\varphi). \tag{5.23}$$

Here we are interested in the asymptotic behavior for large d, which will be captured by the correlation length

$$\xi^{-1} = -\lim_{d\to\infty} \ln |\langle \hat{w}_1 \hat{w}_{1+2d} \rangle| / d. \tag{5.24}$$

To gain further insight we extend the symbol function into the complex plane by substituting $e^{i\varphi} = z \in \mathbb{C}$.

$$\gamma_{11}(z) = i \frac{\sum_{j,l} \nu_j \nu_l e^{i(g_j - g_l)} (z^{j-l} - z^{l-j})}{\sum_{j,l} \nu_j \nu_l e^{i(g_j - g_l)} (z^{j-l} + z^{l-j})}, \tag{5.25}$$

$$\langle w_1 w_{1+2d} \rangle = \sum_{a \in S_1} \mathrm{Res}_a \left[z^{d-1} \gamma_{11}(z) \right], \tag{5.26}$$

where Res_a denotes the residues inside the unit circle S_1, ($|z| \leq 1$). The residue is non-zero only in singular points of $\gamma(z)$. Because numerator $n(z)$ and denominator $d(z)$ of (5.26) are holomorphic, only zeros of the denominator inside the unit circle contribute to the correlations. When changing system parameters the zeros of the denominator change and the system becomes critical when one of the poles approaches the unit circle from the inside. One can show that

$$\xi^{-1} = -\ln |z_0| \approx 1 - |z_0|, \tag{5.27}$$

where z_0 is the closest singularity to the unit circle.

5.2.3 Relaxation time

Besides divergence of the correlation length ξ, critical behavior can be defined via divergent time scales of relaxation. The relaxation towards the stationary state Γ_0 is equivalent to the damping of a perturbation $\Gamma = \Gamma_0 + \delta\Gamma$. It is determined only by the damping matrix X

$$\frac{d}{dt}\delta\Gamma = X^T\,\delta\Gamma + \delta\Gamma\,X. \tag{5.28}$$

The dissipative spectrum is defined as the spectrum of X and is closely related to the relaxation time. In translation invariant systems this spectrum can be calculated via the symbol function $x(\varphi)$.

5.3 Critical Exponents

We now want to discuss the conditions, under which the above defined critical behavior occurs in the model of free fermions with finite range reservoir couplings. To this end we will have to identify the singular points of Eq. (5.25) and discuss their properties.

The denominator of 5.25 is strictly real and non negative as

$$\begin{aligned} d(z,\{g_j\},\{\nu_j\}) &= \sum_{j,l}\nu_j\nu_l e^{i(g_j-g_l)}(z^{j-l}+z^{l-j}) \\ &= |\sum_j \nu_j e^{ig_j}z^j|^2 + |\sum_j \nu_j e^{ig_j}z^{-j}|^2. \end{aligned} \tag{5.29}$$

A configuration $\{s_j\} = \{\nu_j e^{ig_j}\}$ of the complex parameters of the Liouvillian leads to critical behavior, if a z_0 on the unit circle exists, such that the individual sums inside the absolute value in Eq. (5.29) vanish for z_0 and its complex conjugate. This condition yields a pair of implicit equations

$$1 + \sum_{j=1}^{N-1} s_j\, z_0^j = 1 + \sum_{j=1}^{N-1} s_j\, z_0^{j*} = 0, \tag{5.30}$$

where we have used that without loss of generality s_0 can be set equal to unity. Apparently reservoir couplings to a single site ($N = 1$) cannot induce criticality in a fermionic system. Note that this statement is not true for bosonic systems, due to the unboundedness of the particle number on each site and example for criticality with single site reservoirs have been given in [151].

For a given z_0, $2(N-2)$ out of the $2(N-1)$ real parameters ν_j, g_j can be chosen arbitrarily. As there are only a finite number of roots z_0 the non-trivial complex solutions $\{s_j = \nu_j e^{ig_j}\}$ to these equations are limited to a $d-2$ dimensional manifold in the $d = 2(N-2)$ dimensional parameter space.

In the following we want to get some general insight into what are the possible critical exponents of a reservoir-driven phase transition. As we are interested in the behavior in the vicinity of the critical point, we need to expand the denominator $d(z)$ of the symbol function in terms of the relevant system parameter $\{g_j\}, \{\nu_j\}$ around their critical values. Since we do not have an explicit expression for the roots z_0 of $d(z)$, we need to do this in an implicit way, i.e. expanding $d(z)$ both in terms of $z - z_0$ and in their explicit dependence on $\{g_j\}, \{\nu_j\}$.

Due to the positivity of $d(z)$ on the unit circle, all first order partial derivatives with respect to z as well as to the system parameter g_k and ν_k must be zero at the critical point. To find the leading order expansion in $z - z_0$ we thus evaluate higher order partial derivatives with respect to z using the implicit equations (5.30)

$$\begin{aligned}\frac{\partial^2 d}{\partial z^2} &= z^{-2}\sum_{j,l}\nu_j\nu_l e^{i(g_j-g_l)}\Big[(j-l)(j-l-1)z^{j-l} \\ &\quad +(l-j)(l-j-1)z^{l-j}\Big]. \end{aligned} \tag{5.31}$$

If the second order derivative is nonzero at $z = z_0$, we can stop at this level. On the other hand, the second order derivative can vanish if a second pair of independent implicit equations is fulfilled, which can easily be read off from Eq. (5.31). This procedure can be continued and each term $\frac{\partial^{2m} d}{\partial z^{2m}}\Big|_{z_0}$, which is zero, yields a new pair of implicit equations

$$\sum_j \nu_j j^m e^{ig_j} z_0^j = \sum_j \nu_j j^m e^{ig_j} z_0^{*j} = 0. \tag{5.32}$$

Here we have used that the first non-vanishing derivative must be an even one. Let us assume that all derivatives in z vanish up to order $2M-1$. Then it can be shown, that mixed derivatives of the type $\partial_{(\nu_k,g_k)}\partial_z^m d\Big|_{z_0}$ vanish for all $m < M$. Thus what remains are the second order partial derivatives with respect to ν_k or g_k. Second order partial derivatives in the same parameter are always non zero on the unit circle (except for trivial cases), as $\partial^2_{\nu_k} d(z)\Big|_{z_0} = 2$, $\partial^2_{g_k} d(z)\Big|_{z_0} = 2\nu_k^2$. Thus we can write the power expansion of $d(z)$ in the following general way

$$\begin{aligned} d(\tilde{z},\tilde{x}) \approx C_2\tilde{x}^2 + \tilde{x}\Big[C_{1,\tilde{M}}\tilde{z}^{\tilde{M}} + \mathcal{O}(\tilde{z}^{\tilde{M}+1})\Big] \\ +C_{0,2\tilde{M}}\tilde{z}^{2\tilde{M}} + \mathcal{O}(\tilde{z}^{2\tilde{M}+1}), \end{aligned} \tag{5.33}$$

where C_2 and $C_{0,2\tilde{M}}$ are non zero constants. Here $\tilde{x}$ is a linear combination of parameter variations away the critical values $\tilde{g}_k = g_k - g_{kc}$ and $\tilde{\nu}_k = \nu_k - \nu_{kc}$, and $\tilde{z} = z - z_0$. The lowest non-vanishing contributions determine the critical exponent and therefore $\tilde{M}$ is the minimal M of all parameters included in $\tilde{x}$. The zeros z_0 are algebraic functions of the system parameters and we can therefore write $\tilde{z} \approx \tilde{x}^\lambda + \mathcal{O}(\tilde{x}^{\lambda+1})$. At least two terms in the expansion must be of the lowest order and therefore we find $\lambda = \tilde{M}^{-1}$ along the line $\tilde{x}$ if the first $\tilde{M}$ implicit equations are fulfilled. We see that all possible critical exponents are the inverse of integer numbers. The smallest possible critical exponent is determined by the maximum $\tilde{M}$, which is just given by M.

We now can relate M to the number of adjacent sites coupled by each local reservoir N . It is clear that Eqs. (5.32) are linearly independent for different m. On the other hand only N equations can be independent for a finite reservoir coupling. This proves that M can be at most $N-1$. Otherwise all orders vanish, in which case the symbol function must be zero everywhere and the system is not critical. We conclude that if the reservoir coupling is

restricted to N sites, the critical exponent is out of a bounded set of fractional numbers

$$\lambda \in \left\{1, \frac{1}{2}, \frac{1}{3}, \cdots, \frac{1}{N-1}\right\}. \tag{5.34}$$

The corresponding Taylor expansion of the numerator $n(z)$ in a critical point is of higher order than the denominator. Therefore the amplitude of the critical correlations, vanishes as ξ diverges. This is seen in the graphs of Fig. 5.2(b). The remaining non-local correlations, visible for example in part (c) of the same figure, are due to additional singularities inside the unit circle. Only in the case of the minimal critical exponent $\lambda = \frac{1}{N-1}$, these singularities cannot exist due to fundamental laws of algebra. In this case the stationary state is completely mixed in the critical point.

Another result that can be drawn from our analysis is the dimensionality of the critical parameter space. Critical points have to fulfill the set of Eqs. (5.32) and for a given critical exponent the corresponding dimensionality is given by

$$\dim(P_\lambda) = 2\left(N - 1 - \frac{1}{\lambda}\right). \tag{5.35}$$

It is clear that the critical points are always a zero measure subset of parameter space, but they are not necessarily isolated points, with the exception of critical points with minimal exponent for the given configuration, which are always singular.

An important consequence of Eq. (5.35) is, that for any two non critical configurations of the reservoir coupling, one can find a continuous path, which connets the two without crossing a critical point.

5.3.1 Dynamical critical exponent

The relaxation rates of the system are determined by the homogeneous part of Eq. (5.9) and therefore the damping matrix X. More precisely the damping matrix X describes the dynamics on the sub-manifold of Gaussian states, whereas the full system is spanned by the Liouville Operator $\mathcal{L}$ in Eq. (5.1). The trace preservation of the Lindblad dynamics requires $\mathcal{L}$ to have at least one eigenvalue with vanishing real part. The gap in the real spectrum of $\mathcal{L}$ sets the slowest relaxation rate for arbitrary initial states and therefore the dissipative gap Δ of X gives an upper bound for the gap of $\mathcal{L}$, and the gap in the full damping spectrum must vanish as one approaches the critical points.

The eigenvalues of X are purely real, when neglecting the Hamiltonian contributions and strictly negative. In the translation invariant system the eigenvalues are given by the symbol function $-r(\varphi)-r(-\varphi)$, which we have identified before as relevant for the correlation length. In the vicinity of a critical point, the slowest relaxation rate, defining the spectral gap of relaxation, is determined by the roots z_j of $d(z, \{g_j\}, \{\nu_j\})$ closest to the unit circle

$$\Delta = \min_{|z|=1} d(z, \{g_j\}, \{\nu_j\}). \tag{5.36}$$

Therefore the dynamic critical exponent is immediately related to the static exponent λ. The exponent of the divergence however must be modified by the number of roots κ_c, that merge at the same point on the unit circle when the Liouville parameters approach their critical values:

$$\Delta \sim |g - g_c|^{\kappa_c \lambda}. \tag{5.37}$$

The number of roots κ_c is thus identical to the dynamical critical exponent z. For the minimum

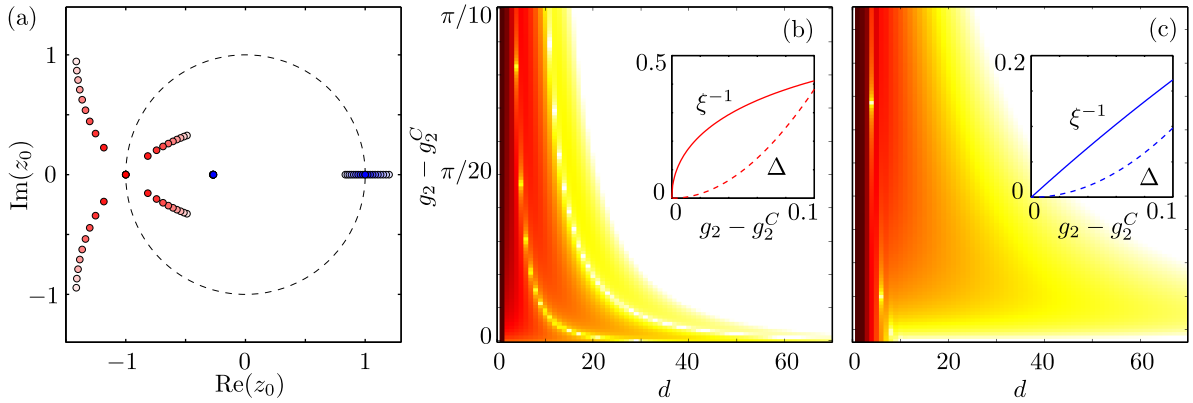

Figure 5.2: Two examples of criticality for reservoirs, which couple three adjacent sites. (a) shows the roots of $d(z)$ as a function of $g_2 - g_2^C$ for the two transitions discussed in the text. The color saturates for parameters closer to the critical point. (b) and (c) are real space correlations as a function of distance. (b) belongs to a $\lambda = 1/2$ transition and belongs to the red points in (a), whereas (b) is a $\lambda = 1$ transition and belongs to the blue points in (a)

critical exponent $\lambda = 1/(N-1)$ all $2(N-1)$ complex roots merge simultaneously on the same point and thus

$$z\,\lambda = 2, \qquad \text{for} \quad \lambda = \lambda_{\min}. \tag{5.38}$$

Moreover for all examples we have considered we found that the damping gap closes as a quadratic function, which suggests that Eq. (5.38) is more general.

5.4 Example

For reservoirs with coupling of range $N = 3$ we now want to give two examples of the critical transitions discussed before. We expect only two classes of critical points, namely those with exponent $\lambda = 1/2$ and $\lambda = 1$. To begin with we identify $\lambda = 1/2$ critical points, which are constructed via the two implicit Eqs. (5.30), which every critical point must satisfy and the two additional Eqs. (5.32) that guarantee the maximal order. Adding up these equations in the proper way yields

$$2 + \nu_1 e^{ig_1} z^1 = 0 \Rightarrow \nu_1 = 2 \Rightarrow z = -e^{ig_1}, \tag{5.39}$$

$$2 + 2e^{ig_1} z^{-1} = 0 \Rightarrow z = -e^{-ig_1} = -e^{ig_1}. \tag{5.40}$$

Therefore we can choose either $g_1^{(a)} = 0$ or $g_1^{(b)} = \pi$ with corresponding $z^{(a)} = -1, z^{(b)} = 1$. Taking differences of the implicit equations furthermore yields

$$1 - \nu_2 e^{ig_2} z^2 = 0 = 1 - \nu_2 e^{ig_2} \Rightarrow \nu_2 = 1, g_2 = 0, \tag{5.41}$$

independent of the choice of g_1. We therefore have identified the complete, zero dimensional set of critical parameters

$$P_{1/2} = \big\{[(2,0),(1,0)],[(2,\pi),(1,0)]\big\}. \tag{5.42}$$

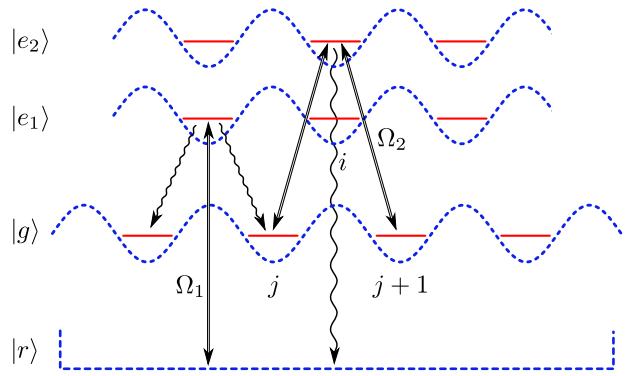

Figure 5.3: Proposal for the experimental realization of two site coupling in a quantum optics experiment. The optical lattice and internal states $|g\rangle, |e_1\rangle$ and $|e_2\rangle$ are chosen such that the excited state lattice is shifted and can be used to couple adjacent sites. Atoms in a fourth internal state $|r\rangle$ act as a broad reservoir.

If we consider the first critical point within $P_{1/2}$ under variation of g_2 we find

$$r(\varphi, g_2) = 6 + 4\cos(\varphi) + 2\cos(2\varphi - g_2) + 4\cos(\varphi - g_2) \tag{5.43}$$

$$\begin{aligned} \Rightarrow y(\varphi, g_2) &= r(\varphi, g_2) - r(-\varphi, g_2) \\ &= 2[\cos(2\varphi - g_1) - \cos(2\varphi + g_2) + 2\cos(\varphi - g_2) + 2\cos(\varphi + g_2)] \\ &\neq y(-\varphi, g_2) \end{aligned} \tag{5.44}$$

for $g_2 \neq (0, \pi)$, which is a signature of the broken TRS.

To find critical points in the much larger set P_1, which has dimension 2, we restrict our four dimensional parameter space by fixing two parameters $\nu_1 = \nu_2 = 1$ and search for solutions of the first pair of implicit equations. This yields

$$\begin{aligned} P_1^{\nu_1=1,\nu_2=1} = \big\{&[(1, 2\pi/3), (1, 4\pi/3)], [(1, 0), (1, 0)] \\ &, [(1, 4\pi/3), (1, 2\pi/3)]\big\} \subset P_1. \end{aligned} \tag{5.45}$$

In Fig. 5.2(a) we show the roots of the denominator $d(z)$ as a function of parameter g_2 around the first critical points in the set $P_{1/2}$ and $P_1^{\nu_1=1,\nu_2=1}$ respectively. The roots of the $\lambda = 1/2$ example are displayed by red dots and roots for the $\lambda = 1$ example in blue. The difference in the character of approach towards the unit circle is apparent as the step size in g_1 is uniform from $g_2 - g_2^{\mathrm{C}} = 0.1...0$. In Fig. 5.2(b) and (c) the respective real space correlations are plotted on a logarithmic color scale illustrating the emergence of long range correlations near the critical parameters and the different character of the transitions. Note that at the $\lambda = 1$ critical point, only two of the four roots merge on the unit circle, whereas another root is well within. This root is responsible for the additional short range correlations visible in Fig. 5.2(c). In the insets of Fig. 5.2(b) and (c) the vanishing of the damping gap is shown, which implies a divergence of relaxation time and a critical slow down. For both cases it shows quadratic behavior despite the different character regarding static properties.

5.5 A Quantum Optics Realization

In order to illustrate the physical context of the present section we now propose a scheme to realize dissipative two-site coupling. To this end let us consider fermionic atoms with four internal states $|g\rangle, |r\rangle, |e_1\rangle, |e_2\rangle$ in state selective, optical lattice traps as shown in Fig. 5.3. The lattice for atoms in states $|g\rangle, |e_1\rangle, |e_2\rangle$ is given by an optical standing wave and has lattice constant $\frac{\lambda}{2}$. The ground state lattice is shifted by half a lattice constant compared to the other two. Atoms in internal state $|r\rangle$ feel a very shallow potential and are delocalized compared to the tightly confined atoms in other internal states. The transition $|r\rangle \leftrightarrow |e_1\rangle$ is driven by a laser field with Rabi frequency Ω_1, whereas $|g\rangle \leftrightarrow |e_2\rangle$ is coupled to a laser with Rabi frequency Ω_2. Spontaneous decay occurs from the two excited levels into the metastable and ground states $|r\rangle, |g\rangle$. The optical lattices are deep so that we can assume that only adjacent Wannier wavefunctions $\varphi_i^\mu(x), \mu \in e_1, e_2$ and φ_i^g or φ_{i+1}^g are optically coupled by the laser fields. Using this setup non trivial pump and loss processes into and from the metastable states $|g\rangle$ are realized. Atoms in the shallow $|r\rangle$ potential act as a reservoir for the optical transitions. First of all atoms from the reservoir $|r\rangle$ are pumped via $|e_1\rangle$ into a superposition of atoms in neighboring lattice sites with fixed relative phase. To see this we note that the spontaneous emission from $|e_1\rangle$ to $|g\rangle$ can be described by the interaction Hamiltonian

$$\mathcal{H}_{int} = \int dx \sum_{\mathbf{k}} \left(g_{\mathbf{k}} \hat{a}_{\mathbf{k}} \hat{\Psi}_g^\dagger(x) \hat{\Psi}_{e_1}(x) e^{ik_x x} + \text{h.c.} \right), \tag{5.46}$$

where $\hat{a}_{\mathbf{k}}$ is the annihilation operator of the electromagnetic mode with wavevector $\mathbf{k}$, and $g_{\mathbf{k}}$ is the corresponding coupling matrix element. Using the decomposition of the fermionic fields in internal states $|g\rangle$ and $|e_1\rangle$ into the Wannier basis $\hat{\Psi}_g(x) = \sum_j \varphi_j^g(x)\hat{c}_j$ and $\hat{\Psi}_{e_1}(x) = \sum_j \varphi_j^{e_1}(x)\hat{e}_{1,j}^\dagger$ yields

$$\mathcal{H}_{int} = \sum_j \sum_{\mathbf{k}} \left[g_{\mathbf{k}} \hat{a}_{\mathbf{k}} \hat{e}_j \left(\eta_{j1}^{(k)} \hat{c}_j^\dagger + \eta_{j2}^{(k)} \hat{c}_{j+1}^\dagger \right) + \text{h.c.} \right], \tag{5.47}$$

where $\eta_{j1}^{(k)} = \int dx\, \varphi_j^{e_1}(x)\varphi_j^g(x)e^{ik_x x}$ and $\eta_{j2}^{(k)} = \int dx\, \varphi_j^{e_1}(x)\varphi_{j+1}^g(x)e^{ik_x x}$ denote the Frank-Condon factors corresponding to the transitions $j \to j, j+1$. Due to the exponentially decreasing Frank-Condon overlaps all transitions with $j' \neq j, j+1$ can safely be neglected. As the Wannier functions in a deep optical lattice are well localized the products $\varphi_j^{e_1}(x)\varphi_j^g(x)$ and $\varphi_j^{e_1}(x)\varphi_{j+1}^g(x)$ are well localized functions at positions $x_j \pm a/4$ with $a \sim \lambda/2$ being the lattice constant. Thus Eq. (5.47) can be rewritten

$$\mathcal{H}_{int} = \sum_j \sum_{\mathbf{k}} \left[g_{\mathbf{k}} \hat{a}_{\mathbf{k}} \hat{e}_j \eta_{j1}^{(k)} \left(\hat{c}_j^\dagger + \nu \hat{c}_{j+1}^\dagger e^{ik_x a/2} \right) + \text{h.c.} \right], \tag{5.48}$$

where the (real) parameter ν can be tuned by shifting the position of the $|e_1\rangle$ lattice, relative to that of $|g\rangle$. Coupling of the many motional states in $|r\rangle$ with a laser to $|e_1\rangle$ leads after elimination of the vacuum modes to an optical pumping that can be described by independent Lindblad generators

$$L_j^{\text{pump}} = \chi(c_j^\dagger + \nu c_{j+1}^\dagger) \tag{5.49}$$

with $\chi \sim \Omega_1^2/\gamma$ which describe the coupling to two adjacent lattice sites. Note that the relative phase term $e^{ik_x a/2}$ in Eq. (5.48) vanishes after averaging over the vacuum modes up to the first order in $k_0 a/2$.

We now show that optical pumping from $|g\rangle$ via $|e_2\rangle$ leads to a loss of fermions in all

superpositions of neighboring sites except for one dark mode. The corresponding Hamiltonian describing the coherent part of the interaction reads

$$\mathcal{H}_{int,2} = \sum_j \Omega_2 \hat{f}_j \left(\tilde{\eta}_{j1}\hat{c}_j + \tilde{\eta}_{j2}\hat{c}_{j+1}\right) + \text{h.c.} \tag{5.50}$$

where $\tilde{\eta}_{j1}^{(k)} = \int dx\, \varphi_j^{e_1}(x)\varphi_j^{g}(x)e^{iq_x x}$ and $\tilde{\eta}_{j2}^{(k)} = \int dx\, \varphi_j^{e_1}(x)\varphi_{j+1}^{g}(x)e^{iq_x x}$ where $q_x = \mathbf{q}\cdot\mathbf{e}_x$ and $\mathbf{q}$ is the wave vector of the laser corresponding to Ω_2. Note that since the wavevector of Ω_2 is well defined $\tilde{\eta}_{j1}$ and $\tilde{\eta}_{j2}$ differ in both amplitude and phase. Considering a fast subsequent decay from $|e_2\rangle$ finally gives rise to an optical pumping out of state $|g\rangle$ described by independent Lindblad generators

$$L_j^{\text{decay}} = \gamma\left(c_j + \nu e^{ig} c_{j+1}\right). \tag{5.51}$$

5.5.1 Solution to the quantum optics example

The Lindblad generators we generate within this example are not within the class we discussed in detail before, as they contain both kinds of Majorana fermions. We can nevertheless analytically solve the Lyapunov-Sylvester Eq. (5.16) and find

$$\gamma(\varphi) = \frac{1}{d(\varphi)}\begin{bmatrix} n_{11}(\varphi) & n_{12}(\varphi) \\ -n_{12}(\varphi) & n_{11}(\varphi)\end{bmatrix}, \tag{5.52}$$

where

$$n_{11}(\varphi) = 4i\nu\chi^2[1+\nu^2+2\nu\cos(\varphi)]\sin(g)\sin(\varphi), \tag{5.53}$$

$$\begin{aligned} n_{12}(\varphi) = {} & [1+\nu^2+2\nu\cos(g)\cos(\varphi)]^2 \\ & - 4\nu^2\sin^2(g)\sin^2(\varphi) - \chi^4[1+\nu^2+2\nu\cos(\varphi)]^2 \end{aligned} \tag{5.54}$$

and

$$\begin{aligned} d(\varphi) = {} & [(1+\nu^2)(1+\chi^2)+2\nu(\chi^2+\cos(g))\cos(\varphi)]^2 \\ & - 4\nu^2\sin^2(g)\sin^2(\varphi). \end{aligned} \tag{5.55}$$

Real space correlations are related to the symbol function via an inverse Fourier transform and the correlation length potentially diverges for parameters, where the denominator $d(\varphi)$ is close to zero. For $\nu = 1$ one finds that $d(\pi) = 0$ for all χ and $g = 0$. To classify this critical point we must determine the behavior of the denominator in the vicinity. We find that the four roots of the denominator merge at $z = -1$ at this critical transition

$$z_{1\cdots4} = \frac{-(1+\chi^2) \pm 2\chi\sin(g/2)}{\chi^2+\cos(g)\pm i\sin(g)} \tag{5.56}$$

$$\approx -1 \pm \frac{\chi \pm i}{1+\chi^2} g + \mathcal{O}(g^2). \tag{5.57}$$

The linear scaling in g reveals that this example belongs to the $\lambda = 1$ class established in this chapter.

Conclusion

We have analyzed the stationary state of translation invariant chains of free fermions coupled to local Markovian reservoirs, described by linear Lindblad generators. We showed that the

analytic solution to this problem can undergo a transition to criticality, which we identify by divergences of length scales and time scales of relaxation. Unlike the TRS models studies by Bardyn et al., all gapped phases of our model can be continuously connected, without the need to cross a critical manifold. The approach to critical points can be characterized by static and dynamic exponents, that describe the divergence of length and time scales respectively. For the specific models at hand, we showed that these exponents must be the inverse of integers between 1 and $N-1$, where N is the range of reservoir coupling.

Part IV

Non-Equilibrium Physics with Rydberg Atoms

Chapter 6

Quasi-Crystallization in 1D Rydberg Lattice Systems

The introduction of Rydberg states to the toolbox of ultra cold atom experiments bears the promise to enable the preparation of strongly correlated and exotic quantum states. Strong dipole-dipole or van der Waals interaction between Rydberg excited atoms, exceed the conventional interactions between cold neutral atoms by orders of magnitude in strength and range.

Experiments on Bose-Einstein condensation and the Mott insulator to superfluid transition, are examples of low temperature phase transitions and probe the ground state properties of the Hamiltonian describing the system. Two approaches are pursued to use Rydberg atoms to realize an interacting Hamiltonian and prepare its correlated ground state. The idea of Rydberg dressing is to couple ground state atoms far off resonantly to Rydberg states, such that a small fraction of the strongly interacting state *dresses* the ground state atom [156, 157]. Proposals based on this admixture of interaction range from the study of BECs with dipolar interaction, to more exotic phases of matter such as supersolids and Laughlin states of the FQH effect [157, 11, 158]. Experimental progress on the realization of these proposals has been slow, due to the effect of heating from scattered photons [159]. Whereas for dressing, the Rydberg state is merely admixed by off resonant coupling, other proposal rely on the resonant excitation of atoms to Rydberg states and realize strongly correlated states of these excited atoms. Pohl et al. showed that small, spatially ordered crystals of excitations can be prepared by adiabatic parameter variation and following of the ground state [160]. This ansatz was further developed and generalized to different geometries of the atomic ensemble in [161, 162]. Schauss et al. recently published experimental results on the adiabatic preparation of ordered structures using optimized protocols for parameter changes [163].

All approaches described above, rely on the assumption that the state of the system remains near the ground state during the preparation procedure, despite non adiabatic corrections and dissipation. The time scales required for the adiabatic preparation typically increase with system size and this scaling ultimately limits the use of adiabatic techniques. We therefore pursue a second approach in the spirit of [10] and the discussion of non-equilibrium steady states in the previous chapter. Diehl et al. proposed to *engineer* the dissipation in such a way, that the attractor of the systems dynamics is a correlated many-body state. In the context of Rydberg experiments, the dissipation results from spontaneous emission and decoherence is difficult to manipulate, but suitable excitation schemes can be identified towards the realization of quasi-crystals of Rydberg excitation in the stationary state.

In the following chapter, we will consider a one dimensional lattice system of atoms excited

to Rydberg states, where the interaction between atoms on adjacent sites is strong. Using a mean field ansatz, Lee et al. first discussed the stationary state phase diagram for a two-level pumping scheme and predicted the emergence of a long range ordered states of excited atoms [164]. By developing an effective model for the dynamics of excitation and deexcitation in the many-body system, we show that the predictions of mean field theories are qualitatively wrong in this one dimensional systems. Whereas antiferromagnetic correlations emerge between excited atoms, they are always of finite range and we identify the origin of this correlation length. Furthermore we show that a two-level excitation scheme can not prepare long range order in any spatial dimension and more sophisticated excitation schemes such as coherent population trapping based on dark-state pumping are required. Numerically exact TEBD simulations for the open system dynamics, based on [165], are used to validate the effective model. As for the fermionic model discussed in the previous chapter, we find a close relation between the emergence order and an increase in the systems relaxation time. The results of this discussion have been published in [H-2013a].

6.1 One Dimensional Rydberg Chain

In this chapter we will discuss one dimensional chains of atoms as illustrated in Fig. 6.1(a). Ground state atoms are trapped by a deep lattice and we assume the motional degrees of freedom to be completely frozen during the relevant time scales of the Rydberg excitation dynamics. The unitary dynamics is governed by a strictly local term $\mathcal{H}_{\text{atom}}$ describing the excitation process of every atom to a Rydberg state and a long range interaction term for excited atoms. We neglect coupling to different Rydberg states, such that the full Hamiltonian is given by

$$\mathcal{H} = \sum_j \mathcal{H}_{\text{atom}}^{(j)} + \sum_{j>k} V(|j-k|)\hat{\sigma}_{\text{rr}}^{(j)}\hat{\sigma}_{\text{rr}}^{(k)}. \tag{6.1}$$

In the interaction part of the Hamiltonian $V(|j-k|)$ is the distance dependent interaction between excited atoms j and k and $\hat{\sigma}_{\text{rr}}^{(j)} = |\text{r}\rangle_j\langle\text{r}|_j$ is the projector onto the Rydberg state for atom j. Here we have two different excitation processes in mind that are most relevant to current experiments. Most experiments use a two photon transition from ground state $|\text{g}\rangle$ to Rydberg state $|\text{r}\rangle$ via an intermediate state $|\text{e}\rangle$. If the process is far off one photon resonance, one can safely eliminate this intermediate state and the single atom physics is described by

$$\mathcal{H}_{\text{atom,2}} = (\Omega|\text{g}\rangle\langle\text{r}| + h.c.) + \Delta_0\hat{\sigma}_{\text{rr}}, \tag{6.2}$$

where the effective Rabi frequency Ω is determined by the intermediate state detuning Δ_e and the two Rabi frequencies $\Omega_{\text{ge}}, \Omega_{\text{er}}$ and given by $\Omega = \Omega_{\text{ge}}\Omega_{\text{er}}/\Delta_e$. For one photon resonant excitation we must take into account the intermediate state and the full three level system has to be considered

$$\mathcal{H}_{\text{atom,3}} = (\Omega|\text{g}\rangle\langle\text{e}| + h.c.) + (\Omega_{\text{C}}|\text{e}\rangle\langle\text{r}| + h.c.) + \Delta_0\hat{\sigma}_{\text{rr}}. \tag{6.3}$$

Both cases are illustrated in Fig. 6.1(b). Notice that we have included a two photon detuning Δ_0 in our definition, which will be of great importance in the subsequent chapter on two dimensional lattice systems and bistability in Rydberg systems.

We here restrict to atoms excited to S states, which display an isotropic long range interaction. Note however that the excitation of D states is equally possible in two photon excitation schemes and enables the study of anisotropic long range interactions. Furthermore

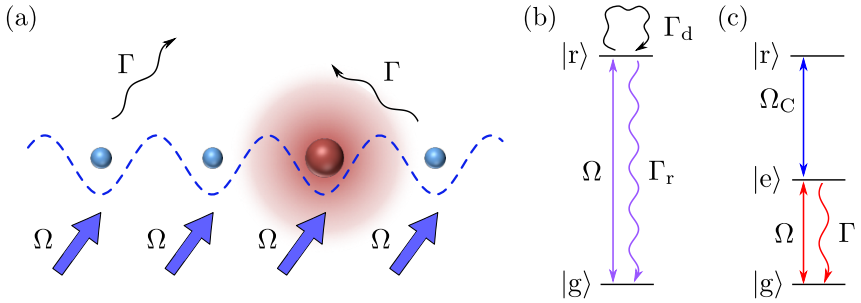

Figure 6.1: (a) Schematics of the one dimensional chain driven by coherent external fields and subject to spontaneous decay of excitations. We discuss two excitation schemes for. Direct one photon transition shown in (b) including finite lifetime of Rydberg state and additional decoherence. (c) displays the alternative coherent population trapping (CPT) scheme.

direct one photon schemes for typical ground states of S symmetry couple to P states, which we will discuss in chapter 9. For S state excited atoms the interaction potential at large distances is of the form

$$V(|j-k|) = C_\alpha/(a|j-k|)^\alpha, \tag{6.4}$$

where a is the lattice constant and $\alpha = 3$ for dipole-dipole (DD) interactions and $\alpha = 6$ for the van der Waals (vdW) case.

The many-body problem in the absence of dissipation, with two level driving as in Eq. (6.2) has been discussed before [161]. In the limit $\Omega = 0$ the ground state can be determined analytically and one finds that it is given by a long range ordered pattern of Rydberg excited atoms. The density of excitations as a function of detuning Δ_0 resembles a staircase, that is a so called devils staircase. In the literature the name Rydberg crystals has evolved for these ordered arrays of excited atoms [161, 160]. Using first and second order perturbation theory in Ω, as well as numerical DMRG simulations it has been shown, how incompressible phases of constant density melt and the long range order of excitations in the ground state is lost [132]. Preparation of the ordered ground state faces two hurdles. First of all the generic initial state in these systems is given by all atoms in their atomic ground state and one has to find an adiabatic path via dynamic tuning of Δ_0 and driving Ω connecting initial state and targeted crystal of excitations. This is only feasible for small systems as necessary time scales rapidly increase with final number of excitations [160]. Second, the system is inherently open as Rydberg excited atoms have a finite lifetime and thus excitations are spontaneously removed. The preparation of crystal states as ground states thus has to compromise between adiabatic slowness and the necessity to be fast and avoid dissipation.

We choose a different approach to the preparation of crystal like states in this system, taking into account the relevant decoherence processes and utilizing them to our advantage. The finite lifetime of excited states and dephasing processes are included in a Lindblad approach as in Eq. (5.1). For the two level scheme in Fig. 6.1(b) we include both finite lifetime of the Rydberg state $\tau_\mathrm{r} = 1/\Gamma_\mathrm{r}$, as well as an excitation preserving dephasing with rate Γ_d described by Lindblad operators

$$\hat{L}_\mathrm{r} = \sqrt{\Gamma_\mathrm{r}}|\mathrm{g}\rangle\langle\mathrm{r}|, \qquad \hat{L}_\mathrm{d} = \sqrt{\Gamma_\mathrm{d}}|\mathrm{r}\rangle\langle\mathrm{r}|. \tag{6.5}$$

For the CPT excitation scheme it is sufficient to include the large intermediate state decay Γ_e as it dominates the other decoherence channels.

6.1.1 Blockade and mean field predictions

Before we approach the full many-body problem we want to discuss two details. At the heart of Rydberg crystals is the blockade effect, which we will illuminate at the simple example of two atoms. Closely related is a mean field approach to the full many-body problem developed by Lee et al. [164].

In appendix 15.1 we derive the text book excitation probability in the stationary state for a single two level atom

$$\langle\hat{\sigma}_{\mathrm{rr}}\rangle = \frac{2\gamma\Omega^2}{4\Omega^2\gamma + \Gamma_{\mathrm{r}}(\gamma^2+\Delta_0^2)}, \tag{6.6}$$

with $\gamma = (\Gamma_{\mathrm{r}}+\Gamma_{\mathrm{d}})/2$. Under resonant driving and in the regime $\Gamma_{\mathrm{d}} \gg \Gamma_{\mathrm{r}}$ and $\Gamma_{\mathrm{r}}\Gamma_{\mathrm{d}} < \Omega^2$ this probability is given by

$$\langle\hat{\sigma}_{\mathrm{rr}}\rangle = \frac{1}{2}\frac{1}{1+\Delta_0^2/\omega^2}, \qquad \text{with } \omega = \Omega\sqrt{2\Gamma_{\mathrm{d}}/\Gamma_{\mathrm{r}}}. \tag{6.7}$$

Now consider two atoms under continuous driving with interaction V of the Rydberg excited atoms. If V is small compared to the linewidth ω the interaction is only a perturbative effect and the probability for concurrent excitation of both atoms is given by $\langle\hat{\sigma}_{\mathrm{rr}}^{(1)}\hat{\sigma}_{\mathrm{rr}}^{(2)}\rangle = 1/4 - \mathcal{O}(V^2/\omega^2)$, whereas in the opposite limit it is strongly suppressed $\langle\hat{\sigma}_{\mathrm{rr}}^{(1)}\hat{\sigma}_{\mathrm{rr}}^{(2)}\rangle = \mathcal{O}(\Omega^2/V^2)$. If the interaction is of vdW type this translates to a blockade of double excitation for two atoms that are within a distance of the blockade radius

$$d_{\mathrm{b}} = \sqrt[6]{C_6/\Omega} \tag{6.8}$$

The parameters we discuss for the extended chain in this chapter will be such, that the blockade radius is in between one and two lattice constants. Therefore atoms on neighboring sites have a strong effect upon each other, whereas longer range interactions are expected to be small perturbations.

A first attempt at the many-body problem has been taken by Lee et al. using a mean field ansatz [164]. The key assumption is a factorization of the density matrix with respect to the individual lattice sites, $\varrho = \otimes_j \varrho^{(j)}$, which excludes the presence of any intersite correlations. One must only consider two local quantities, the inversion $w_j = \varrho_{\mathrm{rr}}^{(j)} - \varrho_{\mathrm{gg}}^{(j)}$ and the atomic coherence $q_j = \varrho_{\mathrm{gr}}^{(j)}$. The dynamic equations for these quantities couple to higher order correlations, however, within the ansatz for ϱ, all correlations factorize to lowest order and a nonlinear, closed set of equation for the q_j and w_j remains to be solved. For all parameters a homogeneous solution $w_j = w, q_j = q$ exists. This solution is not stable for all parameters, instead for intermediate driving the system of equations has stable solutions with alternating excitation probabilities w_1, w_2 for two sublattices, similar to an antiferromagnetic ordering. In Fig. 6.2(a) we show numeric solutions of the mean field equations in one dimension for resonant excitation and $V/\Gamma = 5$ as a function of Ω/Γ. Whereas blue solutions correspond to a homogeneous excitation probability w, the red solutions belong to alternating excitation probabilities with two sublattices of excitation probability w_1 and w_2 respectively.

6.2 Approaching the Full Many-Body Problem

Lee et al. already suspected the absence of this order in one dimension after having done exact calculations for small systems of 10 atoms and finding only weak correlations between adjacent atoms. Using advanced numeric methods such as TEBD and approximate models

we here will study large one dimensional chains and give an analytic understanding for the absence of crystallization. This insight will allow us to identify systems and parameter regimes with an extended range of correlations in one dimension and ultimately describe true long range order in driven lattice systems in two dimensions in chapter 7.

6.2.1 Approximation via MPS

Weakly correlated quantum states in one dimensional systems are routinely approximated with Matrix Product States (MPS) as we have done for topological systems in the first part of this thesis. When studying bistability in far off resonant driven lattice systems in chapter 10 we will rely on MPS based algorithms for dissipative systems and give an introduction into this technique. Simulations for this section have been done by Dominik Muth to benchmark the results of a classical rate equation approach, which we will develop and discuss in the following.

6.2.2 Rate equation model

An invaluable tool for our analysis of driven Rydberg system will be the mapping to classical rate equations, which has been successfully applied on multiple facets of Rydberg many-body physics. Clearly, many interesting effects of many-body systems can not be understood in purely classical terms and we will encounter one example in a later chapter. The reasons for considering Rydberg systems as classical are twofold. First of all, much of the interesting many-body physics encountered is that of strong, non trivial but classical correlations. The quasi-crystallization we discuss in this section is the prime example as we will see in the following discussion. Furthermore, many recent experiments are conducted under imperfect conditions resulting in strong decoherence channels of sometimes unclear origin, that suppress the emergence of quantum coherences but render a classical description valid.

The basis of the rate equation model are the rates for excitation and deexcitation of individual atoms as a function of their detuning, which is influenced by the interaction with other excited atoms. The many-body state is then represented by the joint probabilities $\varrho_{S_1,\cdots,S_N}$ for atoms to be excited ($S_j = 1$) or not ($S_j = 0$) at site j. The dynamic equation for these joint probabilities is given by

$$\begin{aligned}\frac{d}{dt}\varrho_{S_1,\cdots,S_N} = &\sum_j \Big[(1-S_j)\Gamma_\downarrow(\delta_j) + S_j\Gamma_\uparrow(\delta_j)\Big]\varrho_{S_1,\cdots,1-S_j,\cdots,S_N} \\ &- \Big[(1-S_j)\Gamma_\uparrow(\delta_j) + S_j\Gamma_\downarrow(\delta_j)\Big]\varrho_{S_1,\cdots,S_j,\cdots,S_N},\end{aligned} \tag{6.9}$$

with the interaction between atoms encoded in the state dependent detunings

$$\delta_j = \Delta + \sum_{k\neq j} V_{j,k}S_k. \tag{6.10}$$

In Appendix 15.1 we derive single atom rates for the two driving schemes discussed in this chapter and we further motivate the validity of the many-body rate equation approach. Note that the number of equations is still exponential in the number of atoms and as such hard to solve in general. In subsequent chapters we will strongly rely on Monte Carlo methods that sample the classical dynamics of driven Rydberg systems. Here, we will instead discuss a special case where the many-body rate equation problem is indeed exactly solvable.

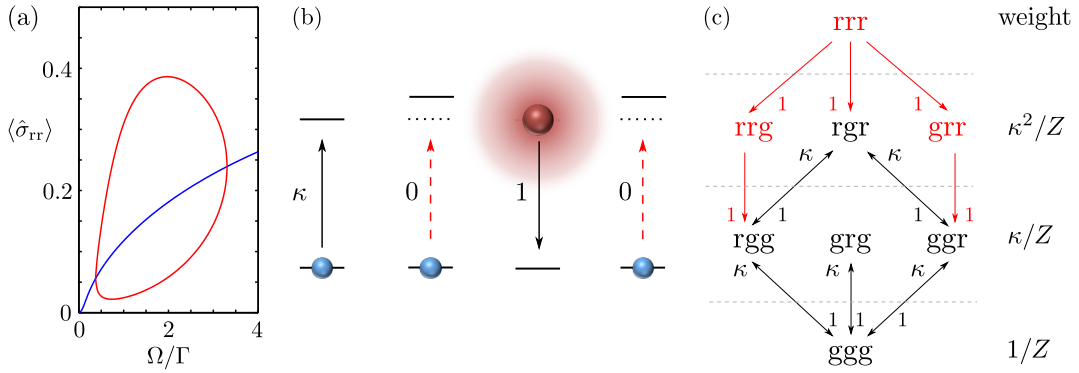

Figure 6.2: (a) Solutions to the mean field equations derived in [164]. The blue solution is uniform across the chain, whereas red solutions predict antiferromagnetic order. Parameters are $V_{\rm NN}/\Gamma = 5$ and $\Delta_0 = 0$. (b) Schematic illustration of the rate equation model within next neighbor approximation on a short one dimensional chain. The full set of states of for example three, atoms shown in (c), can be sorted in layers of fixed excitation number to reveal the detailed balance solution.

6.3 Next Neighbor Approximation

The single atom rates for driven two level atoms are given by

$$\Gamma_\uparrow(\delta) = \frac{2\Omega^2\gamma}{\gamma^2+\delta^2}, \quad \Gamma_\downarrow(\delta) = \Gamma_\uparrow(\delta) + \Gamma_{\rm r}, \tag{6.11}$$

which for a single atom yields the text book stationary state excitation probability of $\langle\hat{\sigma}_{\rm rr}\rangle = [2\gamma\Omega^2]/[4\Omega^2\gamma + \Gamma(\gamma^2+\delta^2)]$. The state dependent detuning is given by

$$\delta_j = \Delta + \sum_{k\neq j} \frac{C_\alpha}{(a|j-k|)^\alpha} S_j, \tag{6.12}$$

which in the case of vdW interactions can be split as

$$\delta_j = \Delta + \frac{C_6}{a^6}(S_{j-1} + S_{j+1}) + \sum_{|k-j|>1} \frac{C_6}{a^6|j-k|^6} S_k. \tag{6.13}$$

The interaction energy of two Rydberg excited atoms on adjacent sites is much larger than for two excitations separated by an additional site $C_6/a^6 := V_{\rm NN}/V_{d>1} \geq 64$. Therefore we consider the regime $V_{\rm NN} \gg \omega \gg V_{d>1}$, where an excited atom strongly shifts adjacent atoms but only weakly affects atoms on sites further away. For two level atoms driven on resonance ($\Delta_0 = 0$) this limit is further simplified by assuming strong interaction of excited atoms on adjacent sites $\omega/V_{NN} \to 0$, which yields an analytically solvable problem.

This limiting case is illustrated in Fig. 6.2(b) and the rate equation dynamics can be represented in more familiar Lindblad form

$$L_{\rm d}^{(j)} = \hat{\sigma}_{\rm gr}^{(j)}, \tag{6.14}$$

$$L_{\rm p}^{(j)} = \sqrt{\kappa}(\hat{\sigma}_{\rm rr}^{(j-1)} - 1)(\hat{\sigma}_{\rm rr}^{(j+1)} - 1)\hat{\sigma}_{\rm rg}^{(j)}. \tag{6.15}$$

The ratio of resonant excitation rate to deexcitation rate is given by

$$\kappa = \Gamma_{\uparrow}(0)/\Gamma_{\downarrow}(0), \tag{6.16}$$

which is the only parameter of relevance to the stationary state as we will now show. The dynamics generated within the classical state space are illustrated in Fig. 6.2(c) for a small chain of three atoms. First of all, every state with two adjacent excitations has weight zero in the stationary state, as it decays but is not refilled. Furthermore the weight of an accessible configuration is only determined by the total number of excitations it contains

$$p_{\{s_j\}} = \frac{1}{Z}\kappa^{\sum_j \delta_{s_j,\mathrm{r}}}. \tag{6.17}$$

This is the detailed balance solution of the graph in Fig. 6.2(c), meaning that the net flux along every single bond is zero. For example $\kappa \times p_{\mathrm{rgg}} = 1 \times p_{\mathrm{rgr}}$ or $0 \times p_{\mathrm{rgg}} = 1 \times p_{\mathrm{rrg}} = 0$ in the stationary state. The partition function Z ensures the normalization $\sum_{\{s_j\}} p_{\{s_j\}} = 1$.

6.3.1 Filling factor and correlation length

For large systems we will now derive analytic expressions for the partition function and discuss quantities such as the filling factor and the correlation length of ordered Rydberg structures. To evaluate the partition function we will use that all states with fixed number of excitations P and no adjacent ones have the same weight κ^P.

A classical configuration with P excited atoms in a finite chain of L atoms, is fully determined by the $P-1$ distances a_i between adjacent excitations, the distance from the left edge to the first excited atom b_0 and from the right edge to the last excited atom b_P. Therefore a state can be identified by integer numbers $b_0, a_1 \cdots, a_{P-1}, b_P \in \mathbb{Z}_0$. Due to the restriction of NN blockade, all a_i must be larger than zero, which we take into account by defining $b_i = a_i - 1$. Each excitation needs its own lattice site and thus

$$b_0 + (b_1 + 1) + \cdots + (b_{P-1} + 1) + b_P + P = L. \tag{6.18}$$

We can rewrite

$$\sum_{i=1}^{P+1} b_i = L + 1 - 2P \tag{6.19}$$

and see that the a_i are a weak composition of an integer given only by system size and the total number of excitations P. The number of weak compositions is known, and we therefore find that the number of unique, allowed states with P excitations is given by

$$N(P, L) = \binom{L - (P-1)}{P}. \tag{6.20}$$

The remaining sum for the partition function can be evaluated analytically

$$Z(\kappa, L) = \sum_{P=0} \kappa^P N(P, L) = 2\kappa^{(L+1)/2} \frac{\cosh[(2+L)\mathrm{arcsinh}(1/(2\sqrt{\kappa}))}{\sqrt{4 + 1/\kappa}}, \tag{6.21}$$

which is exact for an odd number of atoms. The expected number of excitations is calculated

via differentiation with respect to the *chemical potential* $\mu := \log(\kappa)$

$$\langle P \rangle = \partial_\mu \log[Z(e^\mu, L)]. \tag{6.22}$$

For large system sizes this can be simplified and we find for the filling fraction

$$\langle P \rangle / L = \frac{1}{2}\Big(1 - \frac{1}{\sqrt{1+4\kappa}}\Big) + \mathcal{O}(L^{-1}). \tag{6.23}$$

Along previous lines we can also derive analytic results for the fluctuation of filling fraction

$$\Delta_P^2 / L^2 = \frac{\kappa}{(1+4\kappa)^{3/2}} \frac{1}{L} + \mathcal{O}(L^{-2}), \tag{6.24}$$

which decreases in larger systems. The blockade of further excitations is demonstrated by the sub Poissonian nature of the excitation number distribution, which is characterized by the Mandel Q parameter

$$Q = \frac{2\kappa}{(1+4\kappa)(\sqrt{1+4\kappa}-1)} - 1 + \mathcal{O}(L^{-1}). \tag{6.25}$$

In the limiting case of weak driving ($\kappa < 1$) a Poissonian statistics is realized $Q \approx 0 - 2\kappa$, whereas for strong driving ($\kappa \gg 1$) $Q \approx -1 + 1/(4\sqrt{\kappa})$ the sub Poissonian limit is approached.

Besides these global quantities we can calculate local observables. The excitation probability for odd sites in a chain of odd length can be calculated in the limit $L \to \infty$ via

$$\begin{aligned} p_j &= \kappa \frac{Z_{j-2} Z_{L-j-1}}{Z_L} && (6.26)\\ &\approx \frac{\cosh\left(j/\sqrt{4\kappa}\right)\cosh\left((1+L-j)/\sqrt{4\kappa}\right)}{\cosh\left((2+L)/\sqrt{4\kappa}\right)} && (6.27)\\ &\approx \frac{1}{2} + \frac{\cosh\left((L+1-2j)/\sqrt{4\kappa}\right)}{2\cosh\left((2+L)/\sqrt{4\kappa}\right)} && (6.28)\\ &\approx \frac{1}{2} + \frac{e^{(L+1-2j)/\sqrt{4\kappa}}}{e^{(L+2)/\sqrt{4\kappa}}} = \frac{1}{2} + e^{-j/\sqrt{\kappa} - 1/\sqrt{4\kappa}}. && (6.29) \end{aligned}$$

Thus at the edges of the system, Rydberg excitations form a quasi-crystal of finite correlation length

$$\xi = \sqrt{\kappa}. \tag{6.30}$$

These first order correlations are immediately related to second order density-density correlations, if one realizes that an excitation at site j, is identical to an edge at $j+1$ for all sites $j > j+1$. Therefore

$$|\langle \hat{\sigma}_{\mathrm{rr}}^j \hat{\sigma}_{\mathrm{rr}}^{j+d} \rangle - \langle \hat{\sigma}_{\mathrm{rr}}^j \rangle \langle \hat{\sigma}_{\mathrm{rr}}^{j+d} \rangle| \sim e^{-|d|/\sqrt{\kappa}}. \tag{6.31}$$

Fig. 6.3(a) illustrates the numeric evaluation of the filling fraction and its fluctuation (blue) for a finite system of size $L = 31$ and the analytic expression (black) in the thermodynamic limit. The analytic expression for the correlation length is quickly increasing as the system is filled with excitations.

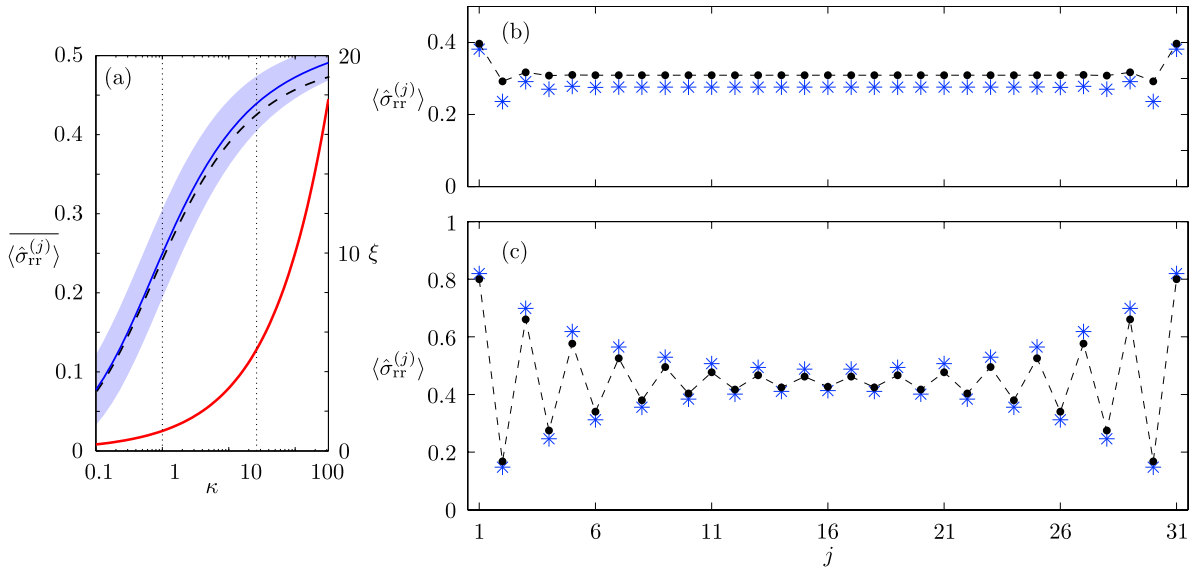

Figure 6.3: (a) shows the mean filling factor and its fluctuations (blue) for the NN rate equation model with open boundary conditions and length $L = 31$ (solid) and in thermodynamic limit (dashed). The corresponding correlation length ξ (red) increases as the system is driven towards maximal filling, reducing the overall fluctuations. The dashed lines correspond to $\kappa_{\rm b,c}$ used for the NN rate equation model in (b) and (c). (b) and (c) display a comparison of excitation probabilities in stationary of quasi exact TEBD results and idealized NN rate equation model results. (b) is a two level driving scheme with $V_{\rm NN} = 2\Omega$ and $\Gamma_{\rm r} = \Omega/4, \Gamma_{\rm d} = 0$ and (c) is under conditions of CPT driving with $V_{\rm NN} = 2\Omega, \Gamma_{\rm e} = 4\Omega, \Omega = 5\Omega_c$.

6.3.2 Two- versus three-level driving

The effective model we discussed in the previous sections is related to the physical realization with two and three level driving schemes. For both schemes we derive the effective driving parameter κ in appendix 15.1 and find

$$\kappa_2 = \frac{\Omega^2}{\Omega^2 + \gamma^2}, \qquad \kappa_3 = \frac{\Omega^2}{\Omega_c^2}. \tag{6.32}$$

Note that the effective driving κ_2 is bounded to values smaller 1, a result of the absence of inversion in the stationary state of a driven two level atom. Instead of saturating the chain with Rydberg excited atoms the mean density is therefore bounded by $\langle P\rangle/L < 1/4$ and strongly fluctuates $\Delta_P^2/\langle P\rangle \approx 1$. Correlations between excitations are restricted to nearest neighbors as $\xi < 1$. Before the information that an atom is excited can propagate through the system, it has already decayed back to its ground state.

Fluctuations can be suppressed by using the coherent population trapping scheme (CPT). Then free atoms are excited into a dark state superposition of ground and Rydberg state $|\Psi_{\rm D}\rangle = (\Omega_c|{\rm r}\rangle - \Omega|{\rm g}\rangle)/(\Omega^2 + \Omega_c^2)$, which for a weak control field $\Omega_c < \Omega$ is dominated by the Rydberg state. By dark-state pumping of atoms into the Rydberg state we thus achive $\kappa_3 \gg 1$, which implies larger fillings and reduced fluctuations. Here correlations can build up and the effective model predicts a tunable correlation length of $\xi = \Omega/\Omega_c$.

6.3.3 Comparison with TEBD results and limits

TEBD simulations of one dimensional lattice systems are most effective when the Lindblad operators and the Hamiltonian can be separated into parts that have support only on adjacent sites. For the Rydberg-Rydberg interaction, this is in general not true, but we have already motivated that in the case of van der Waals interactions on the lattice, we can choose a regime such that a truncation to NN interactions is justified. Simulations for this problem have been carried out by Dominik Muth and we use the results for systems of size $L = 31$ to illustrate the accuracy of the effective model in Fig. 6.3(b) and (c). In (b) we compare results for strong two level driving ($\kappa_b = 16/17$) and in (c) for moderate CPT ($\kappa_c = 5$). For both cases the agreement is good when comparing single site excitation probabilities, even more the correlation length of the density wave at the edges is well reproduced by our analytic solution.

Within the NN model and using CPT driving, correlation length can be tuned to arbitrary large values. If we take into account the long range tail of the interaction this restricts the maximum κ that is achievable for a given exponent α of the interaction potential. To ensure the validity of the model the blockade of atoms next to an excited atom should be strong, which is quantified by the ratio of next neighbor interaction to linewidth $\beta = V_{\mathrm{NN}}/\omega$. On the other hand an excited atom should not restrict dynamics on next next neighboring sites. The maximal κ under the influence of the long range tail is however

$$\kappa < \frac{\omega^2}{V_{\mathrm{NNN}}^2} = \frac{2^{2\alpha}\omega^2}{V_{\mathrm{NN}}^2} = \left(\frac{2^\alpha}{\beta}\right)^2. \tag{6.33}$$

Due to the Lorentzian shape of the excitation probability, large $\beta = 10$ is required to ensure that atoms next to an already excited atom are excited with probability less than one percent. In the case of DD interaction with $\alpha = 3$ the driving parameter is restricted to small values and the correlation length does not exceed one lattice site. For the much sharper vdW interaction however a realistic correlation length is given by $\xi \approx 7a$.

6.4 Time Scales

So far we discussed the stationary properties of the driven system but did not raise the question at what time scales these states are prepared. In Fig. 6.4(a) we show the time evolution of Rydberg state populations of individual atoms in a lattice with open boundary conditions under CPT driving. Parameters are chosen as in Fig. 6.3(c) and the steady state shows correlations over a length scale $\xi \approx 5a$. Initially, the atoms are in the ground state $|g\rangle$ and the the simplest protocol is to turn on all driving lasers for all atoms at $t = 0$ (red dashed lines). The excitation probability for all atoms rapidly increases on the single atom relaxation time scale $T_{\mathrm{eq}} = \Gamma_{eg}/(\Omega_{ge}\Omega_{er})$ but it does not approach the steady state value. Only on a second timescale, more than an order of magnitude slower, does the population for every atom relax towards its steady state value and the correlations between excitations are established.

The reason for this slow down is the fast initial formation of small ordered domains with dislocation defects. A simple example for a dislocation are two excitations with two ground state atoms in between. To heal such a defect one of the two has to be deexcited, which occurs on a longer time scale than the excitation process. For the specific example here, the rates are given by

$$\Gamma_\uparrow \approx T_{\mathrm{eq}}^{-1}, \quad \Gamma_\downarrow \approx T_{\mathrm{eq}}^{-1}/\kappa \approx T_{\mathrm{eq}}^{-1}/25. \tag{6.34}$$

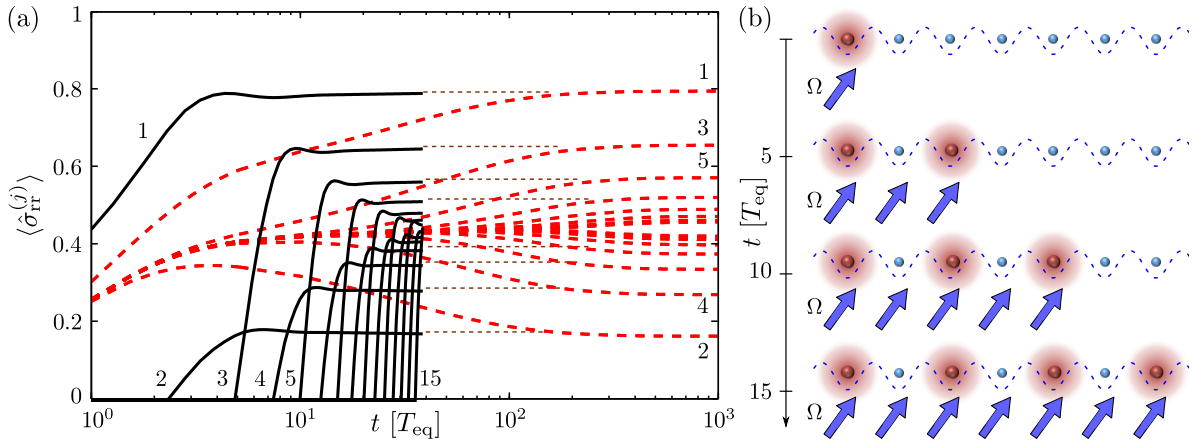

Figure 6.4: (a) Time evolution of excitation probability for a system of length $L = 15$ and parameters as in Fig. 6.3(c) obtained by Dominik Muth with TEBD. The time scale of relaxation is an order of magnitude different for the direct protocol (red dashed) and the growing protocol (black) explained in the text. (b) Growing scheme for a Rydberg excitation crystal. The sweeping rate of one site per $2.4T_{\rm eq}$ corresponds to the results in (a).

This order of magnitude difference between excitation and deexcitation rates is the origin of the two separate time scales we observe and the slow down of relaxation. Note that the relaxation time is independent of system size for $L \gg \xi$. Whereas it increases with ξ it does not diverge in one dimension as the correlation length is always finite.

The slow relaxation can be circumvented by growing the crystal from one edge on. In the present system with boundary conditions, the steady-state is unique and therefore independent of the initial conditions and the details of preparation [166], such as, e.g., the way the light fields are switched on. We propose the protocol illustrated in Fig. 6.4(b). Instead of applying the excitation lasers to all atoms beginning at $t = 0$, we first apply the lasers to the atoms at the lattice boundary ($j = 1$) and then successively extend the irradiated region ($j = 2, 3, \ldots$) until the full Hamiltonian is realized. In Fig. 6.4(a) we verify this intuitive approach (full black lines for atoms $j = 1, 2, \ldots, 15$) and show much faster preparation of the steady state. Since the crystalline order is rooted in the Rydberg blockade of the NN sites, a *sweep* velocity as fast as one lattice period a per single-atom equilibration time $T_{\rm eq}$ can be applied.

Conclusion

In this chapter we laid the foundation for much of the following discussion. First of all we introduced the driven Rydberg system as a an ideal candidate to study the non-equilibrium physics of strongly interacting systems. A good tool for discussing such systems is the rate equation model. This is especially true for the case discussed here, where we showed that in the limit NN blockade the model is analytically solvable.

Based on this solution we characterized the stationary state and identified fluctuations of Rydberg excitations as the limiting factor regarding the emergence of long range correlations that were predicted by mean field theories. We identified the single atom driving scheme as an important means of reducing fluctuations for example by using coherent population trapping of excited atoms. A central result is that we find no phase transition and the correlation length ξ is finite for all parameters.

Finally we considered the time scales of relaxation towards the stationary state and showed

their increase with increasing correlation length. Practically this problem can be circumvented by avoiding the creation of defects and employing crystal growing schemes in one dimension.

Chapter 7

Antiferromagnetic Order in 2D Dissipative Rydberg Lattices

Our discussion of the one dimensional Rydberg chain in the previous chapter exposed the failure of a mean field type treatment for this system. Instead of a long range ordered antiferromagnetic phase, we found only short range correlations in the stationary state. Moreover we showed that an infinitesimal amount of fluctuations leads to exponential decay of correlations, such that despite improved CPT driving no long range order emerges. One can however argue that mean field approaches are in general expected to be more accurate in higher dimensions. In this chapter we will discuss whether this is a valid claim and long range order as predicted by mean field is found in higher dimensions. The results of this discussion have been published in [H-2014a].

We will build upon the framework of rate equations established in the previous chapter and discuss in detail its two dimensional generalization. To begin with, consider the NN blockade model on a 2D rectangular lattice

$$L_{\mathrm{d}}^{(x,y)} = \hat{\sigma}_{\mathrm{gr}}^{(x,y)}, \tag{7.1}$$

$$L_{\mathrm{p}}^{(x,y)} = \sqrt{\kappa}(\hat{\sigma}_{\mathrm{rr}}^{(x-1,y)} - 1)(\hat{\sigma}_{\mathrm{rr}}^{(x+1,y)} - 1)(\hat{\sigma}_{\mathrm{rr}}^{(x,y+1)} - 1)(\hat{\sigma}_{\mathrm{rr}}^{(x,y-1)} - 1)\hat{\sigma}_{\mathrm{rg}}^{(j)}, \tag{7.2}$$

with x, y being the integer indices numbering the sites $x \in 1, \cdots, L_x$ and $y \in 1, \cdots, L_y$. The detailed balance solution we gave for the 1D problem previously, is actually a solution in any dimension. Again the stationary state is a mixture of all allowed states $\{s_{x,y}\}$, i.e. all states with no two excitations on adjacent sites, and the individual weight is given by Eq. (6.17). Many results in 1D could be derived from the analytic expression for the number of allowed states with given number of excitations. In two and higher dimensions such an expression does not exist and we must rely on exact calculations in small systems of size up to $L_x L_y \approx 16$ or stochastic methods for larger lattices. In Sec. 7.4 we will show that the detailed balance solution can be mapped to thermal states of hard sphere models on lattices, which have been extensively studied in the past [167]. It is well known that in the two dimensional NN model a phase transition occurs around $\kappa_{\mathrm{2D}}^{(C)} = 3.79$ and in three dimensions at $\kappa_{\mathrm{3D}}^{(C)} = 2.97$, classified by a breaking of the sublattice symmetry. The order parameter q

$$q = \left\langle \left| \sum_{x,y} (-1)^{x+y} \hat{\sigma}_{\mathrm{rr}}^{(x,y)} \right| \right\rangle \Big/ \left\langle \sum_i \hat{\sigma}_{\mathrm{rr}}^{(x,y)} \right\rangle \tag{7.3}$$

is a sensitive measure of this symmetry breaking. In the thermodynamic limit $L_x, L_y \to \infty$ it is exactly zero for $\kappa < \kappa^{(C)}$ and it is finite beyond the critical point. This critical driving

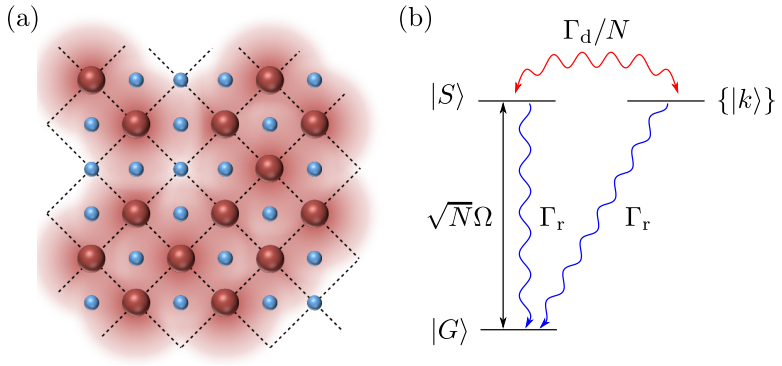

Figure 7.1: (a) Schematic illustration of the two dimensional driven Rydberg gas. In the displayed state sublattice symmetry is broken and only atoms on one sublattice are excited. (b) Reduced level scheme of the superatom in the Dicke representation.

corresponds to a filling of the lattice of $n_{2D}^{C} \approx 0.368$ [167].

If the individual sites of the lattice are occupied with single two level atoms, we have shown in Appendix 15.1 that $\kappa < 1$, thus even in higher dimensions our model does not yield a phase transition for two level atoms. We show that sophisticated driving schemes such as CPT or a superatom (SA) scheme are instead required to prepare an ordered stationary state. The excitation and deexcitation rates $\Gamma_{\uparrow,\downarrow}$ for the SA are derived in Sec. 7.1.

In Sec. 7.2 we account for long range interactions beyond the NN model and use Monte Carlo sampling methods to show that the long range ordered phase must then be stabilized by small laser detunings. We characterize the critical behavior of the system by extracting the static and dynamic critical exponents and find that both exponents fall into the Ising universality class. Whereas the universal properties are described within the Ising class, the stationary state is not the thermal state of a simple Ising model, which we show in the concluding Sec. 7.4.

7.1 The Superatom

The two level and CPT driving scheme employed in the previous chapter rely on the presence of exactly one atom at every site of the lattice. An empty site after preparation or the loss of an atom during excitation of the Rydberg states, immediately translates into an impurity for the Rydberg excitation crystal. Therefore we here propose an alternate driving scheme, the superatom (SA) [168].

Consider an small cluster of N two-level atoms at every site of the lattice, where one of the two levels is a strongly interacting Rydberg state. The distance between atoms is small within a cluster compared to the blockade radius and therefore at most one atom can be excited at a time. The single atom transition is driven with Rabi frequency Ω and is detuned by Δ

$$\mathcal{H} = \sum_{j=1}^{N} \left(\Omega \, \hat{\sigma}_{rg}^{j} \prod_{k \neq j} \hat{\sigma}_{gg}^{k} + h.c. \right) + \sum_{j=1}^{N} \Delta \hat{\sigma}_{rr}^{j}. \tag{7.4}$$

Additionally every excited atom has a finite lifetime and is subject to decoherence, formally described by the jump operators

$$\hat{L}_r^j = \sqrt{\Gamma} \hat{\sigma}_{gr}, \qquad \hat{L}_d^j = \sqrt{\Gamma_d} \hat{\sigma}_{rr}. \tag{7.5}$$

The Hamiltonian is diagonalized in the basis of symmetric Dicke states

$$|G\rangle = |0\rangle, \qquad |R\rangle = \frac{1}{\sqrt{N}} \sum_{j=1}^{L} \hat{\sigma}_{rg} |G\rangle, \tag{7.6}$$

$$\mathcal{H} = (\sqrt{N}\Omega |R\rangle\langle G| + h.c.) + \Delta |R\rangle\langle R|. \tag{7.7}$$

No coherent process couples the symmetric and non-symmetric sector and therefore no coherence is build up. Because we eliminated all states with more than one excitation due to the strong blockade within the small cluster, $\mathcal{H}$ does not affect the non-symmetric sector. We must only consider the decay of excitation into $|G\rangle$ and the backscattering due to decoherence into the symmetric excited state $|R\rangle$. We replace the manifold of $N-1$ non-symmetric states with a single representative A. For the coherence between collective ground and symmetric excited state we find

$$\frac{d}{dt}\varrho_{GR} = i\sqrt{N}\Omega(\varrho_{RR} - \varrho_{GG}) + i\Delta\varrho_{GR} - \gamma\varrho_{GR}, \tag{7.8}$$

with the coherence loss rate $\gamma = (\Gamma + \Gamma_{\mathrm{D}})/2$. Upon adiabatic elimination of the coherence we find

$$\varrho_{GR} = \frac{i\sqrt{N}\Omega(\gamma + i\Delta)}{\Delta^2 + \gamma^2}(\varrho_{RR} - \varrho_{GG}). \tag{7.9}$$

We substitute this in the dynamic equation for ϱ_{GG} and ϱ_{SS} and a three level system described by purely classical rate equations remains. The excitation rate between G and R is given by

$$\chi = \frac{2N\gamma\Omega^2}{\gamma^2 + \Delta^2}, \tag{7.10}$$

thus the full system reads

$$\frac{d}{dt}\begin{pmatrix}\varrho_{GG}\\ \varrho_{RR}\\ \varrho_{AA}\end{pmatrix} = \begin{pmatrix}-\chi & \chi + \Gamma_r & \Gamma_r\\ \chi & -\chi - \Gamma_r - \Gamma_d\frac{N-1}{N} & \Gamma_d\frac{1}{N}\\ 0 & \Gamma_d\frac{N-1}{N} & -\Gamma_r - \Gamma_d\frac{1}{N}\end{pmatrix}\begin{pmatrix}\varrho_{GG}\\ \varrho_{RR}\\ \varrho_{AA}\end{pmatrix}. \tag{7.11}$$

By solving the matrix for its null eigenvector and the smallest eigenvalue away from zero, we retrieve the exact steady state excitation probability and the slowest time scale at which this steady state is approached,

$$\varrho_{RR} + \varrho_{AA} = \varrho_R = \frac{4N(\Gamma_r + \Gamma_d)\Omega^2}{\Gamma_r((\Gamma_r + \Gamma_d)^2 + 4\Delta^2) + 4(\Gamma_d + N\Gamma_d + 2N\Gamma_r)\Omega^2} \tag{7.12}$$

$$\Gamma_{\uparrow}(\Delta) = -\varrho_R T_r, \qquad \Gamma_{\downarrow}(\Delta) = (\varrho_R - 1)T_r. \tag{7.13}$$

In the limit of strong dephasing and large number of atoms per cluster the excitation probability is given by a Lorentzian $\varrho_R \approx p_0/(1 + \Delta^2/\omega^2)$ with

$$p_0 = \frac{1}{1 + \Gamma_r/(\Gamma_r + \Gamma_d) + 1/N}, \qquad \omega = \sqrt{N}\Omega\sqrt{\Gamma_d/(\Gamma_r + \Gamma_d)}. \tag{7.14}$$

In terms of the NN model driving parameter the superatom yields

$$\kappa \approx [(1/N + \Gamma/(\Gamma + \Gamma_d)]^{-1} > \min[N, \Gamma_{\mathrm{d}}/\Gamma + 1], \tag{7.15}$$

which can be tuned into the critical regime $\kappa > \kappa_{2\mathrm{D}}^{\mathrm{C}}$ by increasing the number of atoms per

cluster and the ratio of decoherence and population loss Γ_d/Γ.

The described SA lattices can be realized with magnetic or optical micro trap arrays [169, 170, 171] that accommodate $N \approx 10 \ldots 100$ atoms per site and provide lattice constants of a few μm, for which strong NN interactions can be obtained. An alternative realization of SAs by preparation from ultracold ensembles is discussed in [H-2014c] and will the topic of Chapter 9.

7.2 Phase Diagram for Long Range Interaction

For the one dimensional chain we argued that we can choose the NN interaction V_NN large compared to the linewidth ω, while interaction to the next closest neighbor V_NNN is negligibly small compared to the linewidth. In two and higher dimension however, the ratio $V_\mathrm{NN}/V_\mathrm{NNN} = 2^{\alpha/3}$, with the exponent α of the interaction, scales much worse. Even for vdW interaction ($\alpha = 6$), the ratio is 1/8 instead of 1/64 in one dimension and we must question the results of the NN model.

When taking into account the tail of the interaction in the rate equations, the easy to evaluate detailed balance solution in Eq. (6.17) is no longer correct. Exact solution is non feasible for systems with $L_x L_y > 16$ and we have used two kinds of Monte Carlo (MC) algorithms to sample the stationary state of the many body rate equations for systems up to size $L_x L_y = 22500$. The two variants of MC are dynamic MC (dMC) and stationary state MC (ssMC). Both are introduced in appendix 15.2 and their individual advantages are discussed. To clarify the significance of the NN-approximation, Wildan Abdussalam has performed ssMC simulations for resonantly driven atoms and varying exponent α of the interaction, which are presented in Sec. 7.2.1. One recognizes hat for realistic interaction potentials ($\alpha \leq 6$) the order parameter q vanishes in thermodynamic limit. In Sec. 7.2.2 we will discuss that an off-set detuning of the excitation scheme is required to stabilize the long range ordered phase.

7.2.1 Resonant excitation

In the limit of pure and strong next neighbor interaction $\alpha \to \infty, V_\mathrm{NN}/\omega \gg 1$ the phase transition to long range order in two dimensions occurs at $\kappa_\mathrm{2D}^\mathrm{C} = 3.79$. In Fig. 7.2(a) we show results for the order parameter q from ssMC with $\kappa_0 = 20$ and $V_\mathrm{NN}/\omega = 5$ with a power-law interaction potential of exponent α. As expected, in the limit of large exponent α the order parameter is nonzero. From finite size extrapolation of results with $L = 30, 60, 150$ we find a sharp transition in the thermodynamic limit at $\alpha \approx 11$.

We estimated a realistic κ including the effects of long range interaction for the 1D system in Eq. 6.33. A modified version, which takes the couplings along the diagonal into account yields a sharper bound

$$\kappa < \frac{\omega^2}{V_\mathrm{NNN}^2} = \frac{2^\alpha \omega^2}{V_\mathrm{NN}^2} = \left(\frac{2^{\alpha/2}}{\beta}\right)^2 \tag{7.16}$$

for κ. Assuming again $\beta = V_\mathrm{NN}/\gamma = 10$ we find that $\alpha > 8.5$ is required for a larger than critical driving. We have neglected the blockade effects of multiple excited atoms and therefore the bound is lower than the numeric result, but already precludes the emergence of order for vdW interacting atoms.

7.2.2 Phase diagram with offset detuning

We have to consider one more control parameter to stabilize the long range order with vdW interaction and this is the detuning of the excitation scheme from resonance for the individual

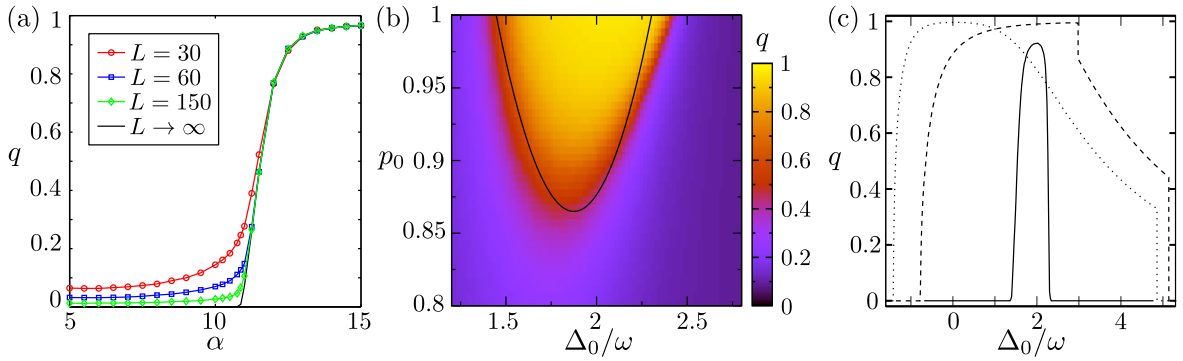

Figure 7.2: (a) Order parameter q as a function of the power-law exponent α, for $\kappa_0 = 20$, $V_{\rm NN} = 5\omega$ and resonant driving $\Delta_0 = 0$. Symbols show results for finite system sizes given in the legend. The thick solid line shows the extrapolation to the thermodynamic limit, $L \to \infty$. (b) Order parameter as a function of p_0 and off-set detuning Δ_0 for a finize size system with $L = 30$. (c) For a fixed $p_0 = 0.96$ and $V_{\rm NN} = 5\omega$, we compare the numeric results (solid) to mean field predictions for NN-interactions (dotted line) and full vdW interaction (dashed line).

atom. An off-set detuning Δ_0 hinders the initial excitation of atoms, but cancels the effect of the interaction tail when the density of excitations is large. This is demonstrated in Fig. 7.2(b), showing the order parameter q for finite detunings and a varying p_0 and $V_{\rm NN}$, where p_0 is the excitation probability is of a single atom subject to driving with κ_0

$$p_0 = \frac{\kappa_0}{1+\kappa_0} \approx 1 - \kappa_0^{-1}. \tag{7.17}$$

Néel-type ordering emerges within a finite detuning range and for $\kappa_0 \approx 6 > \kappa_{\rm 2D}^{(C)}$, slightly larger than the threshold in the NN-blockade model [167]. If the next neighbor interaction $V_{\rm NN}$ is chosen such that $10 > V_{\rm NN}/\omega > 1$ numeric simulation show that an interval of off-set detunings exists, such that the stationary state is long range ordered.

The location of the transition can be understood as follows: A Néel state is characterized by a macroscopic population imbalance on the two sublattices with lattice constant $\sqrt{2}a$. Assuming that an atom on the highly populated sublattice has an average of z next nearest neighbors excited, the laser detuning must compensate the corresponding level shifts such that the reduced

$$\kappa = \kappa_0/[1 + (1+\kappa_0)(\Delta/\omega - zV_{\rm NN}/8\omega)^2/\omega^2] \geq \kappa_{\rm 2D}^{\rm C}, \tag{7.18}$$

with $z \approx 3$ near the crystallization transition. The parameter region where this condition is fulfilled is marked in Fig. 7.2(b) and qualitatively reproduces our numerical results.

Fig. 7.2(c) shows the order parameter as a function of offset detuning Δ_0 in the thermodynamic limit, indicating a second order phase transitions into and out of the ordered phase with increasing Δ_0/ω. In order to quantitatively assess the importance of fluctuations and the shape of the interaction potential, Fig. 7.2(c) also gives a comparison to mean field results under the NN-approximation [172, 173] and for full vdW interactions. Both cases give qualitatively different predictions, suggesting Néel order at negative detunings and a first order transition to the reentrant disordered phase at $\Delta_0 > 0$.

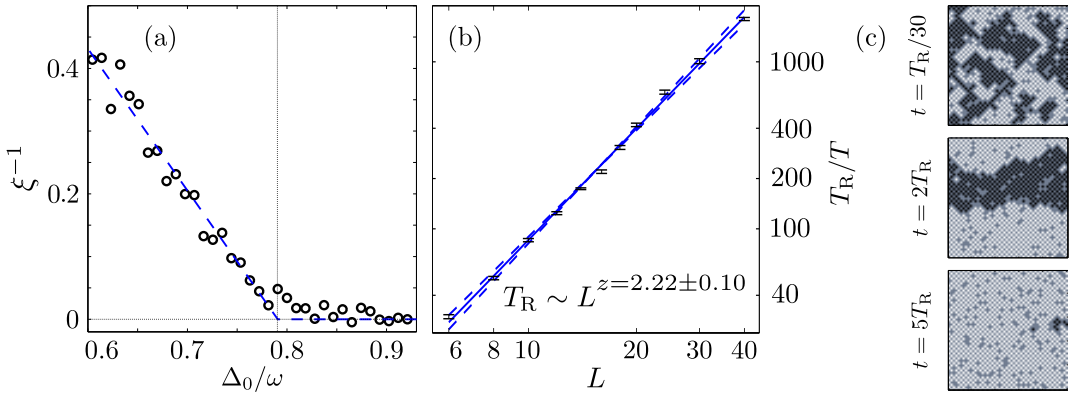

Figure 7.3: Characterization of the phase transition to long range order. (a) displays results for the correlation length of spin-spin correlations in both the disordered and ordered phase. Whereas $\xi \to \infty$ for sufficient offset detuning, we can extract the static critical exponent $\nu \approx 1$ from the divergence for $\Delta_0 < \Delta_c$. The dynamic exponent $z \approx 2.22$ is obtained by quantitative analysis of the divergent relaxation time within the ordered phase shown in (b). (c) illustrates the emergence of large scale domain wall dynamics that give rise to the slow relaxation.

7.3 Critical Exponents of the Phase Transition

After identification of the ordered phases in the previous section with the order parameter q that is sensitive to the global breaking of sublattice symmetry, we now further characterize the phase transition via its static and dynamic properties.

7.3.1 Correlation length

We analyze the MC data with respect to the length of correlations between Rydberg excited atom, which we define as

$$C_d = \frac{1}{L^2} \sum_{x,y} \left[\langle \hat{\sigma}_{\mathrm{rr}}^{(x,y)} \hat{\sigma}_{\mathrm{rr}}^{(x+d,y)} \rangle - \langle \hat{\sigma}_{\mathrm{rr}} \rangle^2 \right] \tag{7.19}$$

with distance d along the x axis and $\langle \hat{\sigma}_{\mathrm{rr}} \rangle$ the mean excitation probability. Numeric simulations are performed on square lattice systems with periodic boundary conditions and linear length L. If the stationary state is long range ordered, only atoms in one sublattice are excited with large probability p_0, and we expect a correlation function of constant amplitude $C_d = (-1)^d \frac{p_0^2}{4}$. For a non ordered system we instead expect exponentially decaying correlations of the form

$$C_d \approx A(-1)^d e^{-d/\xi}, \tag{7.20}$$

where A is a constant prefactor and ξ is the correlation length that diverges near the phase transition. We calculate C_d for different sizes of lattices $L = 10, 20, 30, 40$ and fixed $V_{\mathrm{NN}}/\omega = 2.97, \kappa_0 = 9$ and vary the offset detuning $\Delta_0/\omega \in [0.6, 0.95]$ across the identified phase transition. In the small systems we consider, we can not consider the limit of large d but must restrict to shorter ranges of distances. We here choose $d \leq L/4$ for our analysis and extract the correlation length for different system sizes. The inverse correlation length extrapolated to thermodynamic limit, $L \to \infty$, displayed in Fig. 7.3(a) shows the expected divergence. For the non equilibrium transition steady state discussed here, the static exponent is found to be $\nu = 1.0 \pm 0.1$. This is in agreement with results for the two dimensional Ising model in

equilibrium [174] and already points towards a connection with these models. We will later return to this point.

7.3.2 Dynamical slow down

Our discussion of criticality in free fermion models in Chapter 5 revealed the connection of a divergent correlation length with a divergent relaxation time towards the stationary state. Again in the one dimensional system of driven Rydberg atoms we found a slow down of relaxation with an increase in the range of correlations. A very loose connection between this static property and the dynamic relaxation is already imposed by the presence of a finite speed of correlation propagation [175]. If non local correlations are absent in the initial state, only sites within light cone of finite size can become correlated, within a finite amount of time. For the two dimensional model, within the long range ordered phase the relaxation time must therefore scale at least as

$$T_{\mathrm{R}} \geq \mathcal{O}(L^1), \tag{7.21}$$

with the linear system size L. In the following we will rely on the results from dMC to extract the quantitative relaxation behavior and determine the correct dynamical exponent z for our model.

Using dMC we have access to the full time evolution and we extract the relaxation time from the asymptotic approach of the Neel order parameter $q(t)$ to its steady state value. To reliably extract the relaxation time one must take into account the inherent fluctuations of the order parameter for a finite number of Monte Carlo trajectories N_{MC}. Furthermore q is a self averaging quantity with increasing system size, such that the increased cost of individual trajectories is counteracted by the need for less trajectories

$$\frac{\Delta_q}{q} \approx \frac{1}{\sqrt{N_{\mathrm{MC}} L}}. \tag{7.22}$$

For our analysis we only consider data in the interval $0.05 > |q(t) - q_\infty| > 50\Delta_q$, where the relaxation is exponential and the signal to noise ratio is sufficiently large. In Fig. 7.3(b) we show results for systems of linear size $L = 6$ to $L = 40$. The log-log scale reveals the algebraic relation and the scaling of relaxation time defines the dynamical critical exponent of the model

$$T_{\mathrm{R}} \sim L^{z=2.22\pm0.10}, \tag{7.23}$$

which is notably a much larger exponent than expected from the simple Lieb-Robinson bound argument. Note that in thermodynamic limit the dynamical exponent is defined via the scaling of the relaxation time with the correlation length

$$T_{\mathrm{R}} \sim \xi^{z=2.22\pm0.10}. \tag{7.24}$$

Domain wall dynamics

An intuitive explanation for this exponent becomes apparent from the snapshots shown in Fig. 7.3(c), which display the state of a single MC trajectory at three times of the relaxation towards stationary state. Sites in the ground state are gray, excitations are white or black according to an underlying checkerboard. All atoms are initialized in the ground state. Shortly after switching on the driving Ω local order emerges and small domains of “black“ and “white“ form. The microscopic dynamics of excitation/deexcitation gives rise to slow domain wall dynamics on larger length scales than the blockade radius. General trajectories in our system

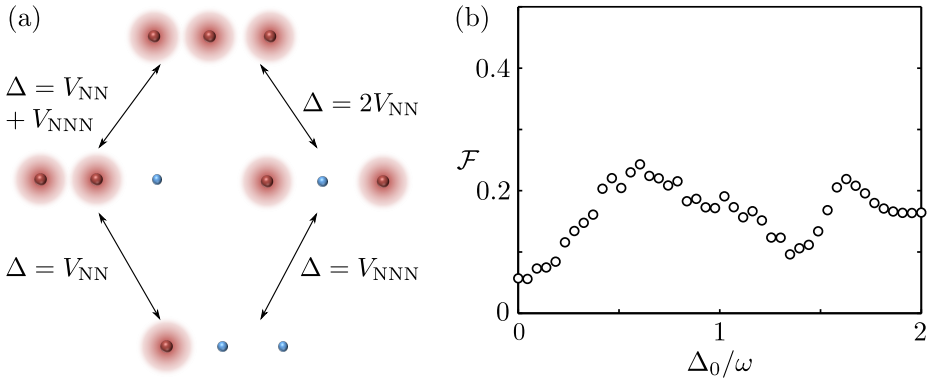

Figure 7.4: (a) Small subset of the many body rate equations to illustrate the broken detailed balance. (b) Trace norm distance $\mathcal{F}$ of the steady state to a thermal state of an Ising model with optimized values of β, h and V_{ij} (cf. Eq. (7.26)) for a 4×4 lattice with periodic boundary conditions and $\alpha = 6, p_0 = 0.9, V_0/\omega = 2.97$.

with periodic boundaries will go through a stage of two similar sized domains and eventually turn either white or black, spontaneously breaking the discrete sublattice symmetry. The split of the system in two parts is the slowest decaying "excitation". In order to form a single domain the domain walls have to touch. The initial distance is at most $L/2$ and the relative motion behaves like a 1D random walk. This diffusive behavior alone explains a dynamical exponent of $z_{\mathrm{diff}} = 2$, close to the observed value of $z = 2.22 \pm 0.10$. Again this value is in agreement with results on kinetic Ising models discussed before in [176, 177].

7.3.3 The Ising iniversality class

A hallmark result of statistical mechanics is the concept of universality classes. The scaling of free energy at a phase transition only depends on the symmetries of the problem and therefore very different physical systems may have similar behavior due to the underlying symmetries. The Ising universality class is a paradigmatic example and a representative is given by the classical Ising Hamiltonian

$$\mathcal{H}_{\mathrm{Ising}} = h \sum_{x,y} \hat{\sigma}_z^{(x,y)} + \sum_{x,y} \sum_{x',y'} V_{x,y,x',y'} \hat{\sigma}_z^{(x,y)} \hat{\sigma}_z^{(x',y')}. \tag{7.25}$$

For members of this universality class a critical exponent of correlation length $\nu_{\mathrm{Ising}} = 1$ is expected and found in equilibrium physics [174], which can be derived from the exact solution of Onsager [178]. The same exponent we determined here for the non equilibrium situation of a driven Rydberg gas. Furthermore our results for the dynamical critical exponent are compatible with results for kinetic Ising models, notably without power-law interaction [176, 177]. The observed dynamical properties are very similar to those of model A in the classification scheme of equilibrium critical dynamics of Hohenberg and Halperin [179].

7.4 Non Thermality

The effects of power-law interactions as well as of the dissipative nature of the phase transition can be illuminated by direct comparison of the steady state $\bar{\varrho}$ to thermal equilibrium states.. In the limit $\alpha \to \infty$, the rate equations fulfill detailed balance conditions and $\bar{\varrho}$ coincides with

the thermal state of an Ising model

$$\varrho_{\rm Is} = \frac{1}{Z}\exp\Big\{-\beta\Big[h\sum_j \hat{\sigma}_j^z + \sum_{i<j} V_{i,j}(\hat{\sigma}_i^z + \frac{1}{2})(\hat{\sigma}_j^z + \frac{1}{2})\Big\}, \tag{7.26}$$

where $\hat{\sigma}_i^z = \hat{\sigma}_{\rm ee}^{(i)} - 1/2$, if $V_{i,j} \to \infty$ for next neighbors and zero otherwise, and $\beta h = \ln\frac{1-p_0}{p_0}$. Such a correspondence no longer holds in the case of power law interactions, for which one can show that the rate equations do not satisfy detailed balance. Consider the small subset of configuration space for three atoms shown in Fig. 7.4(a). Using the rates of excitation and deexcitation in Eq. (7.13) we can consider the detailed balance solution to the ratio of probabilities for all atoms excited and only the leftmost atom excited $\alpha = p_{111}/p_{100}$. If we consider the left path we find

$$\alpha_{\rm L} = \frac{\Gamma_\uparrow(V_{\rm NN})\Gamma_\uparrow(V_{\rm NN}+V_{\rm NNN})}{\Gamma_\downarrow(V_{\rm NN})\Gamma_\downarrow(V_{\rm NN}+V_{\rm NNN})} = \frac{1}{[1+V_{\rm NN}^2/\omega^2][1+(V_{\rm NN}+V_{\rm NNN})^2/\omega^2]}. \tag{7.27}$$

Following the right path yields

$$\alpha_{\rm R} = \frac{1}{[1+V_{\rm NNN}^2/\omega^2][1+(2V_{\rm NN})^2/\omega^2]}, \tag{7.28}$$

which in general is different from $\alpha_{\rm L}$. The notable exception is given $V_{\rm NN} \to \infty$, the NN model.

To demonstrate that thermal states of Ising models $\varrho_{\rm T}$ do not capture the non equilibrium steady state $\bar{\varrho}$, we considered an optimization regarding the trace norm distance

$$\mathcal{F}(\varrho_{\rm T}, \varrho) = \frac{1}{2}\sum_s |\varrho_{{\rm T},s} - \bar{\varrho}_s|, \tag{7.29}$$

which can be used to bound the difference of expectation values in both states

$$|\langle\hat{A}\rangle_T - \langle\hat{A}\rangle| < ||\hat{A}||\mathcal{F}(\varrho_{\rm T}, \varrho). \tag{7.30}$$

One can show that for two random density matrices the trance norm distance is given by $\mathcal{F} = 1/2$. Be $N \gg 1$ the number of states, then the weights of random density matrices X, Y are Poisson distributed with mean $1/N$. Therefore we find

$$\mathcal{F}(X,Y) = \frac{N^3}{2}\int_0^\infty dy \int_0^\infty dy|x-y|e^{-N(x+y)} \tag{7.31}$$

$$= N^3\int_0^\infty dy\int_0^x dy(x-y)e^{-N(x+y)} \tag{7.32}$$

$$= 1/2. \tag{7.33}$$

We here considered Ising models with external field h and couplings to next neighbors $V_{\rm NN}$ and next next neighbors $V_{\rm NNN}$. We used exact calculations for the stationary state in systems of size 4×4 with periodic boundary conditions and optimized the parameters of the thermal model with respect to the trace norm distance. The results of this optimization are shown in Fig. 7.4(b) as a function of the detuning Δ_0 across the phase transition. $\mathcal{F}$ is consistently below 0.5 and therefore the thermal state is an improvement compared to random states. However overall agreement is only on the order of 0.1-0.2 and therefore the thermal states do not describe the specific steady states, although they fall into the Ising universality class

regarding the critical exponents of the phase transition.

Conclusion

In this chapter we have shown that two dimensional lattice gases can undergo a dissipative phase transition towards a state of long range order Rydberg excited atoms. Mean field predictions for this transition were shown to be qualitatively wrong and we showed that the preparation of ordered states, requires excitation schemes like CPT or superatoms that go beyond the possibilities of a single two level atom. Furthermore we showed that a finite off set detuning is required for the case of vdW interacting atoms to compensate the effects of the long range tail.

The analysis of spin-spin correlations regarding the correlation length ξ and relaxation time T_R of the order parameter were used to determine the critical exponents of the steady state phase transition

$$\xi = |\Delta_0 - \Delta_C|^{\nu=1.0\pm0.1}, \tag{7.34}$$

$$T_{\mathrm{R}} \sim \xi^{z=2.22\pm0.10}. \tag{7.35}$$

The static and dynamic critical exponent ν and z are in accordance with the two dimensional Ising universality class. Dynamic Ising models have been further classified as model A systems within the theory of dynamical critical phenomena [179] and it would be interesting to reveal further similarities or deviations between the model we consider and this class.

The stationary state of the NN model is equivalent to the thermal state of a simple, classical Ising model. Similar relations to thermal states have been identified before to describe quasi stationary states for unitary Rydberg systems [180]. As we did for the NN model, the authors did not take into account the tail of the interaction potential and instead considered a perfect blockade for atoms within a finite distance. We here showed, that the inclusion of the real vdW potential breaks the relation between the stationary state and thermal states of Ising models and it would be interesting to investigate, whether this statement holds for earlier studies on thermalization in Rydberg systems.

Chapter 8

Driven Rydberg Continuum Systems

The preparation of long range ordered Rydberg excitations in a two dimensional lattice is a nice example of a non equilibrium phase transition in the stationary state. However, even more ambitious is the preparation of a true crystal of excitations in the absence of an underlying lattice. Furthermore the controlled geometry of a lattice only permits certain distances of atoms and therefore only parts of the interaction potential are probed. This is used, when introducing approximations such as the NN blockade for the vdW potential and the resulting models often are amenable to exact solutions [181][H-2013a]. In contrast, for continuum systems the complete interaction potential is probed and the number of atoms is typically much larger than in lattices. Introducing and validating good approximations and developing numerical techniques for these systems is therefore an important challenge.

One additional reason for the study of continuum systems is, that they are the natural experimental approach towards Rydberg physics. First experiments by Singer et al. showed the effects of vdW interaction in cold atomic vapors by spectral broadening of the Rydberg line [182, 183] and soon thereafter a theoretical approach using rate equations for the excitation dynamics was developed [184]. This approach is closely related to our methods and has been adopted by others as well [185, 186].

The saturation behavior of the density of Rydberg excitations was theoretically studied using mean field calculations in a fully unitary model [187] and experimentally confirmed by Löw et al. [188]. Continuous Rydberg gases can not only be studied with ultra cold atoms but also in hot thermal vapors as shown by Baluktsian et al. [189]. The dynamic behavior of the number of excited atoms and the onset coherent Rabi oscillations were demonstrated in [190], whereas multiple period Rabi oscillations were realized using post selection in [191].

Theoretical study of long range spatial correlations was first addressed in [187] and Schwarzkopf et al. demonstrated the use of accurate ion optics to extract spatial correlations of excited atoms after field ionization [192]. As discussed in the introduction to driven lattice models, two perspectives have been considered regarding the preparation of a Rydberg excitation crystal. First of all the one can try to adiabatically prepare this crystal as the ground state of a Hamiltonian [162]. This approach is only feasible, when the time scales required for adiabatic following are short compared to typical dissipation rates. The second approach is to employ the competition between coherent excitation and dissipation, to prepare a correlated stationary state. Such a correlated state could enable the creation of a low temperature plasma in the regime of strong coupling [193].

Schauss et al. were able to demonstrate the emergence of spatial correlations between

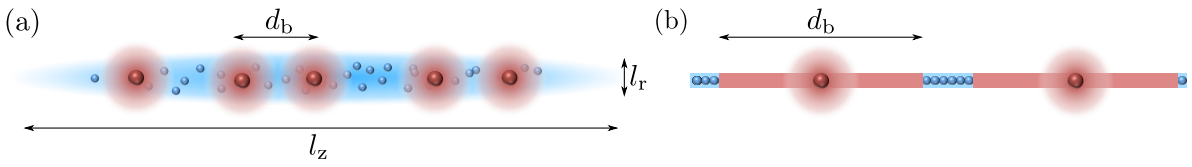

Figure 8.1: (a) Rydberg excitation in dense atomic clouds with an elongated cigar shape such that the radial extension is small compared to the blockade radius $d_\mathrm{b} \gg l_\mathrm{b}$ but multiple excitations can be spread along the long axis $d_\mathrm{b} \ll l_\mathrm{z}$. Our analytic description relies on the lattice representation (b) and an approximation of the interaction potential as hard rod like.

excitations using single site resolution microscopy [194]. They used two dimensional Mott insulators of unit filling, with a lattice spacing $a \approx 0.5$ μm and excited Rydberg states with a blockade radius of $d_\mathrm{b} \approx 5$ μm and therefore in the continuum regime. Whereas the original interpretation of the experiment was in terms of the energy spectrum, it was shown that experimental results are also in agreement with results of an incoherent rate equation simulation [195]. Due to the finite extend of the initial Mott insulator, only short range hexagonal order of excitations could be demonstrated.

We here focus on the emergent spatial correlation in extended one dimensional systems taking into account the tail of the vdW interaction. Similar systems have been considered before, however only for short systems of few blockade radii length [196], or approximate interaction potentials in the absence of dissipation in [197]. To begin with, we generalize the NN rate equation model to large blockade radii [198] and show that the exact solution in the continuum limit is identical to the thermal state of the well known hard rod gas [199, 200]. Based on previous results for this model, we characterize the spatial correlations that emerge between Rydberg excitations. Whereas truncation of the interaction potential to next neighbors is well motivated in lattice systems, it is a rough truncation in the quasi continuous scenario discussed here. We therefore employ the established MC algorithms to study the effect of soft Dipole-Dipole and vdW interactions and compare the results to the analytic hard rod predictions. This discussion is based on the publication [H-2013b] and we conclude the chapter by considering the case of higher dimensional hard sphere models and the implications for Rydberg systems.

8.1 Hard Rod Model

We begin by reconsidering the idealized NN model in chapter 6 and generalize it for dense and continuous systems. By our definition of a dense system the blockade radius is much larger than the average distance between adjacent atoms $d_b \gg 1/\varrho_\mathrm{at}$. Instead of the random distribution of atoms in a real gas, we use an equidistant chain of atoms, with lattice constant $a = \varrho_\mathrm{at}^{-1}$, that approximates a homogeneous density distribution. We introduce the number of atoms within the blockade radius $N_\mathrm{b} = \lfloor d_\mathrm{b} \varrho_\mathrm{at} \rfloor$.

We gain analytic insight by studying the problem of step like interaction potentials first, such that an excitation perfectly blocks further excitations within the blockade radius but does not influence dynamics at further distances directly. Under these conditions we can

again map the dynamics to a classical rate equation model

$$L_{\mathrm{d}}^{(j)} = \hat{\sigma}_{\mathrm{gr}}^{(j)}, \tag{8.1}$$

$$L_{\mathrm{p}}^{(j)} = \sqrt{\kappa}\hat{\sigma}_{\mathrm{rg}}^{(j)} \prod_{j'=j-N_{\mathrm{b}}}^{j+N_{\mathrm{b}}} (\hat{\sigma}_{\mathrm{rr}}^{(j')} - 1). \tag{8.2}$$

In this chapter we focus on atoms driven with a simple two level scheme, such that the driving parameter is on the order of one $\kappa \approx 1$. For the 1D lattice problem we showed that a CPT excitation scheme yields $\kappa \gg 1$, however benchmarking simulations for small number of atoms showed, that a rate equation treatment in continuum systems is only valid in the presence of strong decoherence γ, which renders the coherent trapping of population in the Rydberg state ineffective.

The stationary state is the identical detailed balance solution as in Eq. 6.17, with the difference that allowed states now only have excitations at a minimum distance of N_{b}. The number of possible configurations for P excitations on chain of length L is still analytically solvable

$$N(P, L, l_{\mathrm{b}}) = \binom{L - N_{\mathrm{b}}(P-1)}{P}, \tag{8.3}$$

an analytic expression for the partition function is however not known. For large systems the function $\kappa^P N(P, L, N_{\mathrm{b}})$ is a highly peaked function of P and by solving for its maximum we find

$$\varrho_{\mathrm{ex}} = \frac{\langle P \rangle}{L} = \frac{1}{d_{\mathrm{b}}} \frac{W(\eta)}{1 + W(\eta)}, \tag{8.4}$$

where $\eta = \kappa N_{\mathrm{b}}$ and $W(\eta)$ is the Lambert function defined via $We^W = \eta$. For $\eta \gg 1$ the density approaches $\varrho_{\mathrm{ex}} \to d_{\mathrm{b}}^{-1}$, which is the maximum filling fraction.

8.1.1 Equivalence to thermal continuum hard rods

The partition function for a fixed number of excitations P with minimum distance N_{b} on a lattice of length L can be written as a sum over all possible configurations

$$Z_P = \frac{1}{P!}\kappa^P \sum_{j_1,\cdots,j_P} \prod_{m,n} \Theta(|j_m - j_n| - N_{\mathrm{b}}). \tag{8.5}$$

We now approximate the sum by an integral in the continuum limit

$$\begin{aligned} Z_P &\approx \frac{1}{P!}(\kappa\varrho_{\mathrm{at}})^P \iint_0^{l_z} dz_1 \cdots dz_P \prod_{m,n} \Theta(|z_m - z_n| - d_{\mathrm{b}}) \\ &= \frac{1}{P!}(\kappa\varrho_{\mathrm{at}} d_{\mathrm{b}})^P \iint_0^{l_z/d_r} dx_1 \cdots dx_P \prod_{m,n} \Theta(|x_m - x_n| - 1) \\ &= \frac{1}{P!}(\kappa\varrho_{\mathrm{at}} d_{\mathrm{b}})^P \iint_0^{l_z/d_r} dx_1 \cdots dx_P \prod_{m,n} e^{-u(x_m - x_n)}, \end{aligned} \tag{8.6}$$

with a hard rod pair potential $u(d) = \infty \cdot \Theta(d - d_{\mathrm{b}})$ and rods of length d_{b}. We introduced a rescaled coordinate $x = z/d_{\mathrm{b}}$ to simplify the notation from here on. In the continuum limit the stationary state of the non equilibrium model is identical to the thermal state of a hard rod gas with chemical activity [199]

$$\eta = \kappa\varrho_{\mathrm{at}} d_{\mathrm{b}}. \tag{8.7}$$

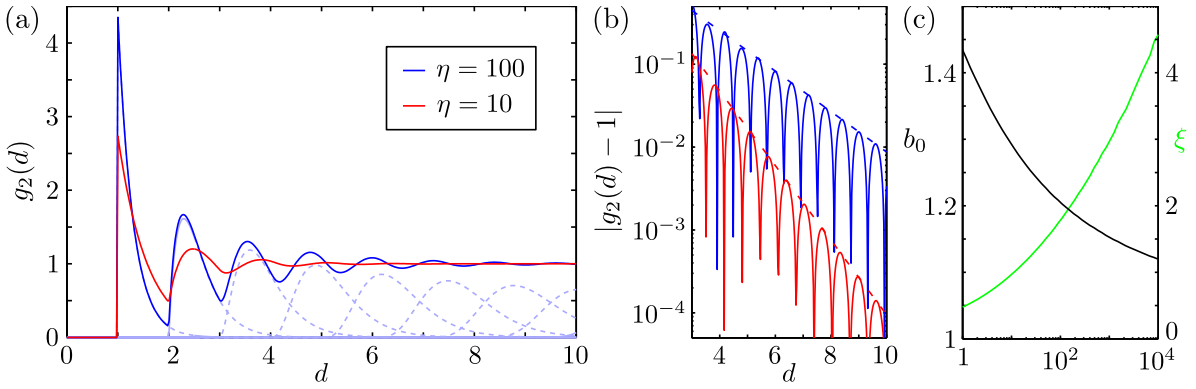

Figure 8.2: Second order correlation function $g_2(d)$ as a function of distance between hard rod centers for two different parameters of the chemical activity η. For the larger η we have added the individual terms in the sum in Eq. (8.8) in (a) to illustrate the distribution of consecutive neighbors. In (b) we show the exponential decay of oscillations at large separations d and have added the semi analytic fits for the decay of amplitude (dashed). The results for oscillation period b_0 and correlation length ξ from numeric solution of Eq. (8.21) are displayed in (c).

The dissipation free time evolution of the continuously driven gas has been studied before by Ates et al. [197]. Similar to our derivations so far, they considered interactions between Rydberg excited atoms of hard rod type. Whereas the dynamic evolution of this system does not relax towards a mixed stationary state, they showed that expectation values are reproduced by a microcanonical maximum entropy state. In terms of our dissipative system, this state corresponds to the choice of $\kappa = 1$, where all configurations, which are not blocked by the hard rod constraint, are equally populated.

A formal expansion of second order correlation functions is given by [200]

$$g_2(x) = \varrho_{\mathrm{ex}}^{-1} e^{-W(\eta)x} \sum_{n=1}^{\infty} \left[\frac{(x-n)^{(n-1)} \eta^n}{(n-1)!} \Theta(x-n) \right]. \tag{8.8}$$

In Fig. 8.2 we display the correlation function for two values of η. The hard rod constraint enforces $g_2(x) = 0$ for $x < 1$ and the largest probability density is found at the position $x = 1_+$. The first term in (8.8) decays exponentially and characterizes the probability distribution for the distance to the next closest excitation. Indeed, the nth term in the sum (8.8) corresponds to the nth closest neighbor distance distribution. In Fig. 8.2(a) we have indicated the individual terms with dashed lines. Note the broadening of the individual distributions that is responsible for the relaxation of $g_2(x)$ towards 1 at large distances.

8.1.2 Asymptotic decay of correlations

The analytic expression for $g_2(x)$ in Eq. (8.8) does not yield immediate insight into the behavior of correlations at large distances. Therefore we will derive analytic expressions for the oscillation period and correlation length that govern the asymptotic behavior of correlations

$$g_2(x) \approx 1 + e^{-\frac{x}{\xi}} \cos\left(2\pi \frac{x}{x_0}\right). \tag{8.9}$$

By differentiating $g_2(x)$ and introducing an index shift for the sum we find the differential equation

$$\frac{d}{dx}g_2(x) = -W(\eta)g_2(x) + \eta e^{-W(\eta)}g_2(x-1), \tag{8.10}$$

with boundary conditions

$$g_2(x<1) = 0, \quad \text{and } g_2(1) = 1 + W(\eta). \tag{8.11}$$

To simplify further notation, we shift the function by defining $g(x) = g_2(x+1)$ and to understand the features of the differential equation we apply a Laplace transformation

$$F(s) = \mathcal{L}(f(x)) = \int_0^\infty e^{-sx} f(x)dx, \tag{8.12}$$

which yields the algebraic equation

$$sG(s) - g(0) = -W(\eta)G(s) + \eta e^{-W(\eta)}G(s)e^{-s}, \tag{8.13}$$

$$\Rightarrow G(s) = \frac{g(0)}{s + W(\eta)(1-e^{-s})}. \tag{8.14}$$

We here have used the properties of the Laplace transform, $\mathcal{L}[f(x+a)] = \exp(as)F(s)$, and of the Lambert function, $W(\eta) = \exp[-W(\eta)]\eta$. The small s behavior, i.e. the long wave length limit, is given by the value of $\lim_{x\to\infty} g(x)$ for which we find

$$\lim_{s\to 0} G(s) = \frac{g(0)}{(1+W(\eta))}\frac{1}{s} \tag{8.15}$$

$$\Rightarrow \lim_{x\to\infty} g(x) = \lim_{x\to\infty} g_2(x) = \frac{g(0)}{1+W(\eta)} = 1 \tag{8.16}$$

as it should be.

To find the period and decay constant of the oscillations we consider the poles of $G(s)$. Of course one pole is located at $s = 0$, corresponding to the background density. Two more poles are indicated by numerical evaluation in the surrounding, however one can not find the roots of the denominator directly. Therefore we make the ansatz $s = a + ib$

$$s + W(\eta)(1-e^{-s}) = 0 \tag{8.17}$$

$$a + W(\eta) - W(\eta)e^{-a}\cos(b) + i\left[b + W(\eta)\sin(b)e^{-a}\right] = 0. \tag{8.18}$$

The imaginary part equations yield

$$W(\eta)e^{-a} = \frac{-b}{\sin(b)} \tag{8.19}$$

$$\Rightarrow a = -\log\left(\frac{-b}{W(\eta)\sin(b)}\right), \tag{8.20}$$

which we can insert in the real part equation

$$\log(W(\eta)) + W(\eta) - \log\left(\frac{-b}{\sin(b)}\right) + \frac{b}{\tan(b)} = 0. \tag{8.21}$$

The equation can not be solved in closed form, but are solved easily using numeric methods. From a, b both the decay $\xi = \frac{-1}{a}$ and the period of oscillations $x_0 = \frac{2\pi}{b}$ are found and shown

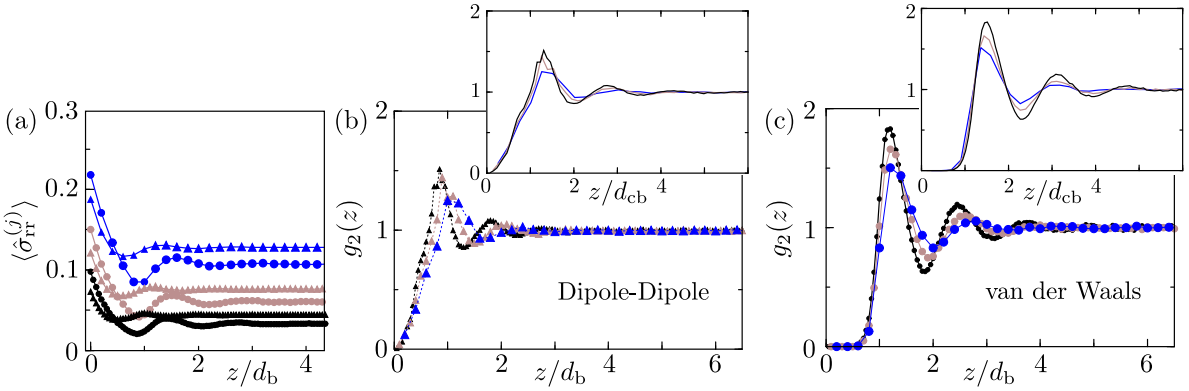

Figure 8.3: (a) Excitation probabilities for atoms at the edge of a one dimensional lattice subject to resonant two level driving with $\Delta_0 = 0, \Gamma_{\rm r} = \Omega/10, \Gamma_{\rm d} = \Omega$. Triangles (connected by dotted lines) correspond to DD interaction, and circles (connected by solid lines) correspond to vdW interaction between excited atoms. The number of excitations per blockade radius is given by $\varrho_{\rm at} d_{\rm b} = 5, 10, 20$ (blue, gray, black). 8.3(b) and (c) show the corresponding spatial correlations $g_2(z)$ for DD and vdW interaction respectively. In the inset of both graphs, $g_2(z)$ is plotted vs z in units of the collective blockade radius $d_{\rm cb}$ of Eq. 8.22.

in Fig. 8.2(c).

Keeping in mind that $\eta = \kappa \varrho_{\rm at} d_{\rm b}$ we find that the correlation length slowly increases with the chemical activity, whereas the oscillation period of the correlation function decreases towards $b_0 = d_{\rm b}$, the $\eta \to \infty$ limit where excitations are perfectly ordered. For small atomic densities per blockade radius on the order of $\mathcal{O}(10)$, the correlation length is only one to two blockade radii, but already for hundreds of atoms hard sphere interacting atoms would display correlations up to ten blockade radii apart.

8.2 Soft Interaction Potentials

We now turn to the discussion of one dimensional gases with soft interaction potentials corresponding to Rydberg excited atoms. The main tool for this discussion is ssMC as described in 15.2 implemented by David Petrosyan to solve the system of rate equations. In Fig. 8.3(a) we show the spatial distribution of Rydberg excitation probabilities in finite systems of $L = 15 d_{\rm b}$ with open boundary conditions and different atomic densities $\varrho_{\rm at}$. Atoms are continuously excited via effective single photon transition on resonance under conditions of strong decoherence $\Delta_0 = 0, \Gamma_{\rm r} = \Omega/10, \Gamma_{\rm d} = \Omega$.

As in the lattice case, the excitation probability for atoms close to the edge is enhanced and a density wave of short range is pinned to the boundary [199]. The two excitation correlation function is extracted from the MC simulations and shown in 8.3(b) and (c) for DD interacting and vdW interacting excitations respectively. Whereas for interaction types excitation within the blockade radius $d_{\rm b}$ is suppressed, only for the vdW case an avoided distance is found. Furthermore, correlations beyond $d_{\rm b}$ are much more pronounced for the sharper vdW potential.

8.2.1 Collective blockade radius

The avoided distance where $g_2(z) \approx 0$ is significantly smaller than the blockade radius. A better measure is given by the collective blockade radius. In a dense system, $\varrho_{\rm at} d_{\rm b} \gg 1$, an

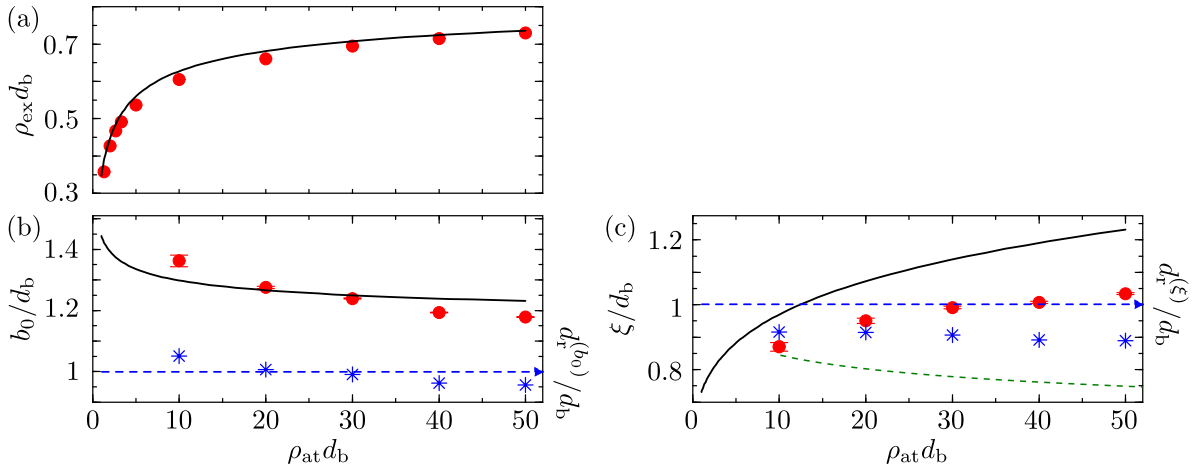

Figure 8.4: (a) Density of Rydberg excitations of vdW interacting atoms as a function of atomic density per blockade distance. Comparison of MC simulations (red circles) and HR potential results with $d_r = d_b$ (dotted black line). (b) Oscillation period b_0 and (c) correlation length ξ extracted from the MC simulation results in comparison with the HR predictions. The effective range of the HR potential $d_r^{(v_0,\xi)}$ (blue stars, right axis) is obtained by equating b_0 and ξ for the vdW and HR interaction results. The dashed lines in (b) and (c) are the blockade distance d_b (blue) and d_{cb} (gree).

atom in the Rydberg state $|r\rangle$ blocks the excitation of other atoms within a certain distance which, due to collective effects, is somewhat smaller than the blockade distance d_b for a pair of atoms. To estimate the collective blockade distance d_{cb}, note that the collective Rabi frequency $\Omega_{cb} = \sqrt{N_{cb}}\Omega$, and thereby the excitation linewidth $w_{cb} \simeq 2\Omega_{cb}\sqrt{\gamma_{rg}/\Gamma_r}$,for $N_{cb} = \varrho_{at} d_{cb}$ atoms, is enhanced by a factor of $\sqrt{N_{cb}}$ [76, 188]. Substituting N_{cb} into the definition of $d_{cb} \equiv \sqrt[p]{C_p/w_{cb}}$ yields

$$d_{cb} = \frac{d_b}{(\varrho_{at} d_b)^{1/(2\alpha+1)}}. \tag{8.22}$$

For the important case of vdW interaction this results in a reduction of the blockade radius $d_{cd}/d_b = (\varrho_{at} d_b)^{-1/13}$ that is on the order of 20% for the densities discussed here. In the insets of Fig. 8.3(b) and (c) we show the correlation function with distance scaled in units of the collective blockade radius and find an avoided distance of range d_{cb} for the vdW interacting atoms across the different atomic densities.

8.2.2 Quantitative comparison

We now want to quantify the suitability of the HR model for the description of the system under the vdW potential. The DD potential is not discussed as already short range correlations reveal that it is too soft. We compare the mean densities of excitations $\bar{\varrho}_{ex}$, as well as the oscillation periods λ and decay lengths ξ of spatial correlations $g_2(x)$ and normalize all quantities by the blockade distance d_b.

Since we need to specify the range of the HR potential let us first equate it to the blockade distance of the vdW potential, $d_r = d_b$. The average densities of excitations obtained from the MC algorithm and the HR rate equation model are then remarkably close, $\bar{\varrho}_{vdW} \simeq \bar{\varrho}_{HR}$, especially at high atomic densities $\varrho_{at} d_b \gg 1$, see Fig. 8.4(a). Also the oscillation period λ of the density wave, shown in Fig. 8.4(b), is well reproduced by the HR model. However,

with increasing the atomic density, the oscillation period b_0 of the density wave decreases slightly faster for the vdW potential. The softness of the vdW potential, compared to the HR potential, is the origin of the shorter correlation lengths ξ, see Fig. 8.4 (c). Nevertheless the HR rate equation model does also allow to extract the correct order of magnitude of the correlation length and predicts correctly the dependence on the atomic density.

Up to now we have set $d_\mathrm{r} = d_\mathrm{b}$. Next, we assume equal oscillation periods b_0 for both potentials and then deduce the corresponding range $d_\mathrm{r}^{(\lambda)}$ of the HR potential, which turns out to be close to d_b but slowly decreasing with increasing the atomic density ϱ_at, Fig. 8.4(b). Alternatively, we equate the correlation lengths ξ and find somewhat smaller corresponding range of the HR potential, $d_\mathrm{r}^{(\xi)} \simeq 0.9 d_\mathrm{b}$, again slowly decreasing with increasing the atomic density ϱ_at, Fig. 8.4(c). It is however significantly larger than the collective blockade distance.

8.3 Remarks on Higher Dimensional Systems

Hard rods in one dimension do not undergo a phase transition to a long range ordered state, when increasing the chemical activity η. Furthermore, the comparison of MC results for realistic interaction potentials with hard rod predictions shows, that vdW interacting atoms are even less likely to support an ordered state under the nonequilibrium conditions discussed here. As for lattice systems, the situation changes in higher dimensions. We here will only give a brief outlook and review the results on the 2D hard disc gas and relate it to the driven Rydberg gas.

8.3.1 Hard disc gas

For hard discs of radius 1, the pair interaction potential is given by $u(r) = \infty \times \Theta(1-r)$, with distance r. The only relevant quantity in the thermodynamic limit is the chemical activity η, which is equivalent to the density of disks. Maximal filling is realized for $\eta \to \infty$, where discs form a hexagonal lattice with filling fraction $f_\mathrm{max} = \pi/2/\sqrt{3} \approx 0.907$. For low densities the relation between chemical activity and filling fraction is well described by a Pade approximation [201]. This expansion breaks down for fillings greater $f_\mathrm{C} \approx 0.7$ [202], where the hard disc gas undergoes a transition away from the fluid. Despite decades of research the presence of a hexatic phase in between the ordered and fluid phase is not clear [203]. In terms of chemical activity, the critical regime occurs around $\log(\eta_\mathrm{C}) \approx 13$ [202].

An important order parameter in two dimensional gases is bond orientation order [202]. Bond orientation of order m for a single disc j is defined as

$$\Psi_j^{(m)} = \frac{1}{m} \sum_{k=1}^{m} e^{mi\Phi_{j,k}}, \tag{8.23}$$

where k sums over the nearest neighbors and $\Phi_{j,k}$ is the angle between a fixed axis and the line through discs j and k. The hexatic order parameter $\Psi^{(6)} = \sum_j \Psi_j^{(6)}$ vanishes in the liquid phase but is finite in the solid phase and would be a suitable order parameter for the discussion of two dimensional Rydberg gases.

8.3.2 Driven Rydberg gases in two dimensions

For the non equilibrium system with hard rod interaction potential in 1D, we showed that the chemical activity is given by $\kappa\varrho_{\mathrm{at}}d_{\mathrm{b}}$. A similar mapping holds in two dimensions

$$\eta = \kappa\varrho_{\mathrm{at}}\frac{\pi d_{\mathrm{r}}^2}{4}, \tag{8.24}$$

which is simply the product of driving parameter κ and the number of atoms within a blockade disc. For two level driving $\kappa \approx 1$ and to reach $\eta > \eta_{\mathrm{C}}$ one requires atomic densities on the order of

$$\varrho_{\mathrm{at}}d_{\mathrm{r}}^2 \approx 10^6. \tag{8.25}$$

Although large, this is within reach of BECs with strong confinement in one direction and peak densities of $\varrho = 10^4\ \mu m^{-2}$ and excitation of high n Rydberg states that have blockade radii on the order of $d_{\mathrm{b}} \approx 10\ \mu m$.

Conclusion

By generalizing the models developed in previous chapters, we have quantitatively analyzed the spatial correlations of Rydberg excitations in driven dissipative 1D systems. Using MC sampling of the many body dynamics we assessed the quality of approximations that replace the long range DD and vdW potential by a hard rod like potential. Whereas we found that the notation of a blockade radius for DD interactions is not correct, agreement with vdW interaction results was qualitatively good.

We derived the asymptotic behavior under the conditions of a hard rod interaction potential and revealed the close relation to long studied distribution models [199]. Whereas this analogy predicts the absence of a phase transition from short to long range correlations in 1D, an intricate transition from fluid to hexagonal order is predicted in 2D, which will be the subject of future investigations.

Chapter 9

The Mesoscopic Superatom

The interaction of single photons with single atoms is in general very weak, but efficient coupling of photonic qubits to atomic qubits is an essential component for the realization of scalable quantum information processing and communication technology. Lukin et al. proposed to use dipole blockaded ensembles of atoms instead of single atoms [13]. The resulting superatom inherits the strong collective coupling of many atoms, but due to Rydberg blockade, it also acts like a single atom, that encodes only one collective qubit.

Such a superatom is an example of a well controlled and strongly interacting quantum system, that constitutes a new kind of matter [204], which displays properties that surpass single particle physics and thus enable advances in various fields. We already gave an example for the use of such superatoms (SA) in Chapter 7 regarding the simulation of many body spin physics. A wide range of theoretical proposals has been inspired by the original idea. Honer et al. discussed how a SA can be facilitated for the creation of non classical light [168] and Müller et al. proposed the realization of quantum gates using SAs [205]. The concept has furthermore strongly influenced the way people think about extended Rydberg systems [198, 206].

Important steps towards the experimental realization of the original idea have been realized during the last years. The excitation blockade for few atoms was demonstrated using strong dipole traps for individual atoms [92, 207]. First measurements on Rydberg blockade in mesoscopic samples and the observation of collective Rabi oscillations was achieved by Reetz-Lamour et al.[208]. Dudin et al. observed multiple periods of collective Rabi oscillations by employing a second mechanism beyond Rydberg blockade to suppress the influence of doubly excitation [191]. They used an optical readout with strong selection regarding the direction of emission. Thereby they took advantage of spin wave dephasing for multiply excited states, which did not contribute to the measurement signal [209]. However, the original proposal of a spatially very small and therefore strongly blockaded ensemble has so far not been realized. We here discuss the realization of a mesoscopic superatom and review results, which have been published in [H-2014c].

The experiment in the group of Herwig Ott demonstrated the controlled creation and excitation of a mesoscopic SA and we contributed the theoretical modeling and simulation via rate equations and the quantitative comparison of experimental and theoretical results. Furthermore, careful analysis of experimental data was used to extract the relevant parameters such as decoherence rates and Rabi frequency from measurements.

To begin with we characterize the experiment and briefly discuss the preparation of the small atomic ensemble. The SA density distribution is characterized with blockade physics in mind and the relevant quantities for the following theoretical analysis are introduced. The experiment uses a single photon transition to directly excite atoms from ground to Rydberg

P-states. Whereas the associated non- isotropic interaction opens possibilities for interesting many-body physics and is a requirement for a number of theoretical proposals, we here motivate an effective potential that approximates it with an isotropic vdW interaction. The key observable is the string of ions from photoionization of excited atoms, that enables in vivo measurement of the SA. The microscopic modeling of the SA requires the extraction of unknown parameters. We therefore consider the ion signal at small excitation power and furthermore discuss decoherence and its origin for the SA. The introductory sections are concluded by discussing details of the numeric simulation.

We then present the results of the experiment together with theoretical simulations, which are shown to be in good, quantitative agreement. The main observables we consider are the peak rate of ions and ion-ion correlations. We demonstrate that the mesoscopic SA under resonant driving can be operated as a strongly antibunched, dipole-blockaded ensemble in the spirit of Ref.[13]. However, the mesoscopic size allows us to go beyond simple two-level physics and further explore the transition to many-body physics in a controlled manner. When driven off resonantly the SA can be used to study antiblockade and gives novel insight into the formation of strongly correlated Rydberg aggregates [210, 84].

9.1 Characterization of the Experiment

The mesoscopic SA is at the interesting transition point between exactly solvable few-body physics to complex, and in general intractable many-body physics. In this section we identify and quantify the most relevant ingredients of the SA dynamics and thereby establish an accurate model. Despite of its small size, an exact solution of this model, especially for a strongly driven SA, is infeasible and we must introduce a second layer of approximation, which we discuss in the following section.

Different aspects of the SA need to be characterized for a quantitative modeling. First of all we discuss the density distribution of ground state atoms, which is the result of compression and reshaping of a BEC and derive the relevant information regarding blockade physics. We furthermore discuss the excitation mechanism and the ionization channels, which are the key element to the experimental observations. We conclude this section with a discussion of the complex pair interaction of atoms excited to Rydberg P-states and introduce an effective vdW potential.

9.1.1 Preparation and geometry

The SA is prepared by reshaping a small Bose-Einstein condensate (BEC) of about 1700 ^{87}Rb atoms as illustrated in Fig. 9.1(a). The initial BEC is confined in an almost isotropic dipole trap at wavelength of $\lambda = 1064$ nm. An additional one dimensional optical lattice with spacing 532 nm freezes the axial movement of atoms and by increasing the radial trapping frequencies of the dipole trap, atoms are confined to small pancakes stacked along the axis of the lattice (middle part of Fig. 9.1(a)). Using a focused electron beam atoms in individual pancakes are depleted by electron impact ionization as proposed in [30]. For the mesoscopic SA we discuss here, all but three adjacent layers are removed in this way. Note however, that arbitrary patterns of removal are possible, making the extension to multiple SA along one dimension with finite separation easily possible. With the addition of further optical lattices preparation of two dimensional arrays of SAs is feasible. In Fig. 9.1(b) we show the density distribution after preparation of the SA measured with electron microscopy [31].

The number of atoms in the SA can be adjusted between $100 - 500$ at a temperature of

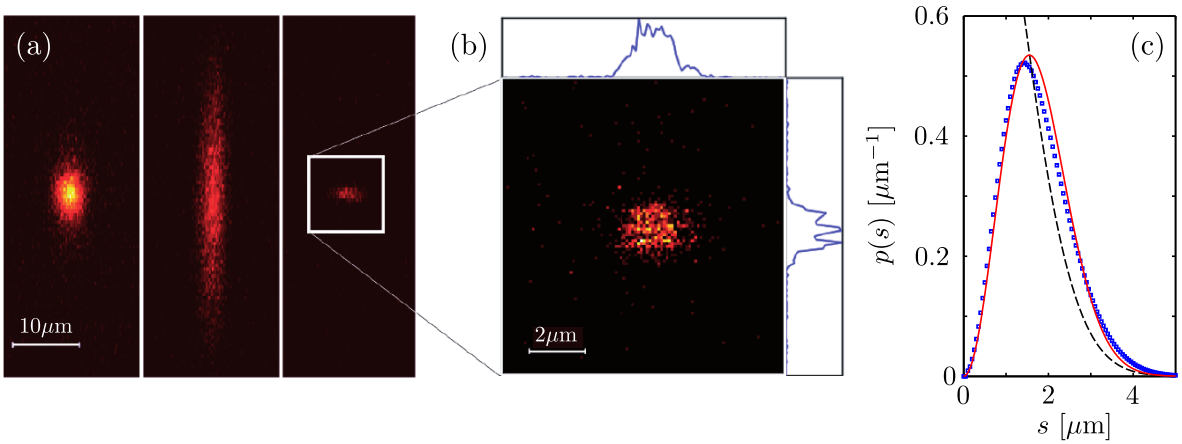

Figure 9.1: (a) Starting from a BEC in a dipole trap (left), atoms are frozen in axial dimension by an additional optical lattice and radially compressed (center) by tuning the dipole trap. Then atoms are removed from all but a few lattice sites with a focused electron beam (right). (b) The resulting atomic sample contains between $100 - 500$ atoms at a temperature of $T = (3.5 \pm 0.5)\ \mu$K. (c) Probability distribution for the separation s of two randomly chosen atoms within the SA (blue squares). The distribution is near identical to the distribution for an isotropic Gaussian systems with $\sigma_{\mathrm{G}} = 0.77\ \mu$m (red). The dashed black line shows the proportion of atoms further apart than separation s from a random atom.

$T = (3.5 \pm 0.5)\ \mu K$. The measured density distribution is approximated by the sum of three shifted Gaussian distributions, each representing one pancake layer,

$$\varrho_{\mathrm{SA}}(r,z) \approx \frac{1}{3\sigma_r\sqrt{8\pi^3\sigma_z}} \sum_{\nu=-1}^{1} e^{-r^2/(2\sigma_r^2)-(z-\nu d_z)^2/(2\sigma_z^2)}, \tag{9.1}$$

with $\sigma_r \approx 0.9\ \mu\mathrm{m}, \sigma_z \approx 0.2\ \mu$m and a separation of $d_y \approx 0.5\ \mu$m. Rydberg blockade originates from the distance dependent interaction shift between two excited atoms and we are therefore less interested in the overall density distribution, but in the distribution of distances between individual atoms. In Fig.9.1(c) we display the numerically calculated distribution of distances $p(s)$ for the density distribution ϱ_{SA} (blue squares) together with results for an isotropic Gaussian density distribution (red). The width $\sigma_{\mathrm{G}} = 0.77\ \mu$m of this distribution is chosen such, that the mean distance between atoms $\bar{s} \approx\ 1.3\mu$m is identical to the mean distance for ϱ_{SA}. Apart from small deviations, the distributions agree very well and thus distance distribution functions for spherically symmetric density distributions are used, which can be derived in an elegant way [211]. For a Gaussian distribution in three dimension one finds

$$\bar{s} = \frac{4}{\sqrt{\pi}}\sigma_{\mathrm{G}} \Rightarrow \sigma_{\mathrm{G}} \approx 0.77\ \mu\mathrm{m}, \tag{9.2}$$

$$p(s)ds = \frac{s^2 e^{-s^2/4/\sigma_{\mathrm{G}}^2}}{\sigma_{\mathrm{G}}^3 2\sqrt{\pi}}ds, \tag{9.3}$$

which will be the basis for different analytic insights into the SA physics. Intuitive length scales can be extracted from the cumulative distribution $P(s) = \int_0^s ds' p(s')$. For more than $\sim 40\%$ of all atom pairs, their distance is larger than 2 μm, despite of the much smaller SA size of only $\sigma_{\mathrm{G}} = 0.77\ \mu$m.

Most experiments are conducted with approximately $N = 125$ atoms, resulting in peak

densities after preparation of $\varrho_0 \approx 140\ \mu\text{m}^3$. At the low temperatures of the SA the mean velocity of atoms is $|\bar{v}| = \sqrt{\frac{3k_\text{b}T}{m_\text{Rb}}} \approx 40$ nm/μs. We thus neglect atomic motion within our model and consider a frozen gas of ground state atoms [212].

9.1.2 Excitation and ionization

Atoms are prepared in the $5S_{1/2}$-ground state and are excited to the $51P_{3/2}$-Rydberg state with a single photon transition at wavelength $\lambda_\text{UV} = 297$ nm. By tuning of the UV laser power the single atom Rabi frequency can be adjusted over four orders of magnitude from 100 Hz up to 1 MHz. The effective lifetime of the $51P_{3/2}$-Rydberg state including the effect of black body radiation is $\tau_\text{nat} \approx 100\ \mu$s [213]. However only 50% of the decay is directed towards the ground state and the remaining 50% leads into other Rydberg states. We here do not take into account the population of different Rydberg states but instead simplify our model. The spontaneous decay to the ground state is taken into account with rate $\Gamma_\text{s} = 5$ kHz and the channels to other Rydberg states are neglected.

The main process of excitation loss is photoionization at rate $\Gamma_\text{ion} = 45 \pm 5$ kHz from the intense dipole trap laser [87]. Other ionization channels are given by Hornbeck-Molnar ionization, Penning ionization, and Rydberg-Rydberg collisions [214], however all of these are small compared to photoionization in this experiment. To detect the ions, a small electric field is used to accelerate them out of the sample and towards an ion detector, which has a detection efficiency of $\eta = 40 \pm 8\%$. A sufficiently large extraction field of $E \geq 60$ mV/cm has to be applied, to prevent ion-ion interactions that result in unwanted correlations.

9.1.3 P-state interaction

Due to the selection rules imposed for single photon transitions, atoms are excited to Rydberg P-states. By applying external magnetic fields, the degeneracy of different m_z states is lifted and the $51P_{3/2}, m_z = 3/2$ state is separated by multiple GHz from the next level. The interaction between excited atoms is in general anisotropic and can be described as a binary interaction [215]. At large atomic separations, the binary interaction potential is of vdW type [90] as described in the Sec. 1.3 of the introduction

$$V(r,\theta) \approx \frac{C_6(\theta)}{r^6}, \tag{9.4}$$

$$C_6^{51P_{3/2},m_z=3/2}(\theta) = [-34.05 + 47.17\cos(2\theta) - 11.59\cos(4\theta)]\ \text{GHz}\ \mu\text{m}^6. \tag{9.5}$$

In the inset of Fig. 9.2(b) we illustrate the angle dependence of $C_6(\theta)$ for the Rydberg state employed here. For angles up to $\theta_0 \approx 0.11\pi$ the asymptotic interaction potential is repulsive, but for $\theta \in (\theta_0, \pi - \theta_0)$ it is attractive. If we only consider the asymptotic behavior it is thus unclear whether strong blockade can be observed for P-states, as one will always find non interacting atom pairs near the angle θ_0.

The main part of Fig. 9.2 (b) shows the molecular potential curves for $51P_{3/2}, m_z = 3/2$ obtained by Tobias Weber using exact diagonalization of the interaction Hamiltonian. Whereas for interatomic separations $s > 5\ \mu$m the vdW interaction is a good approximation, perturbation theory breaks down for the small distances in the mesoscopic SA. An avoided crossing with the $51P_{3/2}, m_z = 1/2$ state bends all interaction curves, which have a negative C_6 for large distances into a repulsive interaction for small distances. Atomic pair distances in the SA are smaller than 3 μm and only probe this repulsive part of the interaction potential. Therefore effective blockade of double excitation is expected.

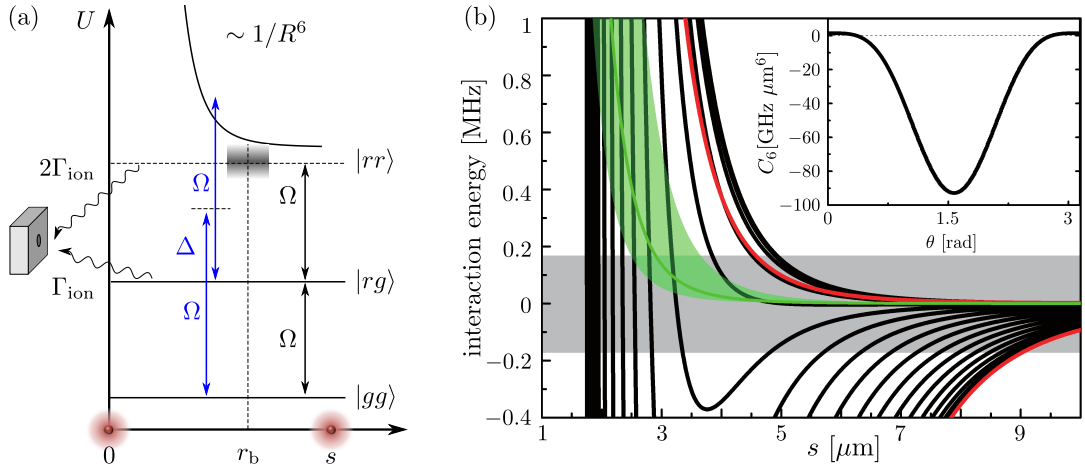

Figure 9.2: (a) Scheme of the SA experiment. Atoms are excited with single-photon transition into a $51P_{3/2}$-state ($\lambda \approx 297$nm), where they strongly interact with other excited atoms. The level scheme for two atoms at separation s is shown with interaction energy scaling of vdW type. Excited atoms are continuously ionized in the trapping field and then detected. (b) Potential curves of the $51P_{3/2}, m_j = 3/2$ pair state obtained by Tobias Weber using exact diagonalization of the interaction Hamiltonian. Black curves represent the potential at fixed orientation angles $\theta \in [0, \pi/2]$ and red curves the C_6 asymptotic for $\theta = 0$ and $\theta = \pi/2$. The green band is the range of isotropic interaction potentials used in the effective rate equation simulation. The inset displays the angular dependency of the vdW coefficient $C_6(\theta)$ as a function of the orientation angle θ.

In our modeling of the SA we do not use the complicated interaction potential obtained from the exact diagonalization, but employ an effective, isotropic vdW potential. The C_6 parameter is one of the fit parameters of the model and is chosen within the range of $40 - 400$ MHz μm^6. The range of interaction energies is shown as a green band in Fig. 9.2(b).

9.2 Parameters of the Experiment

Whereas the number of atoms and the geometry of one SA can be determined accurately via fluorescence measurements, other parameters that are needed for the theoretical description are more difficult to extract. First of all the exact relation between UV laser power and effective Rabi frequency is not accurately known. Straightforward detection of collective Rabi oscillations to *measure* the Rabi frequency is not possible, as we find an overall decoherence rate of $\gamma > 100$ kHZ, that suppresses coherent phenomena. In this section we shortly discuss how to extract both the Rabi frequency and the rate of decoherence from measurements at low intensities of the excitation laser. We will then evaluate different scenarios that contribute to the decoherence.

9.2.1 Ion rates at low excitation laser intensity

The unitary dynamics of the SA can be separated into the single atom driving terms $\mathcal{H}_j = (\Omega|\mathrm{r}\rangle\langle\mathrm{g}|_j + h.c.) + \Delta_0|\mathrm{r}\rangle\langle\mathrm{r}|$ and the intricate many body interaction

$$\mathcal{H} = \sum_{j=1}^{N} \mathcal{H}_j + \mathcal{H}_{\rm int}. \tag{9.6}$$

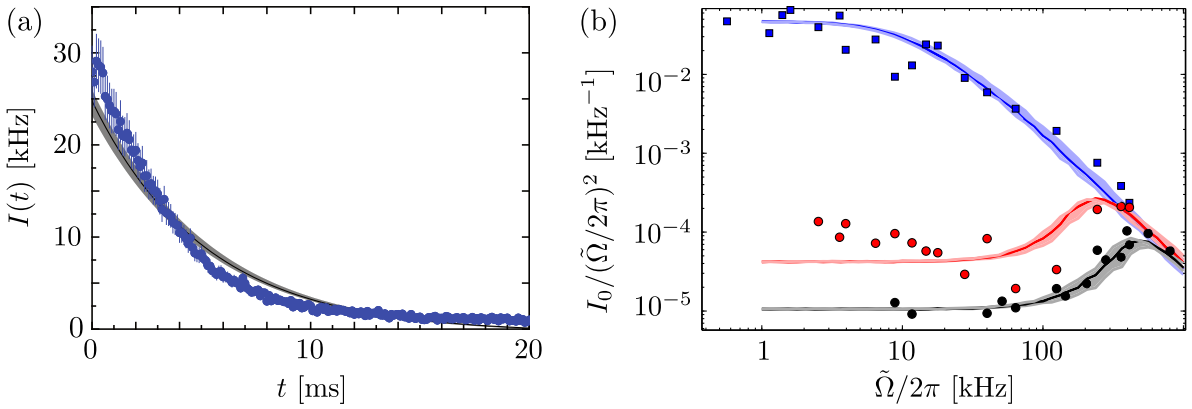

Figure 9.3: (a) Rate of ions (blue curve) emitted from the mesoscopic SA for continuous resonant excitation with $\Omega/2\pi = 6$ kHz. The black line and grey shaded area are results from the rate equation model. (b) Initial rate of ions divided by excitation laser power as a function of not calibrated Rabi frequency $\tilde{\Omega}$. The excitation laser is detuned from single atom resonance by $\Delta_0 = 0$ (blue), $\Delta_0 = 2$ MHz (red) and $\Delta_0 = 4$ MHz (black). Solid points are measurement results and lines are rate equation results for for the range of interaction potentials.

In addition to decoherence Γ_d and spontaneous emission Γ_s we must take into account the strong ionization. Formally we treat ionization as the spontaneous decay with rate Γ_i to a third atomic level $|\mathrm{i}\rangle$, which has no further dynamics. The jump operators are defined as

$$L_{\mathrm{s},j} = \sqrt{\Gamma_\mathrm{s}}|\mathrm{g}\rangle_j\langle\mathrm{r}|_j, \qquad L_{\mathrm{d},j} = \sqrt{\Gamma_\mathrm{d}}|\mathrm{g}\rangle_j\langle\mathrm{r}|_j, \qquad L_{\mathrm{i},j} = \sqrt{\Gamma_\mathrm{i}}|\mathrm{i}\rangle_j\langle\mathrm{r}|_j. \tag{9.7}$$

The ion emission is the main measurement signal and an exemplary signal is shown in Fig. 9.3(a). The excitation coupling is suddenly quenched from zero to fixed value at $t = 0$. The ion signal rapidly increases within $\tau_\mathrm{rise} \approx 20\ \mu s$ to its maximum value and the subsequent decay of the ion signal reflects the steady loss of atoms. The SA is eventually completely ionized after a time of 20 ms for strong driving and saturation of the SA.

To determine the rate of decoherence and the relation between Rabi frequencies and laser power, we use the peak ion rate at small powers of the excitation laser. For weak excitation of the SA the probability of two or more Rydberg excited atoms at once is very small and the effect of interaction can be neglected. In this regime we expect a peak rate of ions smaller than Γ_i, corresponding to an average number of less than one excitation within the SA. For the ion signal we find

$$I_{\Omega\ll\gamma} = \frac{\eta\Gamma_\mathrm{ion}N_\mathrm{a}}{\Gamma_\mathrm{ion}+\Gamma_\mathrm{sp}}\frac{2\Omega^2\gamma}{\gamma^2+\Delta_0^2}, \tag{9.8}$$

where we have used the result for a single two level atom in appendix 15.1, scaled it with the total number of atoms N_a and taken into account that only part of the population decay is due to ionization.

The number of atoms N_a, the detection efficiency η and the loss rates $\Gamma_\mathrm{i}, \Gamma_\mathrm{s}$ are known from independent measurements. The detuning Δ_0 of the excitation laser is calibrated using spectroscopy on dilute, thermal samples and is accurate within $\delta(\Delta_0) = \pm 0.5$ MHz. The Rabi frequency can be controlled via tuning of the laser intensity, but the precise relation between the two is unknown. Calculations by Tobias Weber, which do not take into account the specific shape of the excitation mode, are used as a first approximation $\tilde{\Omega} = \chi'\sqrt{P_\mathrm{UV}}$.

Using multiple measurements at low intensities and different detunings, we can refine this relation $\Omega = \chi\chi'\sqrt{P_{\mathrm{UV}}}$ with a second scaling factor.

By dividing the expected ion signal in Eq. 9.8 with $\tilde{\Omega}^2$ we find the constant

$$I_{\Omega\ll\gamma}/\tilde{\Omega}^2 = \frac{\Gamma_{\mathrm{ion}} N_{\mathrm{a}}}{\Gamma_{\mathrm{ion}} + \Gamma_{\mathrm{sp}}} \frac{2\chi^2\gamma}{\gamma^2 + \Delta_0^2}. \tag{9.9}$$

In Fig. 9.3(b) we show measurements of the peak ion rate at three detunings $\Delta_0/2\pi = 0, 2, 4$ MHz as a function of frequency $\tilde{\Omega}$. The plateaus in the measurement data for small frequencies correspond to the low intensity limit in Eq. 9.8. We extract the three constants and use them to fit χ and γ in Eq. (9.9).

For the extraction of ions from the SA a small, constant electric field is applied. The main set of measurements is conducted at the minimum required extraction field of $E_{\mathrm{low}} = 0.06$ V/cm, whereas a second set of measurements is at a higher field of $E_{\mathrm{high}} = 0.25$ V/cm. We determine χ and γ for both configurations independently. In the case of the low field we use data at detunings $\Delta_0/2\pi = 0, 2, 4$ MHz and find a decoherence rate of $\Gamma_{\mathrm{d,low}}/2\pi = 140 \pm 20$ kHz, whereas for the high field we only have data at $\Delta_0/2\pi = 0, 2$ MHz and find $\Gamma_{\mathrm{d,high}}/2\pi = 340 \pm 20$ kHz. The rescaling factors for the Rabi frequency are identical within error bars. We now have extracted all relevant single atom parameters and calibrated our theoretical model of the SA.

9.2.2 Sources of decoherence

Before we continue with the discussion of the results we want to briefly discuss possible sources of decoherence Γ_{d}. An often cited source of decoherence is the laser linewidth, which in the present experiment is estimated to be below 200 kHz. However, for a small ensemble as the SA the fluctuations in laser frequency are identical for all atoms and thus have a different effect than single atom decoherence.

Thermal motion of atoms results in a Doppler line broadening of width $\delta(f)_{\mathrm{Doppler}} = f_0\sqrt{8k_{\mathrm{B}}T\log(2)/m}/c$, where f_0 is the transition frequency and c the speed of light. For the experimental parameters we calculate $\delta(f)_{\mathrm{Doppler}} \approx 185$ kHz. Note, that this line broadening can only be described by single atom decoherence in the presence of a fast collision rate between atoms. Scattering of ground state atoms and scattering that includes Rydberg atoms has been proposed before as a further source of decoherence.

Rydberg atoms are very sensitive to external electric fields $\mathcal{E}$ due to the scaling of polarizability with the principal quantum number as $\alpha \sim n^7$. For the $51P$ state the polarizability is $\alpha \approx 400\ \mathrm{MHz}\frac{\mathrm{cm}^2}{\mathrm{V}^2}$ [216]. The nonlinear Stark effect is given by

$$\omega_{\mathrm{Stark}} = \frac{1}{2}\alpha|\mathcal{E}|^2, \tag{9.10}$$

$$\Rightarrow \Delta_{\omega_{\mathrm{Stark}}} = \alpha|\mathcal{E}|\delta(\mathcal{E}). \tag{9.11}$$

Fluctuations in the electric field have been determined by Tobias Weber to $\delta(\mathcal{E}) \approx 5$mV/cm, which result in fluctuating energy levels on the order of 120 kHz. Most importantly due to the quadratic nature of the Stark effect, fluctuations of energies increase with the mean of the electric field, which is in accordance with the extracted decoherence rates from the experiment. To identify the electric field as the main source of decoherence further investigations regarding the time scales of these fluctuations are required.

9.3 Numerical Simulation

All numeric simulations in this chapter are performed within the rate equation approach described in previous chapters and appendix 15.2. For every trajectory a sample of atomic positions is generated from the mesoscopic SA density distribution ϱ_{SA} and all atoms are initialized in the ground state. We do not take into account fluctuations in the initial number of atoms and we use the effective, isotropic interaction of vdW type discussed in Sec. 9.1.3. We use dMC to generate a faithful sampling of the system dynamics. Ionization is a new channel for deexcitation and has to be treated differently.

Excited atoms either reemit a photon with rate $\Gamma_{\mathrm{s}} + \frac{2\gamma\Omega^2}{\Gamma(\gamma^2+\Delta^2)}$ or become photoionized and have to be removed with rate Γ_{ion}. We effectively remove atoms from the simulation by reducing their future excitation rate to zero. This treatment is closest to the experimental situation and reproduces the decay of the SA. Tracking the ionization events is identical to the experimental ion detection. Whereas this allows for easy comparison of theory and experiment, we suffer the same bottlenecks of data analysis and requirements regarding the number of realizations.

For all non temporal measurements we have adopted a different approach. The peak ion rate is reached within $\tau_{\mathrm{rise}} = 20\ \mu s$ for strong driving. Within this time, the loss of atoms is limited by the ionization rate Γ_{i} and the mean excitation number of the SA, which is typically on the order of 1. Therefore during this rise time only one out of $N_a = 125$ atoms is lost.

We leverage the slow decay of atom number compared to the fast rise time by running simulations at constant number of atoms. Ionization events are registered but atoms are mapped to the ground state instead of the inactive state i after ionization. Thus the long term steady state is not the trivial vacuum as before, but a SA which continuously emits ions with rate I. The advantage is that we can calculate accurate statistics of Rydberg excitations, with fewer but longer trajectories. We have compared results from these steady state calculations with extracted peak values from the simulations including loss of atoms and have found good agreement.

Further mechanisms have been tested to improve the quantitative agreement between experiment and theoretical model. First of all we implemented the anisotropic interaction potential of the P-state. Results were however unsatisfactory, which we attribute to strong mixing of molecular states not shown in Fig. 9.2(b) and movement of atoms, which averages the anisotropic interaction. We furthermore implemented non linear ionization, which could result from Rydberg Rydberg collisions. Agreement in the regime of saturated SAs was slightly improved but not enough to justify the introduction of this fit parameter.

9.4 Results

Whereas we have a very good understanding of the SA at small driving, which we have used to calibrate our theoretical description, the opposite limit of strong driving is a complex many body problem which we want to understand. Besides the peak rate of ions emitted, we are interested in the statistics of ions, which reflect the internal statistics of Rydberg excitations. An advantage of the extended SA experiment is the capability to measure time resolved correlation functions

$$g_2(\tau) = \frac{\langle I(t)I(t+\tau)\rangle}{\langle I(t)\rangle\langle I(t+\tau)\rangle}. \tag{9.12}$$

The ion signal does not contain further spatial information and we can for example not determine whether a Rydberg atom was ionized in the center of the SA or at its edge. Nonetheless

the spatial resolution is set by the small size of the SA, whereas similar experiments on extended systems, observe signals that are averaged over systems with an extension of many blockade distances.

9.4.1 Blockade and antibunching

In Fig. 9.4(a) we show the peak rate of ions $I_\mathrm{p} = \max_t I(t)$ for resonant excitation as a function of the driving Rabi frequency Ω. As long as the mean number of excitations in the system, which is related to the ion signal by $I(t) = \Gamma_\mathrm{i}\langle\hat{N}_\mathrm{e}(t)\rangle$ is small, the signal follows the Ω^2 slope of single particle physics in Eq. 9.8. For larger drivings the interaction of Rydberg excited states shifts most atoms within the SA out of resonance and suppresses further excitations.

For extended ensemble of atoms Löw et al. showed that the fraction of excited Rydberg atoms follows a characteristic slope in the saturated region [188, 187]. For excited atoms that interact with a DD potential ($\alpha = 3$) a scaling with $\Omega^{2/3}$ and for vdW interaction a scaling with $\Omega^{2/5}$ is expected in the saturated regime. Due to the small size of the superatom, no universal exponent could be extracted from obtained data as the influence of the boundaries is too large. In the case of a very small ensemble, strongly confined to much less than the blockaded volume, one expects a complete saturation of the ionization rate for strong driving. As a result of the mesoscopic size, the rate of ions does not saturate at Γ_i for large Ω, but instead blockade is overcome and more excitations are squeezed within the superatom. Whereas further reduction in size is hard to achieve, an improved control over the fluctuation of the electric field $\delta_\mathcal{E}$ and thereby the decoherence, would render excitation to larger principal quantum number n Rydberg states with stronger blockade feasible.

Nonetheless, the suppression of multiple excitations of the SA manifests itself in the temporal correlation function shown in Fig. 9.4(b) at $\Omega/2\pi = 6$ kHz. The peak ion rate for these parameters is $I_\mathrm{p} \approx 30$ kHz, which corresponds to an average number of 0.6 Rydberg excited atoms within the SA. Ions and therefore excitations in the SA are strongly antibunched with $g_2(0) = 0.08 \pm 0.06$ and we find exponential relaxation of the correlation function with time constant $\tau_\mathrm{res} \approx 10\ \mu$s. Amplitude as well as time constant are reproduced by the rate equation model (shaded area).

Analytic results for the low intensity regime

Within the rate equation model we can calculate the first order corrections to the low intensity limit and gain an intuitive understanding for the interaction and geometry constraints that a SA has to fulfill. To this end we consider the set of rate equations truncated to configurations with at most two excited atoms. The state space is spanned by the 0 state, which denotes all atoms in the ground state, the singly excited states, which we denote by $S_k = 1$, where k is the index of the single excited atom. Similarly we denote the doubly excited state, with atoms k, m in the Rydberg state and all others in the ground state, by $S_k = 1, S_m = 1$, where we avoid double counting by the requirement $k < m$. Within this small configuration space we find a detailed balance solution for the stationary state

$$\varrho_{\{S_k=1\}}/\varrho_{\{0\}} = \Omega^2 \frac{2\gamma}{4\Omega^2\gamma + \Gamma(\gamma^2 + \Delta_0^2)}, \tag{9.13}$$

$$\varrho_{\{S_k=1,S_m=1\}}/\varrho_{\{S_k\}} = \Omega^2 \frac{2\gamma}{4\Omega^2\gamma + \Gamma[\gamma^2 + (\Delta_0 + V_{k,m})^2]}, \tag{9.14}$$

where $V_{k,m}$ is the interaction between atoms k and m. Under conditions of weak, resonant driving, $\Delta_0 = 0, \Omega \to 0$, we can further simplify these relations to $\varrho_{\{S_k=1\}}/\varrho_{\{\}} = 2\Omega^2/(\Gamma\gamma)$ and

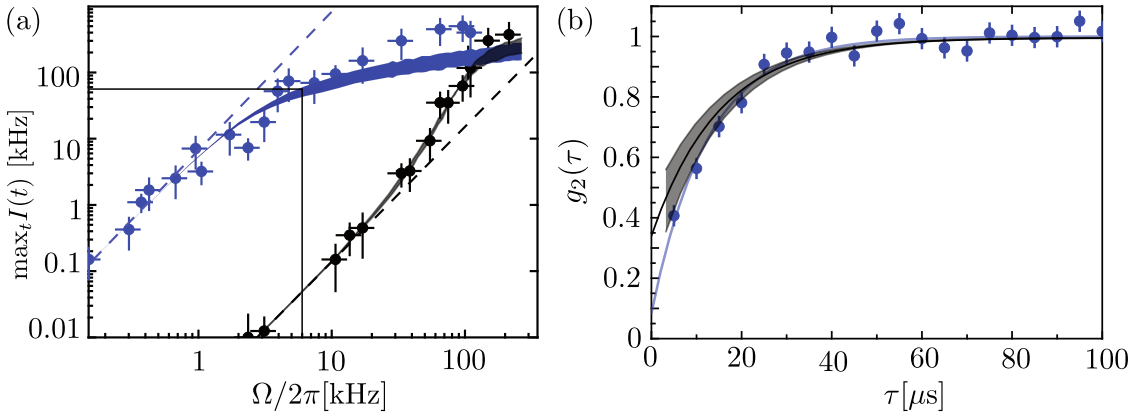

Figure 9.4: (a) Initial rate of ions emitted from the SA for resonant and off resonant ($\Delta_0/2\pi = 4$ MHz) excitation as a function of the driving Rabi frequency. Error bars denote the statistical error, intensity fluctuations and drifts of the excitation laser. Shaded areas are results from the rate equation model and the dashed lines extrapolate the low intensity results, which are used for calibration. Measurements are done with an initial SA size of $N_{\text{atoms}} = 125$ and small external electric field of $E = 60$ mV/cm. (b) Second order temporal correlation function of ions emitted under resonant excitation with $\Omega/2\pi = 6$ kHz. The data is fitted with an exponential and we extract antibunching of $g_2(0) = 0.08 \pm 0.06$.

$\varrho_{\{S_k=1,S_m=1\}}/\varrho_{\{S_k\}} = 2\Omega^2/(\Gamma\gamma)/[1+(V_{k,m}/\gamma)^2]$. Assuming an isotropic Gaussian distributions of atoms with width σ_{G} and isotropic interaction of the form $V(s) = C_\alpha s^{-\alpha}$, we find for the partition function Z

$$\begin{aligned} Z &= 1 + N_{\text{a}}\frac{2\Omega^2}{\Gamma\gamma} + N_{\text{a}}^2\frac{2\Omega^4}{\Gamma^2\gamma^2}\int ds\ \frac{p(s,\sigma_G)}{1+(C_\alpha/s^\alpha/\gamma)^2}, \\ &:= 1 + N_{\text{a}}\frac{2\Omega^2}{\Gamma\gamma} + N_{\text{a}}^2\frac{2\Omega^4}{\Gamma^2\gamma^2}Q(\gamma,\sigma_{\text{G}},C_\alpha,\alpha), \qquad (9.15) \\ &= Z(P_0+P_1+P_2) \qquad (9.16) \end{aligned}$$

with $p(s)$ being the pair distance distribution and P_m the total probability of all configurations with exactly m excited atoms. The integral Q is not analytically solvable, but can be reshaped to yield further insight

$$\begin{aligned} Q &= \int_0^\infty dx\ \frac{1}{\sigma_{\text{G}}^3 2\sqrt{\pi}}\frac{s^2 e^{-s^2/4/\sigma_{\text{G}}^2}}{1+(C_\alpha/s^\alpha/\gamma)^2}, \qquad (9.17) \\ &= \sqrt{\frac{2}{\pi}}\int_0^\infty dx\ \frac{x^2 e^{-x^2/2}}{1+x^{-2\alpha}/2^\alpha(C_\alpha/\sigma_{\text{R}}^\alpha/\gamma)^2} = Q_\alpha(\beta := \sigma_{\text{R}}/d_{\text{B}}). \qquad (9.18) \end{aligned}$$

One finds that Q is only determined by the softness of the interaction α and the ratio β of sample size σ_{G} to blockade distance $d_{\text{B}} = \sqrt[\alpha]{C_\alpha/\gamma}$. The amplitude of the second order correlation function of the ion signal is identical to the second order correlation function of Rydberg excitations in the SA. It is not affected by the finite detection probability, as is for example the Mandel Q parameter [84]. We here only consider singly and doubly excited states

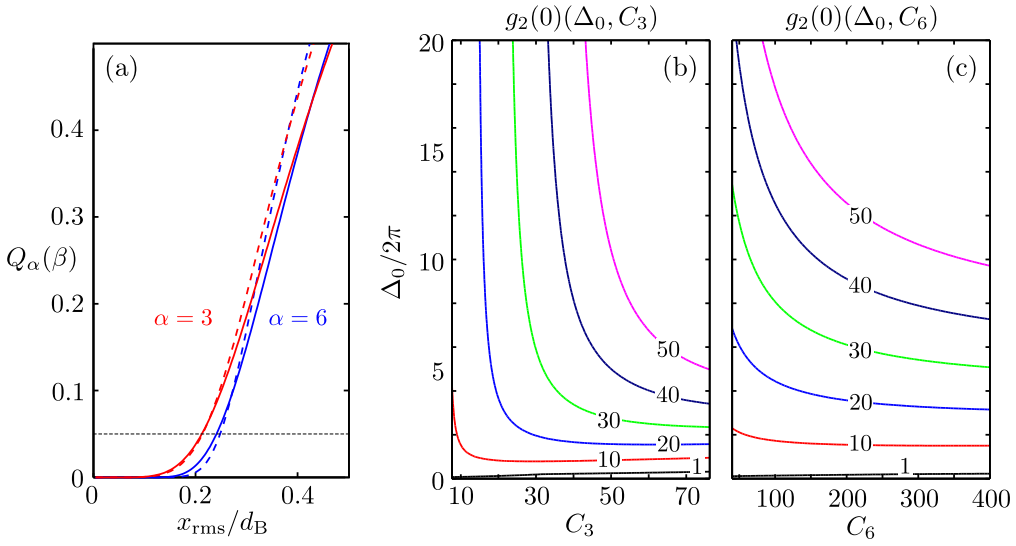

Figure 9.5: (a) Numeric solution of the integral $Q_\alpha(\beta)$ for the most relevant cases of DD- (red) and vdW- (blue) interaction depending on the ratio of sample root mean square $x_{\rm rms}$ and blockade radius $d_{\rm B}$. Solid lines are for a Gaussian distribution and dashed lines for a homogeneously filled sphere. (b) and (c) show the small Ω results for bunching in the extended SA setup ($\sigma_{\rm G} = 0.77$ μm) with DD and vdW interaction and off resonant excitation.

and therefore find

$$g_2(0) = \frac{\langle \hat{N}_{\rm e}(\hat{N}_{\rm e}-1)\rangle}{\langle \hat{N}_{\rm e}\rangle^2} = \frac{2P_2}{(P_1+2P_2)^2} \tag{9.19}$$

$$= Q_\alpha(\beta) + [Q_\alpha(\beta) - 2Q_\alpha(\beta)^2] N_{\rm atoms} \frac{\Omega^2}{\gamma\Gamma} + \mathcal{O}(\Omega^4). \tag{9.20}$$

In Fig. 9.5(a) we show results for $g_2(0)$ for the two common potentials in Rydberg physics, $\alpha = 3$ for DD interaction and $\alpha = 6$ vdW interaction as a function of system size. Note that the root mean square used in the figure, is identical to the width $x_{\rm rms} = \sqrt{(\langle x^2\rangle + \langle y^2\rangle + \langle z^2\rangle)/3} = \sigma_{\rm G}$ for a Gaussian distribution. In addition to results for Gaussian distributions (solid lines), we show results for atoms homogeneously distributed within a sphere (dahed lines). For these distributions one finds that $x_{\rm rms} = 4/\sqrt{3}\sigma_{\rm S}$. The critical size $x^{\rm b}_{\rm rms}$ for the breakdown of blockade, here defined as $g_2(0) = 0.05$, is slightly modified by the exponent of the interaction. Whereas for the softer DD potential we find $x^{\rm b}_{\rm rms} \approx 0.20 d_{\rm B}$, this increases to $0.25 d_{\rm B}$ for vdW interaction. The overall behavior is however determined by the single parameter $x_{\rm rms}/d_{\rm B}$.

For the simulation of experiments on the extended SA we used vdW potentials with $C_6 = 40-400$ MHz μm^6 and $\gamma = (2\pi\times 140\text{ kHz} + 50\text{ kHz})/2 \approx 464$ kHz, resulting in a blockade distance of $d_{\rm B} = 2.1 - 3.1$ μm for weak driving. This results in a ratio of $\beta = 0.25 - 0.37$, which is at the edge of perfect blockade and illustrates the importance of the experimental effort to reduce size.

9.4.2 Antiblockade and bunching

In Fig. 9.4(a) we show results for off resonant excitation at blue detuning of $\Delta_0/2\pi = 2$ MHz, much larger than the linewidth γ. For small Rabi frequencies the amplitude of the peak

ion rate is strongly suppressed compared to resonant excitation but follows the Ω^2 scaling in Eq. (9.8). Unlike the saturation we observe for resonant excitation, we here find a rapid growth of I_p with scaling larger than Ω^2. This is a manifestation of antiblockade for off resonant excitation, which was first experimentally seen in [217]. For strong driving, such that the collective coupling strength $\sqrt{N_\mathrm{a}}\Omega$ becomes comparable with the detuning, the resonant and off-resonant excitation reach a comparable level of mean number of excited atoms. The results of the rate equation simulation nicely follow the rapid intermediate increase in I_p and the transition to saturation for strong driving. We do not require any parameter changes compared to the resonant excitation simulations besides the detuning Δ_0.

Further insight into the SA dynamics can be gained from the temporal correlation function $g_2(\tau)$. To begin with, we will discuss the experimental results for $g_2(0)$ and the implications of the observed bunching. We generalize our analytic results for $g_2(0)$ to off-resonant excitation and find marked differences between the cases of vdW and DD interacting excitation. We then continue with the discussion of relaxation timescales of $g_2(\tau)$ in the next subsection.

For fixed $\Omega/2\pi = 48$kHz we display experimental and theoretical $g_2(0)$ as a function of detuning Δ_0 in Fig. 9.4(c). The strong antibunching observed on resonance turns into extraordinary bunching for large detuning $\Delta_0/2\pi \gg 10$ MHz. At these large detunings the mean excitation probability of the SA is very low, for example at $\Delta_0/2\pi = 21$MHz we find $\langle \hat{N}_\mathrm{e}\rangle \approx N_\mathrm{a}\Omega^2\gamma/[4\Delta_0^2\Gamma] \approx 0.01$. At such low excitation probabilities contributions from configurations with more than two excitations can be neglected. We extract the ratio of doubly excited states P_2 to singly excited states P_1 from the correlation function and find

$$g_2(0) = \frac{2P_2}{\langle \hat{N}_\mathrm{e}\rangle^2} \quad \Rightarrow \quad \frac{P_2}{P_1} \approx g_2(0)\langle N_\mathrm{e}\rangle/2. \tag{9.21}$$

For the strongest bunching at $\Delta_0/2\pi = 21$ MHz we therefore find $P_2/P_1 \approx 0.36$. A short calculations puts this number in perspective and shows, that the dominant excitation process for the SA in this regime is pair excitation.

Assume that all Rydberg excitations are created as pairs, but are ionized independently. The average waiting time for the decay from two to one excitation is $\tau_1 = 1/(2\Gamma)$, half as long as the waiting time for the second excitation to be lost $\tau_2 = 1/\Gamma$. Therefore $P_2/P_1 = 0.5$ in this extreme case. Note that the SA is not an ideal source of ion pairs despite these strong correlations as the total rate of ions is only ≈ 300 Hz.

Analytic results in the low intensity regime

We now generalize our semi analytic expressions for $g_2(0)$ to the case of off-resonant excitation. Starting point is again the partition function

$$Z = 1 + N_\mathrm{s}\frac{2\Omega^2\gamma}{\Gamma(\gamma^2+\Delta_0^2)} + N_\mathrm{s}^2\frac{2\Omega^4}{\Gamma^2(\gamma^2+\Delta_0^2)}\tilde{Q}(\Delta_0, C_\alpha, \gamma, \sigma_\mathrm{G}), \tag{9.22}$$

$$\text{where} \quad \tilde{Q}(\Delta_0, C_\alpha, \gamma, \sigma_\mathrm{G}) = \int ds\ \frac{p(s,\sigma_G)}{1+[(\Delta_0 - C_\alpha/s^\alpha)/\gamma]^2}. \tag{9.23}$$

The correlation function is related to the integral $\tilde{Q}$ by

$$g_2(0) = (1+(\Delta_0/\gamma)^2)\tilde{Q} + \mathcal{O}(\Omega^2). \tag{9.24}$$

In Fig. 9.5(b) and (c) we show results for $g_2(0)$ at low driving strength and a Gaussian distribution of atoms. We consider both DD and vdW interaction and a range of interaction

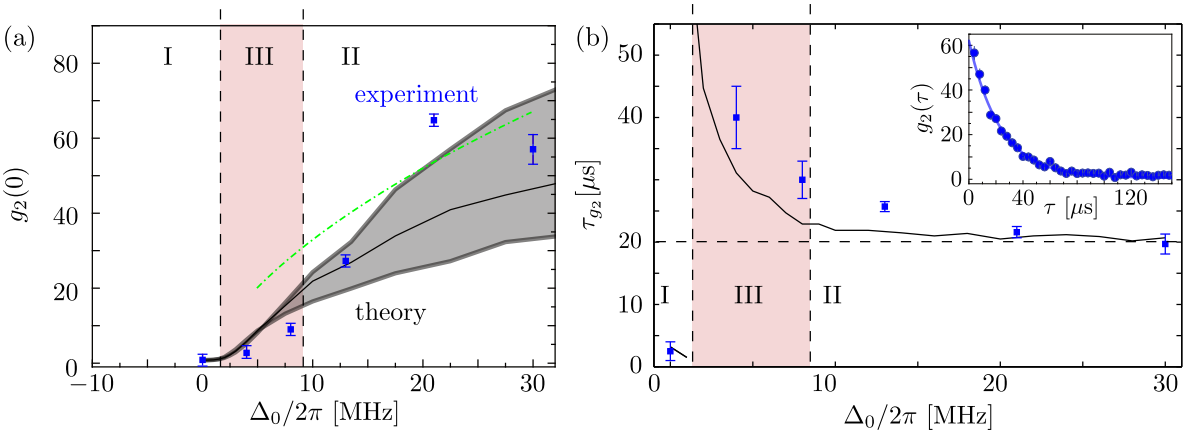

Figure 9.6: Second order correlation function $g_2(0)$ (a) and the associated relaxation time scale τ_{g_2} (b) as a function of the detuning Δ_0 for fixed driving of the SA with $\Omega/2\pi = 48$ kHz. The inset of (b) shows $g_2(\tau)$ for $\Delta_0/2\pi = 21$ MHz.

strengths and detunings Δ_0. The range of C_6 interaction coefficients corresponds to the values used in the simulation of the experiment and the C_3 coefficient interval is rescaled by the mean interatomic distance $C_3 = C_6/(4/\sqrt{\pi}\sigma_\mathrm{R})^3$. For the shallow DD potential the analytic result predicts a very steep initial rise in $g_2(0)$ up to $\Delta_0/2\pi \approx 5$ MHz, which is not compatible with the experimental findings. The results for vdW interaction however predict the correct approximately linear increase of bunching with detuning.

For large detuning we can approximate the integrand of $\tilde{Q}$ by a Lorentzian around the resonance distance $d_\mathrm{R} = \sqrt[\alpha]{C_\alpha/\Delta_0}$ of width $\gamma s_0^{\alpha+1}/(\alpha C_\alpha)$. For the correlation function this yields

$$g_2(0) = \frac{\pi p(d_\mathrm{G})\gamma}{\alpha} C_\alpha^{1/\alpha}\left(1 + \frac{\Delta_0^2}{\gamma^2}\right)\Delta_0^{-1-1/\alpha}, \tag{9.25}$$

which further simplifies in the limit of large detuning $\Delta_0 \gg \gamma$ and which in the case of vdW interaction reads

$$g_2(0) = \frac{\pi p(d_\mathrm{R})}{6}\frac{\Delta_0^{5/6} C_6^{1/6}}{\gamma}. \tag{9.26}$$

Here $p(d_\mathrm{R})$ is the probability density of an atom pair being in distance of the resonance radius d_R. We display this prediction for $C_6 = 100$ MHz μm^6 (green dashed line) alongside the full numeric calculations on the RE model and the experimental findings in Fig. 9.6(a), which are for finite $\Omega/2\pi = 48$ kHz. Therefore the analytic result overestimates bunching, it however reproduces the correct scaling behavior.

9.4.3 Relaxation of $g_2(\tau)$

In the introduction we used the term *in vivo* measurement, regarding the ion signal emitted from the SA. We here make use of this property by exploring correlation functions at unequal times $g_2(\tau \neq 0)$, which gives additional insight into the excitation dynamics of the SA.

To illustrate our approach we begin with discussing a trivial example, where $g_2(0) = 1$. For Poissonian excitation statistics, the probability P_k for a given number of excited atoms is given by $P_k = \lambda^k e^{-\lambda}/k!$, where λ is the mean number of excitations. The ionization and

detection of an excited atom is formally described by a mapping of the probabilities

$$P_k^{\mathrm{pre}} \to k P_{k-1}^{\mathrm{post}}, \tag{9.27}$$

taking into account that the total ionization rate increases with the number of excited atoms. For the example of a Poisson distribution one find

$$P_k^{\mathrm{post}} = \mathcal{N}(k+1)\frac{\lambda^k e^{-\lambda}}{(k+1)!}\lambda P_{k+1}^{\mathrm{pre}}, \tag{9.28}$$

where $\mathcal{N}$ is the necessary renormalization. The correlation function $g_2(\tau)$ is defined as the expectation value of $\hat{N}_{\mathrm{e}}$ after a detection event, normalized by the steady state expectation value. In the special case of the Poisson distribution this is not interesting, as $P_k^{\mathrm{post}} = P_k^{\mathrm{pre}}$ and $g_2(\tau) = 1$. In the case of the SA dynamics we discuss now, we show that the detection of an ion projects the SA to a non equilibrium situation and via $g_2(\tau)$ we study the relaxation back to equilibrium.

The SA dynamics we study Within the RE model the SA dynamics is incoherent by construction. This is justified due to the large dephasing Γ_{d} we do not observe coherent effects, such as Rabi oscillations, in the experimental results. Therefore all correlation functions obey the functional form

$$g_2(\tau) \approx 1 + [g_2(0) - 1]\exp\left(\tau/\tau_{g_2}\right), \tag{9.29}$$

where we introduced the relaxation time τ_{g_2}.

In Fig. 9.7 the probability distribution P_k is displayed for three cases of detunings we want to discuss. The regime I of resonant excitation, shown in (a), regime II of far detuned excitation in (c) and regime III at moderate detuning displayed in (b). We begin by discussing the correlation measurements for resonant excitation. All results are for driving Rabi frequencies of $\Omega/(2\pi) = 48$ kHz. For this strong driving the SA is in the saturated regime with an average excitation number of $\langle \hat{N}_{\mathrm{e}} \rangle \approx 4$ and we find moderate antibunching of $g_2(0) \approx 0.75$. For the resonant case in Fig. 9.7(a), the distribution is sub Poissonian and therefore narrower than a corresponding Poisson distribution (black squares) with equal mean. We show the steady state distribution in blue and the distribution after the projection due to the detection of an ion in red. Here the detection induces only a slight shift to smaller k. The removal of a single excited atom is only a weak, and short lived perturbation of the SA. Many ground state atoms were blockaded by the now ionized atom and are now free to become excited on a time scale of the order $1/\sqrt{N_{\mathrm{a}}}\Omega$.

In the limit of large detuning we found record antibunching of $g_2(0)$ up to 60. The corresponding distribution P_k^{pre} is dominated by $P_0^{\mathrm{pre}} \approx 1$ and has small contributions from singly and doubly excited states as displayed in Fig. 9.7(c). Due to bunching, the probability of single excitations is strongly enhanced after the detection of an ionization, the occupation of higher numbers of excitations however remains negligible. A single decay process is necessary to relax back to the stationary probability distribution and we therefore find $\tau_{g_2} = 1/\Gamma_{\mathrm{i}}$ in the limit of large detuning.

For intermediate detuning of $\Delta_0/2\pi = 3$ MHz (red) the zero component of the probability distribution is still the largest. The distribution is however super Poissonian and pair as well as triplet probabilities are comparable to the single excitation probability. After projection due to an ionization the distribution is strongly shifted into the range of two to four excitations as shown in Fig. 9.7(b). The correlation measurements on the SA here probe the physics of Rydberg aggregates, which has been discussed before in [84]. Whereas at large detunings excitations come in pairs, here small aggregates of multiple atoms form and the detection of

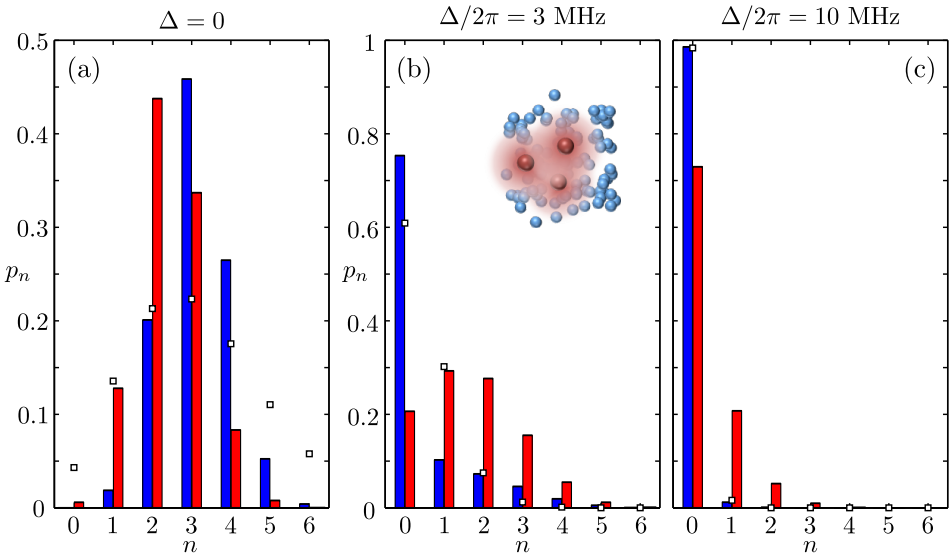

Figure 9.7: Number statistics of Rydberg excitations in the stationary state (blue) immediately after an ionization has been detected (red) for three different detunings. (a) On resonance the sub Poissonian distribution is slightly shifted to smaller excitation numbers. (b) In contrast, the super Poissonian distribution at $\Delta/2\pi = 3$ MHz is strongly shifted towards clusters of multiple excitations. (c) At very large detunings only single excitation contributions are significant after the ionization because most Rydberg excitations come in pairs.

a single ion projects the SA into a state with large probability to find such an aggregate. The relaxation back to the stationary state requires the decay of the entire aggregate and therefore τ_{g_2} is a direct probe of the aggregate lifetime.

The relaxation time of correlation τ_{g_2} as a function of detuning is shown in Fig. 9.6(b) and illustrates the three regimes we discussed. Regime I of antibunching, where the loss of an excitation is quickly replenished by exciting one of the remaining ground state atoms. The far detuned regime II of pair excitations, where the decay of the second excitation sets the time scale of relaxation and finally the most interesting regime III, where we observe an increase in the relaxation time related to the formation of Rydberg aggregates. The behavior of correlation functions is qualitatively reproduced within the RE model.

Conclusion

In this chapter we discussed the results of a close collaboration with the experimental group of Herwig Ott with the aim to prepare and characterize a superatom in the sense of [13]. We used the well understood limit of weak excitation to calibrate our theoretical model and quantitatively compared simulation results from the RE model with experimental findings.

The mesoscopic SA can be used as a strongly antibunched source of single ions, but its capabilities go beyond a simple two level system. We theoretically quantified the effects of the finite extend and clarified the transition to extended many body systems. For off resonant excitation we studied antiblockade and the emergence of Rydberg aggregates. Here the experimental capability to measure time resolved $g_2(\tau)$ was employed to gain insight into the lifetime of these few excitation clusters.

Strong decoherence so far prohibits the use of the SA for quantum information processing. Fluctuations of electric fields have been identified as the potential origin of this decoherence

and could be resolved by technical improvements. An alternative approach would be an increase in the principal quantum number n of the employed Rydberg state. This enables the use of larger Rabi frequencies under blockade conditions and therefore overall shorter time scales.

Already the incoherent SA bears the potential for interesting many body physics, for example the crystallization of excitations in two dimensional lattices [H-2014a]. An example we discussed in Chapter 7.

Chapter 10

Antiblockade in Continuous Rydberg Gases

The wealth of interesting physics that emerged for off-resonant excitation of the mesoscopic superatom shows, that experiments with Rydberg atoms can go beyond blockade physics. Antiblockade of Rydberg excitation at distances, where the binary interaction cancels the detuning of the driving field was theoretically predicted by Ates et al. [218] and Amthor et al. presented first experimental evidence for this [217]. Formation of strongly correlated aggregates of Rydberg excitations was discussed in [210], based on truncation methods for the large Hilbert space, developed with Rydberg blockade on short distances in mind in [219]. Experimental evidence was again found by the Weidemüller group [84] and we presented measurements and theory regarding the lifetime of aggregates in Chapter 9.

Good agreement of theoretical and experimental results in [84] and extensive benchmarking in [15] established rate equation models for the simulation of extended systems that bear the potential for large aggregates. Lesanovsky et al. studied the intricate dynamics of dense Rydberg gases excited off resonantly and found evidence for hierarchical relaxation and glassiness [220, 221]. Besides numerical simulation of many body rate equations, they developed a mean field description for the density of Rydberg excited atoms. Results were compared to experimental results by Urvoy et al. in [222]. Whereas good agreement with the experiment is found for exact simulation of the rate equations, mean field results significantly differed. A better analytic understanding for the many body physics in extended systems is needed and would shed new light on recent experiments, that found phenomena similar to optical bistability in Rydberg ensembles [14, 223].

We here present a conceptually similar mean field approach to [221], but improve significantly the ansatz for the distribution of excited atoms and the analysis of the resulting mean field equations. The derived dynamic equation will be of use for the description of *bistable* behavior as reported in [223] and we show how to extract fluctuations and statistics in the stationary state. For extended systems we predict the absence of bistability, in the sense of a bimodal distribution for excitation probability.To conclude, we benchmark our mean field predictions with RE simulations of extended systems and find quantitative agreement in the expected regime of validity, whereas the simpler ansatz used in [221] fails.

10.1 Average Excitation and Deexcitation Rates

The aim of this section is to derive average excitation and deexcitation rates for atoms subject to single photon driving in a continuous gas with strong interactions between Rydberg excited

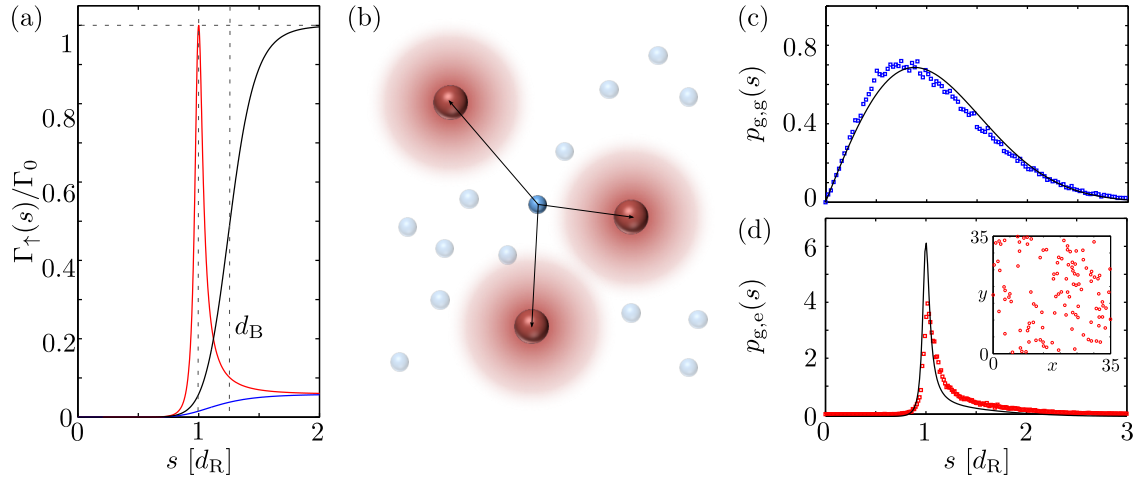

Figure 10.1: (a) Excitation rates $\Gamma_\uparrow$ for a ground state atom at distance s from an atom in a Rydberg state with vdW interaction $C_6 = \gamma$,. (b) Ground state atoms immersed in a field of Rydberg excited atoms. (c) Distribution of the distance of ground state atoms to the next excited atom, extracted from RE simulations and analytic expressions for the given density of excitations. (d) Distribution function $p_n^{(e)}(s, n_{ex})$. Parameters are $C_6/\gamma = 4, \Delta_0/\gamma = -4$ and $\Omega/\gamma = 0.1$.

atoms. The cornerstone of our approach is the excitation rate of ground state atoms subject to single photon driving with Rabi frequency Ω at detuning $\Delta = \Delta_0 + V$

$$\Gamma_\uparrow(\Delta) = \frac{2\Omega^2\gamma}{\gamma^2 + (\Delta_0 + V)^2}, \tag{10.1}$$

where U is the interaction shift due to other excited atoms and $\gamma = (\Gamma + \Gamma_d)/2$ the linewidth. For resonant driving $\Delta_0 = 0$ blockade physics is observed. We here are interested in antiblockade, which we have already introduced in the previous chapter on the SA.

In Fig. 10.1(a) we display the excitation rate for a ground state atom in a distance s to an already excited atom. Throughout this chapter we assume the interaction to be of vdW form

$$V(s) = \frac{C_6}{s^6}. \tag{10.2}$$

For resonant excitation, $\Delta_0 = 0$, the excitation rate $\Gamma_\uparrow(s)$ is strongly suppressed for $s < d_b = \sqrt[6]{C_6/\gamma}$ and then sharply rises to the resonant rate of $\Gamma_0 = 2\Omega^2/\gamma$. If C_6 and Δ_0 are of equal sign, we again find strong suppression for $s < d_b$, followed by a rise to the smaller off resonant rate

$$\Gamma_{\Delta_0} = 2\Omega^2\gamma/(\gamma^2 + \Delta_0^2). \tag{10.3}$$

However, when detuning and interaction have opposite sign, a new distance $d_r = \sqrt[6]{|C_6/\Delta|}$ becomes relevant. Near this distance the interaction cancels the detuning and recovers the resonant excitation rate Γ_0, the ground state atom is *antiblockaded*.

For specific examples in this chapter, we will consider two dimensional systems of homogeneous density of atoms n_a. Our approach can easily be extended to other dimensions and shapes of the interaction potential.

10.1.1 Low density distance distributions

Within the exact rate equation treatment, for every ground state atom j we must calculate its detuning in the presence of other excited atoms

$$\Delta_j = \Delta_0 + \sum_{k \neq j} V_{j,k} S_k, \tag{10.4}$$

where $S_k = 1$ for excited atoms and zero otherwise (cf. Sec. 6.2.2). Relevant for atom j are only the closest surrounding excitations, see Fig. 10.1(b), which we sort by their distance s from small too large $s_j^{(1)} < s_j^{(2)} < \cdots$. Due to the vdW scaling we only consider the closest excited atom in distance $s_j = s_j^{(1)}$ and neglect other excitations. We have compared this approach with calculations, which include the interaction effects from next next excitations and found good agreement within few percent.

The average excitation rate of a ground state atom in a specific configuration $\{S_1, \cdots S_{N_\mathrm{a}}\}$ is given by

$$\langle \Gamma_\uparrow \rangle = \frac{1}{N_\mathrm{a} - N_\mathrm{e}} \sum_{j|S_j=0} \Gamma_\uparrow(\Delta_j) \tag{10.5}$$

$$= \frac{1}{N_\mathrm{a} - N_\mathrm{e}} \sum_{j|S_j=0} \frac{2\Omega^2 \gamma}{\gamma^2 + (\Delta_0 + C_6/s_j^6)^2}, \tag{10.6}$$

where we introduced N_a for the total number of atoms and N_e for the total number of excited atom. $(N_\mathrm{a} - N_\mathrm{e})^{-1} \sum_{j|S_j=0}$ is hereby the averaging over all non excited atoms. In the thermodynamic limit $\langle \Gamma_\uparrow \rangle$ can be rewritten in terms of the distribution function, for the distance of a *ground* state atom to the next closest *excited* atom $p_{\mathrm{g,e}}(s)$

$$\langle \Gamma_\uparrow \rangle = \int_0^\infty ds\ \Gamma_\uparrow(\Delta_0 + C_6/s^6) p_{\mathrm{g,e}}(s). \tag{10.7}$$

In general finding an expression for the distribution $p_{\mathrm{g,e}}(s)$ is as difficult, as solving the full many body problem, but we here use a very simple but effective ansatz. Our assumption is, that at low densities of excitations, $(n_\mathrm{e} d_\mathrm{r}^2, n_\mathrm{e} d_\mathrm{b}^2 \ll 1)$, these excited atom will be distributed uniformly and independently. If this is the case, one expects

$$p_{\mathrm{g,e}}(s, n_\mathrm{e}) = 2\pi n_\mathrm{e} s e^{-\pi s^2 n_\mathrm{e}}, \tag{10.8}$$

which is only dependent on the excitation density n_e. In Fig. 10.1(c) we show results for $p_{\mathrm{g,e}}(s, n_\mathrm{e})$ extracted from exact simulations of the RE model at low excitation density and compare them with our analytic ansatz. Despite of small deviations we find very good agreement.

We do not have an analytic solution to the integral (10.7) for the average excitation rate, but we can gain some insight by reshaping the corresponding expression

$$\langle \Gamma_\uparrow \rangle(n_\mathrm{e}) = \frac{4\pi\Omega^2 n_\mathrm{e}}{\gamma} \int ds\ \frac{s e^{-\pi s^2 n_\mathrm{e}}}{1 + (\Delta_0 - C_6/s^6)^2/\gamma^2}$$

$$= \frac{4\Omega^2}{\gamma} \pi d_\mathrm{R}^2 n_\mathrm{e} \int_0^\infty dx\ \frac{x e^{-x^2 \pi d_\mathrm{R}^2 n_\mathrm{e}}}{1 + (1 - x^{-6})\Delta_0^2/\gamma^2}. \tag{10.9}$$

Note, that the second expression is only well defined for non zero detuning. It shows that the

key parameters are the ratio Δ_0/γ of detuning and linewidth and the density of excitations per area of a disc with radius equal the resonance distance πd_{R}^2.

To complement our effective dynamics we must calculate the average deexcitation rate of atoms. In the case of two level driving the deexcitation rate is related to the excitation rate by $\Gamma_\downarrow(\Delta) = \Gamma_\uparrow(\Delta) + \Gamma$. The average is given by

$$\langle \Gamma_\downarrow \rangle = \int_0^\infty ds\ \Gamma_\uparrow(\Delta_0 + C_6/s^6) p_{\mathrm{e,e}}(s), \tag{10.10}$$

with $p_{\mathrm{e,e}}(s)$ being the distance distribution from an excited atom to the next closest excited atom. Importantly, this distribution is different from $p_{\mathrm{g,e}}(s)$, but closely related. Our idea is to consider the excitation process. We know that excited atoms are created from ground state atoms and we know the distribution function from ground to excited atoms. Even more, we know the rate at which ground state atoms in distance s to an excitation get excited and can derive the distribution of distance for excitations the moment they are created. Our ansatz is then

$$p_{\mathrm{e,e}}(s, n_{\mathrm{e}}) \approx \frac{\Gamma_\uparrow(s) p_{\mathrm{g,e}}(s, n_{\mathrm{e}})}{\langle \Gamma_\uparrow \rangle(n_{\mathrm{e}})}. \tag{10.11}$$

We again validate our approach by comparison with exact numeric MC results in Fig. 10.1(d). Our ansatz is incomplete, because we do not take the effect of excitation loss towards this distribution function into account. Nonetheless we find good agreement.

We want to discuss the similar ansatz for off resonantly driven Rydberg gases by Lesanovsky et al [221]. The main difference is the choice of distribution functions in the derivation of average rates, here they choose simply

$$p_{\mathrm{g,e}}(s) = p_{\mathrm{e,e}}(s) = \delta(s - n_{\mathrm{e}}^{-1/2}), \tag{10.12}$$

which as we have shown is not the case. Within this ansatz is the expressions for the average rates can be evaluated immediately

$$\langle \Gamma_\uparrow \rangle_{\mathrm{L}} = \Gamma_\uparrow(\Delta_0 + C_6 n_{\mathrm{e}}^3),\ \langle \Gamma_\downarrow \rangle_{\mathrm{L}} = \Gamma_\uparrow(\Delta_0 + C_6 n_{\mathrm{e}}^3) + \Gamma. \tag{10.13}$$

We will later return to the implications of this specific result.

10.1.2 A criterion for antiblockade

The integrals Eq. (10.7) and Eq. (10.10) can be evaluated numerically and we display results in Fig. 10.2(a) and (b) as a function of the density of excitations. Solid lines indicate results for off resonant excitation $-C_6 d_{\mathrm{R}}^6 = \Delta_0 = 4\gamma$ and dash dotted lines are for resonant excitation. For the mean excitation rate shown in (a) the large detuning suppresses excitation by a factor of Δ_0^2/γ^2 in absence of excited atoms, but antiblockade reverts this picture at larger n_{e}. Whereas the resonant rate has monotonously fallen off by two orders of magnitude for $n_{\mathrm{e}} d_{\mathrm{R}}^2 = 1$, the off resonant rate is only slightly reduced. The initial slope is given by

$$\langle \Gamma_\uparrow \rangle = \frac{2\Omega^2\gamma}{\gamma^2 + \Delta_0^2} + n_{\mathrm{e}} \frac{4\pi\Omega^2}{\gamma} \int ds\ \left(\frac{s}{1 + (\Delta_0 + C_\alpha/s^6)^2/\gamma^2} - \frac{s}{1 + \Delta_0^2/\gamma^2} \right) + \mathcal{O}(n_{\mathrm{e}}^2), \tag{10.14}$$

where the integral is the first order measure of the interaction impact. On resonance the the integral is always negative, such that the average excitation rate is reduced, whereas for sufficient detuning it turns positive and the rate is increased as is the case for the given example. By separating the integral into the blockade region for $s < d_{\mathrm{b}}$ and taking the

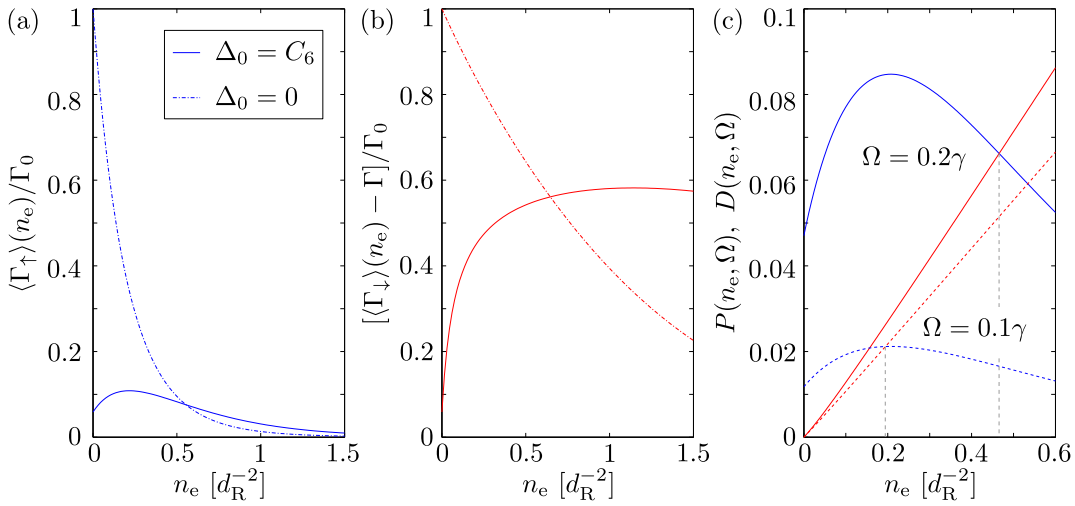

Figure 10.2: Average excitation (a) and deexcitation (b) rate as function of excitation density n_{ex} for $C_6 = 2\gamma$ with resonant $\Delta_0 = 0$ (black) and off resonant $\Delta_0 = -2\gamma$ excitation. Solid lines are calculated with our approximations for the distance distribution, dashed lines with the δ-approximation used in [221]. (c) Excitation (blue) and deexcitation (black) rates for $\langle n_{ex}\rangle$ at different driving Rabi frequencies and atomic density $n_{at} = 10$.

antiblockade into account as a Lorentzian, one finds that the strength of interaction C_6 is not relevant for the sign of the integral. The important factor is the ratio of detuning to linewidth, for a general interaction potential with exponent α this yields a simple criterion for antiblockade

$$\frac{|\Delta_0|}{\gamma} \gtrsim \frac{\alpha}{2\pi}. \tag{10.15}$$

In the relevant case of vdW interaction the detuning should be larger than the linewidth, to observe significant contributions from antiblockde.

Similar behavior to $\langle\Gamma_\uparrow\rangle$ is found for the deexcitation rate displayed in Fig. 10.2(b), with deviations that can be explained from the shape of the distribution function. For resonant excitation the excited atoms obey a minimum distance given by the blockade radius. Therefore they are only detuned by the weak tail of the vdW interaction and the fall off for $\langle\Gamma_\downarrow\rangle$ is much slower than for $\langle\Gamma_\uparrow\rangle$. Similarly in the off resonant case atoms are excited at the resonance distance a_R and therefore excitations are shifted into resonance and are susceptible to immediate deexcitation.

10.2 Dynamics of Excitation Density and Statistics

Based on the average excitation and deexcitation rates derived in the previous section we will now discuss dynamic equations for the total excitation density and identify the fixed points of this dynamics as stationary densities n_e^0. We will then characterize the statistics of the excitation number at these densities in the stationary state and identify the relevant conditions for super Poissonian statistics, which has been used as a signature for antiblockade.

10.2.1 Stationary points of the excitation density

To be specific we consider a finite system of N_a atoms randomly distributed on a two dimensional plane of size $L \times L$ with periodic boundary conditions. We consider the dynamics of

the probabilities for an exact number of N_e excited atoms p_{N_e}. This probability is the sum of the probabilities for all configurations with exactly N_e excited atoms and within the mean field approach the dynamic equation is given by

$$\begin{aligned}\partial_t p_{N_\mathrm{e}} = &(N_\mathrm{a} - N_\mathrm{e} + 1)\langle\Gamma_\uparrow\rangle[(N_\mathrm{e}-1)/L^2]p_{N_\mathrm{e}-1} \\ &- (N_\mathrm{a} - N_\mathrm{e})\langle\Gamma_\uparrow\rangle(N_\mathrm{e})/L^2)p_{N_\mathrm{e}} \\ &+ (N_\mathrm{e}+1)\langle\Gamma_\downarrow\rangle[(N_\mathrm{e}+1)/L^2]p_{N_\mathrm{e}+1} \\ &- N_\mathrm{e}\langle\Gamma_\downarrow\rangle(N_\mathrm{e})/L^2)p_{N_\mathrm{e}},\end{aligned} \tag{10.16}$$

We are interested in the dynamics of the mean number of excitations

$$\partial_t\langle N_\mathrm{e}\rangle = \sum_{N_\mathrm{e}=0}^{N_\mathrm{a}} N_\mathrm{e}\partial_t p_{N_\mathrm{e}}(t) \tag{10.17}$$

$$= \sum_{N_\mathrm{e}=0}^{N_\mathrm{a}} [(N_\mathrm{a} - N_\mathrm{e})\langle\Gamma_\uparrow\rangle(N_\mathrm{e}/L^2) - N_\mathrm{e}\langle\Gamma_\downarrow\rangle(N_\mathrm{e}/L^2)]p_{N_\mathrm{e}}(t). \tag{10.18}$$

From this we derive an equation of motion for the mean density of excitations in thermodynamic limit $L \to \infty$

$$\partial_t\langle n_\mathrm{e}\rangle = \int_0^{n_\mathrm{a}} dn_\mathrm{e}\ [(n_\mathrm{a} - n_\mathrm{e})\langle\Gamma_\uparrow\rangle(n_\mathrm{e}) - n_\mathrm{e}\langle\Gamma_\downarrow\rangle(n_\mathrm{e})]p(n_\mathrm{e}, t), \tag{10.19}$$

where we have introduced the continuous probability distribution for the excitation density $p(n_\mathrm{e}, t)$. Let us consider a narrow probability distribution represented by a δ-distribution

$$p(n_\mathrm{e}, t) = \delta(n_\mathrm{e} - \langle n_\mathrm{e}\rangle), \tag{10.20}$$

$$\begin{aligned}\Rightarrow \partial_t\langle n_\mathrm{e}\rangle(t) &= [n_\mathrm{a} - \langle n_\mathrm{e}\rangle(t)]\langle\Gamma_\uparrow\rangle(\langle n_\mathrm{e}\rangle(t)) - \langle n_\mathrm{e}\rangle(t)\langle\Gamma_\downarrow\rangle(\langle n_\mathrm{e}\rangle(t)) \\ &:= P(\langle n_\mathrm{e}\rangle(t)) - D(\langle n_\mathrm{e}\rangle(t)).\end{aligned} \tag{10.21}$$

In the last step we have defined growth rate P and loss rate D at mean excitation density $\langle n_\mathrm{e}\rangle$. For a specific atomic density of $n_\mathrm{a} = 10$ we show these rates in Fig. 10.2(c) for different values of Ω, where the driving enters through the mean excitation and deexcitation rates. For large atomic densities $n_\mathrm{a} d_\mathrm{B} \gg 1$ the excitation density is in general small $n_\mathrm{e} \ll n_\mathrm{a}$. Therefore the pump rate is to lowest order in the excitation density, given by the average excitation rate $P \approx n_\mathrm{a}\langle\Gamma_\uparrow\rangle(n_\mathrm{e})$. For our example we choose conditions of antiblockade, such that $\partial_{n_\mathrm{e}} P(n_\mathrm{e}) > 0$ and only for large excitation fillings it reduces again. The loss rate D on the other hand is dominated by the spontaneous decay for the parameters chosen here, as $\Omega^2/\gamma < \Gamma = 0.1\gamma$.

Densities of interest are the stationary points of Eq. (10.21)

$$P(n_0^{(m)}) = D(n_0^{(m)}), \tag{10.22}$$

where we use an index m to differentiate between possible different solutions.

One can show that for our mean field approach only a single solution n_0 exists, whereas multiple solutions are found within the ansatz of Lesanovsky et al. [220]. Before we discuss the properties of the stationary state of Eq. (10.16), we want to emphasize, that the presence of multiple solutions $n_0^{(m)}$ does not imply non uniqueness of the stationary state. In such cases, fluctuations, which we neglected in the derivation of Eq. (10.21), are responsible for

distributing population among the different mean field solutions.

10.2.2 Fluctuations around the mean

As illustrated by the last remark in the previous subsection, the dynamics implied within our model can be complicated, the stationary state is however uniquely defined and well known. We will show that the mean field solutions $n_0^{(m)}$ are local maxima in the probability distribution $p(n_\mathrm{e})$ in the stationary state and that fluctuations around this density are characterized by

$$\chi^{(m)} = \frac{\partial_{n_\mathrm{e}}(P-D)|_{n_\mathrm{e}=n_0^{(m)}}}{P(n_0^{(m)})}. \tag{10.23}$$

We show this by considering a finite size example. The probabilities p_{N_e} are dynamically coupled along a one dimensional chain and therefore the stationary state trivially fulfills the detailed balance condition

$$\frac{p_{N_\mathrm{e}+1}}{p_{N_\mathrm{e}}} = \frac{(N_\mathrm{a}-N_\mathrm{e})\langle\Gamma_\uparrow\rangle(N_\mathrm{e}/L^2)}{(N_\mathrm{e}+1)\langle\Gamma_\downarrow\rangle((N_\mathrm{e}+1)/L^2)} \tag{10.24}$$

$$\approx \frac{P(N_\mathrm{e}/L^2)}{D(N_\mathrm{e}/L^2)}. \tag{10.25}$$

Therefore the probabilities are extremal at the stationary state fillings $N_0 = n_0 L^2$ and to lowest order in Δ_N we find $p_{N_0+\Delta N} = \prod_{k=1}^{\Delta_N}(1+k\chi)p_{N_0}$. From this we can immediately derive a limit expression for the probability distribution of the density in thermodynamic limit

$$\begin{aligned}\log(p_{N_0+\Delta_N}) &= \sum_{k=1}^{\Delta_N}\log(1+k\chi) + \log(p_{N_0}) \\ &\approx \chi\frac{(\Delta_N+1)\Delta_N}{2} + \log(p_{N_0}) \qquad (10.26)\\ \Rightarrow p(n_0^{(m)}+\Delta_n) &= p(n_0^{(m)})e^{\Delta_n^2\chi L^2/2}. \qquad (10.27)\end{aligned}$$

As expected only fixed points with $\chi < 0$ are maxima of the stationary state distribution with width $w = \frac{\sqrt{|\chi|}}{L}$. If only a single stationary point is found, we can now characterize whether the number fluctuations are sub- or super- Poissonian as a probe for antiblockade and blockade

$$Q = \frac{\Delta^2_{N_\mathrm{ex}}}{\langle N_\mathrm{ex}\rangle} - 1 = \frac{1}{|\chi| n_0} - 1. \tag{10.28}$$

In the limit of low excitation density and weak driving the loss rate is given by $D(n_\mathrm{e}) \approx n_\mathrm{e}\Gamma$. We can then further simplify and find

$$Q = \frac{\partial_{n_\mathrm{e}} P|_{n_0}}{\Gamma - \partial_{n_\mathrm{e}} P|_{n_0}}, \tag{10.29}$$

from which we see, that the positive slope of P is the origin of super Poissonian statistics here.

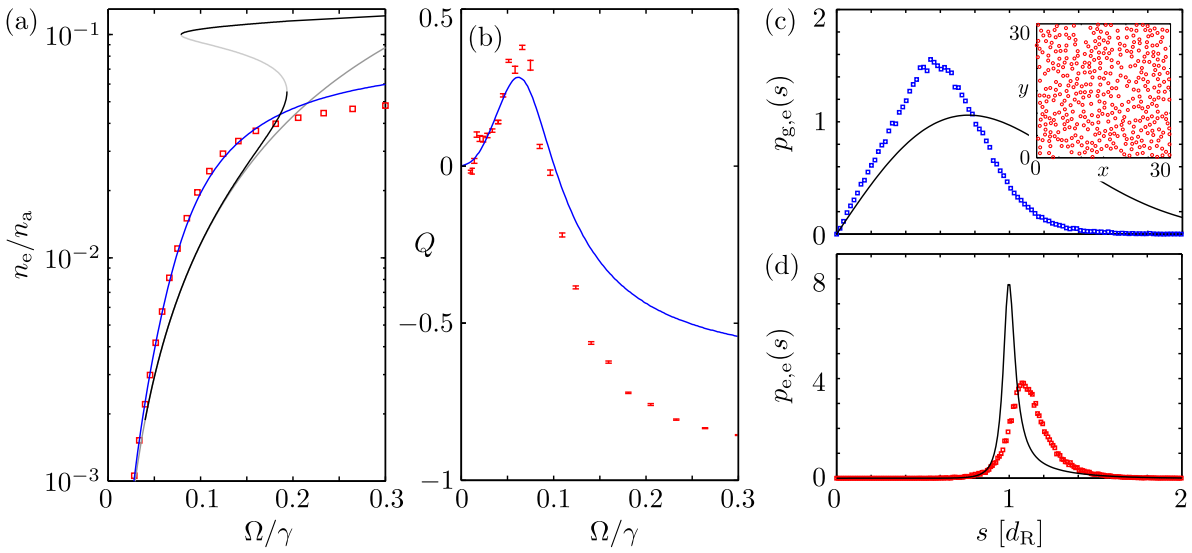

Figure 10.3: (a) Atomic excitation probability in the stationary state for $n_{at} = 10, C_6 = -\Delta_0 = 4\gamma$ and $\Gamma = 0.1\gamma$. Finite system size dMC results (red squares) are compared with our mean field approach (blue), the δ-approach (black/gray) and the result for non interacting atoms (black dashed). (b) Mandel Q parameter for the same system as in (a). (c) and (d) show the distribution functions $p_n(s)$ and $p_n^{(e)}$ for $\Omega = 0.3\gamma$. The system is filled with excitations, see inset of (c) for a snapshot, that correlations between excited atoms become relevant and our initial assumption for the distribution functions fails.

10.2.3 Remark on bistability

Assume $P(n_e)$ and $D(n_e)$ such, that we find two mean field solutions $n_0^{(m)}$ with $\chi^{(m)} < 0$. Whereas the probability distribution $p(n_e)$ in the stationary state exhibits two pronounced local maxima, one of the two will in general be dominant. In thermodynamic limit only a single peaked distribution is observed and we find no bistability in the sense of a bimodal distribution. To show this again consider the finite size system. Be $N_0^{(1)} < N_0^{(2)}$ we find

$$\frac{p_{N_0^{(2)}}}{p_{N_0^{(1)}}} \approx \prod_{N_e=N_0^{(1)}}^{N_0^{(2)}} \frac{P(N_e/L^2)}{D(N_e/L^2)}. \tag{10.30}$$

Taking the logarithm and approximating the right hand sight by an integral yields

$$\log(p_{N_0^{(2)}}/p_{N_0^{(1)}}) \approx \int_{N_0^{(1)}}^{N_0^{(1)}} dN_e \, \frac{P(N_e/L^2)}{D(N_e/L^2)} \tag{10.31}$$

$$= L^2 \int_{n_0^{(1)}}^{n_0^{(1)}} dn_e \, \frac{P(n_e)}{D(n_e)}. \tag{10.32}$$

As the integral is independent of system size the right hand side increases with L^2 and to the thermodynamic limit one of the two densities must be dominant. Thus there cannot be a bimodal probability distribution in the stationary state of a system in the thermodynamic limit.

Note that this strong statement is only true for the stationary state and at transient times

a bimodal distribution can emerge. Furthermore bistability in mean field approaches should be considered with caution. We here assume that correlations between excitations are only short range but, which is in contrast to the assumption that a single number, the mean density of excitations quantifies the state of an extended system. Instead we expect the emergence of domain like structures in large, bistable systems, where the state is ill characterized within a mean field approach that assumes a spatially homogeneous situation. Within our ansatz for the off resonantly driven Rydberg gas, we only find single critical densities and therefore do not face this problem.

10.3 Benchmarking

To benchmark our mean field theory and improved ansatz for the distance distribution we use dMC simulations, cf. Appendix 15.2, for systems up to size 35×35 and atomic densities of $n_{\mathrm{at}} = 10$. In Fig. 10.3(a) we show results for the atomic excitation probability in the regime $n_{\mathrm{e}}/n_{\mathrm{a}} \ll 1$. Parameters are chosen identical to other figures in this chapter. In the limit of very weak excitation $\Omega \to 0$ the exact approach and the δ-function ansatz by Lesanovsky et al. yield the correct Ω^2 scaling. The system then enters the regime of antiblockade, where the growth of excitation probability exceeds the non interacting atom results (lower black). Whereas our approach nicely follows the extracted dMC results, the approach by Lesanovsky et al. yields three mean field solutions, of which two are stable. None agree with the results from dMC simulations.

Fig. 10.3(b) shows the Mandel Q parameter for the same system and we find qualitative agreement of our approach and numeric results. The accuracy of the mean field treatment decreases as the density of excitations increases and the system enters the regime of strong correlations. Our initial assumption of uncorrelated excitations is not valid anymore in this regime, as is illustrated by the extracted distance distribution in Fig. 10.3(c) for $\Omega/\gamma = 0.3$ that differ significantly from the ansatz.

We here want to relate back to our discussion in the outlook of chapter 8 regarding phase transitions in two dimensional hard disc gases. Choosing the blockade radius as the relevant disc size, $d_{\mathrm{B}} = \sqrt[6]{2}$ for our parameters, we find for the filling fraction f

$$f = n_{\mathrm{e}} \pi \frac{d_{\mathrm{B}}^2}{4} \approx 0.5 \ll f_{\mathrm{C}}, \tag{10.33}$$

at the strongest driving we consider $\Omega/\gamma = 0.3$. We therefore do not expect to find long range correlations of excitations. According to the predictions of Eq. (8.25), notably for resonant excitation and a hard disc interaction potential, the atomic density we consider is three orders of magnitude to small, to observe the phase transition towards a hexagonal crystal. The deviations in the distribution functions $p_{\mathrm{g,e}}$ and $p_{\mathrm{e,e}}$ thus originate from liquid like correlations of the many body system.

Conclusion

In this chapter we derived dynamic mean field equations for dense ensembles of atoms driven to Rydberg states and found very good agreement with numerically exact simulations of the full RE system. Our approach is based on an improved ansatz for correlations between ground and excited atoms, which were treated incorrectly in lowest order of the excitation density in [221]. The mean field dynamics we derive, always have unique solutions and we showed, that the fluctuations around these densities can be characterized correctly within our approach.

We have thus developed a very simple and easy to evaluate tool, suitable for comparison with different experimental results [18, 222, 84]. Further research regarding the time scales of relaxation towards the stationary state is needed, to show, whether our mean field results significantly improve on the results presented in [222].

In agreement with extensive numerical simulations in [15] we found no evidence for bistability, in the sense of a bimodal distribution in the stationary state of off resonantly driven Rydberg gases. We furthermore showed, that even the presence of multiple solutions for the dynamic mean field equation, does not give rise to bistability in the thermodynamic limit.

Chapter 11

Bistability in the Dissipative Transverse Ising Model

Studying the dynamics and stationary state of off resonantly driven Rydberg gases, has revealed a multitude of effects from antiblockade to the emergence of complex behavior such as glassiness and bistability. However, most work, including our own approach in the previous two chapters, relies on major approximations such as the restriction to classical, incoherent dynamics. Furthermore, the coexistence of different effects and experimental limitations render the interpretation difficult and often vague. We therefore want to study a model system for antiblockade, that is as simple as possible: the dissipative transverse Ising model DTIM [224].

The DTIM is a one dimensional spin model defined by

$$\mathcal{H} = \sum_j [h\hat{\sigma}_x^{(j)} - J\hat{\sigma}_z^{(j)}\hat{\sigma}_z^{(j+1)}], \tag{11.1}$$

with transverse field h and ferromagnetic next neighbor coupling $J > 0$. $\hat{\sigma}_\mu^{(m)}$ are derived from the Pauli matrices, and fulfill the commutation relations $[\hat{\sigma}_i^{(m)}, \hat{\sigma}_j^{(n)}] = 2i\delta_{m,n}\varepsilon_{i,j,k}\hat{\sigma}_k^{(m)}$. In addition, local incoherent spin flips are introduced via Lindblad generators

$$\hat{L}^{(j)} = \sqrt{\Gamma}\hat{\sigma}_-^{(j)}, \tag{11.2}$$

which break the inversion symmetry regarding z. Ates et al. pointed out the relation of the DTIM to Rydberg physics [224]. By representing the two levels via a spin degree of freedom, $\hat{\sigma}_{\mathrm{z}}^{(j)} = 2(\hat{\sigma}_{\mathrm{rr}}^{(j)} - \frac{1}{2})$, we find for the Hamiltonian

$$\mathcal{H} = \sum_j h\left(\hat{\sigma}_{\mathrm{rg}}^{(j)} + \hat{\sigma}_{\mathrm{gr}}^{(j)}\right) - 4J\left(\hat{\sigma}_{\mathrm{rr}}^{(j)} - \frac{1}{2}\right)\left(\hat{\sigma}_{\mathrm{rr}}^{(j+1)} - \frac{1}{2}\right) \tag{11.3}$$

$$= \sum_j h\left(\hat{\sigma}_{\mathrm{rg}}^{(j)} + \hat{\sigma}_{\mathrm{gr}}^{(j)}\right) - 4J\hat{\sigma}_{\mathrm{rr}}^{(j)}\hat{\sigma}_{\mathrm{rr}}^{(j+1)} + 4J\hat{\sigma}_{\mathrm{rr}}^{(j)} - J. \tag{11.4}$$

The parameters of the Rydberg system therefore have to be chosen as $V_{\mathrm{NN}} = -4J, \Omega = h$ and $\Delta_0 = 4J$. The finite lifetime of the Rydberg excitation naturally maps onto the incoherent spin flip process.

Mean field results predict a regime of parameters, where two stable solutions are found. One solution named inactive, with spins on average pointing downwards $\langle\sigma_z\rangle \approx -1$ and another one named active, with $\langle\sigma_z\rangle \approx 0$. The naming originates from the realization with

Rydberg atoms, where spontaneous fluorescence is strong in the active phase. Ates et al. and later Hu. et al used quantum jump Monte Carlo simulations to gain numerically exact results for one dimensional systems up to size $L = 18$ [225]. Both found signatures of bistable behavior in statistical properties such as the Mandel Q parameter and the emergence of spatial correlations. Systems were however to small to extrapolate results in the thermodynamic limit.

For the benchmarking of our RE model for the resonantly driven lattice gas in Chapter 6, we used MPS based TEBD methods generalized to dissipative systems. The problem at hand seems ideally suited for MPS based methods. First of all, it is a lattice model and second, we are only interested in effects of the next neighbor interaction. However it is a non equilibrium problem and positive results regarding the representation of ground states with MPS do not carry over [110]. The dynamics of the dissipation free limit of the DTIM ($\Gamma \to 0$) has been extensively studied by Calabrese et al. [226]. One important result is, that entanglement entropies grow linearly in time after a quench of the magnetic field h [227], and such a scaling renders the MPS based simulations infeasible [228]. On the other hand the inclusion of dissipation is expected to restrict the growth of entanglement within the system.

We will begin our discussion with a review of the mean field results by Ates et al. and the results on the dissipation-free limit of Calabrese. Afterwards we consider the feasibility of the TEBD approach and show that the presence of dissipation, significantly suppresses the growth of entanglement and thereby allows us to study systems as large as $L = 40$. The dynamics of magnetization $\langle \hat{\sigma}_z \rangle$ in large systems reveals the appearance of long range correlations, which we quantify by extracting the divergent behavior of correlation lengths. Finally we show, that the stationary magnetization distribution becomes increasingly bimodal with increasing system size.

11.1 Analytic Insights

11.1.1 Gutzwiller ansatz

The connection of the dissipative Ising model with Rydberg physics was pointed out by Ates et al. in [197]. Besides exact diagonalization of few spin systems, they calculated the mean field phase diagram of the model. By imposing a factorization of the density matrix in local factors

$$\varrho_{MF} = \bigotimes_j r^{(j)}. \tag{11.5}$$

Higher order cumulants vanish and correlations factorize, for example

$$\langle \hat{\sigma}_x^{(m)} \hat{\sigma}_z^{(m+1)} \rangle = \langle \hat{\sigma}_x^{(m)} \rangle \langle \hat{\sigma}_z^{(m+1)} \rangle. \tag{11.6}$$

This factorization is used in the dynamic equations for the first order correlations, for example

$$\begin{aligned} \frac{d}{dt} \langle \hat{\sigma}_x^{(m)} \rangle = &-\frac{\Gamma}{2} \langle \hat{\sigma}_x^{(m)} \rangle \\ &- 2J(\langle \hat{\sigma}_x^{(m)} \hat{\sigma}_z^{(m+1)} \rangle + \langle \hat{\sigma}_x^{(m)} \hat{\sigma}_z^{(m-1)} \rangle), \end{aligned} \tag{11.7}$$

which in general couple to higher order correlations for $J \neq 0$. By factorizing all higher correlations and imposing translation invariance via $\langle \hat{\sigma}_\mu^{(n)} \rangle = \langle \hat{\sigma}_\mu \rangle$ we find

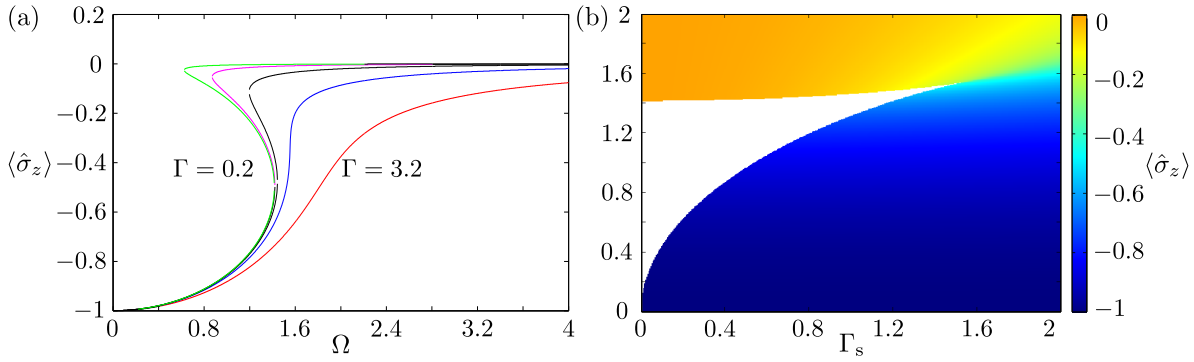

Figure 11.1: Solutions to the mean field Eq. (11.11) for $J = 1$. (a) Magnetization as function of the transverse field Ω for fixed incoherent loss $\Gamma = 0.2, 0.4, 0.8, 1.6, 3.2$. (c) Mean field phase diagram for the magnetization. In the white region more than one solution exists.

$$\frac{d}{dt}\langle\hat{\sigma}_x\rangle = -\frac{\Gamma}{2}\langle\hat{\sigma}_x\rangle - 4J\langle\hat{\sigma}_y\rangle\langle\hat{\sigma}_z\rangle, \tag{11.8}$$

$$\frac{d}{dt}\langle\hat{\sigma}_y\rangle = -\frac{\Gamma}{2}\langle\hat{\sigma}_y\rangle - 2h\langle\hat{\sigma}_z\rangle + 4J\langle\hat{\sigma}_x\rangle\langle\hat{\sigma}_z\rangle, \tag{11.9}$$

$$\frac{d}{dt}\langle\hat{\sigma}_z\rangle = -\Gamma(\langle\hat{\sigma}_z\rangle + 1) + 2h\langle\hat{\sigma}_y\rangle. \tag{11.10}$$

Stationary solutions are obtained by solving the resulting cubic equation for the magnetization

$$\Gamma^2 + \langle\hat{\sigma}_z\rangle(\Gamma + 2h^2) + 64J^2\langle\hat{\sigma}_z\rangle^2(1 + \langle\hat{\sigma}_z\rangle) = 0. \tag{11.11}$$

Solutions to this mean field equation are displayed in Fig. 11.1 for a fixed coupling $J = 1$. For most of the parameter space only a single real solution exists. For small $\Gamma < 1.5$ one finds an extended parameter region, where three solutions to the mean field equation exist. The middle one of these solutions is found to be instable towards linear deviations. All solutions are within the interval $[-1, 0]$.

11.1.2 Unitary limit and exact solution

The limit of small decay is not only interesting because it shows the largest interval of bistability in the mean field treatment, but even more because for $\Gamma = 0$ the model is exactly *solvable*. We introduce a Jordan-Wigner transformation from spins to fermions via the mapping

$$\hat{c}_j^\dagger = (\hat{\sigma}_y^{(j)} + i\hat{\sigma}_z^{(j)})/2 \prod_{k=1}^{j-1} \hat{\sigma}_x^{(k)}, \tag{11.12}$$

where fermions are introduced in the basis parallel to the field h. The resulting Hamiltonian is bilinear in fermionic operators

$$\mathcal{H} = \sum_j \Big[2h\hat{c}_j^\dagger\hat{c}_j - J(\hat{c}_j^\dagger - \hat{c}_j)(\hat{c}_{j+1}^\dagger + \hat{c}_{j+1})\Big], \tag{11.13}$$

where we have neglected boundary terms and constant energy offsets. The Hamiltonian can be diagonalized in momentum space and one finds the dispersion relation of the transverse

Ising model

$$\varepsilon(k) = 2\sqrt{J^2 + h^2 - 2Jh\cos(k)}. \tag{11.14}$$

From the dispersion relation we can extract the speed of sound

$$u = \max_k |\partial_k \varepsilon(k)| = 2J \min(h/J, 1), \tag{11.15}$$

which in the regime relevant to us is given by $u = 2h$.

The Hamiltonian is bilinear in the fermionic operators and as discussed in 5 it is therefore sufficient to discuss the dynamics of two point correlation functions. Calabrese et al. have used this to study the non equilibrium dynamics after a quench of the transverse field at time $t = 0$ [226]. The initial state before the quench is chosen as the ground state at field h_0. We are interested in cases $h_0 < J$, such that the ground state displays ferromagnetic ordering in z direction and is two fold degenerate. With the Rydberg system in mind we here consider the initial state with all spins pointing down $\langle \hat{\sigma}_z \rangle = -1$. It has been shown by Calabrese, that for a quench even within the ordered phase, $h_0 \to h < J$, the magnetization decays exponentially towards zero at late times.

We now want to connect these results with the dissipative Ising model. First of all mapping the system with dissipation is not exactly solvable via Jordan-Wigner transformation due to string terms in the Lindblad operator

$$\hat{L}_j = \frac{\sqrt{\Gamma}}{2}[2\hat{c}_j^\dagger \hat{c}_j - 1 - i(\hat{c}_j^\dagger + \hat{c}_j) \prod_{k=1}^{j-1} (2\hat{c}_k^\dagger \hat{c}_k - 1)]. \tag{11.16}$$

Nonetheless, in the limit of $\Gamma \to 0$ we expect the stationary state of the dissipative Ising model to reflect the quench behavior of the closed Ising system. The magnetization should relax towards $\langle \hat{\sigma}_z \rangle = 0$, corresponding to the upper solution of the mean field equation and the symmetry regarding z, should be reestablished despite the symmetry broken initial state.

11.2 TEBD Simulation of the Dissipative Ising Model

Exact diagonalization in combination with quantum jump MC has been used to calculate dynamics and find the stationary state for systems up to size $L = 18$ for the DTIM in [224, 229]. We here will discuss the use of MPS based TEBD for this specific problem and present results for system sizes up to $L = 40$. The details of using TEBD in open systems are described in Appendix 13.2.2. To begin with, we discuss the feasibility of TEBD simulations for the dissipative transverse Ising model. We therefore investigate the dynamics of entanglement entropies and the important effect of dissipation as a means to suppress entanglement growth within the system. After establishing TEBD as a viable method, we will present results for large systems regarding the dynamics of magnetization and investigate the emergence of long range correlations in the stationary state.

11.2.1 Dynamics of correlations and entropies

In Chapters 2 to 4 we used algorithms based on matrix product states (MPS) to effectively calculate the ground state properties of one dimensional systems [109]. The feasibility of this approach is strongly supported by research on MPS in the context of DMRG for one dimensional systems in the last decade [110]. In Appendix 13.2.2 we review results regarding the scaling of necessary resources to approximate a given state with a MPS. An important

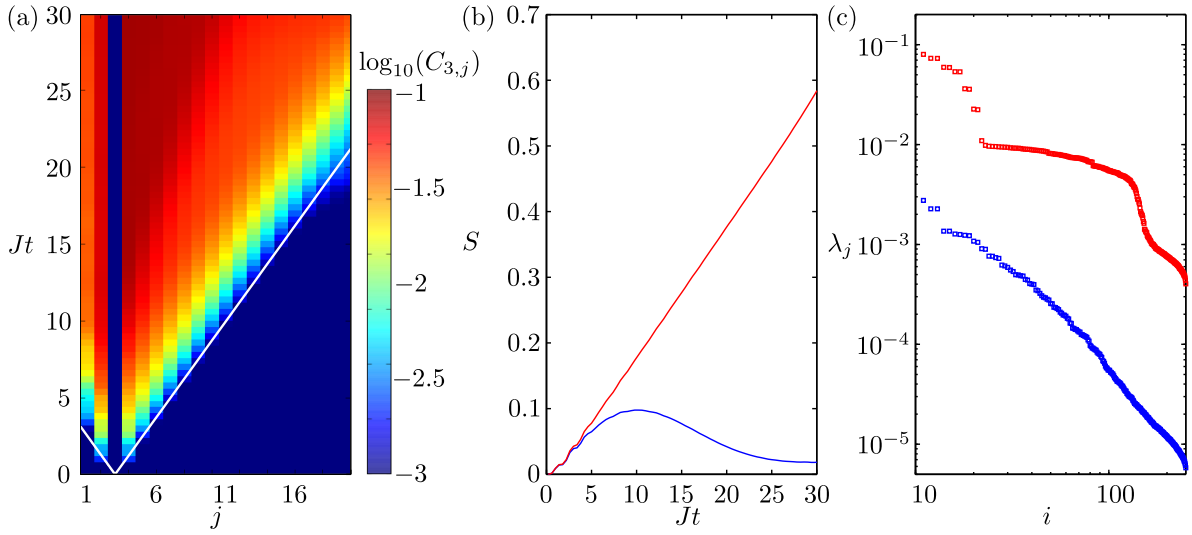

Figure 11.2: TEBD results for the dynamics of an obc chain of length $L = 32$ and $h/J = 0.2$. (a) Second order cumulants $C_{3,j}$ in the dissipation free limit $\Gamma = 0$. Correlations spread within a light cone of speed $u = 2h$. (b) Operator space entanglement entropy $S_{L/2}$ for the bipartition of the system as a function of time. Whereas the entropy increases linearly in absence of dissipation (red) it is strongly suppressed with $\Gamma/J = 0.02$ (blue). (c) Spectrum of Schmidt coefficients λ_i at $Jt = 30$. The maximum bond dimensions for the simulation was $\chi_{\max} = 250$.

figure of merit is the entanglement entropy of a bipartition [228]

$$S_\alpha^{\mathrm{A,B}} = \frac{1}{1-\alpha} \log[\mathrm{Tr}(\varrho_{\mathrm{A}}^\alpha)], \quad \text{with } \varrho_{\mathrm{A}} = \mathrm{Tr}_{\mathrm{B}}(\varrho). \tag{11.17}$$

Unless noted otherwise, we use the equal size bipartition with A representing the left $L/2$ sites and B the sites on the right. The general Renyi entropies in Eq. (11.17) are identical to the von Neumann entropy for $\alpha = 1$. The necessary resources of an MPS calculation scale polynomially with the bond dimension χ of the MPS, which in turn is exponentially related to the entropies by

$$\chi \sim e^S. \tag{11.18}$$

For short ranged Hamiltonians and gapped ground states, area laws have been established that imply scaling of the entanglement entropies with system size $\mathcal{O}(1)$ in one dimensional systems [110]. Even models with a vanishing energy gap and critical behavior in general have entropies scaling as $\mathcal{O}(\log(L))$ with system size in 1D [230]. These properties have established MPS as the standard tool for equilibrium problems in one dimension and naturally the question arises whether this carries over to non equilibrium situations.

For the class of problems that can be described by a sum of Hamiltonians with local support of at most two adjacent lattice sites, Vidal proposed an efficient algorithm for the simulation of dynamics [165]. The efficiency again relies on MPS approximations that require resources exponentially scaling with entanglement measures. It was quickly pointed out that in generic one dimensional systems with a Lieb-Robinson bound [175], entanglement can not grow faster than $\mathcal{O}(t)$, which however is not strong enough to render the simulation efficient [231, 232]. Meanwhile numeric studies found that this bound often is sharp and linear entanglement growth in time, strongly limits TEBD algorithms [233]. A nice example is the dynamics of a

chain of coupled harmonic oscillators. The problem can be solved analytically, but entropies increase linearly in time and simulations using TEBD are thus not feasible [234].

Similarly it has been shown for the transverse Ising model that after a quench of the magnetic field, $h_0 \to h$, the entanglement entropy increases linearly in time [227]. After a transient time, it becomes quasi stationary at a value that linearly increases with system size. The limit $\Gamma \to 0$ for the dissipative Ising model, is therefore not accessible via MPS based TEBD simulations. In Fig. 11.2(a) we show the spreading of correlations in a finite system of size $L = 32$. The finite speed of sound $u = 2h$ imposes a Lieb-Robinson bound that results in a linear initial growth of entanglement entropy as displayed in Fig. 11.2(b). This growth of entropy stops when the light cone extends over the entire system and $ut > L$. Considering the system in the presence of decoherence $\Gamma \neq 0$, we make the important observation that the emergence of large entropies is strongly suppressed. This is illustrated in Fig. 11.2(b).

11.2.2 Algebraic decay of Schmidt spectrum and implications

In panel (c) if Fig. 11.2 we show the Schmidt spectrum of the bipartition for $\chi_{\max} = 250$. Dissipation strongly reduced the weight of the tail of Schmidt coefficients compared to the dissipation free case and we find algebraic decay $\lambda_j \sim j^{-\beta}$ with $\beta = 2 \pm 0.2$ for the specific parameters shown. In Appendix 13.4 we discuss in more detail the relationship between Renyi entropies

$$S_\alpha = \frac{1}{1-\alpha} \log \big(\sum_{j=1}^{2^L} \lambda_j^\alpha \big) \tag{11.19}$$

and the feasibility of approximation with MPS [228]. We here want to discuss the relation between algebraic decay of Schmidt coefficients λ_j and scaling of entropies. For simplicity we assume

$$\lambda_j = N_{L,\beta} j^{-\beta}, \quad \beta > 0 \tag{11.20}$$

for the entire spectrum. Note that the maximal number of non zero Schmidt coefficients is bounded by the size of the system. For a system of length L and a local dimension of d, for a cut in the center we must consider $4^{L/2} = 2^L$ values. First of all we determine the norm

$$N_{L,\beta}^{-1} = \sum_{j=1}^{2^L} j^{-\beta} = H(2^L, \beta), \tag{11.21}$$

where $H(m, n)$ is the generalized harmonic number. For $\beta > 1$ the limit $L \to \infty$ exists and is finite. For $\beta = 1$ the normal harmonic number fulfills

$$H(2^L, 1) = \ln(2^L) + \gamma = L \ln(2) + \gamma, \tag{11.22}$$

where $\gamma \approx 0.58$ is the Euler-Mascheroni constant. For $\beta < 1$ it is divergent with

$$H(2^L, \beta) = \frac{2^{L(1-\beta)}}{1-\beta}. \tag{11.23}$$

Now we turn to the scaling of the Renyi entropies, which using Eq. (11.20) can be expressed as

$$S_\alpha = \frac{1}{1-\alpha} \log \big(H(2^L, \alpha\beta) / H(2^L, \beta)^\alpha \big). \tag{11.24}$$

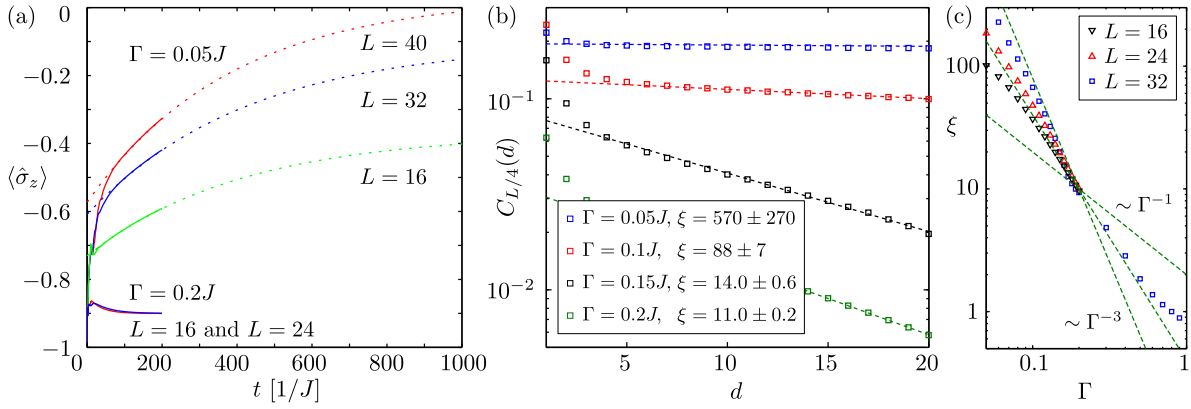

Figure 11.3: TEBD results for magnetization dynamics and correlations in finite size chains up to length $L = 40$ with maximum bond dimension of $\chi_{\max} = 300$ for fixed transverse field of $h = 0.5$. (a) Dynamics of magnetization for weak and strong dissipation and different system sizes. Dotted lines are extrapolations of numeric data towards the stationary state. (b) Spin spin correlations in system of size $L = 40$ at $t = 200/J$, dashed lines are exponential fits to the decay at intermediate distance. (c) Scaling of the correlation length ξ with dissipation strength Γ for various systems of size $L = 16, 24, 32$. Dotted lines indicate algebraic relations with exponent $-1, -2$ and -3.

With above limiting expressions for the harmonic number one can easily show that for $\beta < 1$ all entropies diverge polynomially. Exactly for $\beta = 1$ only the $\alpha < 1$ entropies diverge polynomially, whereas $S_{\alpha>1}$ diverges logarithmically. The most relevant case for us is $\beta > 1$, here the denominator within the logarithmic is trivially constant but the nominator depends on $\alpha\beta$. For $\alpha\beta > 1$ the entropy is constant, for $\alpha\beta = 1$ it diverges logarithmically and for $\alpha\beta < 1$ the divergence is polynomial in system size.

To conclude, for the algebraic decay of Schmidt coefficients we find for the dissipative Ising model with $\beta \approx 2$ all $S_{\alpha\geq 1}$ Renyi entropies are constant in system size. However we can always find $\alpha < 1/\beta$ such that S_α diverges polynomially. Following the results of Schuch et al. [228], the problem at hand is therefore in the class of indefinite problems, which are a priori neither infeasible nor feasible.

11.2.3 Dynamics of magnetization and correlation length

Using the established TEBD method we will now discuss the dynamics of overall magnetization and the stationary state correlations in a parameter regime, where the mean field ansatz yields bistable solutions [235]. Specifically we will focus on tuning the decay rate within the interval $\Gamma = (0.05-0.2)J$ and restrict to results for a fixed transverse field $h = 0.5J$. When considering the unitary dynamics alone, we therefore fixed the speed of sound $u = 2h = 1J$.

TEBD simulations of the dissipative Ising model can go well beyond system sizes that are accessible within approaches that treat the full Hilbert space. Quantum jump Monte Carlo simulations on this system were so far limited to $L = 12$ and $L = 18$ respectively [235, 225]. We here study systems of size up to $L = 40$ and maximal bond dimensions of $\chi_{\max} = 300$. The required bond dimension increases approximately linear with system size as we expect a logarithmic scaling of entropies with the system size based on our discussion in the previous subsection.

In Fig. 11.3(a) we show results for the time evolution of $\langle \hat{\sigma}_z \rangle$ in the center of the system.

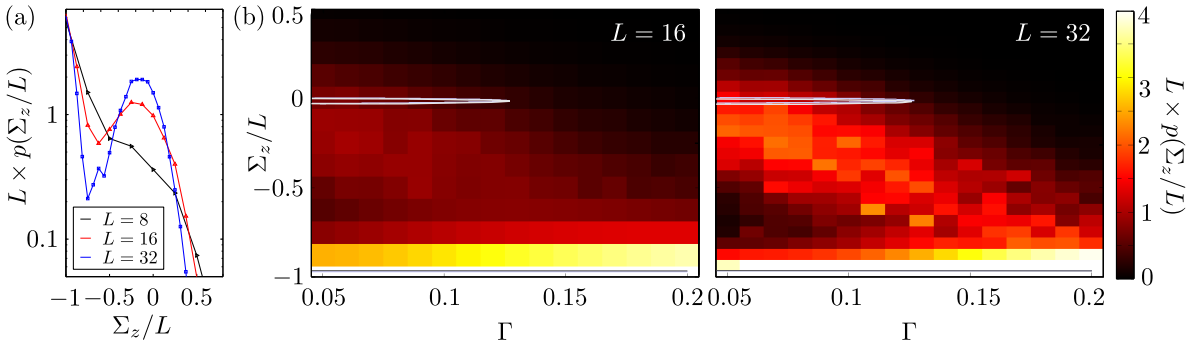

Figure 11.4: (a) Probability distribution $p(\Sigma_z)$ as a function of system size for $tJ = 200$ and $h/J = 0.5$ and $\Gamma/J = 0.05$. (b) $p(\Sigma_z)$ for small $L = 16$ and large $L = 32$ system over the range $\Gamma \in [0.05, 0.2]$. The solid lines indicate the mean field solutions.

For large $\Gamma = 0.2J$ we show results for systems of size $L = 16$ and $L = 24$ and find that they are nearly indistinguishable. On the contrary, for small $\Gamma = 0.05J$, within the mean field bistable regime, results are far from converged in system size and relaxation time is almost an order of magnitude larger than the single atom relaxation time $1/\Gamma = 20$. We extrapolated the data assuming an exponential relaxation towards the steady state value of the magnetization

$$\langle \hat{\sigma}_z(t) \rangle = \langle \hat{\sigma}_z \rangle_\infty [1 - A[\exp(-t/\tau)]]. \tag{11.25}$$

The absence of convergence for large system sizes is related to an increase of the length scale of correlations. We here consider spin spin correlations

$$C_j(d) = \langle \hat{\sigma}_z^{(j)} \hat{\sigma}_z^{(j+d)} \rangle - \langle \hat{\sigma}_z^{(j)} \rangle \langle \hat{\sigma}_z^{(j+d)} \rangle, \tag{11.26}$$

that can be easily calculated within our MPS approach. The results for a system of size $L = 40$ at time $t = 200/J$ are shown in Fig. 11.3(b). To reduce the effects of boundary conditions we consider only correlations of spins in the center half of the system, neglecting the left most and right most quarter of the system. For intermediate distances we find exponentially decaying correlations that we fit with

$$C_{L/4}(d) \sim \exp[-d/\xi]. \tag{11.27}$$

The extracted correlation length is strongly dependent on Γ. To quantify the relation we have extracted ξ for various system sizes over the range $\Gamma \in [0.05, 1]$ and display the results in Fig. 11.3(c). We have added the algebraic relation $\Gamma^{-\alpha}$ with $\alpha = 1, 2, 3$ to guide the eye.

11.3 Bistability

So far we concentrated on single or two site correlation functions that are sufficient to determine the mean magnetization and its fluctuations, which could be characterized by the Mandel Q parameter. We here go beyond this and calculate the full probability distribution of the magnetization, which is defined as

$$p(\Sigma_z) = \mathrm{Tr}(\varrho \hat{P}_{\Sigma_z}), \tag{11.28}$$

where $\hat{P}_{\Sigma_z}$ is the projector on the subspace of fixed magnetization $\Sigma_z \in [-L, -L+1, \cdots L-1, L]$. Evaluating this expectation value is non trivial with our MPS based algorithm as $\hat{P}_{\Sigma_z}$

is a global operator, which can not be factorized in an efficient way. One realization of $\hat{P}_{\Sigma_z}$ is given by

$$\hat{P}_{\Sigma_z} = \sum_{(S_1,\cdots,S_L)|\sum_{S_i}=\Sigma_z} \prod_j \left[(1+S_j\hat{\sigma}_z^{(j)})/2\right], \tag{11.29}$$

with $S_i \in [1,-1]$. Whereas the single terms in the sum are product operators that are easy to evaluate, their number scales as $\binom{L}{(\Sigma_z+L)/2}$ and is intractable for systems larger than $L = 20$. We here calculate the exact sum if the number of states does not exceed $M = 1000$. Beyond this limit we generate a random sample of M spin configurations of a fixed magnetization and evaluate an approximation for $p(\Sigma_z)$ that has small fluctuations. For the intermediate system sizes we present here, our approach is feasible, but note that for larger systems the weight of a single spin configuration reduces exponentially and the limitations of numeric precision are quickly reached.

From the discussion of two site correlations we know that at $\Gamma/J = 0.05$ long range correlations extend over the entire system. For these parameters we show $p(\Sigma_z/L)$ in Fig. 11.4(a) for systems of size $L = 8, 16$ and 32. For the two larger systems the distribution has two maxima, one at maximal negative magnetization and another one slightly below the paramagnet. The emergence of the second, broad peak is already apparent for the smallest size system. In Fig. 11.4(b) we show that the bistability is related to the divergence of the correlation length. For the intermediate and large system we plot the probability distribution as a function of Γ and find a smooth crossover from the bimodal distribution at $\Gamma = 0.05$ to the monomodal distribution at $\Gamma = 0.2$. We added the solutions of the mean field ansatz, which in contrast to our results suggest a discontinuous first order transition, whereas Fig. 11.4(b) suggests a smooth transition.

Conclusion

In this chapter we demonstrated, that the numerical TEBD method originally developed for dissipation-free systems [230], is a valuable tool for the study of one dimensional lattice systems under the influence of dissipation. Whereas simulation of time evolution is infeasible without dissipation, we found strong evidence that dissipation sufficiently suppresses the growth of entanglement to render our approach feasible. The approximations introduced by the truncation of the MPS to finite bond dimensions are well controlled in contrast to previously applied mean field approaches.

From the TEBD results we found that long range spin-spin correlations emerge in the stationary state [225], where the associated length scale is divergent for small dissipation rates $\Gamma \to 0$. Previous results on the magnetization in the stationary are dominated by finite size effects for the small systems that were under consideration [235, 225]. In this lattice system, antiblockade gives rise to a bimodal distribution in the stationary state of the extended system, however the transition towards this bistable region appears to be smooth in contrast to the prediction of a first order transition made within mean field theory.

Clearly, a number of interesting questions remain unanswered by this discussion. For example the emergence of bistability in the extended systems, could again vanish for systems of even larger extend. We already find evidence for this and observe an increase in the amplitude of the peak at zero magnetization in Fig. 11.4(b) in contrast to the constant amplitude of the second maximum. Furthermore we would like to further investigate the divergent behavior of correlation length when approaching the dissipation-free limit and qualitatively understand the observed scaling $\xi \sim \Gamma^{-(1\cdots3)}$. Finally, new results obtained with a variational ansatz for the stationary state can be assessed with the established TEBD algorithm [236].

Chapter 12

Two Rydberg-Polariton Dynamics

Over the course of the last chapters we have discussed the properties of atomic media driven from their weakly interacting ground state to strongly interacting Rydberg states via classical light fields. In the following chapter we will change our point of view and investigate the properties of photons in the presence of strong Rydberg interactions.

In Sec. 1.4 we introduced EIT and the concept of the DSP quasiparticle to describe the propagation of light in coherent atomic media. The DSP originates from the strong coupling of light and matter and is a coherent superposition of electric field excitation $\hat{\mathcal{E}}$ and spin polarization $\hat{\mathcal{S}}$. It inherits the interaction properties of its atomic constituent, however for conventional EIT configurations the atomic interaction is weak and short range. Pritchard et al. combined the idea of DSPs with strongly interacting Rydberg states and thereby paved the way towards extraordinary non linear optics and strong interactions on the single photon level [237].

Conventional EIT employs a metastable spin state to form the three level lambda system required. For Rydberg EIT this level is replaced with a large principal quantum number n Rydberg state as illustrated in Fig. 12.1(a). Like the spin state, the Rydberg state has a long lifetime, but moreover it features strong and long range interactions with other Rydberg excited atoms as discussed in Sec. 1.3. To describe the propagation of excitations in such a medium the equations of motion for the field operators have to be modified. Whereas the dynamic equations for electric field $\hat{\mathcal{E}}$ and polarization $\hat{\mathcal{P}}$ remain unchanged from Eqs. (1.56) and (1.57), the interaction between Rydberg excited atoms enters the spin polarization via the two photon detuning in Eq. (1.58)

$$\delta \to \delta + \int dz\; V(z-z')\hat{\mathcal{S}}(z',t)^\dagger \hat{\mathcal{S}}(z',t)\; \hat{\mathcal{S}}(z,t), \tag{12.1}$$

$$\Rightarrow \partial_t \hat{\mathcal{S}}(z,t) = i\Omega\hat{\mathcal{P}}(z,t) - i\int dz\; V(z-z')\hat{\mathcal{S}}(z',t)^\dagger \hat{\mathcal{S}}(z',t)\; \hat{\mathcal{S}}(z,t). \tag{12.2}$$

In this chapter we restrict to vdW interaction $V(z-z') = C_6/[a^6 + (z-z')^6]$ with a short range cutoff a required for the numeric simulation and a two photon detuning of zero in the absence of interaction $\delta = 0$. Convergence for $a \to 0$ has been checked.

Initial experiments on Rydberg EIT showed the breakdown of transparency for media saturated with Rydberg polaritons and the resulting attenuation of classical pulses [237]. Theoretical descriptions with very good agreement to experimental results were given soon thereafter by Ates et al., using Monte Carlo sampling of single atom dynamics [235] and Petrosyan et al., using an effective superatom model [206]. Gorshkov et al. investigated the emergence of spatial correlations between single Rydberg DSPs using two excitation wave-

function calculations, which will be introduced later. In the dissipative regime $\gamma > |Delta_\mathrm{p}|$ they predicted the emergence of strong antibunching of DSPs for distances shorter than the resonant blockade radius $d_\mathrm{B} = \sqrt[6]{C_6/\gamma}$, where 2γ is the intermediate state decay and $Delta_\mathrm{p}$ is the one photon detuning. Peyronel et al. experimentally demonstrated these non linear effects on the level of few photons, by direct measurement of photon-photon correlations and observed $g_2(0)$ as low as 0.2 [238]. Other groups demonstrated strong interaction effects via indirect measurement of large optical nonlinearities and the detection of sub Poissonian number statistics for DSPs within the medium [239, 240]. An application of these strong dissipative non linearities has been the realization of single-photon transistors based on Rydberg blockade [241, 98]. Meanwhile the generation of non classical light via a single photon absorber has been proposed theoretically [242]. Firstenberg et al. showed the emergence of photon bunching under specific conditions in the non dissipative regime $\gamma < |\Delta_\mathrm{p}|$ [243] and thereby sparked new research regarding attractive forces between photons. Using diagrammatic methods Bienias et al. recently derived an effective low energy theory and found evidence for bound states of photons [244].

A perturbative description of DSP at low densities has been introduced by Otterbach et al. Based on this description, the preparation of a long range ordered Wigner crystal of photons by storage was proposed [16]. The aim of this chapter is to validate the assumptions made regarding the description of DSPs and the initial state of the protocol in this proposal. We therefore apply two excitation wavefunction techniques. First of all, we will show that the description in terms of DSPs alone is valid after a short transient time and second, that for sufficiently slow storage, the final state of the dynamic protocol is the ground state proposed by Otterbach et al. To quantitatively understand our numeric results, we will derive an effective theory for the unitary problem of two excitations on a ring and consider the adiabaticity conditions for storage.

We finally discuss an emergent feature in our numeric results, that goes beyond the perturbative regime and reveals non polaritonic resonances at short distances of excitations. We identify the origin of these resonances and the essential role the forces between excited atoms play.

12.1 Unitary Dynamics of Dark State Polaritons

For low densities of excitations, where strong interaction effects at short distances can be neglected, the vdW interaction between the atomic contribution of the DSPs can be perturbatively treated as an additional two photon detuning [16]. In lowest order of $\cos(\theta)$ the DSP many body dynamics is then described by the Hamiltonian

$$\mathcal{H}_\mathrm{DSP} = \int dz\, \hat{\Psi}^\dagger(z)(-\frac{\partial_z^2}{2m} - v_g\partial_z)\hat{\Psi}(z) + \frac{C_6 \sin^2(\theta)}{2}\int dz \int dz' \frac{\hat{\Psi}^\dagger(z')\hat{\Psi}^\dagger(z)\hat{\Psi}(z)\hat{\Psi}(z')}{a^6 + |z-z'|^6}, \quad (12.3)$$

with effective mass m and reduced group velocity v_g

$$m = \frac{g^2}{\Delta}\frac{1}{\cos^2(\Theta)c^2}, \quad \text{and } v_\mathrm{g} = c\cos(\Theta)^2. \quad (12.4)$$

We here introduced the notation $\Delta = \Delta_p + i\gamma$ and therefore in the limit $|\Delta_p| \gg \gamma$ the real part of the mass is the dominant contribution. Via a transformation to a frame co-moving with the group velocity v_g, the first order derivative ∂_z can be eliminated. We will briefly review the dynamic crystallization of photons described in [16] and then proceed with a numerical

analysis of this storage process for two excitations in small systems to validate the model.

12.1.1 Wigner Crystallization of Photons

The low energy theory of one dimensional systems is often described within Luttinger liquid theory [245]. Relevant parameters of a Luttinger liquid are the speed of sound u and the Luttinger K-parameter. The K parameter alone determines the asymptotic behavior of first and second order correlation functions

$$\langle\hat{\Psi}(z)\hat{\Psi}(0)\rangle \sim z^{-1/(2K)}, \tag{12.5}$$

$$\langle\hat{\Psi}^\dagger(z)\hat{\Psi}^\dagger(0)\hat{\Psi}(0)\hat{\Psi}(z)\rangle \sim z^{-2K}, \tag{12.6}$$

which decay algebraically. For $K > 1/2$ the first order correlation is dominant at large distances, whereas for smaller K it is the second order density-density correlation. The K parameter is known for the special cases of non interacting bosons ($K = \infty$) and non interacting fermions ($K = 1$), but in general it can not be derived analytically for a microscopic theory, such as Eq. (12.3). Dalmonte et al. derived K parameters for the vdW case in the limits of strong and weak interaction, as parametrized by $\Theta = \pi^3/180\varrho_0^4 m C_6$, where ϱ_0 is the density of particles and found [246]

$$K \approx \frac{1}{\sqrt{1+2\Theta}}. \tag{12.7}$$

Using numeric DMRG simulations of Eq. (12.3), the validity of this expression has been discussed in [16].

A Wigner crystal of DSPs is characterized by long range second order correlations and therefore a small K parameter, respectively a large Θ is required. True long range order can of course not be achieved in 1D, but the correlation length can exceed the relevant system size. From its definition we see that Θ is proportional to the mass of the DSP, which can be manipulated in time by changes of the control field $\Omega(t)$. This is the main idea of the proposal by Otterbach et al.. An initially uncorrelated photon pulse enters the medium and is adiabatically stored in the presence of interaction, by slowly decreasing the control field and thereby increasing the mass of the quasiparticles.

Within Luttinger liquid theory, the energy gap between ground state and states with low momentum excitations vanishes, such that non-adiabatic effects can never be neglected. However for slow changes, the corrections will be restricted to small momenta and therefore large distances in real space. If these distances are large compared to experimental length scales, the non-adiabatic corrections are inconsequential in practice. For the specific switching protocol below, the non adiabatic corrections can be derived analytically within time dependent Luttinger theory [247]. The protocol is defined by

$$\Omega(t) = \frac{g}{\sqrt{f(t)-1}}, \tag{12.8}$$

$$\text{where} \quad f(t) = e^{x(t)}\sinh[x(t)]e^{-\operatorname{arccosh}(C)}/\sqrt{C^2-1}, \tag{12.9}$$

$$\text{and} \quad x(t) = \operatorname{arccosh}(t/T_0 + C), \quad C = (K_0^2+1)/(2K_0). \tag{12.10}$$

with the switching time T_0 as the main control parameter. Under the assumption of a ground state as the initial state of the protocol, it can be shown that after storage correlations are

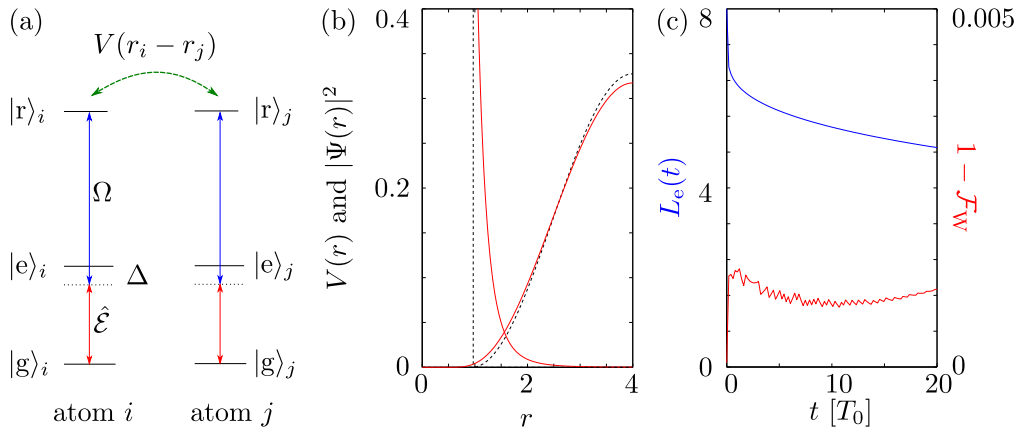

Figure 12.1: (a) Level Scheme of Rydberg EIT. (b) Interaction potential $V(r)$ (solid) for the model system of two excitations on a ring in comparison with the effective hard wall potential (dashed). The corresponding ground state wavefunctions are almost indistinguishable. (c) Effective well width $L_e(t)$ as a function of time t for a system of length $L = 8$. Other parameters are $C_6/\gamma = 1, g/\gamma = 5, \Delta/\gamma = 5$.

established over a finite length

$$L_0 = \frac{\pi^4}{90} C_6 \varrho_0^5 T_0. \tag{12.11}$$

Within this distance, the second order correlation functions show an algebraic decay with the instantaneous exponent $2K(t)$. For distances larger than L_0, the power law decay is instead determined by the original $K_0 = K(0)$, which in general is large. Therefore the notion of a Wigner crystal of photons is correct up to length scales smaller L_0.

A critical assumption for the success of the proposal is that the input state of the storage protocol is sufficiently close to the ground state. Otterbach et al. argue that the off-resonant EIT linewidth $\Omega^2/|\Delta|$ sets an upper limit for the energies of incoming photons converted to DSPs. With this bound they determine the thermal length scale L_t that characterizes the exponential decay of correlations in the initial state. The time dependent Luttinger theory derivation can be generalized to the case of a thermal input state and a corrected length scale was derived in [16]

$$L_\mathrm{corr} = 2\sqrt{L_0 L_T}/\pi K_0 \big(\log[K_0/K(t)]\big)^{1/4}. \tag{12.12}$$

The corrected length scales as the geometric mean of thermal and optimal length L_0 and under the assumption of an initial temperature within the EIT window, it was shown that experimental preparation of a Wigner crystal of DSPs over the length of a typical Rydberg EIT medium is feasible.

12.1.2 Exact solutions on a ring and adiabaticity criterion

We now discuss in more detail our contributions regarding the presented proposal. We consider small systems of just two excitations that are amenable to exact numeric treatment and can therefore be used to validate and benchmark the previous results. To begin with, we consider the model in Eq. (12.3) for two DSPs in a one dimensional system with periodic boundary conditions. The many-body Hamiltonian $\hat{\mathcal{H}}_\mathrm{DSP}$ can be separated in terms of center of mass

and relative coordinates, defined via $r = z_1 - z_2$ and $R = (z_1 + z_2)/2$

$$\hat{\mathcal{H}}_{\mathrm{DSP-ring}} = \frac{\partial_{z_1}^2}{2m} + \frac{\partial_{z_2}^2}{2m} + V(|z_1 - z_2|) \tag{12.13}$$

$$= \frac{\partial_R^2}{4m} + \frac{\partial_r^2}{m} + \frac{C_6 \sin(\theta)^2}{r^6 + (L-r)^6}. \tag{12.14}$$

Note that we decided to add the interactions in forward and backward direction on the ring and we are only interested in the dynamics regarding relative distance of the two excitations. Since the center of mass momentum is conserved, the two particle problem Eq. (12.14) can be mapped to a single particle problem with mass $2m$ in an external potential. We will now develop an approximate description of this problem in terms of a shrinking hard-wall square well to gain insight into the adiabaticity conditions for this system.

The ground state energy of two a single particle confined to a potential well of width L_e is given by $E_1 = \pi^2/(4mL_\mathrm{e}^2)$. We choose the effective length such, that $\sin(\theta)^2 C_6/r_\mathrm{W}^6 = E_1$, with $r_\mathrm{W} = (L - L_\mathrm{e})/2$ is identical to the energy in the lowest energy state in the infinite well. Solving for L_e we find

$$L_e = L - (\beta L)^{1/3} + \frac{1}{3}(\beta^2/L)^{1/3} + \mathcal{O}(\beta/L^2), \tag{12.15}$$

$$\text{with } \beta = \frac{2}{\pi}\sqrt{C_6 \sin(\theta)^2 m}. \tag{12.16}$$

During the storage protocol introduced in Eq. (12.8), the mixing angle $\theta(t/T_0)$ and the effective mass of the DSP $m(t/T_0)$ are functions of the progress in the protocol t/T_0.

In Fig. 12.1(b) we show one example of the effective interaction potential and compare it with the full vdW potential. The vdW interaction potential already has a large exponent and therefore the agreement of the ground state wavefunction obtained for the two potentials is unsurprisingly good. To quantify the quality of the square well solution, we calculate the overlap of the ground state of the full problem with the corresponding approximation and show the results in Fig. 12.1(c). For the range of parameters used in the storage protocol discussed later, infidelities are below one percent.

We now employ the effective square well model to gain insight into the adiabaticity conditions of the protocol on the ring. By changes of the control field $\Omega(t)$, two parameters of the model are varied over time, the mass of the particle $m(t)$ and the length $L_e(t)$ of the well. The eigenfunctions in a deep well are independent of the particle mass and therefore changes in the mass can be arbitrarily fast. This is not true for changes in the size of the well. This problem has been extensively studied before [248] and is amendable to analytic solution in special cases.

The figure of merit for non-adiabatic corrections is

$$\alpha(t, T_0) = \frac{m(t/T_0)}{2} L_\mathrm{e}(t/T_0)\ \partial_t L_\mathrm{e}(t/T_0) \tag{12.17}$$

$$\text{with } \tilde{t} = t/T_0 \quad \Rightarrow \alpha(\tilde{t}) = \frac{1}{T_0}\frac{m(\tilde{t})}{2} L_\mathrm{e}(\tilde{t})\ \partial_{\tilde{t}} L_\mathrm{e}(\tilde{t}) := \frac{\tilde{T}_0}{T_0}, \tag{12.18}$$

where $\tilde{T}_0$ is independent of the switching time. For non-adiabatic corrections to be small, α, which is dimensionless because of $\hbar = 1$, should be much smaller than 1. This result is intuitive, the heavier the particle, the slower the change in size has to be. Furthermore the larger a system, the slower the change has to be, which is a consequence of the increasing time it takes information to propagate from one end to the other. We will return to the

adiabaticity parameter α, when discussing the fidelity of the storage protocol in detail.

12.2 Two Excitation Dynamics

In the previous section we have characterized the ground state of the unitary model on the ring and introduced the approximate description in terms of a shrinking potential well. From this we derived adiabaticity conditions for the storage protocol. We will use these insights to understand the results from the two excitation wavefunction calculations we present in this section.

12.2.1 Methods and observables

The state of two excitations is described within a wavefunction ansatz [238]

$$|\Psi(t)\rangle = \iint dz_1 dz_2 \Big[\frac{1}{\sqrt{2}} EE(z_1,z_2,t)\hat{\mathcal{E}}^\dagger(z_1)\hat{\mathcal{E}}^\dagger(z_2) + \frac{1}{\sqrt{2}} PP(z_1,z_2,t)\hat{\mathcal{P}}^\dagger(z_1)\hat{\mathcal{P}}^\dagger(z_2) + \frac{1}{\sqrt{2}} SS(z_1,z_2,t)\hat{\mathcal{S}}^\dagger(z_1)\hat{\mathcal{S}}^\dagger(z_2) + EP(z_1,z_2,t)\hat{\mathcal{E}}^\dagger(z_1)\hat{\mathcal{P}}^\dagger(z_2) + ES(z_1,z_2,t)\hat{\mathcal{E}}^\dagger(z_1)\hat{\mathcal{S}}^\dagger(z_2) + PS(z_1,z_2,t)\hat{\mathcal{P}}^\dagger(z_1)\hat{\mathcal{S}}^\dagger(z_2) \Big] |0\rangle. \quad (12.19)$$

We choose the symmetry $EE(z_1,z_2) = EE(z_2,z_1)$ without loss of generality and the components of the wavefunction are given by $|\langle 0|\hat{\mathcal{E}}_z\hat{\mathcal{E}}_{z'}|\Psi(t)\rangle|^2 = |[EE(z,z') + EE(z',z)]/\sqrt{2}|^2 = |\sqrt{2}EE(z,z')|^2$ and $|\langle 0|\hat{\mathcal{E}}_z\hat{\mathcal{P}}_{z'}|\Psi(t)\rangle|^2 = |EP(z,z')|^2$. To simplify numeric solution of the Maxwell Bloch equations that govern the dynamics of two excitations on the ring system, we introduce new variables

$$EP_\pm(z_1,z_2) = [EP(z_1,z_2) \pm EP(z_2,z_1)]/\sqrt{2} \quad (12.20)$$

and respectively $ES_\pm$ and $PS_\pm$. For the ring system, we further make use of the translation invariance and only consider dynamics in the relative coordinate $r = z_1 - z_2 \bmod L \in (0, L]$. Center of mass momentum is a conserved quantity and zero for our choice of initial state. The complete set of dynamic equations for the reduced set of variables

$$ee(r,t) = \sqrt{L}EE(r,0), \cdots, \quad (12.21)$$

which take into account translation invariance by construction, is presented in Appendix 17.

Our ansatz does not take into account the entry of the pulse into the medium and we choose a homogeneous distribution of two photons as the initial state

$$ee(r, t=0) = \frac{1}{\sqrt{L}}. \quad (12.22)$$

The dynamic equations are discretized on an evenly spaced grid, where the typical number of grid points is on the order of 10^3. The interaction potential is truncated by the cutoff a for small distances to avoid divergences at $r \to 0$. We apply a split step method to numerically solve the dynamic Eqs. (17.24)-(17.32) [249]. Whereas the couplings g and Ω, the detuning Δ and the decay of the excited state γ as well as the interaction V are taken into account in real space, the kinetic term $c\partial_r = -ick$ is applied in Fourier space.

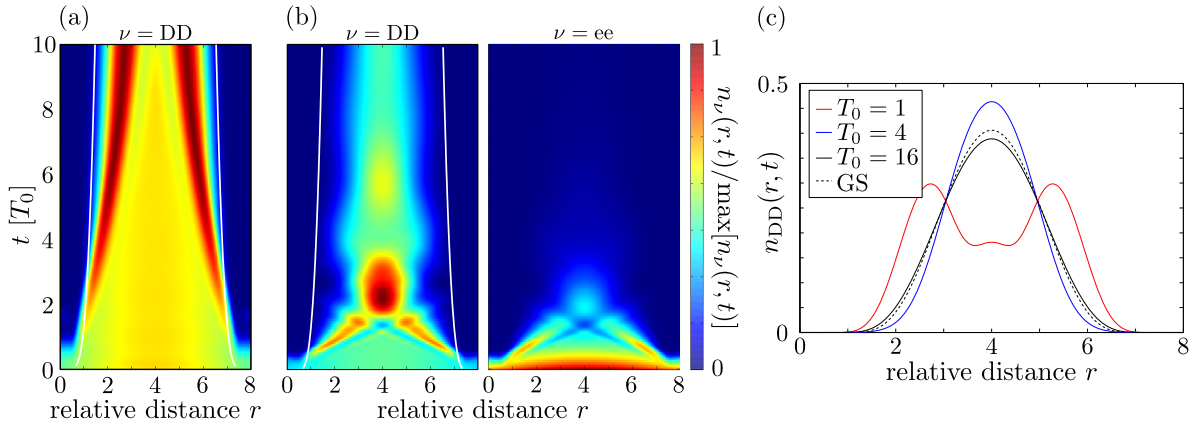

Figure 12.2: (a) Density distribution of two DSP on a short ring during storage with switching time $T_0 = 1$. Density is normalized to the peak value for the individual plots. Parameters are $\gamma = 1, C_6 = 1, g = 5, \Delta = 5$ and the ring has length $L = 8$. (b) Density distribution for DSP and photonic field component for $T_0 = 16$. (c) Comparison of the normalized DSP density with the ground state density after $t = 10T_0$ for different switching times and parameters as in (a) and (b).

Note that the norm of the two excitation wavefunction

$$\mathcal{N} = \langle\Psi(t)|\Psi(t)\rangle = \int dr \left[|ee(r,t)|^2 + |pp(r,t)|^2 + |ss(r,t)|^2 \right. \tag{12.23}$$

$$\left. + |ep(z_1,t_2)|^2 + |es(r,t)|^2 + |ps(r,t)|^2\right], \tag{12.24}$$

at the beginning of the storage protocol is $\mathcal{N} = 1$, but it is not a conserved quantity in the presence of decay γ. Our description is incomplete as we do not take into account the dynamics of single excitation after a decay event. This can be resolved by using the losses of the two excitation calculation as input to a single excitation density matrix calculation [242].

The DSP continuously changes character during the protocol, as the mixing angle $\theta(t)$ changes in time and we must take this into account when calculating the DSP density

$$L\left|\langle 0|\hat{\Psi}(r)\hat{\Psi}(0)|\Psi(t)\rangle\right|^2 = \left|[dd(r) + dd(-r)]/\sqrt{2}\right|^2 = 2|dd(r)|^2, \tag{12.25}$$

where the last term is related to our numeric variables via

$$dd(r) = \cos^2(\theta)ee(r) - \sqrt{2}\sin(\theta)\cos(\theta)es(r) + \sin^2(\theta)ss(r) \tag{12.26}$$

$$= \cos^2(\theta)ee(r) - \sin(\theta)\cos(\theta)[es_+(r) + es_-(r)] + \sin^2(\theta)ss(r). \tag{12.27}$$

This allows us to extract the probability distribution for the distance between two DSPs

$$n_{\mathrm{DD}}(r,t) = |dd(r,t)|^2. \tag{12.28}$$

12.2.2 Results in the near-resonant regime

In Fig. 12.2(a) we show exemplary results for the DSP density on a ring of length $L = 8$. The protocol for the control field is chosen such, that $\Omega(t \to 0)/g \gg 1$ and therefore $\cos^2(\theta) \approx 1$ and therefore the initial DSP distribution is identical to the homogeneous photon distribu-

tions. Dynamics of large separation components is initially dominated by single particle effects [100], that are a consequence of non-adiabatic corrections due to the fast change of the control field $\Omega(t)$ and are not a consequence of the strong interaction. At short distances $r < \sqrt[6]{C_6/(g^2+\Omega^2)}$, the strong interaction suppresses the adiabatic following of the wavefunction with the DSP towards the spin-spin component. The remaining electric field is absorbed with the off resonant rate $\gamma g^2/|\Gamma|^2$.

The interesting physics occurs at the boundary of the blockade region. Note that for our choice of parameters this is within the regime of validity of the DSP description in Eq. (12.3), as $r > \sqrt[6]{C_6/(g^2+\Omega^2)}$. We display results for two different values of the switching time T_0 in Fig. 12.2(a) and (b). The white lines denote the effective square well of width L_e we derived in Eq. (12.15). Results in Fig. 12.2(a) are for fast storage with a switching $T_0 = 1$. The compression of the wavefunction by the shrinking square well is too for adiabatic following.

By increasing the switching time, the relative speed of correlation propagation compared to the compression of L_e is increased and fewer excitations are introduced into the system. This is exemplified for $T_0 = 16$ in Fig. 12.2(b). In addition to the density of DSPs we show the distribution of the photonic component, which is rapidly vanishing.

The final state of DSPs for three switching times is compared to the exact ground state of Eq. (12.3) in Fig. 12.2(c). Overlap for the long switching time is much improved compared to the intermediate time $T_0 = 4$. Note however that this increase in total time results in larger losses and a smaller remaining norm of the wavefunction. This effect has been omitted in the figure and will be quantified in the next section.

12.2.3 Fidelity of storage protocol in the near-resonant regime

Based on the quantities introduced in the previous section we will now quantitatively analyze the relation between system size L, switching period T_0 and the efficiency of the preparation protocol. The key figure of merit is the overlap between the final two excitation wavefunction and the ground state for two DSPs within the unitary model

$$\begin{aligned}\mathcal{F}_\mathrm{G}(t,T_0) &= |\langle\Psi_\mathrm{G}|\Psi(t)\rangle|^2/|\langle\Psi(t)|\Psi(t)\rangle| \\ &= \int |d_r\ dd^*_\mathrm{G}(t)dd(r)|^2/|\langle\Psi(t)|\Psi(t)\rangle|. \end{aligned} \tag{12.29}$$

Our intuition is, that with increasing switching time the fidelity of preparation in general increases, which we will show to be true. The total time is however limited by the presence of losses, which is quantified by the norm $\mathcal{N}$ of the two excitation wavefunction. We furthermore consider the norm of only DSP contributions to the wavefunction to show that the system is fully described in terms of DSPs.

In Fig. 12.3 we show the infidelity $1-\mathcal{F}_\mathrm{G}(t,T_0)$ of ground state preparation, (b), and the remaining norm after storage $\mathcal{N}$, (c), for systems of size $L = 6$ and $L = 8$ as a function of the switching time T_0. The minimum switching time is limited by the adiabaticity condition for storage in the absence of interaction. For switching times shorter than $T_1 = \Delta/g^2$ we find significant deviations of the norm $\mathcal{N}$ (dashed) and the norm of DSP components $\mathcal{N}_\mathrm{DD}$ (solid) as the single excitations can not follow the change of the control field.

For larger times the wavefunction is dominated by DSP components ($\mathcal{N}_\mathrm{DD}/\mathcal{N} \approx 1$), the infidelity $1-\mathcal{F}$ is however still large. This is due to non-adiabaticy regarding the changes in the unitary model. We have numerically evaluated the adiabaticity parameter $\tilde{T}_0(\tilde{t})$ in Eq. (12.17) and display the results in Fig. 12.3(a). For $T_0 < \tilde{T}_0(\tilde{t})$ we expect non-adiabatic excitations to appear at this stage of the storage protocol. We find that the initial phase of the

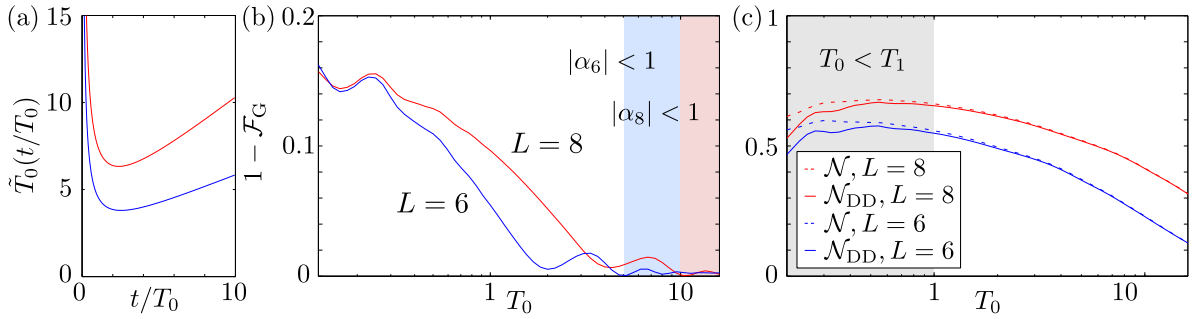

Figure 12.3: (a) Switching time $\tilde{T}_0$ such that $\alpha = 1$ at that time in the storage protocol. Colors as in (b). (b) Overlap of two excitation state after time $T = 10T_0$ and $T = 5T_0$ (inset) with the DSP ground state for two system sizes. Parameters are $C_6 = 1, g = 5, \Delta = 5$ and $c = 1$. (c) Remaining norm of the two excitation wavefunction after $T = 10T_0$ (solid) and $T = 5T_0$ (dashed) and parameters as in (a).

storage and the continued storage at late times, with large mass of the DSPs, are most critical regarding adiabaticity. The rapid initial compression of the square well, cf. Fig. 12.1(c), is non-adiabatic for all T_0 we consider. The consequences can be seen in Fig. 12.2(a), after short times, density peaks appear near the boundaries of the shrinking square well, which then propagate away from the boundaries towards larger distances. However, we find that the excitations created in the initial phase of the protocol are damped during storage and do not prohibit the preparation of the targeted ground state. The required switching for large times increases and we find that infidelities of less than one percent are reached, if T_0 is chosen such that $\alpha(t = 10T_0) = 1$ at the end of the protocol. Note, that the bound derived within Luttinger liquid theory in Eq. 12.11 is not suitable here. The density of DSPs is fixed for the ring system to $\varrho_0 = w/L$ and for $L_0 = L$ we obtain from the bound derived in [16]

$$T_0 > \frac{45}{16\pi^4}\frac{L^6}{C_6} \overset{L=8}{\approx} 8000, \tag{12.30}$$

which is much larger than the switching times required for the small system.

In this section we discussed the storage of two initial photon excitations in the form of Rydberg excitations in a small ring system. We validated the assumption of Otterbach et al. that after a transient time only DSP components of the wavefunction remain. Furthermore we showed that despite imperfections of the initial state and non-adiabaticity during the initial stages of the storage protocol, the ground state of Eq. (12.3) can be prepared.

12.3 Scattering Resonances of Rydberg-Polaritons

An interesting feature emerges for the exact numeric solution of the two excitation problem, when considering very large one photon detunings $|\Delta_p| \gg g, \Omega$. This effect we want to discuss in the following section does not fall within the bound state regime discussed in the literature, where $|\Delta_p| < g$ [243, 244].

12.3.1 Results in the far-off-resonant regime

In Fig. 12.4 (a) we show the DSP density for the identical storage protocol as before, but with increased one photon detuning $\Delta_p/\gamma = 25 \gg g/\gamma$. The left part of the figure compares the

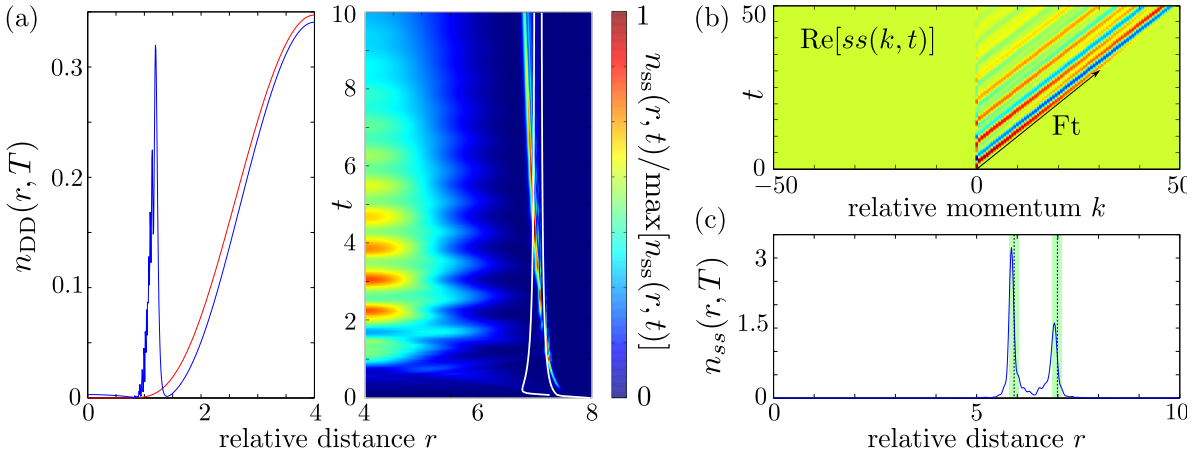

Figure 12.4: (a) Final distance distribution of two Rydberg DSP in comparison with the DSP ground state (left) and time evolution during the storage protocol. For large detuning $\Delta/\gamma = 25$ resonance like structures emerge. (b) Results for a linear interaction potential and constant parameters $g = 5\gamma, \Omega = \gamma, \Delta = 25\gamma$ on a ring of length $L = 10$. Distance distribution for the spin-spin component after $T = 50 = 10T_0$ (c) Evolution of the spin-spin component in momentum space.

final density of DSPs after $T = 10T_0$ with the ground state distribution of $\hat{\mathcal{H}}_{\mathrm{DSP}}$. Whereas agreement for large separations is near perfect apart from the overall normalization factor, a resonance like feature emerges at short distances for the exact solution. The aim of this section is to identify the origin and further characterize this feature that goes beyond the perturbative DSP theory.

12.3.2 Linear model system

Two factors contribute to the emergence of the resonance features for large detunings. First of all two Rydberg excited atoms apply strong forces $\sim \partial_r V(r)$ on each other, which takes population out of the low momentum sector and effectively decouples spin-spin population from the remaining components. Furthermore we identify the positions of resonance features with an energy match between $V(r)$ and oscillation frequencies in the low momentum dynamics.

To gain analytic insight we use a simplifies linear interaction potential

$$V(r) = Fr - \frac{FL}{2}, \tag{12.31}$$

which yields a constant force F between excitations and restrict ourselves to fixed values of Ω. We are interested in the behavior for small interaction at maximum distance on the ring and therefore the discontinuity of $V(r)$ at $r = 0 = L$ is irrelevant.

Consider the dynamic equation for the spin-spin component in momentum space

$$\partial_t ss(k) = i\frac{FL}{2} ss(k) - i\Omega ps_+(k) + F\partial_k ss(k). \tag{12.32}$$

The last term represents the force that accelerates population away from $k = 0$. In Fig. 12.4 (b) we show the real part of $e^{i\frac{Lk}{2}} ss(k,t)$ for a ring of length $L = 10$ and $F = 1$. We have introduced the phase factor to take into account the energy of $ss(k)$ in Eq. (12.32). The population in $ss(k)$ follows the force without significant coupling to ps_+ away from $k = 0$ and

therefore

$$ss(k,t) \sim ss(0,t-k/F)e^{i\frac{Lk}{2}}\theta(k)\theta(t-k/F). \tag{12.33}$$

The zero momentum component $ss(k=0,t)$ is coupled to the other components at zero momentum. At $k=0$ the coupling to antisymmetric components of the wavefunction vanishes and we must only consider the dynamics of the symmetric components

$$\partial_t \begin{pmatrix} ee \\ pp \\ ep_+ \\ es_+ \\ ps_+ \end{pmatrix} = i \begin{pmatrix} 0 & 0 & g & 0 & 0 \\ 0 & -2\Delta & g & 0 & \Omega \\ 2g & 2g & -i\Gamma & \Omega & 0 \\ 0 & 0 & \Omega & 0 & g \\ 0 & 2\Omega & 0 & g & -\Delta \end{pmatrix} \begin{pmatrix} ee \\ pp \\ ep_+ \\ es_+ \\ ps_+ \end{pmatrix}. \tag{12.34}$$

In the limit of small control field and large detuning $\Omega \ll g \ll |\Delta|$ we consider the two eigenvalues of magnitude closest to zero

$$\lambda_{\mathrm{ee}} = -\Delta + \sqrt{4(g^2+\Omega^2)+\Delta^2},\ \lambda_{\mathrm{es}_+} = (-\Delta + \sqrt{4(g^2-\Omega^2)+\Delta^2})/2. \tag{12.35}$$

These two frequencies will be imprinted onto the $ss(k,t)$ population that is dragged through momentum space.

To illustrate the consequences, we here consider an oscillation of $ss(0,t)$ for a single frequency $\lambda \in \{\lambda_{\mathrm{ee}}, \lambda_{\mathrm{es}_+}\}$. Due to the force on the spin-spin components we find

$$\begin{aligned} ss(k,t) &\sim e^{i(\lambda(t-k/F)+\frac{Lk}{2})}\ \theta(k)\ \theta(t-k/F), \\ \Rightarrow ss(r,t) &\sim \frac{1-\exp[it/F(r-\lambda/F-L/2)]}{r-\lambda/F-L/2}. \end{aligned} \tag{12.36}$$

We are interested in the behavior in the vicinity of the root of the denominator. For $\lambda \in \mathbb{R}$ this root is located at $Fr - FL/2 = V(r) = \lambda$, the distance where the interaction potential energy, is resonant with the eigenvalue. Expanding expression (12.36) around this point we find

$$|ss(r,t)|^2 \sim \frac{t^2}{F^2}\big[1 - \frac{t^2}{F^2}\frac{(r-\lambda/F-L/2)^2}{24}\big]. \tag{12.37}$$

A pronounced peak in the spin-spin component emerges over time, with quadratically increasing amplitude and narrowing width

$$w \approx 2\sqrt{6}F/t. \tag{12.38}$$

The total probability weight of this resonance therefore increases linearly. When taking into account the imaginary part of λ, we find that the increase in amplitude changes into a linear regime for $t\mathrm{Im}(\lambda) \gtrsim 1$ and that the amplitude saturates to a constant value for $t\mathrm{Im}(\lambda) \gg 1$.

In Fig. 12.4(c) we show the density distribution of the spin spin component after time $t = 50$. The relevant eigenvalues here are given by $\mathrm{Re}(\lambda_{\mathrm{ee}_+}) \approx 2.0$ and $\mathrm{Re}(\lambda_{\mathrm{es}_+}) \approx 0.9$. In Fig. 12.5(a) we show time dependent density distribution of the spin-spin component for the resonance near $r \approx 5.8$ in the linear potential example. The density is normalized, such that the peak of the density distribution is of constant value. Due to this normalization the narrowing of the distribution is apparent in the figure and the expected width is indicated with white dashed lines in good agreement with the numeric calculation. For $t > 50$ the narrowing stops, which is due to the loss of population in the zero momentum space. This is also seen in Fig. 12.4(b). In Fig. 12.5(b) the maximum amplitude corresponding to (a) is

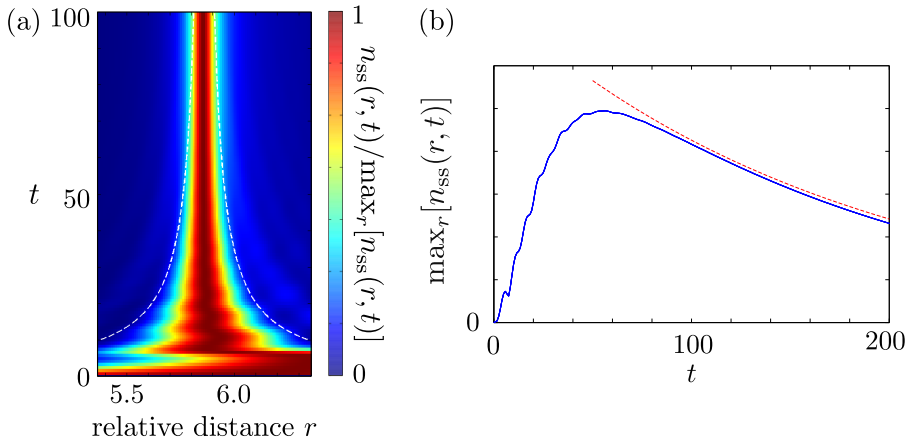

Figure 12.5: (a) Distribution of spin-spin component for the left resonance feature normalized to the maximum value. White dashed lines indicate the predicted width of the feature. (b) Maximum amplitude of (a) as a function of time. The red dashed line indicates exponential decay due to the off resonant coupling to the polarization. All parameters are as in Fig.12.4(b).

displayed. We here find the initial linear increase as predicted by Eq. (12.37), followed by exponential decay on the time scale $\tau_{ss} = 4\gamma^{-1}|\Delta^2|/\Omega^2$, of the off resonant coupling to the ep_+ component.

We now return to the simulation of the storage protocol with vdW interaction. Whereas we can not immediately transfer our derivation to the dynamic storage protocol, we will use the results of the simplified model as a guide. For small $\Omega(t)$ the two eigenvalues discussed above simplify to $\lambda_{ee} = g^2/\Delta$ and $\lambda_{es_+} = g^2/\Delta$. From the model discussion we expect resonance features to appear where the interaction potential is resonant with these frequencies

$$r_\mu = (C_6/\lambda_\mu)^{(1/6)}. \tag{12.39}$$

In the figure we added white lines denoting the predicted position of resonances. Again agreement is qualitatively good besides unexplored drifts at late stages of the protocol.

Conclusion

This chapter was a short glimpse into the expanding field of Rydberg EIT with the very specific goal to validate the assumptions of the proposal by Otterbach et al.[16]. To do so we considered the dynamic storage of only two excitations in finite size systems with periodic boundary conditions. As in the previous Chapter 8 the replacement of the vdW potential with a hard rod potential was shown to yield good approximations and analytic insight into the storage procedure. Based on the square well picture we derived adiabaticity conditions for the storage in the small system.

We then used the two excitation wavefunction techniques to validate the DSP approach and showed that for sufficiently slow switching times and sufficient distance of the excitations the initial photons are coherently converted into spin excitations. Furthermore for switching times large enough to be adiabatic regarding the many body Hamiltonian, the prepared state showed very good agreement with the targeted ground state. However this increase in overlap comes at the price of increased losses, which need to be further characterized.

For large one photon detuning we observed short distance resonance features that are not described within the perturbative DSP theory. We identified the origins of these resonances

and showed that the force between Rydberg excited atoms is a key ingredient. Our numeric approach is at the moment limited by the slowly varying envelope approximation made in the derivation of the dynamic equation of $\hat{\mathcal{E}}$. This approximation is only valid for small momentum changes around the central wavevector k_0, which is violated by the strong forces at the resonance position.

Bound states of polaritons have become a hot topic recently, motivated by the experimental findings in [243]. The theoretical description of Rydberg EIT systems beyond the perturbative regime remains a challenge and unifying framework for the different theoretical proposals is missing. The two excitation simulations employed and developed within this chapter will be an equally important tool to validate other aspects of Rydberg EIT.

Part V

Appendices

Chapter 13

MPS Based Simulation of Quantum Systems

Classical simulation of many body quantum systems is relevant for both benchmarking of experimental results and research on new theoretical models. Matrix-product state (MPS) based approaches originate from the classical statistical mechanics of two dimensional systems [250] and have been established as a valuable tool for the simulation of one dimensional quantum systems [109]. In this chapter we will first introduce MPS and their properties and then continue to discuss their application in DMRG and TEBD algorithms. We employ MPS for the simulation of open one dimensional lattice systems, where the density operator must be represented as a state in Liouville space and then approximated using MPS. We here focus on the relevant modifications to a TEBD algorithm to simulate such driven, open systems. The chapter concludes with a review on results regarding the feasibility of simulation and the relation to the scaling of entropies.

13.1 Matrix Product States

Consider a one dimensional lattice, partitioned in parts A and B with L sites each and local Hilbert space dimension d. The challenge of numerical simulation of quantum systems is the exponential scaling of Hilbert space with system size. In general, an exact representation of a quantum state

$$|\Psi\rangle_{\mathrm{AB}} = \sum_{j,k} c_{j,k} |j\rangle_{\mathrm{A}} |k\rangle_{\mathrm{B}}, \quad |j\rangle_{\mathrm{A}} \in \mathcal{H}_{\mathrm{A}}, \quad |k\rangle_{\mathrm{B}} \in \mathcal{H}_{\mathrm{B}} \tag{13.1}$$

requires d^{2L} coefficients c_j and is thus infeasible. The Schmidt decomposition of the state $|\Psi\rangle_{\mathrm{AB}}$ is given by

$$|\Psi\rangle_{\mathrm{AB}} = \sum_{m=1}^{d^L} c_m |m\rangle_{\mathrm{A}} |m\rangle_{\mathrm{B}}, \quad |m\rangle_{\mathrm{A}} \in \mathcal{H}_{\mathrm{A}}, \ |m\rangle_{\mathrm{B}} \in \mathcal{H}_{\mathrm{B}}, \tag{13.2}$$

with $\sum |c_m|^2 = 1$, where $|c_{m+1} \leq c_m|$, and complete orthonormal sets, spanning both Hilbert spaces. The number of Schmidt coefficients required does not scale with the total Hilbert space, but the maximum Hilbert space dimension of system A or B. We are interested in a truncation scheme for the sum in Eq. (13.2) that guarantees to approximate expectation values with controlled error bounds. It has been shown that $|\Psi\rangle_{\mathrm{AB}}^{(\chi)} = \sum_{m=1}^{\chi} c_m |m\rangle_{\mathrm{A}} |m\rangle_{\mathrm{B}}$ is

the best possible truncation and the error is simply given by the sum of the discarded weights in the Schmidt decomposition [228]

$$\varepsilon(\chi) = \sum_{m=\chi+1}^{d^L} |c_m|^2. \tag{13.3}$$

A MPS is generated from $|\Psi\rangle_{\mathrm{AB}}$, by repeatedly applying Schmidt decompositions of smaller and smaller subsets of the system and truncating in every step to the targeted bond dimension χ. In the representation introduced by Vidal the final MPS is of form

$$|\Psi\rangle = \sum_{\sigma_1 \cdots \sigma_{2L}} \Gamma^{\sigma_1} \Lambda^{[1]} \Gamma^{\sigma_2} \Lambda^{[2]} \cdots \Gamma^{\sigma_{2L-1}} \Lambda^{[2L-1]} \Gamma^{\sigma_{2L}} |\sigma_1 \cdots \sigma_{2L}\rangle. \tag{13.4}$$

The matrices Γ^{σ_i} contain a set of χ states on site i and the $\Lambda^{[i]}$ are the diagonal bond matrices that contain the Schmidt coefficients. Note that the Γ matrices are limited in size to $(\chi d)\times(\chi d)$ and therefore the overall resources required for the storage of an MPS only scale linearly in the system size L.

13.2 Algorithms

In the following we will briefly review the two most relevant algorithms based on MPS. First of all DMRG for efficient approximation of ground states of one dimensional systems, and then TEBD for the simulation of time evolution in one dimensional lattice systems.

13.2.1 DMRG

The density matrix renormalization group originated from real space renormalization and was later reformulated in the language of MPS [111, 251]. We here only describe a modern variant of DMRG and the algorithm we have used throughout this thesis.

Our goal is to find the MPS of dimension χ, that best approximates the ground state of Hamiltonian $\mathcal{H}$ on a lattice. Straight forward optimization of the MPS regarding the energy expectation value is a large, nonlinear problem in the coefficients of the Γ and Λ matrices. We must instead use iterative methods that only optimize few matrices in each step. Consider a partition of the lattice in four parts $\mathrm{A}, j, j+1, \mathrm{B}$. The current approximation is then given by

$$|\Psi\rangle = \sum_{\alpha,\beta,\gamma=1}^{\chi} \sum_{m,n=1}^{d} \Lambda_{\alpha}^{[j-1]} \Gamma_{\alpha,\beta}^{[j],m} \Lambda_{\beta}^{[j]} \Gamma_{\beta,\gamma}^{[j+1],n} \Lambda_{\gamma}^{[j+1]} |\alpha\rangle_{\mathrm{A}} |m\rangle_j |n\rangle_{j+1} |\gamma\rangle_{\mathrm{B}}, \tag{13.5}$$

where we have contracted all internal bonds in A and B. The energy expectation value is minimized by only optimizing matrices on the two lattice sites j and $j+1$. To optimize the state with respect to the energy, one contracts all bonds in the product $\langle\Psi|\mathcal{H}|\Psi\rangle$, where $\hat{\mathcal{H}}$ is also represented by a matrix product operator, except for the sites $j, j+1$. As the result of this contraction we find an effective Hamiltonian for these two sites of dimension $\chi^2 d^2 \times \chi^2 d^2$. The smallest eigenvalue and corresponding eigenstate of this operator is determined via exact diagonalization. This state is Schmidt decomposed regarding lattice sites j and $j+1$, truncated to the chosen bond dimension χ and brought into MPS form. This procedure is repeated for all pairs of adjacent sites in a sweeping scheme that continues until the energy expectation value is sufficiently converged.

DMRG algorithms can in principle be applied to Hamiltonians with long range interaction, which however requires larger bond dimensions for the matrix product operator representing the Hamiltonian and reduces efficiency.

13.2.2 TEBD

As we saw in the previous subsection, DMRG using MPS is based on the idea to locally optimize the state on two adjacent sites. The insight of Vidal was, that this idea could easily be adapted to simulate the time evolution of a specific class of one dimensional problems [252, 253]. Consider a Hamiltonian that can be written as a sum of terms $\hat{\mathcal{H}}_j$ with support on only adjacent sites $j, j+1$

$$\hat{\mathcal{H}} = \sum_j \hat{\mathcal{H}}_j. \tag{13.6}$$

The time evolution operator $\hat{U} = \exp(-i\hat{\mathcal{H}}t)$ can then be approximated and efficiently decomposed using a Suzuki Trotter decomposition. We partition the Hamiltonian in even and odd parts, $\hat{\mathcal{H}} = \sum_{j=\text{odd}} \hat{\mathcal{H}}_j + \sum_{j=\text{even}} \hat{\mathcal{H}}_j = \hat{\mathcal{H}}_{\text{odd}} + \hat{\mathcal{H}}_{\text{even}}$, and find

$$e^{-i\hat{\mathcal{H}}dt+\mathcal{O}(dt^3)} = e^{-i\hat{\mathcal{H}}_{\text{odd}}dt/2} e^{-i\hat{\mathcal{H}}_{\text{even}}dt} e^{-i\hat{\mathcal{H}}_{\text{odd}}dt/2}. \tag{13.7}$$

The operator exponential $\exp[-i\hat{\mathcal{H}}_{\text{odd}}dt/2]$ can be factorized, because the included $\hat{\mathcal{H}}_j$ have disjunct support and thus commute with each other. To time evolve the MPS, we must therefore apply operations $\hat{U}_j = e^{-i\hat{\mathcal{H}}_j dt}$ and then use a Schmidt decomposition to retrieve the truncated MPS representation.

13.3 Open System TEBD

The relevant equation of motion for the open systems we discuss is the Lindblad equation

$$\frac{d}{dt}\varrho = -i[\mathcal{H}, \varrho] + \frac{1}{2}\sum_\mu \left(2L_\mu \varrho L_\mu^\dagger - \{L_\mu^\dagger L_\mu, \varrho\}\right). \tag{13.8}$$

We here reformulate the problem in Liouville space $\mathcal{L} = \mathcal{H} \otimes \mathcal{H}$, to reveal the analogy to the conventional Schrödinger equation. The density matrix operator is represented by a state $|\varrho\rangle \in \mathcal{L}$ and its dynamics is given by

$$\begin{aligned} i\frac{d}{dt}|\varrho\rangle &= \left(-\hat{\mathcal{H}} \otimes \mathbb{1} + \mathbb{1} \otimes \hat{\mathcal{H}} - \frac{i}{2}(2L_\mu \otimes L_\mu - L_\mu^\dagger L_\mu \otimes \mathbb{1} - \mathbb{1} \otimes L_\mu^\dagger L_\mu)\right)|\varrho\rangle \\ &= \hat{\mathcal{L}}|\varrho\rangle. \end{aligned} \tag{13.9}$$

For an open system with non-vanishing Lindblad operators the Liouville operator is in general non Hermitian. However, for systems with a unique stationary state, the Liouville operator must have a single eigenvector with eigenvalue 0, which is the stationary state of the density matrix. The unitary dynamics can be interpreted as a forward evolution on one lattice and a time reversed evolution on the mirrored chain. The two chains are only coupled by the last terms that emerge from the dissipation.

If $\hat{\mathcal{H}}$ can be separated in local Hamiltonians with support on adjacent sites and the Lindblad generators also have local support, the Liouville operator can be decomposed in even and odd parts as well and dynamics is simulated using conventional TEBD. This analogy has

been exploited in various fields from transport in spin chains to polariton dynamics in the past [254, 255, 256, 257].

Notable differences have to be taken into account regarding the normalization of the density matrix and the calculation of expectation values. In conventional form we require for the density matrix $\mathrm{Tr}(\varrho) = 1$ which translates into a simple scalar product in Liouville space

$$\langle 1|\varrho\rangle = \mathrm{Tr}(\varrho) = 1, \qquad \text{with } |1\rangle = \sum_{\mathbf{m}} |\mathbf{m}\rangle \otimes |\mathbf{m}\rangle. \tag{13.10}$$

Similarly the expectation value of a projector onto a local state n at site k is given by

$$\langle k, n|\varrho\rangle = \mathrm{Tr}(|n\rangle_k\langle n|_k \varrho), \qquad \text{with } |k, n\rangle = \sum_{\mathbf{m}} \delta_{m_k,n} |\mathbf{m}\rangle \otimes |\mathbf{m}\rangle. \tag{13.11}$$

Calculating expectation values of local operators is therefore very easy within this representation of the density matrix. Note however, that as for conventional DMRG the calculation of global observables, such as the total particle number is hard, as it can not be represented by a small matrix product operator.

13.4 Feasibility of MPS Approximation

The set of MPS of fixed bond dimension χ only covers a small subset of Hilbert space. We here quickly review how to identify states that are not well approximated via MPS and review why MPS based approaches are nonetheless a valuable tool for one dimensional systems.

Be $|\Psi\rangle$ the pure state of a bipartite system, then we define the von Neumann entropy of the bipartition as

$$S_{\mathrm{A,B}} = -\mathrm{Tr}(\varrho_{\mathrm{A}} \ln \varrho_{\mathrm{A}}), \qquad \varrho_{\mathrm{A}} = \mathrm{Tr}_{\mathrm{B}}(|\Psi\rangle\langle\Psi|). \tag{13.12}$$

The reduced density matrix ϱ_{A} can be represented via the coefficients and states of the Schmidt decomposition as in Eq. (13.2)

$$\varrho_{\mathrm{A}} = \sum_{m=1}^{\chi} |c_m|^2 |m\rangle_{\mathrm{A}}\langle m|_{\mathrm{A}}, \tag{13.13}$$

where we have used orthonormality of the $|m\rangle_{\mathrm{A}}$. As ϱ_{A} is diagonal in this basis, the von Neumann entropy is given by

$$S_{\mathrm{A,B}} = -\sum_{m=1}^{\chi} |c_m|^2 \ln |c_m|^2. \tag{13.14}$$

This entropy is maximal for $|c_m| = |c_n|$ for all m, n and the normalization requires $|c_m|^2 = 1/\chi$ such that the entropy of a MPS with bond dimension χ is bounded by

$$S_{\mathrm{A,B}} \leq \ln(\chi), \tag{13.15}$$

which has the immediate consequence, that states with increasing entropy $S_{\mathrm{A,B}}$ require exponentially increasing resources χ.

The von Neumann entropy is a specific case of Renyi entropies $S_\alpha = \ln(\mathrm{Tr}\,\varrho^\alpha)/(1-\alpha)$ and it has been shown that the scaling of Renyi entropies with system size is a good figure of merit for the feasibility of MPS based simulations [228]. Note that the von Neumann entropy corresponds to $S_{\alpha=1}$. First of all, if $S_{\alpha<1} \sim$ const. or $S_{\alpha<1} \sim \ln(L)$ the approximation with

MPS is feasible. On the other hand, if $S_{\alpha>1} \sim L^{\kappa}$ or $S_{\alpha=1} \sim L$ the simulation is infeasible. In between these two regimes the situation is can not be determined by the scalings alone.

Several results have been obtained regarding the scaling of entropies of generic systems. Most importantly ground states of one dimensional systems with finite range interaction and an energy gap obey an area law such that entropies remain constant with increasing system size [110]. In critical regimes where the energy gap vanishes, the scaling behavior changes to logarithmic growth. This does not render the simulation infeasible, but then the necessary χ for accurate simulation increases with system size [230].

Chapter 14

Shaking Assisted Tunneling

In Chapter 4 we propose to use shaking assisted tunneling to realize the thin torus limit of the 2D FQH effect in a one dimensional ladder system. We here briefly review the most relevant aspects of the derivation of the effective Hamiltonian [39, 258] and discuss the example of a simple two site model.

14.1 Derivation of Two-Site Effective Coupling

Consider a system of two sites with small hopping J and an offset potential of strength Δ. For $\Delta \gg J$, tunneling is strongly suppressed. By introducing a time dependent modulation of the local potentials with frequency Δ, tunneling can be restored with control regarding amplitude and phase.

$$\mathcal{H}_0 = -J(\hat{a}_1^\dagger \hat{a}_2 + \hat{a}_2^\dagger \hat{a}_1) + \frac{\Delta}{2}(-\hat{a}_1^\dagger \hat{a}_1 + \hat{a}_2^\dagger \hat{a}_2), \tag{14.1}$$

$$\mathcal{H}_t = V_0[\hat{a}_1^\dagger \hat{a}_1 \cos(\Delta t + g_1) + \hat{a}_2^\dagger \hat{a}_2 \cos(\Delta t + g_2)]. \tag{14.2}$$

First of all, we transform into a frame rotating with the off set detuning Δ

$$\hat{W} = -\hat{n}_1 + \hat{n}_2, \qquad \psi = e^{-i(\Delta/2)\hat{W}t}\tilde{\psi} \tag{14.3}$$

$$\Rightarrow i\partial_t \tilde{\psi} = e^{i(\Delta/2)\hat{W}t}(\mathcal{H}_0 + \mathcal{H}_t)e^{-i(\Delta/2)\hat{W}t}\tilde{\psi} - \frac{\Delta}{2}\hat{W}\tilde{\psi} \tag{14.4}$$

$$= \tilde{\mathcal{H}}\tilde{\psi}. \tag{14.5}$$

The time dependent part of the Hamiltonian is unchanged, whereas the tunneling matrix element rotates with the off set detuning

$$\tilde{\mathcal{H}} = -J(e^{-i\Delta t}\hat{a}_1^\dagger \hat{a}_2 + e^{i\Delta t}\hat{a}_2^\dagger \hat{a}_1) + \mathcal{H}_t. \tag{14.6}$$

We now split $\tilde{\mathcal{H}}$ into these rotating parts $\tilde{\mathcal{H}} = e^{i\Delta t}\hat{V}^{(+)} + e^{-i\Delta t}\hat{V}^{(-)}$

$$V^{(+)} = -J\hat{a}_2^\dagger \hat{a}_1 + \frac{V_0}{2}(e^{ig_1}\hat{n}_1 + e^{ig_2}\hat{n}_2), \tag{14.7}$$

$$V^{(-)} = -J\hat{a}_1^\dagger \hat{a}_2 + \frac{V_0}{2}(e^{-ig_1}\hat{n}_1 + e^{-ig_2}\hat{n}_2). \tag{14.8}$$

By expanding the dynamic equation in powers of $\frac{1}{\Delta}$, one introduces a truncation scheme to restrict to the slow dynamics of the system. For the effective Hamiltonian that described this

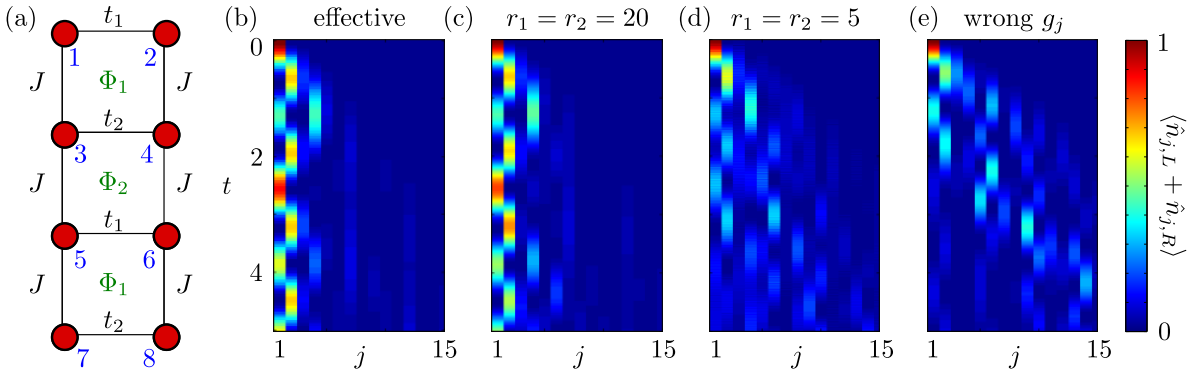

Figure 14.1: (a) Effective ladder scheme realized by fast lattice shaking, which creates an artificial magnetic flux Φ_1, Φ_2 alternately piercing plaquettes. (b)-(e) Comparison of single particle dynamics on a ladder with $L_y = 24$ (obc). For sufficient separation of time scales between static hopping J, lattice shaking V_0 and modulation frequency Δ, effective (b) and full dynamics agree (c). The effects of small ratios $r_1 = \Delta/V_0$ and $r_2 = V_0/J$, and wrongly chosen phases g_j are shown in (d) and (e).

slow dynamics we find

$$\mathcal{H}_{\text{eff}} = \frac{1}{\Delta}[V^{(+)}, V^{(-)}] + \mathcal{O}(\frac{1}{\Delta^2}) \tag{14.9}$$

$$= -\frac{JV_0}{2\Delta}[\hat{a}_2^\dagger \hat{a}_1 (e^{-ig_1} - e^{-ig_2}) + h.c.] + \frac{J^2}{\Delta}(-\hat{n}_1 + \hat{n}_2) + \mathcal{O}(\frac{1}{\Delta^2}). \tag{14.10}$$

In addition one has to consider an initial kick to the wavefunction

$$\hat{K} = \frac{1}{i\Delta}(V^{(+)} - V^{(-)}) + \mathcal{O}(\frac{1}{\Delta^2}) \tag{14.11}$$

$$= \frac{V_0}{\Delta}(\hat{n}_1 \sin(g_1)) + \hat{n}_2 \sin(g_2)) + \frac{J}{\Delta}(i\hat{a}_2^\dagger \hat{a}_1 - i\hat{a}_1^\dagger \hat{a}_2) + \mathcal{O}(\frac{1}{\Delta^2}), \tag{14.12}$$

such that the time evolved state is given by

$$\psi(t) = e^{-i\Delta 2\hat{W}t} e^{-i\hat{K}} e^{-i\mathcal{H}_{\text{eff}}t} e^{i\hat{K}} \psi(0). \tag{14.13}$$

14.2 Benchmarking the Single Particle Physics

With above expression for $\mathcal{H}_{\text{eff}}$ we have discussed the effective model of the FQH on the ladder in Chapter 4. We here want to benchmark the agreement of effective and full dynamics, however restrict ourselves to single particle physics. In Fig. 14.1(a) we show the effective ladder scheme we want to realize with flux $\Phi_{1,2} = \pi, 0$ piercing every second plaquette. The exact dynamics of a single particle initialized at site $j = 1$ at $t = 0$ is displayed in Fig. 14.1(b) and shows the confinement to the edge due to the magnetic field. The Floquet treatment is exact in the limit of large static detuning and small static hopping compared to the modulation

$$r_1 = \frac{\Delta}{V_0} \gg 1, \quad \text{and } r_2 = \frac{V_0}{J} \gg 1. \tag{14.14}$$

In Fig. 14.1(c) we display the propagation of the single particle for large ratios $r_1 = r_2 = 20$ and with the g_j chosen according to Eq. (4.10) in Chapter 4. Indeed we find very good

agreement with the results for the effective model in (b). If ratios are chosen smaller as in (d), where $r_1 = r_2 = 5$ the correspondence with the effective dynamics breaks down and the particle is not confined to the edge. In (e) we show results for differently chosen phases $g_j = 0$ for all j of the lattice shaking. For such a configuration no flux pierces the plaquettes and the particle propagates freely aways from its initial position.

Chapter 15

Rate Equation Models

In this thesis we repeatedly use the mapping from many body quantum dynamics to many body classical dynamics that are described by systems of rate equations, introduced in Chapter 6. The most important input for this models is the rate of excitation $\Gamma_\uparrow(\Delta)$ and deexcitation $\Gamma_\downarrow(\Delta)$ for a single site at a given detuning. In Chapter 7 we have derived these rates for the case of superatom clusters in detail. The text book derivation for simple two level atoms, as well as a derivation for coherent population trapping (CPT), constitute the first part of this appendix. Similar derivations as below can be found in the literature [184].

Although classical, the state space grows exponentially in the number of sites and straightforward numeric solution of the set of rate equations is infeasible. Both, classical and quantum dynamics, can be unraveled using Monte Carlo methods that sample over a large set of randomly generated trajectories. The resources for describing a single state of a classical trajectory however scale linear in system size, whereas they are exponential in the quantum case. We will introduce two sampling methods for classical systems and discuss their individual benefits.

15.1 Derivation of Single Atom Rates

15.1.1 Two-level driving

We consider a single atom with ground state $|\mathrm{g}\rangle$ and excited state $|\mathrm{r}\rangle$ subject to a classical driving field Ω

$$\mathcal{H} = (\Omega\hat{\sigma}_{\mathrm{gr}} + h.c.) + \Delta\hat{\sigma}_{\mathrm{rr}}. \tag{15.1}$$

In addition to this coherent dynamics we take into account the finite lifetime of the excited state and decoherence via the jump operators

$$L_{\mathrm{s}} = \sqrt{\Gamma}\hat{\sigma}_{\mathrm{gr}}, \qquad L_{\mathrm{d}} = \sqrt{\Gamma_{\mathrm{d}}}\hat{\sigma}_{\mathrm{rr}}. \tag{15.2}$$

Both dissipation channels contribute to the damping of the atomic coherence $\varrho_{gr} = \langle g|\varrho|r\rangle$ with rate $\gamma = (\Gamma + \Gamma_d)/2$

$$\frac{d}{dt}\varrho_{\mathrm{rg}} = \frac{d}{dt}\langle \mathrm{r}|\varrho|\mathrm{g}\rangle = -i\Omega(\varrho_{\mathrm{gg}} - \varrho_{\mathrm{rr}}) - i\Delta\varrho_{\mathrm{rg}} - \gamma\varrho_{\mathrm{rg}}. \tag{15.3}$$

In the stationary state and for strong damping $\gamma > \Omega, \Delta$ we can adiabatically eliminate the coherence

$$\frac{d}{dt}\varrho_{\mathrm{rg}} \stackrel{!}{=} 0 \Rightarrow \varrho_{rg} = \frac{i\Omega(\varrho_{\mathrm{rr}} - \varrho_{\mathrm{gg}})}{\gamma + i\Delta}. \tag{15.4}$$

Substituting this coherence into the dynamic equation for the populations yields

$$\frac{d}{dt}\varrho_{\mathrm{gg}} = \Gamma\varrho_{\mathrm{rr}} - i\Omega(\varrho_{\mathrm{rg}} - \varrho_{\mathrm{gr}}) \tag{15.5}$$

$$= \Gamma\varrho_{\mathrm{rr}} + \frac{2\Omega^2\gamma}{\gamma^2+\Delta^2}(\varrho_{\mathrm{rr}} - \varrho_{\mathrm{gg}}). \tag{15.6}$$

Therefore the effective excitation and deexcitation rates are given by

$$\Gamma_\uparrow(\Delta) = \frac{2\Omega^2\gamma}{\gamma^2+\Delta^2}, \qquad \Gamma_\downarrow(\Delta) = \Gamma_\uparrow(\Delta) + \Gamma. \tag{15.7}$$

From this we calculate the steady state excitation probability

$$\varrho^0_{\mathrm{rr}} = 2\gamma\Omega^2/[4\Omega^2\gamma + \Gamma(\gamma^2+\Delta^2)], \tag{15.8}$$

which is bounded from above by $\varrho^0_{\mathrm{rr}} < 1/2$.

15.1.2 Coherent population trapping

The second excitation scheme we use employs dark state driving for three level atoms

$$\mathcal{H} = (\Omega\hat{\sigma}_{\mathrm{ge}} + h.c.) + (\Omega_{\mathrm{C}}\hat{\sigma}_{\mathrm{er}} + h.c.) + \Delta\hat{\sigma}_{\mathrm{rr}}. \tag{15.9}$$

The intermediate state $|\mathrm{e}\rangle$ has a short lifetime and is the only dissipation, we here take into account

$$\hat{L}_{\mathrm{e}} = \sqrt{\Gamma}_{\mathrm{e}}\hat{\sigma}_{\mathrm{ge}}. \tag{15.10}$$

For resonant excitation, $\Delta = 0$, we find that $|\Phi\rangle = (\Omega_{\mathrm{C}}|\mathrm{g}\rangle - \Omega|\mathrm{r}\rangle)/\sqrt{\Omega^2+\Omega_{\mathrm{C}}^2}$ is an eigenstate of the Hamiltonian and at the same time a dark state regarding the dissipation, $\hat{L}_{\mathrm{e}}|\Phi\rangle = 0$. All population accumulates in this fixed point of the dynamics and the stationary state is simply given by

$$\varrho^0(\Delta = 0) = |\Phi\rangle\langle\Phi|. \tag{15.11}$$

For the general case, we start by eliminating the coherences. Again note that $\partial_t\varrho_{\mathrm{eg}} = 0$ is only exact in the stationary state but a valid approximation for the dynamics in the regime $\Gamma_{\mathrm{e}} > \Omega, \Omega_{\mathrm{C}}, \Delta$

$$\varrho_{\mathrm{eg}} = \frac{2i\Omega(\varrho_{\mathrm{ee}} - \varrho_{\mathrm{gg}})}{\Gamma_{\mathrm{e}}} - i\frac{2\Omega_{\mathrm{C}}}{\Gamma_{\mathrm{e}}}\varrho_{\mathrm{rg}}, \tag{15.12}$$

$$\varrho_{\mathrm{re}} = \frac{2i\Omega_{\mathrm{C}}(\varrho_{\mathrm{rr}} - \varrho_{\mathrm{ee}})}{\Gamma_{\mathrm{e}} + 2i\Delta} + i\frac{2\Omega}{\Gamma_{\mathrm{e}} + 2i\Delta}\varrho_{\mathrm{rg}} \tag{15.13}$$

In a second step of adiabatic elimination we consider the coherence between ground and Rydberg state

$$\varrho_{\mathrm{rg}} = 2\Omega\Omega_{\mathrm{C}}\Big(\frac{\varrho_{\mathrm{ee}} - \varrho_{\mathrm{gg}}}{\Gamma_{\mathrm{e}}} + \frac{\varrho_{\mathrm{ee}} - \varrho_{\mathrm{rr}}}{\Gamma_{\mathrm{e}} + 2i\Delta}\Big)/\Big(\frac{2\Omega_{\mathrm{C}}^2}{\Gamma_{\mathrm{e}}} + \frac{2\Omega^2}{\Gamma_{\mathrm{e}} + 2i\Delta} + i\Delta\Big). \tag{15.14}$$

Substituting Eq. (15.14) in Eqs. (15.12), (15.13) yields all three coherences as a function of the populations only. Combined with the dynamic equations for the populations, this yields

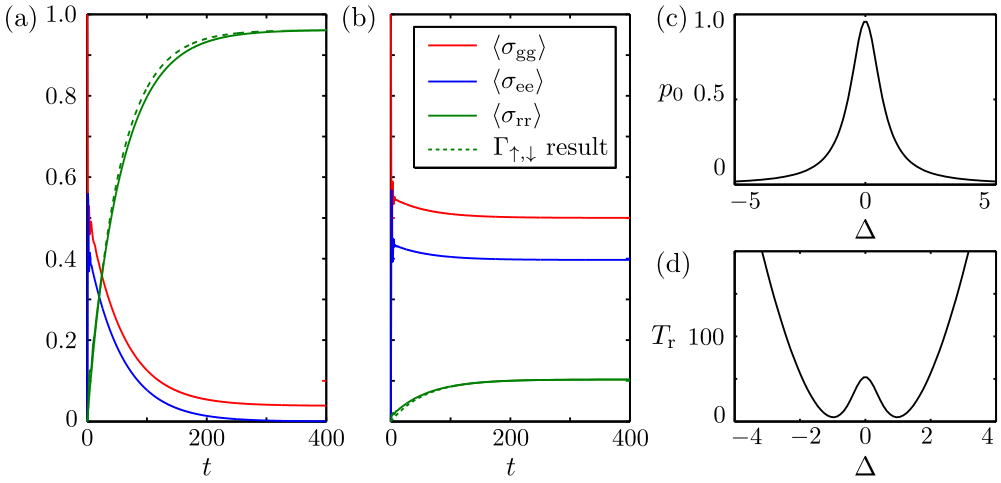

Figure 15.1: Classical rate equation model of single atom CPT for $\Omega = \Gamma_e = 1$ and $\Omega_C = \Gamma_e/5$. In (a) and (b) we compare exact dynamics of the populations with the rate equation result for the excitation probability in the resonant ($\Delta = 0$) and off resonant ($\Delta = 2\Gamma_e$) case. In (c) we display the steady state excitation probability as a function of detuning and in (d) the corresponding relaxation time.

purely classical rate equations

$$\frac{d}{dt}\left(\varrho_{gg}, \varrho_{ee}, \varrho_{rr}\right)^t \approx X(\Omega, \Omega_C, \Delta, \Gamma_e)\left(\varrho_{gg}, \varrho_{ee}, \varrho_{rr}\right)^t. \tag{15.15}$$

The stationary state of Eq. (15.15) is exact, whereas the time evolution is only an approximation based on the validity of the adiabatic elimination of coherences. For the general case we numerically diagonalize X. Its nullvector $X|0\rangle = 0$ with appropriate normalization is the steady state population vector $\left(\varrho^0_{gg}, \varrho^0_{ee}, \varrho^0_{rr}\right)^t$ and from the eigenvalue spectrum u_i we gain an estimate for the relaxation time $T_r = \max_{u_i \neq 0}(1/|u_i|)$, which is the inverse of the smallest non-zero eigenvalue. We define effective rates for excitation and deexcitation via

$$\Gamma_\uparrow = \varrho^0_{rr}/T_r, \qquad \Gamma_\downarrow = (1 - \varrho^0_{rr})/T_r. \tag{15.16}$$

In Fig. 15.1 (a) and (b) we show comparisons of exact quantum dynamics and the single atom rate equations and find that not only the stationary value, but also the dynamics is well approximated. In Fig. 15.1 (c) and (d) we display the excitation probability and relaxation time respectively as a function of the detuning. For $\Omega_C \ll \Omega, \Gamma_e$ we find

$$\varrho^0_{rr} = \frac{\Omega^2}{\Omega^2 + \Omega_C^2}\frac{1}{1 + \Delta^2/\omega^2}, \quad \text{with } \omega = \frac{\Omega^2}{\sqrt{2\Omega^2 + (\Gamma_e/2)^2}}. \tag{15.17}$$

Note that ϱ^0_{rr} is possible in the limit $\Omega \gg \Omega_c$ and $\Delta \ll \omega$.

15.2 Monte Carlo Simulations

For systems of many sites N, tracking all elements of the classical density matrix is infeasible as the number of different configurations scales exponentially as 2^N. Each configuration $\{S_i\}$ is uniquely identified via the state S_i of every site, either $S_i = 0$ for non excited or $S_i = 1$

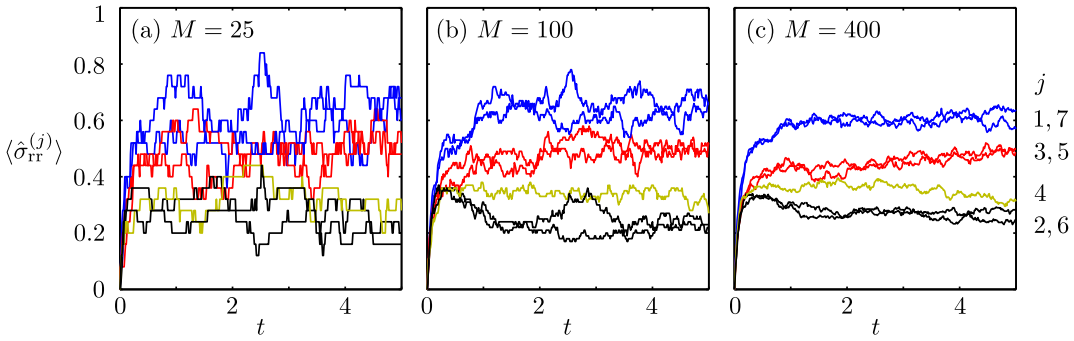

Figure 15.2: dMC simulation of the NN rate equation model on a finite chain of length $L = 7$ and $\kappa = 5$. The subfigures show the excitation probability for the individual atoms for increasing number of trajectories M such that the expected fluctuations are reduced by a factor of two in each step.

for excited respectively. The goal of a Monte Carlo algorithms is to generate a set of M configurations $\{S_i^{(k)}\}$ for the density matrix ϱ, such that

$$\mathrm{Tr}\,\varrho\hat{O} = \frac{1}{M}\sum_{k=1}^{M} O_{\{S_i^{(k)}\}} + \mathcal{O}(1/\sqrt{M}), \tag{15.18}$$

where $\hat{O}$ is an arbitrary operator. With an algorithm that can generate such faithful representations of the steady state density matrix, one can calculate expectation values with high precision. The memory constraints of exact numeric evolution have been shifted to processing constraints regarding the number of representatives $\{S_i^{(k)}\}$ we generate.

15.2.1 Dynamic trajectory Monte Carlo

Our primary choice of Monte Carlo algorithm is dynamic trajectory Monte Carlo (dMC). Here, we not only generate a faithful representation of the steady state but of $\varrho(t)$. We restrict to a trivial initial state $\Psi_0^{(k)} = \{S_i^{(0)} = 0\}$, all sites non excited, at time $t_0^{(k)} = 0$, where k enumerates the different trajectories and l the points in time, where the state of the system changes. The dMC algorithm generates a Markov chain $(\Psi_l^{(k)}, t_l^{(k)})$, until $t_l^{(k)}$ is larger than the maximum time we consider. Step one in generating this chain is to calculate the rates r_i of all possible single site state changes. If $S_i^l = 0, r_i = \Gamma_\uparrow(\Delta_i)$, where Δ_i is the effective detuning of site i in the configuration $\Psi_l^{(k)}$. For an excited site $S_i^l = 1, r_i = \Gamma_\downarrow(\Delta_i)$ respectively. The second step consists in calculating the waiting time until a change occurs. The total rate of change is given by $r = \sum_i r_i$, such that the expected waiting time is $\langle\tau\rangle = 1/r$. Using a random number generator, we draw a waiting time τ from a Poisson distribution with mean $\langle\tau\rangle$. The next time point is determined by $t_{l+1}^{(k)} = t_l^{(k)} + \tau$. In the third and final step, we randomly choose one of the sites , c, with weights r_i. The updated state Ψ_{l+1}^k is identical to Ψ_l^k, except for the change of the atomic state at site c. A faithful representation of $\varrho(t_1)$ is given by the set of states $\Psi_{l(k)}^{(k)}$, with $l(k)$ such, that $t_{l(k)}^{(k)} \leq t_1$ and $t_{l(k)+1}^{(k)} > t_1$.

In Fig. 15.2 we show an example of the dMC convergence when simulating the rate equation model developed in chapter 6. Whereas results with $M = 25$ trajectories are strongly fluctuating, we clearly see the alternating pattern of excitation probabilities for $M = 400$ trajectories, which results in a factor four reduction in MC noise. A similar ansatz for the description of Rydberg systems has been introduced in [185].

15.2.2 Steady state Monte Carlo

dMC samples the entire time evolution towards the stationary state, which for example enabled our discussion of dynamical critical exponents for the two dimensional Rydberg lattice gas. However, this feature can quickly turn into a problem, when relaxation to the stationary state is slow in real time. Again the two dimensional Rydberg lattice gas is a good example. Different points in configuration space may have equal weight in the stationary state, but are connected by a strongly suppressed path in real dynamics. The two configurations of a fully excited sublattice and a fully excited complementary sublattice displayed in Fig. 15.3, are equally likely in the stationary state, but relaxation from one to the other is very slow in real time. Steady State MC enables the use of more complicated steps, such as flipping all spins at once for connecting the two states, and still generates a faithful representation of the stationary state.

A faithful representation of the stationary state ϱ is generated, as for dMC, by sampling trajectories. In every step a random state change, out of a predefined set is chosen. This could be the excitation of a single atom, or the flip of all atoms. Whether this change is applied to the configuration, is determined by the ratio of weights in the stationary state

$$p_{\text{change}} = \varrho^0_{\text{candidate}}/\varrho^0_{\text{old}}. \tag{15.19}$$

After evaluation of this probability and stochastically updating the state or not, this procedure is repeated. Clearly the generated path through configuration space, is not the true time evolution and many different sets of potential changes are applicable. For representing the stationary state faithfully, one must not take all configurations into account, as subsequent elements of the Markov chain are correlated and not independent. The relevant step number for relaxation of such correlations is the equivalent to the system relaxation time in dMC simulations and is strongly dependent on the set of changes [259].

Imposing detailed balance

Calculation of p_{change} is *easy* for conventional equilibrium problems, where the thermal state of a canonical ensemble is given by $\varrho = Z^{-1}e^{-\beta\mathcal{H}}$. As only the ratio of weights is important, one finds $p_{\text{change}} = e^{-\beta(E_{\text{change}}-E_{\text{old}})}$, which can often be calculated quickly. When applying ssMC to Rydberg rate equations, we face the severe problem, that we have no access to p_{change} in general. An exception are the idealized hard sphere problems, where the stationary state is given by the detailed balance ansatz. We and others rely on imposing detailed balance for the single atom transitions. One chooses the single atom excitation and deexcitation as set of possible changes and approximates

$$p_{\text{excitation}} \approx \frac{\Gamma_\uparrow}{\Gamma_\downarrow + \Gamma_\uparrow}, \qquad p_{\text{deexcitation}} \approx \frac{\Gamma_\downarrow}{\Gamma_\downarrow + \Gamma_\uparrow}, \tag{15.20}$$

where the excitation and deexcitation rates $\Gamma_{\uparrow,\downarrow}$ are dependent on the interaction with excited atoms.

We now want to discuss a small example that illustrates the potential failure of ssMC. Consider a two site rate equation problem, as illustrated in Fig. 15.3(b). All processes change the state of only one of the two atoms and therefore two pathways exists from both atoms in the ground state g and both atoms in excited state r. The matrix of rates on the configuration

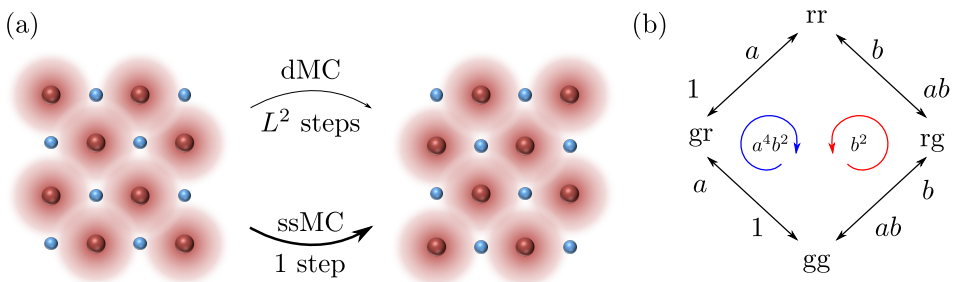

Figure 15.3: (a) Sampling of configuration space with dMC is slow, if different configurations are relevant but far separated in terms of the number of required steps. ssMC can circumvent this by introducing unconventional steps. (b) Minimal model to reveal the failure of ssMC in absence of detailed balance.

space $\{\mathrm{gg}, \mathrm{gr}, \mathrm{rg}, \mathrm{rr}\}$ is given by

$$R = \begin{pmatrix} -a-b & 1 & ab & 0 \\ a & -1-a & 0 & 1 \\ b & 0 & -ab-b & ab \\ 0 & a & b & -1-ab \end{pmatrix} \tag{15.21}$$

with a the ratio of pump to decay on one path and the reverted ratios on the other path. b is a time scale difference between the two paths.

If we consider the approach of steady state sampling with imposed detailed balance along every bond, we must consider for each transition the probability for the atom to be excited or not. This quantity is independent of the timescale b and indeed ssMC the state $\varrho_{\mathrm{ssMC}}\left(1,1,1,1\right)/4$. In the limit $a \to 0, b \to 0$ the true dynamics is dominated by the transitions around gr, that drive the stationary state towards gg and indeed one finds the exact solution $\varrho_{\mathrm{a}\to 0,\mathrm{b}\to 0}\left(1,0,1,0\right)/2$ in striking difference to the ssMC result. Only in the special cases $a = 1$, where detailed balance is restored and $b = 1$, where left and right path have equal time scales, the true steady state agrees with the ssMC result.

Above model is chosen to illustrate the potential errors of ssMC with imposed detailed balance. A good measure of detailed balance violation, would give insight into the validity of ssMC for the typical Rydberg systems under consideration.

Chapter 16

Superatom Benchmarks

16.1 Benchmarking of Rate Equation Simulations

To describe the complex many-body dynamics of strongly interacting Rydberg atoms, a classical rate equation description is used [184, 260, 185, 84]. Intuitively, such an approach is valid in the presence of strong decoherence and a formal derivation can be found for example in [220].

We here present results for a model system that exhibits important aspects of the superatom physics discussed in Chapter 9, but is so small, that the full quantum dynamics can be simulated. The model is displayed in Fig.16.1(a) and is comprised of two very small clusters of N atoms each. The size r of the individual clusters is small, such that the Rydberg-Rydberg interaction within the cluster strictly suppresses multiple excitations. On the other hand, the distance between the two ensembles $l \gg r$ is much larger and therefore the interaction U between excitations in different clusters is finite. Atoms are excited with Rabi frequency Ω and subject to spontaneous decay Γ and decoherence with rate $\Gamma_{\rm d}$ and exact simulations are feasible in the small Hilbert space of dimension $(1+N)^2$. In the absence of decoherence $\Gamma_m athrmd$, dynamics is restricted to the completely symmetric Hilbert space of only four states.

In Fig.16.1(b) we show results for the mean number of Rydberg excitations $\langle N_{\rm r}\rangle$ and their statistics $g_2(0)$ as a function of the driving Ω in the stationary state. At strong dephasing of $\Gamma_{\rm d}/2\pi = 140$ kHz (red), rate equation (full line) and exact results (squares) agree within small errors. We identify three regimes, first of all the weak driving regime which we also use to calibrate the rate equation model to the experiment. Furthermore we find a pronounced plateau of blockade between the two clusters, where at most one of the two clusters is excited and finally for large drivings, blockade breaks down and the number of excitations increases again. In absence of decoherence (black) the rate equations yield incorrect results for both the number of excitations and their statistics.

For off resonant excitation the mesoscopic superatom and the model system exhibit antiblockade and pronounced bunching of Rydberg excitations. Here we have chosen the detuning such, that it exactly cancels the interaction $\Delta_0 = -U$ and the second excitation process is resonant. Both statistics and excitation number are well reproduced by the rate equations in the presence of decoherence across the range of driving Rabi frequencies, but the classical ansatz fails in absence of decoherence.

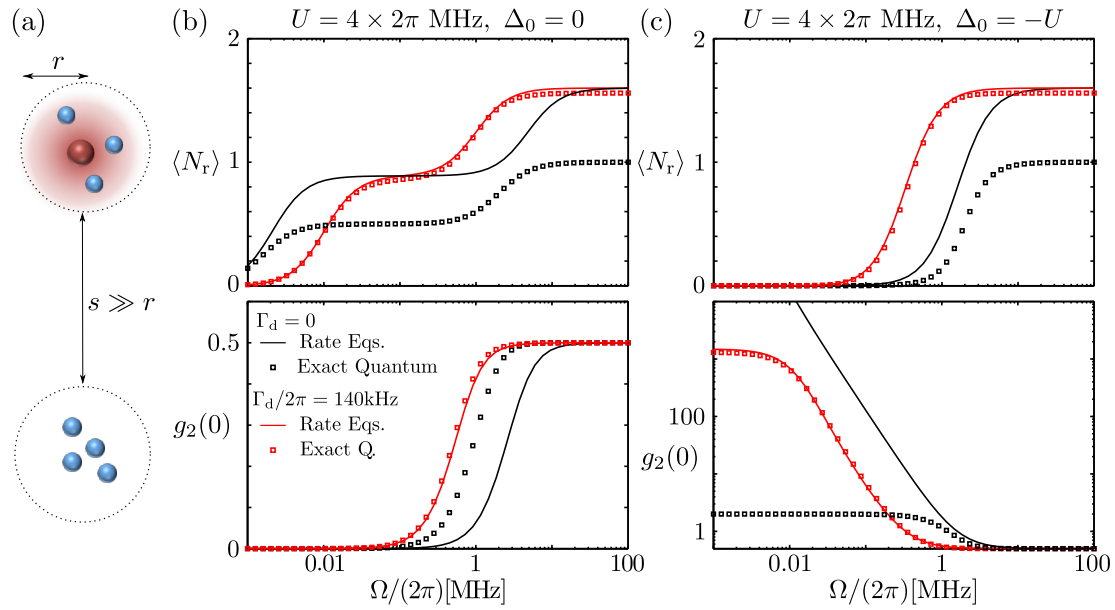

Figure 16.1: (a) Model system for validating the rate equation simulations with cluster of 4 atoms. (b) Mean number of Rydberg excited atoms and two excitation correlations for resonant excitation with decoherence $\Gamma_d/2\pi = 140$ kHz (red) and $\Gamma_d = 0$ (black). Solid lines are results of the rate equation model and exact quantum simulation results are displayed as squares. (c) Results for off resonant excitation with $\Delta_0 = -U$, $U = 4 \times 2\pi$ MHz, symbols as in (b).

16.2 Coherent Dynamics

As shown in the previous section, the long time excitation statistics is well described by rate equation simulations. However on short time scales the number of excited atoms is more sensitive to coherent effects as shown in Fig.16.2. Parameters are chosen as in Fig.16.1(a) with driving $\Omega/2\pi = 270$ kHz, such that $g_2(0) = 0.1$ and we are in the steady-state blockade regime. The initial dynamics reveals coherent, collective Rabi oscillations, which are rapidly damped by the decoherence. Note that in the experiment due to the larger number of atoms and the presence of weakly interacting atom pairs, a smaller value of Ω has to be chosen to preserve antibunching.

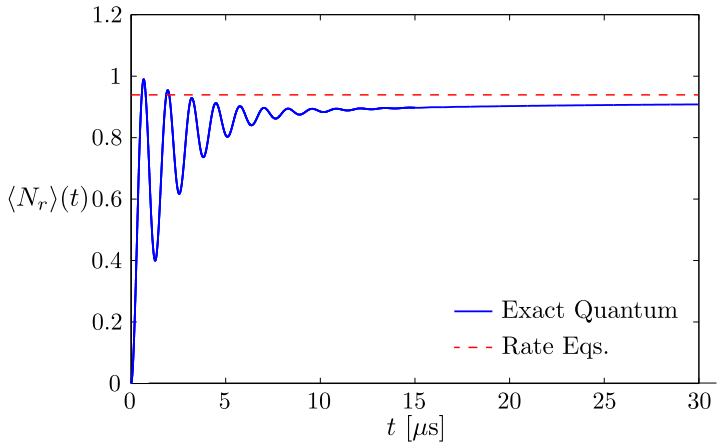

Figure 16.2: Expectation value of Rydberg excitations as a function of time since driving of model systems with $N = 4$ atoms per cluster started. For a decoherence rate of $\Gamma_\mathrm{d}/2\pi = 140$ kHz, interaction $U/2\pi = 4$ MHz and $\Omega/2\pi = 270$ kHz the full quantum simulation (blue) reveals damped coherent dynamics. At longer times, exact results converge towards the rate equation model results (dashed red) in the stationary state.

Chapter 17

Dynamic Equations for Two Rydberg Polaritons

Within this thesis we consider homogeneous media and must not separate between spatial regions within and outside of the atomic medium. As motived in the introduction 1.4 the relevant fields for the propagation are the electric field $\hat{\mathcal{E}}(z)$, the polarization $\hat{\mathcal{P}}(z)$ and the spin coherence $\hat{\mathcal{S}}(z)$, which obey the commutation relation $[\hat{\mathcal{E}}(z), \hat{\mathcal{E}}^\dagger(z')] = [\hat{\mathcal{P}}(z), \hat{\mathcal{P}}^\dagger(z')] = [\hat{\mathcal{S}}(z), \hat{\mathcal{S}}^\dagger(z')] = \delta(z, z')$. Our ansatz and notation are closely related to the methods used in [238].

17.1 Two-Excitation Wave Function

The factors of the wave function defined in Eq. (12.19) are chosen such, that for the norm we find

$$\begin{aligned}\langle\Psi(t)|\Psi(t)\rangle = \iint dz_1 dz_2 \big[&|EE(z_1,z_2)|^2 + |PP(z_1,z_2)|^2 + |SS(z_1,z_2)|^2 \\ &+ |EP(z_1,z_2)|^2 + |ES(z_1,z_2)|^2 + |PS(z_1,z_2)|^2\big],\end{aligned} \tag{17.1}$$

which for the initial state will be unity. Our description is incomplete in that we do not include single excitations that result from the loss of the second excitation.

17.1.1 Equations of Motion

The dynamic equations in the Heisenberg picture for the field operators $\hat{\mathcal{E}}(z), \hat{\mathcal{P}}(z)$ and $\hat{\mathcal{S}}(z)$ are given in Eqs. (1.56),(1.57) and (12.2) and can be translated into dynamic equations for the components of the wave function in the Schrödinger representation

$$\partial_t EE(z_1,z_2) = \frac{1}{\sqrt{2}}\langle 0|[\partial_t \hat{\mathcal{E}}(z_1)]\hat{\mathcal{E}}_{z_2} + \hat{\mathcal{E}}_{z_1}[\partial_t \hat{\mathcal{E}}(z_2)]|\Psi\rangle. \tag{17.2}$$

The full set of equations of motion is given by

$$\partial_t EE(z_1,z_2) = -c(\partial_{z_1} + \partial_{z_2})EE(z_1,z_2) + ig[EP(z_1,z_2) + EP(z_2,z_1)]/\sqrt{2}, \tag{17.3}$$

$$\begin{aligned}\partial_t PP(z_1,z_2) = &-2(\gamma + i\Delta)PP(z_1,z_2) + ig[EP(z_1,z_2) + EP(z_2,z_1)]/\sqrt{2} \\ &+ i\Omega[PS(z_1,z_2) + PS(z_2,z_1)]/\sqrt{2}\end{aligned} \tag{17.4}$$

and for the mixed components

$$\partial_t SS(z_1,z_2) = -iV(z_1,z_2)SS(z_1,z_2) + i\Omega[PS(z_1,z_2)+PS(z_2,z_1)]/\sqrt{2}, \tag{17.5}$$

$$\partial_t EP(z_1,z_2) = -[c\partial_{z_1} + (\gamma+i\Delta)]EP(z_1,z_2) + ig\sqrt{2}[EE(z_1,z_2)+PP(z_2,z_1)] + i\Omega ES(z_1,z_2), \tag{17.6}$$

$$\partial_t ES(z_1,z_2) = -c\partial_{z_1} ES(z_1,z_2) + igPS(z_1,z_2) + i\Omega EP(z_1,z_2), \tag{17.7}$$

$$\partial_t PS(z_1,z_2) = -\gamma PS(z_1,z_2) + igES(z_1,z_2) + i\Omega\sqrt{2}[PP(z_1,z_2)+SS(z_1,z_2)]. \tag{17.8}$$

The above set is inconvenient as it is non local due to the exchange of z_1 and z_2 in some equations. We resolve this inconvenience by introducing symmetric and antisymmetric functions $EP_\pm(z_1,z_2) = [EP(z_1,z_2) \pm EP(z_2,z_1)]/\sqrt{2}$ and respectively $ES_\pm$ and $PS_\pm$. This increases the number of variables to nine, where the newly introduced fields are cross coupled by the propagation.

$$\partial_t EE = -c(\partial_{z_1}+\partial_{z_2})EE + igEP_+, \tag{17.9}$$

$$\partial_t PP = -2(\gamma+i\Delta)PP + igEP_+ + i\Omega PS_+, \tag{17.10}$$

$$\partial_t SS = -iV(z_1,z_2)SS + i\Omega PS_+, \tag{17.11}$$

$$\partial_t EP_+ = -(\gamma+i\Delta)EP_+ + 2ig(EE+PP) + i\Omega ES_+ - c[(\partial_{z_1}+\partial_{z_2})EP_+ + (\partial_{z_1}-\partial_{z_1})EP_-]/2, \tag{17.12}$$

$$\partial_t EP_- = -(\gamma+i\Delta)EP_+ + i\Omega ES_- - c[(\partial_{z_1}-\partial_{z_2})EP_+ + (\partial_{z_1}+\partial_{z_1})EP_-]/2, \tag{17.13}$$

$$\partial_t ES_+ = igPS_+ + i\Omega EP_+ - c[(\partial_{z_1}+\partial_{z_2})ES_- + (\partial_{z_1}-\partial_{z_1})ES_-]/2, \tag{17.14}$$

$$\partial_t ES_- = igPS_- + i\Omega EP_- - c[(\partial_{z_1}-\partial_{z_2})ES_+ + (\partial_{z_1}+\partial_{z_1})ES_-]/2, \tag{17.15}$$

$$\partial_t PS_+ = -(\gamma+i\Delta)PS_+ + 2i\Omega(PP+SS) + igES_+, \tag{17.16}$$

$$\partial_t PS_- = -(\gamma+i\Delta)PS_- + igES_- \tag{17.17}$$

17.1.2 Translation invariant systems

We employ two-excitation wavefunction techniques in Chapter 12 only for translation invariant systems of finite size L with periodic boundary conditions. To exploit this property, we introduce new variables

$$EE(z_1,z_2) = EE(z_1-z_2,0) := \frac{ee(r)}{\sqrt{L}}, \tag{17.18}$$

where we used that the initial center of mass momentum to be small in the co-moving frame. Due to translation invariance, momentum associated to the center of mass coordinate $R := (z_1+z_2)/2$ is conserved and we here only consider the dynamics in relative coordinate $r := z_1 - z_2$. The factor $1/\sqrt{L}$ is chosen such, that the new variables obey the same normalization conditions as the old ones

$$\int dr|ee(r)|^2 = L\int dr|EE(r,0)|^2 = \iint dz_1 dz_2 |EE(z_1,z_2)|^2. \tag{17.19}$$

We here show the derivation of the new dynamic equations only for the new ep_+ component

$$\partial_t ep_+(r) = \sqrt{L}\partial_t\ EP_+(r,0) \tag{17.20}$$

$$= \cdots - \frac{c\sqrt{L}}{2}\left[\partial_{z_1} + \partial_{z_2}\right] EP_+(r,0) - \frac{c\sqrt{L}}{2}\left[\partial_{z_1} - \partial_{z_2}\right] EP_-(r,0) \tag{17.21}$$

$$= \cdots - \frac{c\sqrt{L}}{2}\left[\partial_r - \partial_r\right] EP_+(r,0) - \frac{c\sqrt{L}}{2}\left[\partial_r + \partial_r\right] EP_-(r,0) \tag{17.22}$$

$$= \cdots - c\partial_r\ ep_-(r). \tag{17.23}$$

The complete set of equations of motion for the reduced variables in relative coordinates is given by

$$\partial_t\ ee = ig\ ep_+, \tag{17.24}$$

$$\partial_t\ pp = -2(\gamma + i\Delta)pp + igep_+ + i\Omega ps_+, \tag{17.25}$$

$$\partial_t\ ss = -iV(r)ss + i\Omega\ ps_+, \tag{17.26}$$

$$\partial_t\ ep_+ = -(\gamma + i\Delta)\ ep_+ + 2ig(ee + pp) + i\Omega es_+ \qquad -c\partial_r\ ep_-, \tag{17.27}$$

$$\partial_t\ ep_- = -(\gamma + i\Delta)\ ep_+ + i\Omega es_- \qquad -c\partial_r\ ep_+, \tag{17.28}$$

$$\partial_t\ es_+ = ig\ ps_+ + i\Omega\ ep_+ \qquad -c\partial_r\ es_-, \tag{17.29}$$

$$\partial_t\ es_- = ig\ ps_- + i\Omega\ ep_- \qquad -c\partial_r\ es_+, \tag{17.30}$$

$$\partial_t\ ps_+ = -(\gamma + i\Delta)\ ps_+ + 2i\Omega(pp + ss) + ig\ es_+, \tag{17.31}$$

$$\partial_t\ ps_- = -(\gamma + i\Delta)\ ps_- + ig\ es_-. \tag{17.32}$$

The propagation term for the two photon component for example, is trivially zero in relative coordinates, because they propagate at equal speed and therefore constant distance. This reduced set of equations is the basis for our numerical analysis.

Bibliography

[1] M H Anderson, J R Ensher, M R Matthews, C E Wieman, and E A Cornell. Observation of Bose-Einstein Condensation in a Dilute Atomic Vapor. *Science*, 269(5221):198–201, July 1995.

[2] Markus Greiner, Olaf Mandel, Tilman Esslinger, Theodor W Hänsch, and Immanuel Bloch. Quantum phase transition from a superfluid to a Mott insulator in a gas of ultracold atoms. *Nature*, 415(6867):39–44, 2002.

[3] Immanuel Bloch, Wilhelm Zwerger, and Jean Dalibard. Many-body physics with ultracold gases. *Reviews of Modern Physics*, 80(3):885–964, July 2008.

[4] Waseem S Bakr, Jonathon I Gillen, Amy Peng, Simon Fölling, and Markus Greiner. A quantum gas microscope for detecting single atoms in a Hubbard-regime optical lattice. *Nature*, 462(7269):74–77, November 2009.

[5] Jacob F Sherson, Christof Weitenberg, Manuel Endres, Marc Cheneau, Immanuel Bloch, and Stefan Kuhr. Single-atom-resolved fluorescence imaging of an atomic Mott insulator. *Nature*, 467(7311):68–72, August 2010.

[6] Jean Dalibard, Fabrice Gerbier, Gediminas Juzeliūnas, and Patrik Öhberg. Colloquium: Artificial gauge potentials for neutral atoms. *Reviews of Modern Physics*, 83(4):1523–1543, November 2011.

[7] L Santos, M Lewenstein, and Tilman Pfau. The physics of dipolar bosonic quantum gases. *Reports on Progress in Physics*, 72:126401, 2009.

[8] A Yu Kitaev. Fault-tolerant quantum computation by anyons. *Annals of Physics*, 303(1):2–30, 2003.

[9] M. Aidelsburger, M. Lohse, C. Schweizer, M. Atala, J. T. Barreiro, S. Nascimbene, N. R. Cooper, I. Bloch, and N. Goldman. Measuring the chern number of Hofstadter bands with ultracold bosonic atoms. *Nature Physics*; advance online publication, December 2014 (DOI 10.1038/nphys3171).

[10] S Diehl, A Micheli, A Kantian, B Kraus, Hans Peter Büchler, and Peter Zoller. Quantum states and phases in driven open quantum systems with cold atoms. *Nature Physics*, 4(11):878–883, September 2008.

[11] F Cinti, T Macrì, W Lechner, G Pupillo, and T Pohl. Defect-induced supersolidity with soft-core bosons. *Nature Communications*, 5:3235, 2014.

[12] Alexander W Glaetzle, Marcello Dalmonte, Rejish Nath, Ioannis Rousochatzakis, Roderich Moessner, and Peter Zoller. Quantum Spin Ice and dimer models with Rydberg atoms. *Physical Review X*, 4:041037, November 2014.

[13] Mikhail D Lukin, Michael Fleischhauer, and R Cote. Dipole Blockade and Quantum Information Processing in Mesoscopic Atomic Ensembles. *Physical Review Letters*, 87(3):037901, June 2001.

[14] N Malossi, M M Valado, S Scotto, P Huillery, P Pillet, D Ciampini, E Arimondo, and O Morsch. Full counting statistics and phase diagram of a dissipative Rydberg gas. *Physical Review Letters*, 113(2):023006, July 2014.

[15] D W Schönleber, M Gärttner, and J Evers. Coherent versus incoherent excitation dynamics in dissipative many-body Rydberg systems. *Physical Review A*, 89(3):033421, 2014.

[16] J Otterbach, M Moos, Dominik Muth, and M Fleischhauer. Wigner Crystallization of Single Photons in Cold Rydberg Ensembles. *Physical Review Letters*, 111(11):113001, 2013.

[17] S Diehl, E Rico, M A Baranov, and Peter Zoller. Topology by dissipation in atomic quantum wires. *Nature Physics*, 7:971, 2011.

[18] N Malossi, M M Valado, S Scotto, P Huillery, P Pillet, D Ciampini, E Arimondo, and O Morsch. Full Counting Statistics and Phase Diagram of a Dissipative Rydberg Gas. *Phys. Rev. Lett.*, 113(2):023006, July 2014.

[19] E Schrödinger. Are there quantum jumps? Part II. *The British Journal for the Philosophy of Science*, III(11):233–242, November 1952.

[20] C C Bradley, C A Sackett, J J Tollett, and R G Hulet. Evidence of Bose-Einstein condensation in an atomic gas with attractive interactions. *Physical Review Letters*, 75(9):1687–1690, 1995.

[21] K Davis, M Mewes, M Andrews, N van Druten, D Durfee, D Kurn, and W Ketterle. Bose-Einstein Condensation in a Gas of Sodium Atoms. *Physical Review Letters*, 75(22):3969–3973, 1995.

[22] Immanuel Bloch. Interference pattern of Mott Insulator and superfluid. www.quantum-munich.de/media/mott-insulator.

[23] M Aidelsburger, M Atala, M Lohse, J T Barreiro, B Paredes, and I Bloch. Realization of the Hofstadter Hamiltonian with Ultracold Atoms in Optical Lattices. *Phys. Rev. Lett.*, 111(18):185301, October 2013.

[24] H A Gersch and G C Knollman. Quantum Cell Model for Bosons. *Physical Review*, 129(2):959–967, 1963.

[25] Ana Maria Rey. *Ultracold bosonic atoms in optical lattices.* PhD thesis, University of Maryland, November 2004.

[26] Thorsten Köhler, Krzysztof Góral, and Paul Julienne. Production of cold molecules via magnetically tunable Feshbach resonances. *Reviews of Modern Physics*, 78(4):1311–1361, December 2006.

[27] D Jaksch, C Bruder, J Cirac, C Gardiner, and P Zoller. Cold Bosonic Atoms in Optical Lattices. *Physical Review Letters*, 81(15):3108–3111, 1998.

[28] W S Bakr, A Peng, M E Tai, R Ma, J Simon, J I Gillen, S Fölling, L Pollet, and M Greiner. Probing the superfluid-to-Mott insulator transition at the single-atom level. *Science*, 329(5991):547–550, July 2010.

[29] Christof Weitenberg, Manuel Endres, Jacob F Sherson, Marc Cheneau, Peter Schauß, Takeshi Fukuhara, Immanuel Bloch, and Stefan Kuhr. Single-spin addressing in an atomic Mott insulator. *Nature*, 471(7338):319–324, April 2012.

[30] T Gericke, C Utfeld, N Hommerstad, and H Ott. A scanning electron microscope for ultracold atoms. *Laser Physics Letters*, 3(8):415–419, August 2006.

[31] Tatjana Gericke, Peter Würtz, Daniel Reitz, Tim Langen, and Herwig Ott. High-resolution scanning electron microscopy of an ultracold quantum gas. *Nature Physics*, 4(12):949–953, October 2008.

[32] Patrick Windpassinger and Klaus Sengstock. Engineering novel optical lattices. *Reports on Progress in Physics*, 76(8):086401, July 2013.

[33] Alexander L Gaunt and Zoran Hadzibabic. Robust Digital Holography For Ultracold Atom Trapping. *Scientific reports*, 2:721, October 2012.

[34] M W Zwierlein, J R Abo-Shaeer, A Schirotzek, C H Schunck, and W Ketterle. Vortices and superfluidity in a strongly interacting Fermi gas. *Nature*, 435(7045):1047–1051, June 2005.

[35] J Ruseckas, G Juzeliūnas, P Öhberg, and M Fleischhauer. Non-Abelian Gauge Potentials for Ultracold Atoms with Degenerate Dark States. *Phys. Rev. Lett.*, 95(1):010404, June 2005.

[36] Y J Lin, R L Compton, K Jiménez-García, J V Porto, and I B Spielman. Synthetic magnetic fields for ultracold neutral atoms. *Nature*, 462(7273):628–632, March 2009.

[37] R Peierls. Zur Theorie des Diamagnetismus von Leitungselektronen. *Zeitschrift für Physik*, 80(11-12):763–791, November 1933.

[38] D Jaksch and P Zoller. Creation of effective magnetic fields in optical lattices: the Hofstadter butterfly for cold neutral atoms. *New Journal of Physics*, 5(1):56–56, May 2003.

[39] A R Kolovsky. Creating artificial magnetic fields for cold atoms by photon-assisted tunneling. *Europhysics Letters*, 93(2):20003, February 2011.

[40] Philipp Hauke, Olivier Tieleman, Alessio Celi, Christoph Ölschläger, Juliette Simonet, Julian Struck, Malte Weinberg, Patrick Windpassinger, Klaus Sengstock, Maciej Lewenstein, and André Eckardt. Non-Abelian Gauge Fields and Topological Insulators in Shaken Optical Lattices. *Phys. Rev. Lett.*, 109(14):145301, October 2012.

[41] Hirokazu Miyake, Georgios A Siviloglou, Colin J Kennedy, William Cody Burton, and Wolfgang Ketterle. Realizing the harper hamiltonian with laser-assisted tunneling in optical lattices. *Physical Review Letters*, 111(18):185302, November 2013.

[42] Gregor Jotzu, Michael Messer, Rémi Desbuquois, Martin Lebrat, Thomas Uehlinger, Daniel Greif, and Tilman Esslinger. Experimental realization of the topological Haldane model with ultracold fermions. *Nature*, 515:237-240, November 2014.

[43] D Thouless, M Kohmoto, M Nightingale, and M den Nijs. Quantized Hall Conductance in a Two-Dimensional Periodic Potential. *Phys. Rev. Lett.*, 49(6):405–408, August 1982.

[44] K Klitzing, G Dorda, and M Pepper. New Method for High-Accuracy Determination of the Fine-Structure Constant Based on Quantized Hall Resistance. *Phys. Rev. Lett.*, 45(6):494–497, August 1980.

[45] C L Kane and E J Mele. Quantum spin Hall effect in graphene. *Physical Review Letters*, 95:226801, 2005.

[46] B Andrei Bernevig, Taylor L Hughes, and Shou-Cheng Zhang. Quantum spin Hall effect and topological phase transition in HgTe quantum wells. *Science*, 314(5806):1757–1761, December 2006.

[47] B Andrei Bernevig and Shou-Cheng Zhang. Quantum Spin Hall Effect. *Phys. Rev. Lett.*, 96(10):106802, March 2006.

[48] Markus König, Steffen Wiedmann, Christoph Brüne, Andreas Roth, Hartmut Buhmann, Laurens W Molenkamp, Xiao-Liang Qi, and Shou-Cheng Zhang. Quantum spin hall insulator state in HgTe quantum wells. *Science*, 318(5851):766–770, November 2007.

[49] D Hsieh, D Qian, L Wray, Y Xia, Y S Hor, R J Cava, and M Z Hasan. A topological Dirac insulator in a quantum spin Hall phase. *Nature*, 452(7190):970–974, April 2008.

[50] S Ryu, A P Schnyder, A Furusaki, and et al. Topological insulators and superconductors: tenfold way and dimensional hierarchy. *New Journal of Physics*, 12:065010, 2010.

[51] Xie Chen, Zheng-Cheng Gu, and Xiao-Gang Wen. Classification of gapped symmetric phases in one-dimensional spin systems. *Physical Review B*, 83(3):035107, January 2011.

[52] Xie Chen, Zheng-Cheng Gu, Zheng-Xin Liu, and Xiao-Gang Wen. Symmetry protected topological orders and the group cohomology of their symmetry group. *Physical Review B*, 87(15):155114, April 2013.

[53] Xiao-Liang Qi and Shou-Cheng Zhang. Topological insulators and superconductors. *Reviews of Modern Physics*, 83(4):1057–1110, October 2011.

[54] R Laughlin. Quantized Hall conductivity in two dimensions. *Physical Review B*, 23(10):5632–5633, May 1981.

[55] Gregory Moore and Nicholas Read. Nonabelions in the fractional quantum hall effect. *Nuclear Physics B*, 360(2-3):362–396, August 1991.

[56] Yasuhiro Hatsugai. Chern number and edge states in the integer quantum Hall effect. *Phys. Rev. Lett.*, 71(22):3697–3700, November 1993.

[57] Fenner Harper, Steven H Simon, and Rahul Roy. Perturbative approach to flat Chern bands in the Hofstadter model. *Physical Review B*, 90(7):075104, August 2014.

[58] Hall resistance in the integer quantum Hall effect. http://www.nobelprize.org/nobel_prizes/physics/laureates/1998/press.html.

[59] D Thouless. Quantization of particle transport. *Physical Review B*, 27(10):6083–6087, May 1983.

[60] J Zak. Berry's phase for energy bands in solids. *Phys. Rev. Lett.*, 62(23):2747–2750, June 1989.

[61] M V Berry. Quantal Phase Factors Accompanying Adiabatic Changes. *Proceedings of the Royal Society of London. A. Mathematical and Physical Sciences*, 392(1802):45–57, March 1984.

[62] RD King-Smith and D Vanderbilt. Theory of polarization of crystalline solids. *Physical Review B*, 47(3):1651–1654, January 1993.

[63] Mikio Nakahara. Geometry, Topology and Physics. IOP Publishing Ltd, 1990.

[64] M Z Hasan and C L Kane. Colloquium: Topological insulators. *Reviews of Modern Physics*, 82(4):3045–3067, November 2010.

[65] B Halperin. Quantized Hall conductance, current-carrying edge states, and the existence of extended states in a two-dimensional disordered potential. *Physical Review B*, 25(4):2185–2190, 1982.

[66] P Delplace, D Ullmo, and G Montambaux. Zak phase and the existence of edge states in graphene. *Physical Review B*, 84(19):195452, November 2011.

[67] E.J. Bergholtz and Z. Liu. Topological flat band models and fractional Chern insulators. *International Journal of Modern Physics B*, 27(24):1330017, September 2013.

[68] Daniel Arovas, J Schrieffer, and Frank Wilczek. Fractional Statistics and the Quantum Hall Effect. *Physical Review Letters*, 53(7):722–723, 1984.

[69] B Halperin. Statistics of Quasiparticles and the Hierarchy of Fractional Quantized Hall States. *Physical Review Letters*, 52(26):2390–2390, 1984.

[70] Parsa Bonderson, Kirill Shtengel, and J Slingerland. Probing Non-Abelian Statistics with Quasiparticle Interferometry. *Phys. Rev. Lett.*, 97(1):016401, July 2006.

[71] R B Laughlin. Anomalous quantum Hall effect: an incompressible quantum fluid with fractionally charged excitations. *Physical Review Letters*, 50(18):1395–1398, 1983.

[72] Chetan Nayak, Ady Stern, Michael Freedman, and Sankar Das Sarma. Non-Abelian anyons and topological quantum computation. *Reviews of Modern Physics*, 80(3):1083–1159, September 2008.

[73] Herman Feshbach. Unified theory of nuclear reactions. *Annals Phys.*, 5(4):357–390, 1958.

[74] E Tiesinga, B J Verhaar, and HTC Stoof. Threshold and resonance phenomena in ultracold ground-state collisions. *Physical Review A*, 47(5):4114–4122, 1993.

[75] H Weimer, M Müller, I Lesanovsky, and P Zoller. A Rydberg quantum simulator. *Nature Physics*, 6:382, 2010.

[76] Mark Saffman, T G Walker, and Klaus Mølmer. Quantum information with Rydberg atoms. *Reviews of Modern Physics*, 82(3):2313, 2010.

[77] Axel Griesmaier, Jörg Werner, Sven Hensler, Jürgen Stuhler, and Tilman Pfau. Bose-Einstein Condensation of Chromium. *Phys. Rev. Lett.*, 94(16):160401, April 2005.

[78] S Kotochigova, P Julienne, and E Tiesinga. Ab initio calculation of the KRb dipole moments. *Physical Review A*, 68(2):022501, August 2003.

[79] Kaden R A Hazzard, Bryce Gadway, Michael Foss-Feig, Bo Yan, Steven A Moses, Jacob P Covey, Norman Y Yao, Mikhail D Lukin, Jun Ye, Deborah S Jin, and Ana Maria Rey. Many-Body Dynamics of Dipolar Molecules in an Optical Lattice. *Phys. Rev. Lett.*, 113:195302, November 2014.

[80] Thomas F Gallagher. *Rydberg Atoms*. Cambridge University Press, November 2005.

[81] R Jastrow. On the Rydberg-Ritz Formula in Quantum Mechanics. *Physical Review*, 73(1):60–67, 1948.

[82] Wenhui Li, I Mourachko, M Noel, and T Gallagher. Millimeter-wave spectroscopy of cold Rb Rydberg atoms in a magneto-optical trap: Quantum defects of the ns, np, and nd series. *Physical Review A*, 67(5):052502, May 2003.

[83] Sébastien Gleyzes, Stefan Kuhr, Christine Guerlin, Julien Bernu, Samuel Deléglise, Ulrich Busk Hoff, Michel Brune, Jean-Michel Raimond, and Serge Haroche. Quantum jumps of light recording the birth and death of a photon in a cavity. *Nature*, 446(7133):297–300, March 2007.

[84] H Schempp, G Günter, M Robert-de Saint-Vincent, C S Hofmann, D Breyel, A Komnik, D W Schönleber, M Gärttner, J Evers, S Whitlock, and M Weidemüller. Full Counting Statistics of Laser Excited Rydberg Aggregates in a One-Dimensional Geometry. *Phys. Rev. Lett.*, 112(1):013002, January 2014.

[85] Matthieu Viteau, Paul Huillery, Mark G Bason, Nicola Malossi, Donatella Ciampini, Oliver Morsch, Ennio Arimondo, Daniel Comparat, and Pierre Pillet. Cooperative excitation and many-body interactions in a cold Rydberg gas. *Phys. Rev. Lett.*, 109:053002, August 2012.

[86] S Anderson, K Younge, and G Raithel. Trapping Rydberg Atoms in an Optical Lattice. *Physical Review Letters*, 107(26):263001, December 2011.

[87] R M Potvliege and C S Adams. Photo-ionization in far-off-resonance optical lattices. *New Journal of Physics*, 8:163, 2006.

[88] G Günter, M Robert-de Saint-Vincent, H Schempp, C S Hofmann, S Whitlock, and M Weidemüller. Interaction Enhanced Imaging of Individual Rydberg Atoms in Dense Gases. *Physical Review Letters*, 108(1):013002, January 2012.

[89] G Günter, H Schempp, M Robert-de Saint-Vincent, V Gavryusev, S Helmrich, C S Hofmann, S Whitlock, and M Weidemüller. Observing the dynamics of dipole-mediated energy transport by interaction-enhanced imaging. *Science*, 342(6161):954–956, November 2013.

[90] A Reinhard, T Liebisch, B Knuffman, and G Raithel. Level shifts of rubidium Rydberg states due to binary interactions. *Physical Review A*, 75(3):032712, March 2007.

[91] Miroshnychenko Y Gaetan A, Wilk T, Chotia A, Viteau M, Comparat D, Pillet P, Browaeys A, and Grangier P. Observation of collective excitation of two individual atoms in the Rydberg blockade regime. *Nature Physics*, 5:115, 2009.

[92] E Urban, T A Johnson, T Henage, L Isenhower, D D Yavuz, T G Walker, and M Saffman. Observation of Rydberg blockade between two atoms. *Nature Physics*, 5(2):110–114, 2009.

[93] L Béguin, A Vernier, R Chicireanu, T Lahaye, and A Browaeys. Direct Measurement of the van der Waals Interaction between Two Rydberg Atoms. *Physical Review Letters*, 110(26):263201, June 2013.

[94] Peter Lambropoulos and David Petrosyan. *Fundamentals of Quantum Optics and Quantum Information*. Springer, Berlin, 2006.

[95] Johannes Otterbach. *Single- and Many-Body Phenomena of Dark-State Polaritons*. PhD thesis, University of Kaiserslautern, October 2011.

[96] Michael Fleischhauer, Atac Imamoglu, and J P Marangos. Electromagnetically induced transparency: Optics in coherent media. *Reviews of Modern Physics*, 77, 2005.

[97] L V Hau, S E Harris, Z Dutton, and C H Behroozi. Light speed reduction to 17 metres per second in an ultracold atomic gas. *Nature*, 397(6720):594–598, 1999.

[98] H Gorniaczyk, C Tresp, J Schmidt, H Fedder, and S Hofferberth. Single-Photon Transistor Mediated by Interstate Rydberg Interactions. *Phys. Rev. Lett.*, 113(5):053601, July 2014.

[99] William Louisell. *Quantum statistical properties of radiation*. New York, Wiley, 1973.

[100] M Fleischhauer and M Lukin. Dark-State Polaritons in Electromagnetically Induced Transparency. *Physical Review Letters*, 84(22):5094–5097, 2000.

[101] W P Su, J R Schrieffer, and A J Heeger. Solitons in Polyacetylene. *Phys. Rev. Lett.*, 42(25):1698–1701, June 1979.

[102] Shinsei Ryu and Yasuhiro Hatsugai. Topological Origin of Zero-Energy Edge States in Particle-Hole Symmetric Systems. *Phys. Rev. Lett.*, 89(7):077002, July 2002.

[103] Li-Jun Lang, Xiaoming Cai, and Shu Chen. Edge States and Topological Phases in One-Dimensional Optical Superlattices. *Phys. Rev. Lett.*, 108(22):220401, May 2012.

[104] Marcos Atala, Monika Aidelsburger, Julio T Barreiro, Dmitry Abanin, Takuya Kitagawa, Eugene Demler, and Immanuel Bloch. Direct measurement of the Zak phase in topological Bloch bands. *Nature Physics*, 9(12):795–800, November 2013.

[105] Yasuhiro Hatsugai. Quantized Berry Phases as a Local Order Parameter of a Quantum Liquid. *Journal of the Physical Society of Japan*, 75(12):123601, December 2006.

[106] Y Hatsugai. Quantized Berry phases for a local characterization of spin liquids in frustrated spin systems. *Journal of Physics: Condensed Matter*, 19:145209, 2007.

[107] F D M Haldane. Nonlinear Field Theory of Large-Spin Heisenberg Antiferromagnets: Semiclassically Quantized Solitons of the One-Dimensional Easy-Axis Néel State. *Phys. Rev. Lett.*, 50(15):1153–1156, April 1983.

[108] T Kennedy. Exact diagonalisations of open spin-1 chains. *Journal of Physics: Condensed Matter*, 2(26):5737–5745, July 1990.

[109] Ulrich Schollwöck. The density-matrix renormalization group in the age of matrix product states. *Annals Phys.*, 326:96, 2011.

[110] Frank Verstraete and J Cirac. Matrix product states represent ground states faithfully. *Physical Review B*, 73(9):094423, March 2006.

[111] Steven R White. Density-matrix algorithms for quantum renormalization groups. *Phys.Rev.B*, 48:10345–10356, 1993.

[112] Dominik Muth, A Mering, and M Fleischhauer. Ultracold bosons in disordered superlattices: Mott insulators induced by tunneling. *Physical Review A*, 77(4):043618, April 2008.

[113] P Buonsante and A Vezzani. Phase diagram for ultracold bosons in optical lattices and superlattices. *Physical Review A*, 70(3):033608, September 2004.

[114] P Buonsante, V Penna, and A Vezzani. Fractional-filling loophole insulator domains for ultracold bosons in optical superlattices. *Physical Review A*, 70(6):061603, December 2004.

[115] Pascual Jordan and Eugene P Wigner. About the Pauli exclusion principle. *Z.Phys.*, 47(9-10):631–651, 1928.

[116] J K Freericks and H Monien. Strong-coupling expansions for the pure and disordered Bose-Hubbard model. *Physical Review B*, 53:2691, 1996.

[117] Q Niu, D J Thouless, and Y S Wu. Quantized Hall conductance as a topological invariant. *Physical Review B*, 31:3372, 1985.

[118] R Resta and S Sorella. Many-Body Effects on Polarization and Dynamical Charges in a Partly Covalent Polar Insulator. *Phys. Rev. Lett.*, 74(23):4738–4741, June 1995.

[119] Yuichi Motoyama and Synge Todo. Path-integral Monte Carlo method for the local $\mathbb{Z}_2$ Berry phase. *Physical Review E*, 87(2):021301, February 2013.

[120] P Buonsante, V Penna, and A Vezzani. Strong-coupling expansions for the topologically inhomogeneous Bose-Hubbard model. *Physical Review B*, 70(18):184520, November 2004.

[121] N C Murphy, R Wortis, and W A Atkinson. Generalized inverse participation ratio as a possible measure of localization for interacting systems. *Physical Review B*, 83(18):184206, May 2011.

[122] Gerardo Ortiz and Richard Martin. Macroscopic polarization as a geometric quantum phase: Many-body formulation. *Physical Review B*, 49(20):14202–14210, May 1994.

[123] A Mering and M Fleischhauer. One-dimensional Bose-Fermi-Hubbard model in the heavy-fermion limit. *Physical Review A*, 77(2):023601, February 2008.

[124] H Guo, S Q Shen, and S Feng. Fractional topological phase in one-dimensional flat bands with nontrivial topology. *Physical Review B*, 86:085124, 2012.

[125] Z Xu, L Li, and S Chen. Fractional topological states of dipolar fermions in one-dimensional optical superlattices. *Physical Review Letters*, 110:215301, 2013.

[126] Haiping Hu, Chen Cheng, Zhihao Xu, Hong-Gang Luo, and Shu Chen. Topological nature of magnetization plateaus in periodically modulated quantum spin chains. *Phys. Rev. B*, 90:035150, Jul 2014.

[127] H Guo and S Q Shen. Topological phase in a one-dimensional interacting fermion system. *Physical Review B*, 84:195107, 2011.

[128] H Guo. Hard-core bosons in one-dimensional interacting topological bands. *Physical Review A*, 86:055604, 2012.

[129] Erez Berg, Michael Levin, and Ehud Altman. Quantized pumping and topology of the phase diagram for a system of interacting bosons. *Phys. Rev. Lett.*, 106:110405, Mar 2011.

[130] Zhihao Xu and Shu Chen. Topological Mott insulators of ultracold atomic mixtures induced by interactions in one-dimensional optical superlattices. *Physical Review B*, 88(4):045110, 2013.

[131] F J Burnell, Meera M Parish, N R Cooper, and S L Sondhi. Devil's staircases and supersolids in a one-dimensional dipolar Bose gas. *Physical Review B*, 80(17):174519, November 2009.

[132] Achim Lauer, Dominik Muth, and Michael Fleischhauer. Transport-induced melting of crystals of Rydberg dressed atoms in a one-dimensional lattice. *New Journal of Physics*, 14(9):095009, September 2012.

[133] F Grusdt, D Abanin, and E Demler. Measuring $\mathbb{Z}_2$ topological invariants in optical lattices using interferometry. *Physical Review A*, 89(4):043621, April 2014.

[134] Emil Bergholtz and Anders Karlhede. Half-Filled Lowest Landau Level on a Thin Torus. *Phys. Rev. Lett.*, 94(2):026802, January 2005.

[135] Emil J Bergholtz and Anders Karlhede. 'One-dimensional' theory of the quantum Hall system. *Journal of Statistical Mechanics: Theory and Experiment*, 2006(04):L04001–L04001, April 2006.

[136] B Andrei Bernevig and N Regnault. Thin-Torus Limit of Fractional Topological Insulators. *arXiv.org:1204.5682*, April 2012.

[137] Anders Sørensen, Eugene Demler, and Mikhail Lukin. Fractional Quantum Hall States of Atoms in Optical Lattices. *Phys. Rev. Lett.*, 94(8):086803, March 2005.

[138] M Hafezi, A Sørensen, E Demler, and M Lukin. Fractional quantum Hall effect in optical lattices. *Physical Review A*, 76(2):023613, August 2007.

[139] Dario Hügel and Belén Paredes. Chiral ladders and the edges of quantum Hall insulators. *Physical Review A*, 89(2):023619, February 2014.

[140] S Fölling, S Trotzky, P Cheinet, M Feld, R Saers, A Widera, T Müller, and I Bloch. Direct observation of second-order atom tunnelling. *Nature*, 448(7157):1029–1032, August 2007.

[141] Marcos Atala, Monika Aidelsburger, Michael Lohse, Julio T Barreiro, Belén Paredes, and Immanuel Bloch. Observation of chiral currents with ultracold atoms in bosonic ladders. *Nature Physics*, 10(8):588–593, July 2014.

[142] M Aidelsburger, M Atala, S Nascimbène, S Trotzky, Y A Chen, and I Bloch. Experimental Realization of Strong Effective Magnetic Fields in an Optical Lattice. *Phys. Rev. Lett.*, 107(25):255301, December 2011.

[143] D Jaksch and P Zoller. Creation of effective magnetic fields in optical lattices: the Hofstadter butterfly for cold neutral atoms. *New Journal of Physics*, 5(1):56–56, May 2003.

[144] Douglas R Hofstadter. Energy levels and wave functions of Bloch electrons in rational and irrational magnetic fields. *Phys.Rev.*, B14(6):2239–2249, 1976.

[145] Di Xiao, Ming-Che Chang, and Qian Niu. Berry phase effects on electronic properties. *Reviews of Modern Physics*, 82(3):1959–2007, July 2010.

[146] David Vanderbilt and R King-Smith. Electric polarization as a bulk quantity and its relation to surface charge. *Physical Review B*, 48(7):4442–4455, August 1993.

[147] C E Bardyn, M A Baranov, C V Kraus, E Rico, A Imamoğlu, P Zoller, and S Diehl. Topology by dissipation. *New Journal of Physics*, 15(8):085001, August 2013.

[148] S Diehl, W Yi, A Daley, and Peter Zoller. Dissipation-Induced d-Wave Pairing of Fermionic Atoms in an Optical Lattice. *Physical Review Letters*, 105(22):227001, November 2010.

[149] G Kordas, S Wimberger, and D Witthaut. Dissipation-induced macroscopic entanglement in an open optical lattice. *EPL (Europhysics Letters)*, 100:30007, 2012.

[150] Emanuele G Dalla Torre, Johannes Otterbach, Eugene Demler, Vladan Vuletic, and Mikhail D Lukin. Dissipative preparation of spin squeezed atomic ensembles in a steady state. *Physical Review Letters*, 110(12):120402, March 2013.

[151] J Eisert and T Prosen. Noise-driven quantum criticality. *arXiv.org:1012.5013*, December 2010.

[152] Michael Höning. Badinduzierte Korrelationen und Liouville Entropien in fermionischen Gittermodellen. Diplomarbeit, TU Kaiserslautern, May 2011.

[153] Sergey Bravyi. Classical capacity of fermionic product channels. *arXiv:quant-ph/0507282*, 2005.

[154] Eliska Greplova. *Quantum Information with Fermionic Gaussian States.* PhD thesis, Ludwig-Maximilians-Universität München, October 2013.

[155] Alexander Altland and Martin R Zirnbauer. Nonstandard symmetry classes in mesoscopic normal-superconducting hybrid structures. *Physical Review B*, 55(2):1142–1161, 1997.

[156] J E Johnson and S L Rolston. Interactions between Rydberg-dressed atoms. *Physical Review A*, 82, 2010.

[157] N Henkel, R Nath, and T Pohl. Three-Dimensional Roton Excitations and Supersolid Formation in Rydberg-Excited Bose-Einstein Condensates. *Physical Review Letters*, 104(19):195302, May 2010.

[158] F Grusdt and M Fleischhauer. Fractional quantum Hall physics with ultracold Rydberg gases in artificial gauge fields. *Physical Review A*, 87(4):043628, 2013.

[159] Jonathan B Balewski, Alexander T Krupp, Anita Gaj, Sebastian Hofferberth, Robert Löw, and Tilman Pfau. Rydberg dressing: understanding of collective many-body effects and implications for experiments . *New J. Phys.*, 16:063012, June 2014.

[160] Thomas Pohl, Eugene Demler, and Mikhail D Lukin. Dynamical crystallization in the dipole blockade of ultracold atoms. *Physical Review Letters*, 104:043002, January 2010.

[161] J Schachenmayer, I Lesanovsky, A Micheli, and A J Daley. Dynamical crystal creation with polar molecules or Rydberg atoms in optical lattices. *New Journal of Physics*, 12:103044, March 2010.

[162] R M W van Bijnen, S Smit, K A H van Leeuwen, E J D Vredenbregt, and S J J M F Kokkelmans. Adiabatic formation of Rydberg crystals with chirped laser pulses. *Journal of Physics B: Atomic, Molecular and Optical Physics*, 44(18):184008, September 2011.

[163] Peter Schauß, Johannes Zeiher, Takeshi Fukuhara, Sebastian Hild, Marc Cheneau, Tommaso Macri, Thomas Pohl, Immanuel Bloch, and Christian Gross. Dynamical crystallization in a low-dimensional Rydberg gas. *arXiv.org:1404.0980*, April 2014.

[164] T E Lee, H Häffner, and M C Cross. Antiferromagnetic phase transition in a nonequilibrium lattice of Rydberg atoms. *Physical Review A*, 84:031402, September 2011.

[165] Guifré Vidal. Efficient Classical Simulation of Slightly Entangled Quantum Computations. *Physical Review Letters*, 91(14):147902, October 2003.

[166] Herbert Spohn. An algebraic condition for the approach to equilibrium of an open N-level system. *Letters in Mathematical Physics*, 2(1):33–38, August 1977.

[167] Paul A Pearce and Katherine A Seaton. A classical theory of hard squares. *Journal of statistical physics*, 53(5-6):1061–1072, December 1988.

[168] J Honer, Robert Löw, Hendrik Weimer, Tilman Pfau, and Hans Peter Büchler. Artificial atoms can do more than atoms: Deterministic single photon subtraction from arbitrary light fields. *Physical Review Letters*, 107(9):093601, 2011.

[169] S Whitlock, R Gerritsma, T Fernholz, and R J C Spreeuw. Two-dimensional array of microtraps with atomic shift register on a chip. *New Journal of Physics*, 11(2):023021, February 2009.

[170] R Dumke, M Volk, T Müther, F Buchkremer, G Birkl, and W Ertmer. Micro-optical Realization of Arrays of Selectively Addressable Dipole Traps: A Scalable Configuration for Quantum Computation with Atomic Qubits. *Phys. Rev. Lett.*, 89(9):097903, August 2002.

[171] J Weinstein and K Libbrecht. Microscopic magnetic traps for neutral atoms. *Physical Review A*, 52(5):4004–4009, November 1995.

[172] J Qian, G Dong, L Zhou, and W Zhang. Phase diagram of Rydberg atoms in a nonequilibrium optical lattice. *Physical Review A*, 85:065401, June 2012.

[173] Anzi Hu, Tony E Lee, and Charles W Clark. Spatial correlations of one-dimensional driven-dissipative systems of Rydberg atoms. *Physical Review A*, 88(5):053627, 2013.

[174] Andrea Pelissetto and Ettore Vicari. Critical phenomena and renormalization-group theory. *Physics Reports*, 368(6):549–727, October 2002.

[175] E H Lieb and D W Robinson. The finite group velocity of quantum spin systems. *Commun.Math.Phys.*, 28(3):251–257, 1972.

[176] M Nightingale and H Blöte. Dynamic Exponent of the Two-Dimensional Ising Model and Monte Carlo Computation of the Subdominant Eigenvalue of the Stochastic Matrix. *Phys. Rev. Lett.*, 76(24):4548–4551, June 1996.

[177] E Stoll, K Binder, and T Schneider. Monte Carlo Investigation of Dynamic Critical Phenomena in the Two-Dimensional Kinetic Ising Model. *Physical Review B*, 8(7):3266–3289, October 1973.

[178] Lars Onsager. Crystal statistics. 1. A Two-dimensional model with an order disorder transition. *Phys.Rev.*, 65(3-4):117–149, 1944.

[179] P Hohenberg and B Halperin. Theory of dynamic critical phenomena. *Reviews of Modern Physics*, 49(3):435–479, July 1977.

[180] Beatriz Olmos, M Müller, and Igor Lesanovsky. Thermalization of a strongly interacting 1D Rydberg lattice gas. *New Journal of Physics*, 12(1):013024, January 2010.

[181] S Ji, C Ates, and Igor Lesanovsky. Two-dimensional Rydberg Gases and the Quantum Hard-Squares Model. *Physical Review Letters*, 107(6):060406, August 2011.

[182] Kilian Singer, Markus Reetz-Lamour, Thomas Amthor, Luis Gustavo Marcassa, and Matthias Weidemüller. Suppression of Excitation and Spectral Broadening Induced by Interactions in a Cold Gas of Rydberg Atoms. *Physical Review Letters*, 93(16):163001, October 2004.

[183] Kilian Singer, Markus Reetz-Lamour, Thomas Amthor, Simon Fölling, Michaela Tscherneck, and Matthias Weidemüller. Spectroscopy of an ultracold Rydberg gas and signatures of Rydberg–Rydberg interactions. *Journal of Physics B: Atomic, Molecular and Optical Physics*, 38(2):S321–S332, January 2005.

[184] C. Ates, T. Pohl, T. Pattard, and J. M. Rost. Many-body theory of excitation dynamics in an ultracold rydberg gas. *Phys. Rev. A*, 76:013413, Jul 2007.

[185] Amodsen Chotia, Matthieu Viteau, Thibault Vogt, Daniel Comparat, and Pierre Pillet. Kinetic Monte Carlo modeling of dipole blockade in Rydberg excitation experiment. *New Journal of Physics*, 10(4):045031, April 2008.

[186] K P Heeg, M Gärttner, and J Evers. Hybrid model for Rydberg gases including exact two-body correlations. *Physical Review A*, 86(6):063421, 2012.

[187] Hendrik Weimer, Robert Löw, Tilman Pfau, and Hans Peter Büchler. Quantum Critical Behavior in Strongly Interacting Rydberg Gases. *Physical Review Letters*, 101(25):250601, December 2008.

[188] Robert Löw, Hendrik Weimer, Ulrich Krohn, Rolf Heidemann, Vera Bendkowsky, Björn Butscher, Hans Büchler, and Tilman Pfau. Universal scaling in a strongly interacting Rydberg gas. *Physical Review A*, 80(3):033422, September 2009.

[189] T Baluktsian, B Huber, R Löw, and T Pfau. Evidence for Strong van der Waals Type Rydberg-Rydberg Interaction in a Thermal Vapor. *Phys. Rev. Lett.*, 110(12):123001, March 2013.

[190] M Reetz-Lamour, J Deiglmayr, T Amthor, and M Weidemüller. Rabi oscillations between ground and Rydberg states and van der Waals blockade in a mesoscopic frozen Rydberg gas. *New Journal of Physics*, 10(4):045026, April 2008.

[191] Y O Dudin, L Li, F Bariani, and A Kuzmich. Observation of coherent many-body Rabi oscillations. *Nature Physics*, 8(11):790–794, September 2012.

[192] A Schwarzkopf, R E Sapiro, and G Raithel. Imaging Spatial Correlations of Rydberg Excitations in Cold Atom Clouds. *Phys. Rev. Lett.*, 107(10):103001, August 2011.

[193] M Robert-de Saint-Vincent, C Hofmann, H Schempp, G Günter, S Whitlock, and M Weidemüller. Spontaneous Avalanche Ionization of a Strongly Blockaded Rydberg Gas. *Phys. Rev. Lett.*, 110(4):045004, January 2013.

[194] Peter Schauß, Marc Cheneau, Manuel Endres, Takeshi Fukuhara, Sebastian Hild, Ahmed Omran, Thomas Pohl, Christian Gross, Stefan Kuhr, and Immanuel Bloch. Observation of spatially ordered structures in a two-dimensional Rydberg gas. *Nature*, 491(7422):87–91, October 2012.

[195] David Petrosyan. Two-dimensional crystals of rydberg excitations in a resonantly driven lattice gas. *Phys. Rev. A*, 88:043431, Oct 2013.

[196] Martin Gärttner, Kilian P Heeg, Thomas Gasenzer, and Jörg Evers. Finite-size effects in strongly interacting Rydberg gases. *Physical Review A*, 86(3):033422, September 2012.

[197] C. Ates and I. Lesanovsky. Entropic enhancement of spatial correlations in a laser-driven rydberg gas. *Phys. Rev. A*, 86:013408, Jul 2012.

[198] David Petrosyan, Michael Höning, and Michael Fleischhauer. Spatial correlations of Rydberg excitations in optically driven atomic ensembles. *Physical Review A*, 87(5):053414, 2013.

[199] A Robledo and J S Rowlinson. The distribution of hard rods on a line of finite length. *Molecular Physics*, 58(4):711–721, July 1986.

[200] Z W Salsburg, R W Zwanzig, and J G Kirkwood. Molecular Distribution Functions in a One-Dimensional Fluid. *The Journal of chemical physics*, 21:1098, 1953.

[201] Francis H Ree and William G Hoover. Fifth and Sixth Virial Coefficients for Hard Spheres and Hard Disks. *The Journal of chemical physics*, 40(4):939, 1964.

[202] G Döge, K Mecke, J Møller, and D Stoyan. Grand canonical simulations of hard-disk systems by simulated tempering. *International Journal of Modern Physics C*, 15, 2004.

[203] C H Mak. Large-scale simulations of the two-dimensional melting of hard disks. *Physical Review E*, 73, 2006.

[204] P W Anderson. More is different. *Science*, 177:393, 1972.

[205] M Müller, I Lesanovsky, H Weimer, H P Büchler, and P Zoller. Mesoscopic Rydberg Gate Based on Electromagnetically Induced Transparency. *Phys. Rev. Lett.*, 102(17):170502, April 2009.

[206] David Petrosyan, Johannes Otterbach, and Michael Fleischhauer. Electromagnetically induced transparency with rydberg atoms. *Phys. Rev. Lett.*, 107:213601, Nov 2011.

[207] Alpha Gaëtan, Yevhen Miroshnychenko, Tatjana Wilk, Amodsen Chotia, Matthieu Viteau, Daniel Comparat, Pierre Pillet, Antoine Browaeys, and Philippe Grangier. Observation of collective excitation of two individual atoms in the Rydberg blockade regime. *Nature Physics*, 5(2):115–118, January 2009.

[208] M Reetz-Lamour, T Amthor, J Deiglmayr, and M Weidemüller. Rabi Oscillations and Excitation Trapping in the Coherent Excitation of a Mesoscopic Frozen Rydberg Gas. *Phys. Rev. Lett.*, 100(25):253001, June 2008.

[209] Bariani, F, Dudin, Y, Kennedy, T, and Kuzmich, A. Dephasing of Multiparticle Rydberg Excitations for Fast Entanglement Generation. *Physical Review Letters*, 108(3):030501, January 2012.

[210] Martin Gärttner, Kilian P Heeg, Thomas Gasenzer, and Jörg Evers. Dynamic formation of Rydberg aggregates at off-resonant excitation. *Physical Review A*, 88(4):043410, October 2013.

[211] Shu-Ju Tu and Ephraim Fischbach. Random distance distribution for spherical objects: general theory and applications to physics. *Journal of Physics A: Mathematical and General*, 35(31):6557–6570, August 2002.

[212] I Mourachko, D Comparat, F De Tomasi, and A Fioretti. Many-body effects in a frozen Rydberg gas. *Physical Review*, 80(2):253–256, 1998.

[213] I Beterov, I Ryabtsev, D Tretyakov, and V Entin. Quasiclassical calculations of blackbody-radiation-induced depopulation rates and effective lifetimes of Rydberg nS, nP, and nD alkali-metal atoms with n$\leq$80. *Physical Review A*, 79(5):052504, May 2009.

[214] T. M. Weber, T. Niederprüm, T. Manthey, P. Langer, V. Guarrera, G. Barontini, and H. Ott. Continuous coupling of ultracold atoms to an ionic plasma via rydberg excitation. *Phys. Rev. A*, 86:020702, Aug 2012.

[215] D Barredo, S Ravets, H Labuhn, L Béguin, A Vernier, F Nogrette, T Lahaye, and A Browaeys. Demonstration of a Strong Rydberg Blockade in Three-Atom Systems with Anisotropic Interactions. *Phys. Rev. Lett.*, 112(18):183002, May 2014.

[216] Brenton J Knuffman. *Rydberg Atoms in Ponderomotive Potentials.* PhD thesis, University of Michigan, December 2008.

[217] Thomas Amthor, Christian Giese, Christoph S Hofmann, and Matthias Weidemüller. Evidence of Antiblockade in an Ultracold Rydberg Gas. *Phys. Rev. Lett.*, 104(1):013001, January 2010.

[218] C Ates, T Pohl, T Pattard, and J Rost. Antiblockade in Rydberg Excitation of an Ultracold Lattice Gas. *Phys. Rev. Lett.*, 98(2):023002, January 2007.

[219] K Younge, A Reinhard, T Pohl, P Berman, and G Raithel. Mesoscopic Rydberg ensembles: Beyond the pairwise-interaction approximation. *Physical Review A*, 79(4):043420, April 2009.

[220] Igor Lesanovsky and Juan P Garrahan. Kinetic constraints, hierarchical relaxation, and onset of glassiness in strongly interacting and dissipative Rydberg gases. *Physical Review Letters*, 111(21):215305, November 2013.

[221] Igor Lesanovsky and Juan P Garrahan. Out-of-equilibrium structures in strongly interacting Rydberg gases with dissipation. *Physical Review A*, 90(1):011603, 2014.

[222] A Urvoy, F Ripka, I Lesanovsky, D Booth, J P Shaffer, T Pfau, and R Löw. Strongly correlated growth of Rydberg aggregates in a vapour cell. *arXiv.org:1408:0039*, August 2014.

[223] C Carr, R Ritter, C G Wade, C S Adams, and K J Weatherill. Nonequilibrium Phase Transition in a Dilute Rydberg Ensemble. *Physical review letters*, 111(11):113901, 2013.

[224] Cenap Ates, Beatriz Olmos, Juan P. Garrahan, and Igor Lesanovsky. Dynamical phases and intermittency of the dissipative quantum ising model. *Phys. Rev. A*, 85:043620, Apr 2012.

[225] Anzi Hu, Tony E Lee, and Charles W Clark. Spatial correlations of one-dimensional driven-dissipative systems of Rydberg atoms. *Physical Review A*, 88(5):053627, November 2013.

[226] Pasquale Calabrese, Fabian H L Essler, and Maurizio Fagotti. Quantum quench in the transverse field Ising chain: I. Time evolution of order parameter correlators. *Journal of Statistical Mechanics: Theory and Experiment*, 2012(07):P07016, July 2012.

[227] Pasquale Calabrese and John Cardy. Evolution of entanglement entropy in one-dimensional systems. *Journal of Statistical Mechanics: Theory and Experiment*, 2005(04):P04010, April 2005.

[228] Norbert Schuch, Michael M Wolf, Frank Verstraete, and J Cirac. Entropy Scaling and Simulability by Matrix Product States. *Physical Review Letters*, 100(3):030504, January 2008.

[229] T E Lee and C K Chan. Dissipative transverse-field Ising model: Steady-state correlations and spin squeezing. *Physical Review A*, 88(6):063811, 2013.

[230] G Vidal, J I Latorre, E Rico, and A Kitaev. Entanglement in Quantum Critical Phenomena. *Phys. Rev. Lett.*, 90(22):227902, June 2003.

[231] S Bravyi, M Hastings, and Frank Verstraete. Lieb-Robinson Bounds and the Generation of Correlations and Topological Quantum Order. *Physical Review Letters*, 97(5):050401, July 2006.

[232] Jens Eisert and Tobias Osborne. General Entanglement Scaling Laws from Time Evolution. *Phys. Rev. Lett.*, 97(15):150404, October 2006.

[233] Andreas M Läuchli and Corinna Kollath. Spreading of correlations and entanglement after a quench in the one-dimensional Bose–Hubbard model. *Journal of Statistical Mechanics: Theory and Experiment*, 2008(05):P05018, May 2008.

[234] R G Unanyan and M Fleischhauer. Entanglement dynamics in harmonic-oscillator chains. *Physical Review A*, 89(6):062330, June 2014.

[235] C. Ates, S. Sevinçli, and T. Pohl. Electromagnetically induced transparency in strongly interacting rydberg gases. *Phys. Rev. A*, 83:041802, Apr 2011.

[236] Hendrik Weimer. Variational principle for steady states of dissipative quantum many-body systems. *arXiv.org:1409.8307*, September 2014.

[237] J D Pritchard, D Maxwell, A Gauguet, K J Weatherill, M P A Jones, and C S Adams. Cooperative Atom-Light Interaction in a Blockaded Rydberg Ensemble. *Phys. Rev. Lett.*, 105(19):193603, November 2010.

[238] Thibault Peyronel, Ofer Firstenberg, Qi-Yu Liang, Sebastian Hofferberth, Alexey V Gorshkov, Thomas Pohl, Mikhail D Lukin, and Vladan Vuletic. Quantum nonlinear optics with single photons enabled by strongly interacting atoms. *Nature*, 488(7409):57–60, July 2012.

[239] Valentina Parigi, Erwan Bimbard, Jovica Stanojevic, Andrew J Hilliard, Florence Nogrette, Rosa Tualle-Brouri, Alexei Ourjoumtsev, and Philippe Grangier. Observation and Measurement of Interaction-Induced Dispersive Optical Nonlinearities in an Ensemble of Cold Rydberg Atoms. *Phys. Rev. Lett.*, 109(23):233602, December 2012.

[240] C S Hofmann, G Günter, H Schempp, M Robert-de Saint-Vincent, M Gärttner, J Evers, S Whitlock, and M Weidemüller. Sub-Poissonian Statistics of Rydberg-Interacting Dark-State Polaritons. *Phys. Rev. Lett.*, 110(20):203601, May 2013.

[241] Simon Baur, Daniel Tiarks, Gerhard Rempe, and Stephan Dürr. Single-Photon Switch Based on Rydberg Blockade. *Phys. Rev. Lett.*, 112(7):073901, February 2014.

[242] Alexey V. Gorshkov, Rejish Nath, and Thomas Pohl. Dissipative many-body quantum optics in rydberg media. *Phys. Rev. Lett.*, 110:153601, Apr 2013.

[243] Ofer Firstenberg, Thibault Peyronel, Qi-Yu Liang, Alexey V Gorshkov, Mikhail D Lukin, and Vladan Vuletic. Attractive photons in a quantum nonlinear medium. *Nature*, 502(7469):71–75, April 2014.

[244] P Bienias, S Choi, O Firstenberg, M F Maghrebi, M Gullans, M D Lukin, A V Gorshkov, and H P Büchler. Scattering resonances and bound states for strongly interacting Rydberg polaritons. *arXiv.org:1402.7333*, February 2014.

[245] T Giamarchi. *Quantum physics in one dimension*. Oxford University Press, 2003.

[246] M Dalmonte, G Pupillo, and Peter Zoller. One-Dimensional Quantum Liquids with Power-Law Interactions: The Luttinger Staircase. *Physical Review Letters*, 105(14):140401, September 2010.

[247] Balázs Dóra, Masudul Haque, and Gergely Zaránd. Crossover from Adiabatic to Sudden Interaction Quench in a Luttinger Liquid. *Phys. Rev. Lett.*, 106(15):156406, April 2011.

[248] D. N. Pinder. The contracting square quantum well. *American Journal of Physics*, 58(1):54–58, 1990.

[249] T R Taha and M J Ablowitz. *Analytical and numerical aspects of certain nonlinear evolution equations IV. Numerical, modified Korteweg-de Vries equation*, volume 55. Journal of Computational Physics, 1988.

[250] R J Baxter. Dimers on a Rectangular Lattice. *Journal of Mathematical Physics*, 9(4):650, 1968.

[251] Ulrich Schollwöck. The density-matrix renormalization group. *Reviews of Modern Physics*, 77:259–315, Apr 2005.

[252] Juan José García-Ripoll. Time evolution of Matrix Product States. *New Journal of Physics*, 8(12):305–305, December 2006.

[253] A J Daley, C Kollath, Ulrich Schollwöck, and G Vidal. Time-dependent density-matrix renormalization-group using adaptive effective Hilbert spaces. *Journal of Statistical Mechanics: Theory and Experiment*, 2004(04):P04005, April 2004.

[254] Michael Zwolak and Guifré Vidal. Mixed-State Dynamics in One-Dimensional Quantum Lattice Systems: A Time-Dependent Superoperator Renormalization Algorithm. *Physical Review Letters*, 93(20):207205, November 2004.

[255] Tomaz Prosen and Marko Znidaric. Matrix product simulations of non-equilibrium steady states of quantum spin chains. *Journal of Statistical Mechanics: Theory and Experiment*, 2009(02):P02035, February 2009.

[256] Michael J Hartmann. Polariton Crystallization in Driven Arrays of Lossy Nonlinear Resonators. *Phys. Rev. Lett.*, 104(11):113601, March 2010.

[257] S R Clark, J Prior, M J Hartmann, D Jaksch, and M B Plenio. Exact matrix product solutions in the Heisenberg picture of an open quantum spin chain. *New Journal of Physics*, 12(2):025005, February 2010.

[258] N Goldman and J Dalibard. Periodically Driven Quantum Systems: Effective Hamiltonians and Engineered Gauge Fields. *Physical Review X*, 4(3):031027, 2014.

[259] Debashish Chowdhury and Dietrich Stauffer. Principles of Equilibrium Statistical Mechanics. Wiley-VCH Verlag GmbH & Co. KGaA, Weinheim, FRG, 2000.

[260] C Ates, Thomas Pohl, T Pattard, and et al. Strong interaction effects on the atom counting statistics of ultracold Rydberg gases. *Journal of Physics B: Atomic, Molecular and Optical Physics*, 39(11):L233, 2006.

Publications

Publications relevant for this thesis

In the following I list publications containing parts of the material of this thesis. All of these are the result of collaborations of several authors, which all contributed to the conception of the project, discussion of results and writing of the manuscript. Parts predominantly contributed by me are indicated.

[H-2012] M. Höning, M. Moos, and M. Fleischhauer. *Critical exponents of steady-state phase transitions in fermionic lattice models.* Phys. Rev. A, **86**, 013606, 2012

Parts of this publication were already included in my Diploma thesis [152]. This work was done in collaboration with M. Fleischhauer and with contributions by M. Moos. In particular all analytic and numeric work was done by me.

[H-2013a] M. Höning, D. Muth, D. Petrosyan, and M. Fleischhauer. *Steady-state crystallization of Rydberg excitations in an optically driven lattice gas.* Phys. Rev. A **87**, 023401, 2013

This work was done in collaboration with D. Muth, D. Petrosyan and M. Fleischhauer. In particular numeric simulations for the RE model and the derivation of analytic results for the NN model were done by me.

[H-2013b] D. Petrosyan, M. Höning, and M. Fleischhauer. *Spatial correlations of Rydberg excitations in optically driven atomic ensembles.* Phys. Rev. A, **87**, 053414, 2013

This publication was a collaboration of D. Petrosyan, myself and M. Fleischhauer. In particular the analytic results for the hard rod model were contributed by me.

[H-2013c] F. Grusdt, M. Höning, and M. Fleischhauer. *Topological edge states in the one-dimensional superlattice Bose-Hubbard model.* Phys. Rev. Lett., **110**, 260405, 2013

This work was a collaboration of F. Grusdt, myself and M. Fleischhauer. Particularly the DMRG simulations were provided by me.

[H-2014a] M. Höning, W. Abdussalam, M. Fleischhauer, and T. Pohl. *Antiferromagnetic long-range order in dissipative Rydberg lattices.* Phys. Rev. A, **90**, 021603(R), 2014

This publication is the result of a collaboration of M. Fleischhauer and myself with W. Abdussalam and T. Pohl from Dresden. In particular the analysis of critical exponents was provided by me.

[H-2014b] F. Grusdt, and M. Höning. *Realization of Fractional Chern Insulators in the Thin-Tours-Limit with Ultracold Bosons* Phys. Rev. A, **90**, 053623, 2014

This work is a collaboration of Fabian Grusdt and myself. In particular I did the numerical simulations and developed the scheme for the experimental implementation.

[H-2015a] T.M. Weber, M. Höning, T. Niederprüm, T. Manthey, O. Thomas, V. Guarrera, M. Fleischhauer, G. Barontini, and H. Ott. *Creation, excitation and ionization of a mesoscopic superatom.* Nature Physics doi:10.1038/nphys3171, 2015

This publication is the result of a collaboration of M. Fleischhauer and myself with the group of H. Ott. In particular all numerical simulations were done by me.

Publications in preparation

[H-2015b] M. Höning, F. Grusdt, R. Jen, and M. Fleischhauer. *Topological aspects of the one-dimensional extended superlattice Bose-Hubbard model.*

[H-2015c] M. Moos, M. Höning and M. Fleischhauer. *Wigner crystallization of polaritons by light storage in Rydberg gases*

[H-2015d] M. Höning, D. Linzner, and M. Fleischhauer. *The dissipative transverse Ising chain: bistability and long range order*

Publications not related to this thesis

[H-2010] E.M. Graefe, M. Höning, and H.J. Korsch. *Classical limit of a non-Hermitian quantum dynamics-a generalized canonical structure.* J. Phys. A, **43**, 075306, 2010

List of Figures

Lebenslauf

Persönliche Angaben

Name	Michael Höning
Geburtsdatum, Ort	20.03.1989 in Worms, Deutschland
Familienstand	verheiratet, keine Kinder
Staatsangehörigkeit	Deutsch

Studium

05/2011 - 12/2014	Technische Universität Kaiserslautern Arbeitsgruppe Prof. Fleischhauer Theoretische Quantenoptik Angestrebter Abschluss: Dr. rer. nat.
04/2008 - 05/2011	Technische Universität Kaiserslautern Studiengang: Physik Abschluss: Diplom Physiker (Note 1.2)
10/2006 - 03/2008	Technische Universität Kaiserslautern Studiengang: Früheinstieg ins Physikstudium

Auszeichnungen und Stipendien

06/2012	Nachwuchspreis Physik 2011 Technische Universität Kaiserslautern
01/2009 - 04/2011	Stipendium Studienstiftung des Deutschen Volkes
04/2008	Achter Platz Auswahlwettbewerb für die internationale Physik Olympiade

Beruflicher Werdegang

05/2011 - heute	Technische Universität Kaiserslautern AG Fleischhauer Position: wissenschaftlicher Mitarbeiter Aufgaben: Forschung (offene und wechselwirkende Systeme), Betreuung von Tutorien

10/2008 - 03/2011	Fachbereich Mathematik Position: wissenschaftliche Hilfskraft Aufgaben: Betreuung von Tutorien (Höhere Mathematik für Ingenieure)
05/2009 - 09/2009	AG Eggert Position: wissenschaftliche Hilfskraft Aufgaben: Forschung
10/2008 - 03/2009	AG Korsch Position: wissenschaftliche Hilfskraft Aufgaben: Forschung
04/2008 - 03/2009	AG Aeschlimann Position: wissenschaftliche Hilfskraft Aufgaben: Forschung

Ausbildung

1999 - 04/2008	Gauß Gymnasium Worms Abschluss: Abitur (Note 1.0)
07/2005 - 09/2005	Belmont Secondary School, Victoria, Canada

Engagement

2003 - 2008	Organisation vielfältiger Veranstaltungen für katholische Kirche Worms - Eisbachtal
2005 - 2010	Trainer und Mannschaftsführer für Tischtennis Abteilung des TV 1879 Horchheim
2008 - 2014	Betreuer für Landeswettbewerb Physik an der TU Kaiserslautern
seit 2013	Wissenschaftlicher Gutachter für Physical Review A, B und X

Danksagung

Mein primärer Dank gilt allen, die in den vergangenen Jahren enthusiastische und scharfsinnige Diskussionspartner waren. Ohne Ihre Beiträge und Herausforderungen wäre diese Arbeit nicht möglich gewesen.

Eine unentbehrliche Bedeutung für diese Dissertation trägt mein Betreuer Michael Fleischhauer. Vielen Dank, dass du mich nicht einen vorgezeichneten Weg entlang geleitet hast, sondern immer auf meine Ideen und Ziele eingegangen bist. Das entgegengebrachte Vertrauen und die vielen ermöglichten Chancen werden mir als gutes Vorbild für die Zukunft dienen. Ebenso die Fähigkeit in den entscheidenden Momenten meinen Ehrgeiz herauszufordern

Die nicht lokale Wechselwirkung mit Fabian Grusdt in Boston und darüber hinaus, war Grundlage der Arbeiten zu Topologie in Quantengasen. Mit Freude erinnere ich mich zurück an die mit Verve geführte Diskussionen über den Sinn und Unsinn von Topologie, aber vor allem an den Eifer und die Effizienz mit der unserer Projekte vorangetrieben wurden. Den restlichen Mitgliedern der AG Fleischhauer ein herzliches Dank für die vielen Diskussionen bei Keks und Kaffee und die geteilten Abenteuer rund um die Welt.

Insbesondere in der Anfangsphase meiner Arbeit teilte David Petrosyan seinen Erfahrungsschatz über Rydberg-Physik mit mir und in den gemeinsamen Arbeiten legten wir die Basis für viele weitere Projekte. Ich danke Thomas Pohl und Wildan Abdussalam für die gemeinsame Erkundung von Rydberg-Kristalle und Thomas Pohl gebührt weiterer Dank für seine Bereitschaft Gutachter meiner Arbeit zu sein.

Das Feld der Quantenoptik und meine Arbeit leben von der Verschränkung zwischen Theorie und Experiment. Ich danke Tobias Weber und Herwig Ott, dass wir uns gemeinsam den Herausforderungen eines mesoskopischen Superatoms gestellt haben und so ein weiteres Beispiel für diese erfolgreiche Kollaboration geben konnten.

Für die aufgezeigten Chancen auf dem Weg hin zu meiner Promotion bin ich Andreas Christoph, Hans-Jürgen Korsch, Eva-Maria Gräfe und der Studienstiftung des deutschen Volkes zu tiefem Dank verpflichtet.

Abschließend danke ich Klara für die geteilte Zeit und die liebevolle Unterstützung aller meiner Pläne.